72-481

OKOYE, Josephat Kanayo, 1941-
CHARACTERISTICS OF TRANSVERSE MIXING IN
OPEN-CHANNEL FLOWS.

California Institute of Technology,
Ph.D., 1971
Engineering, general

University Microfilms, A XEROX Company, Ann Arbor, Michigan

THIS DISSERTATION HAS BEEN MICROFILMED EXACTLY AS RECEIVED.

CHARACTERISTICS OF TRANSVERSE MIXING IN OPEN-CHANNEL FLOWS

Thesis by

Josephat Kanayo Okoye

In Partial Fulfillment of the Requirements

For the Degree of

Doctor of Philosophy

California Institute of Technology

Pasadena, California

1971

(Submitted November 5, 1970)

PLEASE NOTE:

Some pages have small
and indistinct type.
Filmed as received.

University Microfilms

ACKNOWLEDGMENTS

The writer expresses his deepest gratitude to his adviser, Dr. Norman H. Brooks, who suggested this project and was constantly a source of unwavering advice, assistance, and encouragement.

The writer also wishes to thank Dr. Vito A. Vanoni and Dr. Fredric Raichlen for their kind advice and assistance, and Dr. E. John List for his comments during the writing of the thesis.

For his invaluable assistance and instruction in the design and construction of the laboratory equipment, the writer is especially indebted to Mr. Elton F. Daly, supervisor of the shop and laboratory. The assistance of Robert L. Greenway in the construction of the apparatus is also much appreciated.

The writer also wishes to thank Mr. Carl A. Green Jr., for the preparation of the drawings; Mr. Carl T. Eastvedt for the photography; Mrs. Alrae Tingley for typing the manuscript; and Mrs. Patricia A. Rankin and Mrs. Arvilla F. Krugh for their helpful secretarial aid. The writer also appreciates the efforts of the laboratory assistants: Messrs. Raul Basu, George Chan, Yoshiaki Daimon, Brady Farrand, Edward F. Thompson, W. H. Waggy, Paul T. Wegener, and Mashio Yatsuzuka who performed various duties during the investigation.

This study was supported by the Federal Water Quality Administration (formerly Federal Water Pollution Control Administration) through Grants No. 16000 DGY and No. 16070 DGY. The experiments were conducted in the W. M. Keck Laboratory of Hydraulics and Water

Resources of the California Institute of Technology.

ABSTRACT

The transverse spreading of a plume generated by a point source in a uniform open-channel flow is investigated. A neutrally-buoyant tracer was injected continuously at ambient velocity through a small round source at a point within the flow. Tracer concentration was measured in situ at several points downstream of the source using conductivity probes.

Tracer concentration was analyzed in two phases.

In Phase I, time-averaged concentration was evaluated, its distribution within the plume determined, and characteristic coefficients of transverse mixing calculated. It was shown that the transverse mixing coefficient varied with the flow level and was highest near the water surface where the flow velocity was greatest. In contrast to previous speculation, the ratio of the depth-averaged coefficient of transverse mixing $\overline{D}_z$ to the product of the (bed) shear velocity u_* and the flow depth d was not a constant but depended on the aspect ratio $\lambda = d/W$, where W = flume width. For laboratory experiments $\overline{D}_z/u_*d$ decreased from 0.24 to 0.093 as λ increased from 0.015 to 0.200.

In Phase II, the temporal fluctuation of tracer concentration was studied in three sections. In the first, the intermittency factor technique was used to delineate three regions of the plume cross section: an inner core where tracer concentration $c(t)$ was always greater than the background C_b; an intermittency region where $c(t)$ was only intermittently greater than C_b; and the outer region

where c_b was never exceeded. Dimensional analysis furnished universal curves for prediction of the geometric characteristics of the three regions. In the second section, the entire plume, at a fixed station, was treated as a fluctuating cloud. Variances characterizing the fluctuation of the plume centroid and the variation of the plume width were calculated and compared. In the third section, the intensity and probability density of the concentration fluctuations at fixed points were calculated. The distribution of the peak-to-average ratio was also determined.

Finally the results of the two phases of study were interrelated to evaluate their contributions to the transverse spreading of the plume.

TABLE OF CONTENTS

Chapter		Page
1	INTRODUCTION	1
	1.A. Objective of Study	1
	1.B. Structure of Report	5
2	PAST STUDIES, ANALYTICAL INVESTIGATIONS, AND EXPERIMENTAL OBJECTIVE (Phase I)	6
	2.A. Past Studies	6
	2.A.1. The Conservation of Mass Equation	6
	2.A.2. Solutions of the Diffusion Equation	11
	2.A.3. Statistical Models for Turbulent Mixing	15
	2.A.4. Measurements of the Transverse Mixing Coefficient	19
	2.B. Analytical Investigations	24
	2.B.1. The Concept of a Turbulent Mixing (or Exchange) Coefficient	24
	2.B.2. The Transverse Exchange Coefficient as Derived From the Convective-Diffusion Equation	26
	2.B.3. The Transverse Mixing Coefficient as a Function of Depth	29
	2.B.4. Method of Calculating the Transverse Mixing Coefficient	30
	2.B.5. The Combined Effect of Shear and Vertical Mixing on Initial Distributions	32
	2.C. Experimental Objective	34
	2.C.1. General	34
	2.C.2. Calculation of the Transverse Mixing Coefficient	35

Chapter		Page
	2.C.3. Determination of Other Parameters	36
	a. Attenuation of peak concentration	36
	b. Iso-concentration maps	38
	c. Other related parameters	38
	2.C.4. Summary of the Experimental Objective (Phase I)	38
3	PAST STUDIES, ANALYTICAL INVESTIGATIONS, AND EXPERIMENTAL OBJECTIVE (Phase II)	40
	3.A. Past Studies	40
	3.A.1. Conservation Equation for Mean-Square Concentration Fluctuations (msf)	40
	3.A.2. The Fluctuating Plume Model	43
	3.A.3. Previous Measurements of Point Concentration Fluctuation Parameters	46
	3.A.4. Summary of Previous Studies (Phase II)	49
	3.B. Analytical Investigations	50
	3.B.1. Relationship Between Variances for the Generalized Fluctuating Plume	50
	3.B.2. The Concept and Application of the Intermittency Factor	53
	3.B.3. Characteristics of the Region of Intermittency	61
	3.C. Experimental Objective	64
	3.C.1. General	64
	3.C.2. Determination of the Characteristics of the Plume Front Oscillation	65
	a. The intermittency factor, $I_f(z)$	65
	b. Geometric parameters	66
	c. Frequency of "zero occurrence"	67

Chapter			Page
		d. Probability densities $p_1(T_1)$, $p_2(T_2)$	68
	3.C.3.	Photo Analysis	69
	3.C.4.	Statistical Analysis of Point Concentration Variations	70
	3.C.5.	Summary of the Experimental Objective (Phase II)	72
4	LABORATORY EXPERIMENTS (Phases I and II)		73
	4.A.	Apparatus for the Experiments	73
	4.A.1.	Flumes--Gross Characteristics	73
		a. The 85-cm flume	73
		b. The 110-cm flume	77
		c. Roughening of the 110-cm flume bottom	79
	4.A.2.	Concentration Detection Equipment	82
		a. The overall system	82
		b. The conductivity probe	84
		c. Bridge circuit	86
		d. Analog recording system	88
		e. Analog-to-digital (A/D) data acquisition system	89
	4.A.3.	Velocity Measuring Device	93
	4.A.4.	The Tracer Injection System	94
	4.A.5.	Photo Analysis Equipment	96
	4.B.	Experimental Procedure	97
	4.B.1.	Identification Code for Flumes and Experiments	97
	4.B.2.	Typical In Situ Measurement	99

Chapter			Page
		a. Establishment of uniform flow and calculation of hydraulic parameters	99
		b. Tracer preparation	102
		c. Calibration of probes	105
		d. A typical run	107
	4.B.3. Photo Studies		109
	4.B.4. Velocity Measurements and Results		110
	4.B.5. Probe Response to High Frequency Loading		113
	4.C. Reduction of Data		117
	4.C.1. Recorded Concentration Data		117
	4.C.2. Effects of Sampling Period and Sampling Rate on Calculated Parameters		119
		a. Effects on the time-mean concentration	119
		b. Effects on the intermittency factor, I_f	122
		c. Choice of the sampling period and the sampling rate	122
	4.C.3. Choice of the Threshold Concentration C_t for Determination of the Intermittency Factor, I_f		125
5	PRESENTATION AND DISCUSSION OF EXPERIMENTAL RESULTS (Phase I)		129
	5.A. Hydraulic Data		129
	5.B. Transverse Distributions of Time-Averaged Concentration		132
	5.C. Variance of the Transverse Concentration Distribution		138
	5.C.1. Calculation of the Variance		138

Chapter		Page
	5.C.2. Growth of the Variance σ^2 with Distance x Downstream of Source	141
5.D.	The Transverse Mixing Coefficient	146
	5.D.1. The Depth-Averaged Mixing Coefficient, $\overline{D}_z$	146
	a. Calculation of the depth-averaged mixing coefficient	146
	b. Variation of $\overline{\theta} = \overline{D}_z/u_* d$ with the aspect ratio $\lambda = d/W$	149
	c. Dependence of $\overline{\theta}$ on λ for experiments performed by other investigators	153
	5.D.2. Variation of the Transverse Mixing Coefficient with Depth Caused by Shear and the Non-Uniform Distribution of the Vertical Diffusivity with Depth	155
5.E.	Near-Source Vertical Distribution of Tracer Due to Shear and the Vertical Diffusivity	163
5.F.	Distribution of the Tracer Concentration $C(\xi,\eta,0)$ Along the Axial Plane	169
	5.F.1. Vertical Distribution of $C(\xi,\eta,0)$ at Various ξ	169
	5.F.2. Longitudinal Attenuation of the Tracer Concentration Along the Plume Axis	170
5.G.	Iso-Concentration Maps	178
	5.G.1. Tracer Distribution on Cross-sectional Planes	178
	5.G.2. Tracer Distribution on Lateral Planes Parallel to the Flume Bottom	182
5.H.	Summary	184

Chapter		Page
6	PRESENTATION AND DISCUSSION OF EXPERIMENTAL RESULTS (Phase II)	187
	6.A. Parameters Associated with the Plume Front Oscillation Model	187
	6.A.1. The Transverse Distribution of the Intermittency Factor	187
	6.A.2. Growth of the Geometric Parameters W_f, $\tilde{Z}$, Δ, and σ_I^2 of the Intermittency Region with Distance x	196
	a. Overall characteristics	
	b. Prediction of the extreme limit of the plume boundary, W_f	200
	c. Prediction of the mean position $\tilde{Z}$ of the plume edge	204
	d. Growth of the variance σ_I^2 of the region of intermittency	208
	6.A.3. Temporal Characteristics of the Plume Front Oscillation	209
	a. Frequency of "zero occurrence" $\omega_0(z)$	209
	b. Characteristic period, wave length and amplitude of the frontal oscillation	213
	c. Probability densities $p_1(T_1)$, $p_2(T_2)$, and $p(T)$ of the intermittency function $h(z,t)$ at a Fixed Point	215
	d. Cross-correlation analysis of $h(z,t)$ for two points located at $z = \tilde{Z}$ and $z = -\tilde{Z}$	218
	6.B. Analysis of Plume Variation Using the Fluctuating Plume Model	223
	6.C. Concentration Variations at Fixed Points Within the Plume	228

Chapter		Page
	6.C.1. Transverse Distribution of the Intensity of Concentration Variation	228
	6.C.2. Distribution of the Peak-to-Average Ratio, P_a	232
	6.C.3. Probability Density Functions of Concentration Variations	236
	6.D. Summary Discussion (Phase II)	237
7	SUMMARY AND CONCLUSIONS	242
	7.A. Results Related to Phase I	242
	7.B. Results Related to Phase II	245
LIST OF SYMBOLS		250
LIST OF REFERENCES		257
APPENDIX		263

LIST OF FIGURES

Figure		Page
2.1	Definition sketch of plume geometry and coordinate axes.	12
2.2	Development of the vertical profile of material within the plume with increasing distance from the source: near-source plume behavior.	33
3.1	Gifford's one-dimensional fluctuating plume model.	44
3.2	Sketch of a typical concentration record at a fixed point as a function of time.	56
3.3	Forms of the intermittency function $h(z,t)$ at the fixed point z for selected threshold levels.	58
3.4	The intermittency factor model for cross-wise plume variation.	60
3.5	Transverse distributions of the intermittency factor for selected plume front oscillation models.	62
4.1	Overall view of the 85-cm flume looking upstream (adapted from Fischer (2)).	74
4.2	The instrument carriage with probes placed in flume S1 during an experiment.	76
4.3	Schematic of the 110-cm flume (adapted from Prych (39)).	78
4.4	Size distribution of the rocks used for roughening the 110-cm flume bottom.	80
4.5	Plan view of the rocks as placed on the flume bottom.	81
4.6	Perspective view of the entire flume with the bottom covered with rocks.	81
4.7	Flow diagram of the concentration detection system.	83
4.8	Details of the conductivity probe.	85

LIST OF FIGURES (Cont'd)

Figure		Page
4.9	Details of the bridge circuit and related external connections to the Sanborn analog recorder.	87
4.10	Data acquisition system for digitizing analog records and storing the digitized output on tape.	90
4.11	Flow diagram of the digital data system.	91
4.12	Sketch of the tracer injection system.	95
4.13	Determination of the energy slope S_f in the 85-cm flume RUN 508.	101
4.14	Calibration curves for the conductivity probes.	106
4.15	Velocity profiles at two stations and several sections in flume S2; RUN 706V.	111
4.16	Velocity contours at a station 15 m from the flume entrance for RUNS 404V and 708V. Cross-marks indicate points where velocities were measured. Velocities on isovels in cm/sec.	112
4.17	Response of the conductivity probes to high frequency loading showing (a) the transient response curves, and (b) the corresponding frequency response.	115
4.18	Typical concentration data at two points as recorded by the analog recorder shown in a(i) and a(ii). The same data digitized by the A/D converter at 60 samples/sec are correspondingly plotted in b(i) and b(ii); RUN 806.	118
4.19	The effect of sampling period on time-mean concentration; RUN 904.	120
4.20	The effect of sampling rate on time-mean concentration; RUN 904.	121
4.21	The effect of sampling period on the intermittency factor; RUN 904.	123
4.22	The effect of sampling rate on the intermittency factor; RUN 904.	124

LIST OF FIGURES (Cont'd)

Figure		Page
4.23	The effect of the choice of threshold concentration C_t on the intermittency factor. Each curve applies to a fixed point, and C_t is normalized by the local mean concentration; RUN 904.	126
4.24	Modification of the transverse distribution of the intermittency factor by the choice of the threshold concentration; RUN 804.	127
5.1	Transverse distributions of the time-averaged concentration measured at various distances $\xi = x/d$ downstream of source, and at various levels of the flow: (a) $\eta = \eta_h = 0.368$, (b) $\eta = 0.800$, (c) $\eta = 0.236$; RUN 706.	133
5.2	Transverse distributions of the cumulative mean concentration measured at various distances ξ from the source and at the flow level $\eta = 0.632$. Plots on arithmetic probability paper; RUN 708.	134
5.3	Transverse distributions of the cumulative mean concentration measured at various distances ξ from the source and at the flow level $\eta = 0.368$. Plots on arithmetic probability paper; RUN 405.	135
5.4	Growth of the variance σ^2 with distance x at various levels of the flow η and as a depth average; RUN 706.	142
5.5	Growth of the variance σ^2 with distance x at various levels of the flow η and as a depth average; RUN 701.	143
5.6	Growth of the variance σ^2 with distance x at various levels of the flow η and as a depth average; RUN 607.	144
5.7	Growth of the variance σ^2 with distance x at various levels of the flow η and as a depth average; RUN 708.	145
5.8	Growth of the depth-averaged variance $\overline{\sigma^2}$ with distance x downstream of source for various normal depths; RUNS 707, 702, 704, 509, 511, 603.	148

LIST OF FIGURES (Cont'd)

Figure		Page
5.9	Variation of the depth-averaged, dimensionless mixing coefficient $\overline{\theta}$ with the aspect ratio λ for experiments performed in this study. The average value of $\overline{\theta}$ for RUNS 508, 509, 510, 511, and 512 is plotted for $\lambda = 0.062$.	152
5.10	Variation of the depth-averaged, dimensionless mixing coefficient $\overline{\theta}$ with the aspect ratio λ for all experiments performed in the present and past studies.	154
5.11	Depth variation of the normalized transverse mixing coefficient θ_1 due to shear only; RUNS 511, 704, 512.	157
5.12	Depth variation of the normalized transverse mixing coefficient θ due to shear and the interaction between the vertical distributions of the variance σ^2 and of the vertical diffusivity D_y; RUN 511.	160
5.13	Depth variation of the normalized transverse mixing coefficient θ due to shear and the interaction between the vertical distributions of the variance σ^2 and of the vertical diffusivity D_y; RUN 704.	161
5.14	Vertical distribution of material $\overline{M}_0(\xi,\eta) = M_0(\xi,\eta)/(Q_s/\overline{ud})$ for (a) RUN 510 and (b) RUN 509. The curves are theoretical solutions of Eq. 5.15 at various ξ. The plotted points were measured.	166
5.15	Theoretical levels of maximum $\overline{M}_0(\xi,\eta)$ for four levels of tracer injection η_h. The plotted points were measured; RUNS 512, 510, 509, 511.	168
5.16	Attenuation of the normalized tracer concentration β at four levels of the flow η on the vertical axial plane; RUN 512, $\eta_h = 0.850$.	171
5.17	Attenuation of the normalized tracer concentration β at four levels of the flow η on the vertical axial plane; RUN 510, $\eta_h = 0.632$.	171

LIST OF FIGURES (Cont'd)

Figure		Page
5.18	Attenuation of the normalized tracer concentration β at four levels of the flow η on the vertical axial plane; RUN 704, $\eta_h = 0.368$.	172
5.19	Attenuation of the normalized tracer concentration β at four levels of the flow η on the vertical axial plane; RUN 511, $\eta_h = 0.051$.	172
5.20	Attenuation of the depth-averaged concentration $\bar{\beta}$ on the vertical axial plane for four levels of tracer injection; RUNS 512, 704, 511, 510.	174
5.21	Iso-concentration contours on cross-sectional planes. Crosses show points where tracer was detected. Concentration values on the contour lines are rendered dimensionless (as in Eq. 5.22) when multiplied by 2.08; RUN 511, $\eta_h = 0.051$.	179
5.22	Iso-concentration contours on cross-sectional planes. Crosses show points where tracer was detected. Concentration values on the contour lines are rendered dimensionless (as in Eq. 5.22) when multiplied by 1.56; RUN 509, $\eta_h = 0.368$.	180
5.23	Iso-concentration contours on cross-sectional planes. Crosses show points where tracer was detected. Concentration values on the contour lines are rendered dimensionless (as in Eq. 5.22) when multiplied by 2.11; RUN 512, $\eta_h = 0.850$.	181
5.24	Iso-concentration contours plotted on transverse planes (parallel to the flume bottom) at four levels of the flow. Concentration values on the contour lines are rendered dimensionless (as in Eq. 5.22) when multiplied by 2.11; RUN 512, $\eta_h = 0.850$.	183
5.25	Dimensionless distances ξ_m from the source where concentration is maximum at given levels of the flow η for injection levels $\eta_h = 0.850$, 0.368, and 0.095.	185

LIST OF FIGURES (Cont'd)

Figure		Page
6.1	Plots of digitized concentration data c(t) and the corresponding intermittency function, h(t). Sampling rate = 60 samples/sec. Typical periods of "occurrence" T_{1j} and "non-occurrence" T_{2j} are shown on h(t); RUN 804.	188
6.2	Transverse distributions of the intermittency factor for three normal depths d. Measurements were made at the level of tracer injection $\eta_h = 0.368$ and at the same stations for all runs; RUNS 802, 804, 406.	190
6.3	Photographs of the tracer plume taken in flume S1 for four different normal depths d.	191
6.4	Transverse distribution of the intermittency factor at various levels of the flow η. All measurements were made at x = 380 cm from the source; RUN 808.	193
6.5	Representation of the transverse distribution of the intermittency factor on a universal curve. Measurements were made at four stations and four levels at one station; RUN 808.	195
6.6	Growth of the geometric characteristics of the region of intermittency; RUN 802.	197
6.7	Plots of $(W_f/d)^2$ versus $(\chi/d)(u_{*b}/\bar{u})$ for experiments performed in flume 2 with the bottom hydraulically smooth (A) or rough (B); RUNS 808, 804, 802, 406, 404, 405.	202
6.8	Universal representation of the growth of the extreme limit W_f of the plume boundary (where $I_f = 0.0$) for all experiments; RUNS 808, 804, 802, 406, 404, 405.	203
6.9	Universal representation of the growth of the mean position of the plume front $\tilde{Z}$ (where $I_f \approx 0.50$) for all experiments; RUNS 808, 804, 802, 406, 404, 405.	207
6.10	Transverse distribution of the frequency of zero occurrence ω_0. Cumulative values of ω_0 are plotted on arithmetic probability scales. Fitted lines are Gaussian; RUN 404.	212

LIST OF FIGURES (Cont'd)

Figure		Page
6.11	Probability densities $p_1(T_1)$, $p_2(T_2)$ of the pulse lengths (or periods) T_1, T_2 of the intermittency function h(t) at various distances ξ; RUN 904.	216
6.12	Probability density p(T) for the combined periods (or pulse lengths) of occurrence and non-occurrence of the intermittency function h(t) at various distances ξ; RUN 904.	217
6.13	Temporal variation of the plume boundaries at fixed stations downstream of the source. Five seconds of data plotted at intervals of 1/6-sec is shown at each station; RUN 300.	224
6.14	Temporal variation of the instantaneous plume width at fixed stations for the plume boundaries shown in Figure 6.13; RUN 300.	225
6.15	Transverse distribution of the rms σ_s of the concentration fluctuation at various distances ξ from the source. Measurements made at the level of tracer injection $\eta_h = 0.368$; RUN 804.	229
6.16	Transverse distributions of the coefficient of variation $C_v = \sigma_s/C$ at several ξ. Measurements made at the level of tracer injection $\eta_h = 0.368$; RUN 804.	231
6.17	Transverse distributions of the peak-to-average ratios P_a at several ξ. Measurements made at the level $\eta = \eta_h = 0.368$; RUN 804.	233
6.18	Attenuation of the peak-to-average ratios P_1 (along $z = 0$), P_2 (along $z = W_p$), and of the coefficients of variation V_1 (along $z = 0$), V_2 (along $z = W_c$) with ξ; RUN 804.	235
6.19.	Typical transverse distribution of the mean concentration C, the rms of concentration fluctuation σ_s, the intermittency factor I_f, and the frequency of zero occurrence ω_0 at a fixed distance $x/d = 16.6$ from the source; RUN 804.	239

LIST OF TABLES

Table		Page
2.1	Previous measurements of the transverse diffusion coefficient in open-channel flows	20
3.1	Summary of previous measurements of concentration fluctuations at fixed points	47
3.2	Summary of previous measurements of the intermittency factor, γ	55
4.1	Classification of flumes and experiments	98
4.2	Relative conductivities of the constituents of the tracer solution	102
5.1	Summary of hydraulic data	130
5.2	Comparison of the variances σ^2 computed by the moment method and σ_p^2 derived from the probability method	140
5.3	Comparison of $d\sigma^2/dx$ at various levels η with $d\overline{\sigma^2}/dx$, the rate of growth of the depth-averaged variance	146
5.4	Summary of measured depth-averaged mixing coefficient $\overline{D}_z$ and related parameters	151
5.5	Summary of measured parameters related to the decay of concentration along $z = 0$	175
6.1	Comparison between $\tilde{Z}$ and $z_{0.5}$	198
6.2	Values of x_v and x_I for various experiments	199
6.3	Values of the exponents γ_2 and γ_3 for different flows	205
6.4	Relative wave length $L_f(x)/d$ of the plume front oscillation	214
6.5	Cross-correlation analysis of $h(z,t)$ at the two opposite points $z = -\tilde{Z}$ and $z = \tilde{Z}$; RUN 904	220
6.6	Parameters associated with the fluctuating plume; RUN 300	226

LIST OF TABLES (Cont'd)

Table		Page
A.1	Variance σ^2 (cm^2) of the transverse concentration distributions at various distances ξ and flow levels η; all experiments included	264
A.2	Reference guide to Experiments and Figures	268

CHAPTER 1

INTRODUCTION

This chapter is divided into two sections: the first summarizes the objective of this investigation, the second describes the form of the presentation that follows.

1.A. OBJECTIVE OF STUDY

This is an experimental investigation of the transverse mixing characteristics of a two-dimensional shear flow. It seeks to determine, through appropriate measurements and analysis of pertinent data, the parameters controlling the rate of transverse spreading of a tracer continuously injected at ambient velocity into an open-channel flow from a point source. Calculation of the transverse diffusion coefficient D_z which expresses the rate of the cross-wise mixing is emphasized.

Knowledge of the value and variation of D_z is a key to the determination of the other mixing characteristics of the flow and an indispensable input in practically all pollution control analyses especially those involving mathematical modelling. The transverse mixing rate controls the rate of attenuation of the time-averaged peak concentration of a dispersant. For the instantaneous source, D_z is inversely related to the coefficient of longitudinal dispersion in a manner demonstrated by Elder (1) and corroborated by Fischer (2). Simply stated this relationship implies that the faster the spread in the transverse direction, the slower the rate of elongation of the

pollutant cloud parallel to the flow. Accurate prediction and reproducibility of D_z would justify the use of the diffusion equation as a tool in the analysis of turbulent mixing processes in a shear flow.

Attempts to solve the conservation equation theoretically in an effort to predict the downstream concentration of a plume generated by a continuous point source have resulted mainly in providing qualitative results under very restrictive conditions. Smith (3), for example, determined that, for the diffusion of smoke in an isotropic, turbulent atmosphere, the cross-wise concentration profile is Gaussian only if $u(y)$ and D_z grow as the $\frac{1}{2}$-power of y, where $u(y)$ is the flow velocity at height y above the ground. Analytical solutions for the more realistic logarithmic velocity profile are too complicated to yield meaningful results. In view of the apparent theoretical deadlock, an experimental study seems to be a potential basis for further progress.

In an open-channel flow of infinite width, the depth-averaged vertical diffusivity $\overline{D}_y$ can be determined theoretically by assuming that the transfer of mass and momentum are analogous. Using the logarithmic velocity profile, the ratio $\overline{D}_y/u_*d$ is found to be $\kappa/6$ where u_* is the shear velocity, d is the mean flow depth, and κ the von Kármán constant. Since κ approximately equals 0.40, $\overline{D}_y/u_*d \approx 0.067$. This value has been confirmed by measurements in open-channel flows by Vanoni (4) and Al-Saffar (5).

Theoretical evaluation of the depth-averaged transverse mixing coefficient $\overline{D}_z$ along similar lines is not possible because of zero shear. Experimental values of the dimensionless coefficient

$\overline{\theta} = \overline{D}_z/u_*d$ reported in the literature are always greater than $\overline{D}_y/u_*d$, and exhibited larger scatter. For example Elder's (1) data, as corrected by Sullivan (6), gave a value of $\overline{\theta} = 0.16$ for mixing in a small laboratory flume. Fischer (7) calculated $\overline{\theta} = 0.24$ for a canal flow, and Yotsukura et al. (8) reported $\overline{\theta} = 0.60$ for mixing in the Missouri River.

This experimental study seeks to determine more accurate values of $\overline{\theta}$ and to formulate a universal relationship for predicting $\overline{\theta}$ for various flow configurations. Detailed measurements of time-averaged concentrations are made in order to establish both sectional and lateral distributions of tracer fluid within the plume. Such measurements, although reported for some wind-tunnel experiments, for example Davar (9), are virtually non-existent in open-channel flows. The attenuation of the axial concentration with diffusion time is also studied to check the power-law decay exponent of 0.50 predicted by Fickian diffusion. Vertical variation of time-averaged characteristics of the mixing process is also investigated.

A second and equally important objective of this study is to examine, in the Eulerian framework, the temporal variation of the tracer concentration as a factor in the transverse mixing phenomenon. In many pollution control problems especially where highly toxic or radio-active material is the pollutant, there is interest in not only the mean concentration values (at any given point) but also the duration and probability distribution of these values. Quantitative data on this problem for the open-channel flow are again scarce in the literature.

Concentration fluctuations were analyzed in three sections.

In the first, the intermittency factor technique is used to compute the incidence and duration of concentrations above some threshold value, C_t. The intermittency factor I_f is defined as the fraction of time when the instantaneous concentration c exceeds C_t at a fixed point. Values of I_f are calculated for given stations at various points along a transverse line on a fixed level of the flow. By adopting analyses similar to those utilized for the growth of wakes behind cylinders (Townsend (10), Corrsin and Kistler (11), and Demetriades (12)), or the development of boundary layers (Klebanoff (13), and Fielder and Head (14)), a region of intermittency where $0 < I_f < 1.0$ is determined. The geometric and temporal characteristics of this region are studied in an attempt to understand the mechanism of plume growth.

In the second section, the plume is photographed rapidly from above the water surface at various stations from the source. The resulting record is analyzed according to the fluctuating plume model proposed by Gifford (16). The measurements are compared with theoretical predictions.

In the third section, concentration values recorded at fixed points are subjected to the usual statistical analysis to determine the parameters: mean squares, rms, coefficients of variation, peak-to-average ratios, probability density and distribution functions and power spectra. Appropriate profiles are developed to verify theoretical prediction of self-similarity of the transverse distribution of the mean square fluctuation by Csanady (15). Other profiles are presented. The results are compared to measurements made in atmospheric turbulence. Finally the relationship between the three

methods of analysis is discussed.

1.B. STRUCTURE OF REPORT

The presentation, in keeping with the aims of the study, falls naturally into two phases. Phase I deals with parameters derived from time-averaged concentrations. Phase II considers temporal variations of c within the plume. Rather than divide the report into two separate parts, the chapters are set up to identify the two phases distinctly and at the same time avoid redundancy and duplication.

Chapter 2 summarizes the past studies, analytical investigations, and the experimental objective relevant to phase I. Chapter 3 is structured identically to Chapter 2 except that all considerations relate to concentration fluctuations, phase II.

The experiments described in Chapter 4 cover phases I and II because the apparatus for experiments and the experimental procedure are generally the same for both phases. The distinction in methods of data analysis, however, is appropriately delineated.

Chapter 5 contains experimental results and a discussion of these results for phase I only. Similarly, Chapter 6 presents results and their discussion for the study of concentration variations.

An overall summary of the entire investigation is the subject of Chapter 7. It presents the principal conclusions drawn from this study as they relate to both time-mean concentration and concentration variations.

CHAPTER 2

PAST STUDIES, ANALYTICAL INVESTIGATIONS, AND EXPERIMENTAL OBJECTIVE (Phase I)

This chapter deals with the transverse distributions of the time-averaged concentration of a tracer injected continuously at ambient velocity. The source is essentially a point and the environment is a turbulent shear flow in a wide rectangular channel. Previous theoretical and experimental investigations are discussed. The experimental objective of this phase of the study is also presented.

2.A. PAST STUDIES

2.A.1. The Conservation of Mass Equation. The statement of mass conservation is a logical starting point for evaluating the distribution of a scalar quantity transported and diffused in a moving environment. By considering the convection of this quantity through an incremental control volume and applying mass balance, the following mass conservation equation is derived:

$$\frac{\partial(\rho\phi)}{\partial t} + \frac{\partial}{\partial x_i}(\rho u_i \phi) = \frac{\partial}{\partial x_i}\left(\epsilon_m \frac{\partial(\rho\phi)}{\partial x_i}\right) + R - S. \qquad (2.1)$$

In Eq. 2.1, ϕ is the scalar concentration in mass of tracer per unit mass of solution; x_i is the coordinate in the i^{th} direction where $i = 1$, 2, and 3; u_i is the instantaneous fluid velocity in the direction x_i; ρ is the fluid density; ϵ_m is the molecular diffusion coefficient; t is time; and R and S are the source and sink strengths per unit

volume respectively. For example, sediment precipitation can be considered a source and bacterial die-off a sink if these processes occur within the flow field.

Derivation of Eq. 2.1 involves no assumptions with regard to the mixing mechanism. Rather, it states that there is an exact balance between mass flows through the control surface and the rate of change of mass within the control volume. Eq. 2.1 is therefore exact and forms the basis for all phenomenological equations pertaining to turbulent (or indeed laminar) mixing processes.

For an incompressible flow, where $\Delta\rho/\rho$ is small (see for example List (17))

$$\frac{\partial \rho}{\partial t} = - \frac{\partial \rho}{\partial x_i} = 0. \tag{2.2}$$

and thus the continuity equation becomes approximately

$$\frac{\partial u_i}{\partial x_i} = 0. \tag{2.3}$$

Thus, if the flow is incompressible, the mass conservation equation for the solute reduces to

$$\frac{\partial \phi}{\partial t} + u_i \frac{\partial \phi}{\partial x_i} = \frac{\partial}{\partial x_i}\left(\epsilon_m \frac{\partial \phi}{\partial x_i}\right) + \frac{1}{\rho}(R - S). \tag{2.4}$$

If, further, there are no sources and sinks,

$$\frac{\partial \phi}{\partial t} + u_i \frac{\partial \phi}{\partial x_i} = \frac{\partial}{\partial x_i}\left(\epsilon_m \frac{\partial \phi}{\partial x_i}\right). \tag{2.5}$$

For the special case of turbulent flow, u_i and ϕ can each be decomposed to a time-averaged value and a fluctuating element such that

$$u_i = U_i + u_i' \tag{2.6a}$$

and

$$\phi = \Phi + \phi' \tag{2.6b}$$

where the time averages are defined by

$$U_i = \frac{1}{T_m} \int_{t_o}^{t_o + T_m} u_i(t)\, dt \tag{2.7a}$$

$$\Phi = \frac{1}{T_m} \int_{t_o}^{t_o + T_m} \phi(t)\, dt \tag{2.7b}$$

t_o is an arbitrary time base, T_m is the period of averaging, and u_i' and ϕ' are the fluctuating components. The period T_m must be so large that the mean quantities remain invariant for averages taken over longer periods.

Averaging Eq. 2.5 in the sense of Eqs. 2.7, the following result ensues:

$$\frac{\partial \Phi}{\partial t} + U_i \frac{\partial \Phi}{\partial x_i} = \frac{\partial}{\partial x_i} \left(\epsilon_m \frac{\partial \Phi}{\partial x_i} - \overline{u_i' \phi'} \right). \tag{2.8}$$

This form applies for quasi-steady cases, i.e. where $\partial\Phi/\partial t$ reflects only the slow changes over periods much longer than T_m.

Further simplification of Eq. 2.8 requires expression of the

turbulent flux term, $-\overbrace{u_i'\phi'}$ into a form similar to the other terms of the equation. This is accomplished by the combination of the Boussinesq (18) approximation which relates flux to a local gradient and the Reynolds (19) analogy which states that the transfer coefficient of mass is proportional to that of momentum. The result is that the turbulent mass flux is related directly to the local gradient of the time-averaged concentration by means of the turbulent-transport coefficient, ϵ_{ij}, such that

$$-\overbrace{u_i'\phi'} = \epsilon_{ij} \frac{\partial \Phi}{\partial x_j} \tag{2.9}$$

where ϵ_{ij} is either a constant or a second-order tensor with $i,j = 1,2,3$. Since ϵ_{ij} is hardly expected to remain constant in the entire flow field, especially for anisotropic conditions, it is usually retained as a tensor. The physical implications of Eq. 2.9 will be discussed further in a later section of this chapter.

Combining Eqs. 2.8 and 2.9 yields the relationship

$$\frac{\partial \Phi}{\partial t} + U_i \frac{\partial \Phi}{\partial x_i} = \frac{\partial}{\partial x_i}\left(\epsilon_m \frac{\partial \Phi}{\partial x_i} + \epsilon_{ij} \frac{\partial \Phi}{\partial x_j}\right) \tag{2.10}$$

which states that the rates of local and convective change of Φ are balanced by the negative divergence of the flux of Φ due to molecular and turbulent diffusion.

It has been recognized (see for example Batchelor and Townsend (20)) that even at a high Reynolds number the interaction between molecular and turbulent diffusion might substantially increase molecular contribution to total mixing in a turbulent flow. Mickelsen

(21) found, however, that in an air stream accelerated molecular diffusion was negligible in comparison to eddy mixing--indicating that $\epsilon_{ij} >> \epsilon_m$.

The fluid particles in this study will be assumed "tagged" so that each "marked" particle is much larger than the molecular dimension but much smaller than the smallest length scale of turbulence. Molecular mixing is thus restricted to within each particle and the redistribution of the particles (or turbulent mixing) will be effected by eddies. The particles also occur at very low concentrations and are of the same density, ρ, as the fluid.

If the "marked"-particle concentration is denoted by c, all operations performed on ϕ can, similarly, be applied to c with the result:

$$\frac{\partial C}{\partial t} + U_i \frac{\partial C}{\partial x_i} = \frac{\partial}{\partial x_i}\left(D_{ij} \frac{\partial C}{\partial x_j}\right) \qquad (2.11)$$

where D_{ij} represents the mass transfer coefficient characteristic of the diffusion of the "marked" particles in the turbulent environment, and C is the time-averaged concentration defined in the sense of Eq. 2.7b.

By assuming that the axes x_i are oriented along the principal directions, D_{ij} becomes a diagonal tensor for which $D_{ij} = 0$ for $i \neq j$, and $D_{ij} = D_{ii}$ for $i = j$. Dagan (22) has shown that this diagonalization is valid in the flow regions away from boundary corners. Thus Eq. 2.11 becomes

$$\frac{\partial C}{\partial t} + U_i \frac{\partial C}{\partial x_i} = \frac{\partial}{\partial x_i}\left(D_{ii}\frac{\partial C}{\partial x_i}\right). \qquad (2.12)$$

This is frequently termed the convective-diffusion equation.

2.A.2. Solutions of the Diffusion Equation. Adopting cartesian coordinates oriented as shown in the definition sketch, Fig. 2.1, the diffusion equation takes the form

$$\frac{\partial C}{\partial t} + u\frac{\partial C}{\partial x} + v\frac{\partial C}{\partial y} + w\frac{\partial C}{\partial z} = \frac{\partial}{\partial x}\left(D_x \frac{\partial C}{\partial x}\right) + \frac{\partial}{\partial y}\left(D_y \frac{\partial C}{\partial y}\right) + \frac{\partial}{\partial z}\left(D_z \frac{\partial C}{\partial z}\right) \qquad (2.13)$$

where u, v, and w are, respectively, the time-averaged velocity components in the x, y, and z directions, and D_x, D_y, and D_z are the mass transfer coefficients of the tracer particles in the respective directions x, y, and z.

For the mixing of a plume from a continuous point source in a shear flow as is shown in Figure 2.1, the following assumptions can be introduced:

(i) $$v = w = 0, \qquad (2.14)$$

(ii) the plume is "slim" (or the "boundary-layer" approximation applies):

$$\frac{\partial}{\partial x}\left(D_x \frac{\partial C}{\partial x}\right) \ll \frac{\partial}{\partial z}\left(D_z \frac{\partial C}{\partial z}\right),$$

$$\frac{\partial}{\partial y}\left(D_y \frac{\partial C}{\partial y}\right) = O\left[\frac{\partial}{\partial z}\left(D_z \frac{\partial C}{\partial z}\right)\right], \qquad (2.15)$$

As a consequence, Eq. 2.13 (for the steady state: $\partial C/\partial t = 0$) reduces to

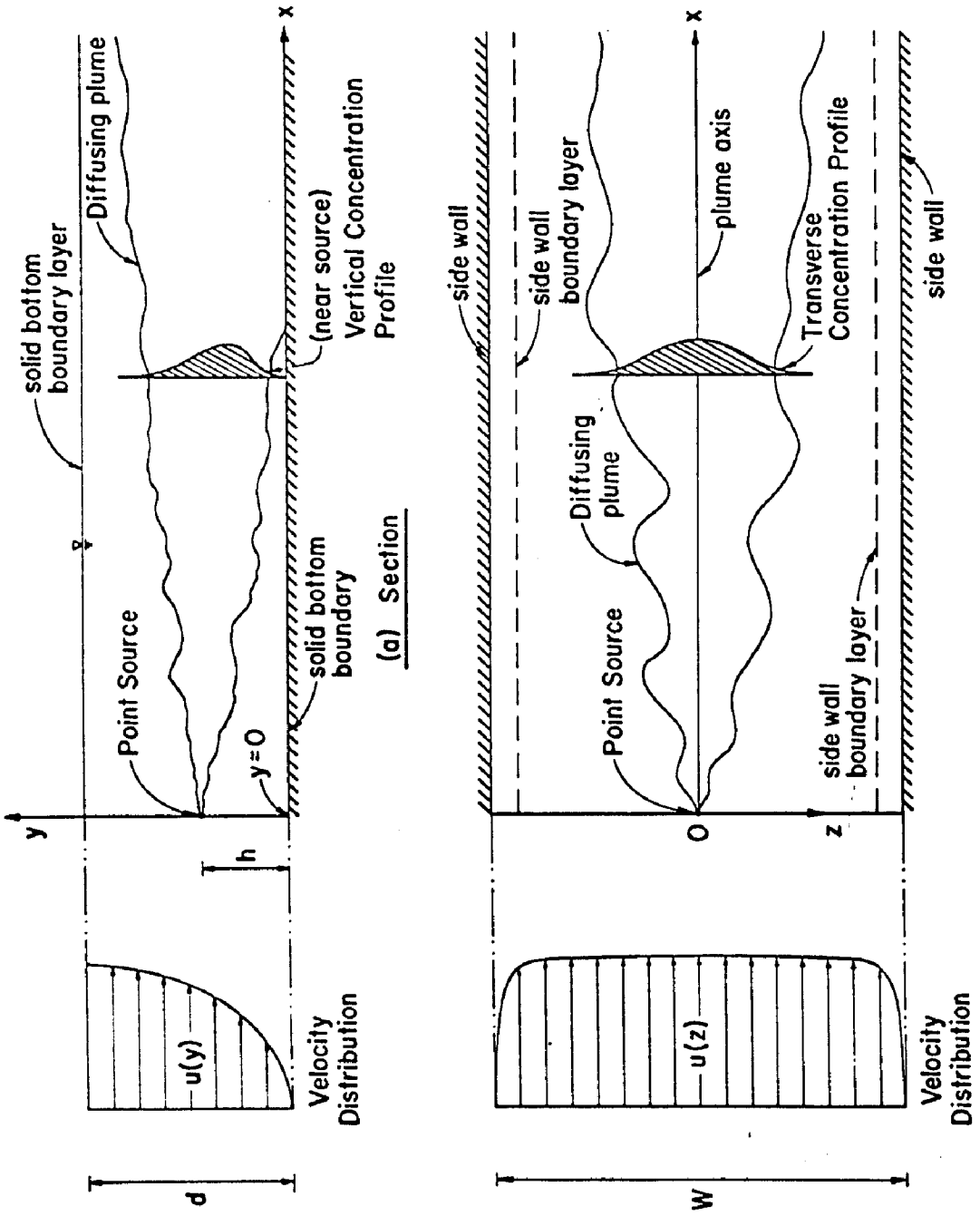

Fig. 2.1. Definition sketch of plume geometry and coordinate axes

$$u\frac{\partial C}{\partial x} = \frac{\partial}{\partial y}\left(D_y \frac{\partial C}{\partial y}\right) + \frac{\partial}{\partial z}\left(D_z \frac{\partial C}{\partial z}\right). \qquad (2.16)$$

The difficulty in solving Eq. 2.16 arises mostly because the characteristics and variation of D_y, D_z, and u are either unknown or too complex to permit a functionally representable solution. To facilitate the solution, a conjugate power law, which relates u, D_y, and D_z to powers of y, has been adopted by several investigations especially for atmospheric diffusion (Sutton (23), Davies (24), Yih (25), and Smith (3)). Smith (3), for example, in an attempt to solve Eq. 2.16 for a continuous elevated point source in the atmosphere assumed that $u \propto (y+h)^{\mu}$, $D_y = D_z = D_2(y+h)^{1-\mu}$, where h = height of the source and μ and D_2 are constants. He applied the following boundary conditions:

(i) $$C = Q_s \delta(y)\delta(z) \qquad (2.17)$$

where δ is the Dirac delta function and Q_s, the source strength defined below,

(ii) $$D_y \frac{\partial C}{\partial y} = 0 \quad \text{at} \quad y = 0, \qquad (2.18)$$

(iii) $$C \to 0 \quad \text{as} \quad y, |z| \to \infty. \qquad (2.19)$$

Ignoring diffusive transport, material conservation requires that the source strength

$$\int_{-\infty}^{\infty}\int_{0}^{\infty} uC \, dy \, dz = Q_s = \text{constant}. \qquad (2.20)$$

Smith found that, for $\mu = \frac{1}{2}$, an exact solution could be derived. For this case, the cross-wise concentration profiles were Gaussian. He also showed analytically that both the zeroth and second moments of the transverse distribution of C were complicated functions of x, y, h, and μ from which qualitative relationships could be derived. A significant contribution of Smith's analysis is that it provided a mathematical system for testing the sensitivity of the solutions to variations of the parameters h, D_2, and μ which, in turn, indicate the effects of source height, the diffusion coefficients, and shear.

Another approach used for solution of the convective-diffusion equation is a form of the moment-integral method formally introduced by Aris (26) and extended by Saffman (27) for the unsteady longitudinal distribution of C due to an instantaneous point source. Basically the q^{th} moment of C is evaluated by the relation

$$M_q(x,y) = \int_{-\infty}^{\infty} z^q C(x,y,z)\, dz\,, \qquad (2.21)$$

and then M_q is integrated over the flow depth, and substituted into the diffusion equation to obtain solutions for the various moments usually zeroth, first, and second.

Aris (26) applied this method to the dispersion of an instantaneous source in a pipe flow and derived that the variance of the longitudinal distribution of the solute grows linearly with time. He also found that the asymptotic distribution for C(x,t) is Gaussian in x, where C is averaged over the cross section, and the time t is large.

Saffman (27), in analyzing the dispersion of a cloud of material in the atmosphere, defined his moments by

$$M_{pq}(y,t) = \int_{-\infty}^{\infty} \int_{-\infty}^{\infty} x^p z^q c \, dx \, dz, \quad (p,q \geq 0) \tag{2.22}$$

and, differentiating between a bounded and an unbounded atmosphere, developed solutions for the various moments. He asserted that the asymptotic solution is attained if the time

$$t >> \frac{d^2}{2D}, \tag{2.23}$$

where $y = d$ is the height below which the material is confined and D is a characteristic lateral diffusion coefficient. He obtained useful expressions for the centroid and variance of the longitudinal concentration distribution.

Although the moment approach of Aris and Saffman was used for material distribution of a slug in the direction of flow, the method is useful for analysis of the transverse distribution of the continuous source plume as will be illustrated later.

2.A.3. Statistical Models for Turbulent Mixing. The basis for statistical modelling in the analysis of turbulent diffusion is the classical paper by G. I. Taylor (28), "Diffusion by Continuous Movements," a Lagrangian analysis in which the coordinate system moves with the mean particle velocity in the direction of flow. Taylor showed that the variance of the displacement of a fluid particle due to turbulent velocity fluctuations can be expressed completely in

terms of the mean square eddy velocity and the Lagrangian correlation coefficient $R(t')$ defined by

$$R(t') = \frac{\overline{w'(t)w'(t+t')}}{\overline{w'^2}}, \tag{2.24}$$

where $w'(t)$ = eddy velocity of the fluid particle at time t, and $w'(t+t')$ = the value of w' at time $t+t'$ for the same particle. He deduced that if the turbulence is homogeneous and stationary a characteristic coefficient D_z of lateral mixing can be defined by

$$D_z = \frac{1}{2}\frac{d\sigma^2}{dt} \tag{2.25}$$

valid for large time T such that

$$T_* = \int_0^T R(t')\,dt' = \text{constant}.$$

In Eq. 2.25, σ^2 = mean square of the lateral displacement of the fluid particle.

Direct use of Eq. 2.25 for the calculation of D_z has been hampered by the fact that $R(t')$ cannot be measured but only estimated (see for example Taylor (28), Van Driest (29), Kalinske and Pien (30), and Orlob (31,32)). For shear flows intercorrelations between eddy velocities in the y and z directions would have to be evaluated. These cannot, at present, be measured either. Nevertheless Taylor's theory laid the foundation for other statistical models which have immensely aided interpretation of turbulent diffusion processes.

Batchelor (33) generalized Taylor's one particle analysis to the case of three dimensions for steady homogeneous turbulence, establishing in the process, criteria for the existence of a diffusion coefficient. He defined the mean concentration for a finite volume of marked fluid by

$$P(\underline{x},t) = \int P(\underline{x}',0)q(\underline{x}-\underline{x}',t)\ dv(\underline{x}') \tag{2.26}$$

where $P(\underline{x},t)$ is the probability that the point defined by the position vector $\underline{x}$ lies within the marked fluid at time t. The probability $P(\underline{x},0)$ is unity or zero according to whether $\underline{x}$ lies within or outside the volume V defined by

$$V = \int P(\underline{x},t)\ dv(\underline{x}), \tag{2.27}$$

where $dv(\underline{x})$ is a volume element, and $q(\underline{x}-\underline{x}',t)$ is the probability density function (p.d.f.) of the displacement $\underline{x}-\underline{x}'$ at time t. Thus, the generalized dispersion d_{ij} is given by

$$d_{ij}(t) = d_{ij}(0) + \overline{X_i(t)X_j(t)} \tag{2.28}$$

where $X_i(t)$ is the i^{th} component of the fluid particle displacement in time t and i, j take values 1, 2, 3 in the normal tensor notation. Assuming that X_1, X_2, and X_3 are Gaussian both jointly and separately, it can be shown by substitution that the probability $P(\underline{x},t)$ described by the equation

$$\frac{\partial P}{\partial t}(\underline{x},t) = D_{ij}\frac{\partial^2 P(\underline{x},t)}{\partial x_i \partial x_j} \tag{2.29}$$

is a solution of Eq. 2.26 if

$$D_{ij} = \frac{1}{2} \frac{\partial \Omega_{ij}}{\partial t} \tag{2.30}$$

where

$$\Omega = \begin{vmatrix} \overline{X_1^2} & \overline{X_2X_1} & \overline{X_3X_1} \\ \overline{X_1X_2} & \overline{X_2^2} & \overline{X_3X_2} \\ \overline{X_1X_3} & \overline{X_2X_3} & \overline{X_3^2} \end{vmatrix} . \tag{2.31}$$

Thus, under the conditions specified, a general diffusion coefficient D_{ij} can be defined such that

$$D_{ij} = \frac{1}{2} \frac{d\overline{X_iX_j}}{dt} . \tag{2.32}$$

This result is consistent with Taylor's one-dimensional relation, but while Eq. 2.24 requires T_* to be constant, existence of the coefficient D_{ij} for $i = j = 3$ requires only that X_i have a Gaussian p.d.f.

Furthermore, it has been shown that if the coordinates of a diffusing particle are assumed to vary in time according to a Markov random process, the diffusion Eq. 2.13 (for $v = w = 0$) is a Fokker-Planck equation for this random motion (Monin (34)). As such the mass transfer coefficients can be defined as in Eq. 2.25 for all t.

From these and other statistical models, the following deductions can be made:

(i) a coefficient of turbulent mixing can be represented completely by the mean square of the velocity fluctuation and a Lagrangian correlation coefficient,

(ii) the probability density function for the fluid particle displacement $X_i(t)$ tends to a Gaussian function of the transverse coordinates for large t as demonstrated by application of the Central Limit Theorem, and

(iii) without recourse to a "mixing length" approximation, a diffusion coefficient satisfying a Fickian type equation can be defined in the form of Eq. 2.32 even for small t.

2.A.4. Measurements of the Transverse Mixing Coefficient.

Table 2.1 summarizes measurements of the transverse mixing coefficient made by several investigators in various flow configurations. The result obtained by Elder (1) and used by Fischer (2, 7), and Sayre and Chang (35) provided the stimulus for the present study. Elder assumed that the velocity distribution was logarithmic so that

$$u = u_{max} + \frac{u_*}{\kappa} \ell n\ \eta, \tag{2.33}$$

where ℓn is the natural logarithm, u_{max} the maximum velocity, $\eta = y/d$, and d = mean flow depth. For the linear shear distribution,

$$\frac{\tau}{\rho} = (1 - \eta)u_*^2 = -\overline{v'u'}, \tag{2.34}$$

where τ = local shear. Assuming Reynolds analogy for vertical diffusivity within the entire flow field,

$$D_y = -\overline{v'c'} \Big/ \frac{\partial C}{\partial y} = -\overline{v'u'} \Big/ \frac{\partial u}{\partial y}. \tag{2.35}$$

Using Eqs. 2.33, 2.34, and 2.35, the depth-averaged value $\overline{D}_y$ of

Table 2.1. Previous measurements of the transverse diffusion coefficient in open-channel flows

Source	Channel	Channel Bottom Roughness	Tracer	Injection Depth η_h [1]	Level of Concentration Measurement $\eta = y/d$	Test Reach m	Channel Width W m	Mean Depth of Flow d cm	Mean Velocity $\bar{u}$ cm/sec	Shear Velocity u_* cm/sec	Aspect Ratio d/W	Dimensionless Diffusion Coefficient $\bar{\epsilon}$, ϵ_p [2]	Method of determining tracer concentration
(1)	(2)	(3)	(4)	(5)	(6)	(7)	(8)	(9)	(10)	(11)	(12)	(13)	(14)
				Dissolved Tracers (A)									
Elder (1)	laboratory flume	smooth	Permanganate solution	1.0	over the entire depth	2.2	0.36	1.2	21.6	1.59	0.033	0.16 [3]	Illumination on photo films
Fischer (2)	Atrisco Feeder Canal (N. M.)	sand-bed	Rhodamine WT dye	≈1.0	≈1.0	490	18.30	67.4	64.6	6.25	0.037	0.24	Fluorometer analysis of grab samples
Glover (42) [4]	laboratory flume	smooth	salt solution [5]	≈1.0	N/A [6]	18.3	2.42	14.1	66.3	7.16	0.058	0.07 [7]	Electrical strain gage
Glover (42)	Columbia River	sand-bed	radioisotope mixture	0.67	0.0	9200	305	306.0	135	8.76	0.010	0.73	Probably scintillation or GM counter
Kalinske and Pien (30) [4] Pien (41) [4]	laboratory flume	smooth	HCl and alcohol mixture	0.39	0.39	1.5	0.69	15.8	94.5	5.19	0.229	0.08	Chemical analysis of samples collected for about two minutes
Patterson and Gloyna (43)	Colorado River nr. Austin, Tex.	sand-bed	fluorescent dyes	1.0	≈1.0	900	N/A	N/A	57.3-80.8	N/A	0.025	D_s=492 cm²/sec	Fluorometer analysis of continuous samples
Sayre and Chang (35) [8]	laboratory flume	wooden cleats	fluorescent dyes	0.25 0.50 0.75	0.25 0.50 0.75	35.0	2.38	14.7	23.5	3.90	0.062	0.17	Fluorometer analysis of continuous samples
Sullivan (6)	laboratory flume	smooth	Gentian violet dye	over the entire depth	over the entire depth	5.5	0.76	7.3-10.2	22.9-15.3	1.21-0.83	0.096-0.134	0.133-0.108	Photo analysis
Yotsukura et al (8)	Missouri River nr. Blair, Nebr.	sand-bed	Rhodamine B dye	1.0	≈1.0	10,000	226	270.0	175 0	7.40	0.012	0.60	Fluorometer analysis of grab samples
				Floating Particle Tracers (B)									
Engelund (40)	laboratory flume	sand roughness	9 mm plastic ball	1.0 1.0	1.0 1.0	8.5 8.5	2.20 2.20	5.5 17.3	30.0 34.4	3.60 1.60	0.025 0.079	0.20 [9]	Photographed ball position on a horizontal grid
Orlob [10] (31, 32)	laboratory flume	expanded metal screens	polyethylene discs	1.0	1.0	4.6	1.22	5.3	30.8	3.68	0.044	0.16	Counting particles caught in compartmentalized collector
Sayre and Chamberlain (38)	laboratory flume	sand bed (small dunes)	polyethylene particles	1.0	1.0	33.0	2.44	17.7	48.7	3.51	0.073	0.24	Identical to Orlob's
Sayre and Chang (35) [7]	laboratory flume	wooden cleats	polyethylene particles	1.0	1.0	35.0	2.38	14.7	23.5	3.90	0.062	0.23	Identical to Orlob's

NOTES:

(A) Dissolved tracers were introduced as continuous point sources. However, Elder (1) used both dye drops and continuous point sources. Sullivan (6), and Patterson and Gloyna (43) injected pulses of dye.

(B) Floating particles were released singly on the water surface at a point on the flume center line.

[1] η_h = h/d where h=injection height above channel bottom and d=flow depth.

[2] $\bar{\epsilon} = \bar{D}_s/u_*d$ for dissolved tracers. $\epsilon_p = D_p/u_*d$ for floating particles.

[3] Depth-integrated value.

[4] A typical experiment has been chosen.

[5] The tracer was heavier than the ambient water; thus producing a density flow.

[6] N/A = not available.

[7] Inconsistent results were shown by the author.

[8] Runs LA-D-1 and LA-P-1 were selected for the dissolved tracer and the floating particle experiments respectively.

[9] Calculated from Engelund's data on the growth of the cross-wise variance.

[10] The values of d, $\bar{u}$, u_*, d/W and D_{spn} listed are the average values for the 120 experiments reported by Orlob (31).

the vertical diffusivity becomes

$$\frac{\overline{D}_y}{u_* d} = \frac{\kappa}{6} . \tag{2.36}$$

Assuming that the depth-averaged transverse mixing coefficient, $\overline{D}_z$, could be expressed in a form similar to Eq. 2.36, Elder predicted that, for isotropic turbulence,

$$\overline{\theta} = \frac{\overline{D}_z}{u_* d} = \frac{\kappa}{6}$$

$$\approx 0.067 \tag{2.37}$$

since the von Kármán constant, $\kappa \approx 0.40$.

To evaluate $\overline{D}_z$ experimentally, Elder measured the depth-integrated concentration distributions for both dye slugs and a fixed, continuous point source in an open-channel flow about 1.0 cm deep. He calculated the lateral half-width W_z (lateral distance between points where C equals one half of its peak value) at various distances from the source. From the growth of W_z^2 with x, he calculated $\overline{D}_z$ using the modified Einstein equation:

$$\overline{D}_z = \frac{1}{2} \overline{u} \frac{d\overline{\sigma^2}}{dx} , \tag{2.38}$$

where $\overline{\sigma^2}$ is the depth-averaged variance of the transverse distribution of the tracer concentration. By his data, the dimensionless coefficient $\overline{\theta} = \overline{D}_z/u_* d$ was 0.16.†

---

† The value 0.228 reported by Elder (1) has been shown to be in error by Sullivan (6). According to Sullivan (6), Elder assumed that $W_z = 2\sigma$ instead of the true value of 2.36σ. The correct normalized value is thus $0.228(2/2.36)^2 = 0.16$.

Sullivan (6) introduced pulses of dye over the flow depth in a flume 76.3 cm wide. The working section was about 2 meters long. He photographed the slug at various downstream positions. Using a Joyce Microdensitometer, he developed depth-averaged cross-wise concentration profiles. His calculated values of $\overline{\theta}$ ranged from 0.108 to 0.133 for normal depths 10.19 cm to 7.32 cm.

Fischer (7) measured the transverse spread of Rhodamine WT dye tracer injected continuously into a canal 18.3 meters wide in a flow 67 cm deep. He calculated variances σ^2 directly from measured concentration distributions across the channel at various stations. For both centerline and bank injections of the tracer, he found that the normalized transverse mixing coefficient $\overline{\theta} = 0.24$.

In a similar experiment, Yotsukura et al. (8) measured the diffusion of Rhodamine B dye injected continuously on the surface of the Missouri River. The source was located at the river center line just downstream of the Blair (Neb.) bridge and measurements were made over a 10 km stretch of the river. The transverse coefficient, determined from an Einstein-type equation was $\overline{\theta} \approx 0.60$.

Other experiments designed to simulate diffusion in homogeneous turbulence involve releasing slightly-buoyant particles on the water surface and observing their lateral distribution at various downstream stations. The idea was introduced by Orlob (31, 32) who released small polyethylene discs on the water surface of an open channel 122 cm wide. The particles were collected, at various distances downstream of the release point, in 1-cm compartments of a collector extending the full width of the channel. He analyzed his

measurements by using Kolmogoroff's (36) theory of local similarity for very high Reynolds number flow and by assuming an analogy between molecular and turbulent diffusion. He asserted that the transverse diffusion coefficient D_p for the particles could be represented by

$$D_p = 0.0136\, E^{1/3} L_z^{4/3}, \qquad (2.39)$$

where E is the mean rate of energy dissipation per unit mass of fluid, and L_z a characteristic length scale which, according to Orlob, is proportional to the 4/3-power of the flow depth. It is doubtful, however, that Eq. 2.39 applies to Orlob's experiments. Batchelor (37) has clearly shown that validity of such a relationship (i.e. Eq. 2.39) requires that $\sigma^2 \ll L_1^2$, where L_1 is the largest eddy size effecting mixing. Orlob's experiments, in which the flow depth d ranged from 1.6 cm to 10.70 cm and the test reach was 460 cm, were outside the prescribed limit.

Sayre and Chang (35) studied, among other things, the lateral dispersion of both dissolved solute and floating particles in a flume 238 cm wide and roughened at the bottom with wooden cleats. In experiments practically identical to those of Orlob, they determined that $D_p/u_*d = 0.23$ for floating polyethylene particles, and $\overline{D}_z/u_*d = 0.17$ for dissolved tracers. When the same flume was roughened with sand, Sayre and Chamberlain (38) found that $D_p/u_*d = 0.24$ for floating polyethylene particles.

Prych (39) obtained $D_p/u_*d = 0.20$ for floating particles and, on the average, $\overline{D}_z/u_*d = 0.135$ for dissolved tracers. Engelund (40)

released a 9 mm plastic ball at the speed of the water surface velocity and photographed its subsequent positions on a horizontal grid. Measurements were made for two depths of flow: 5.4 cm and 17.3 cm. He calculated D_p by assuming that the Eulerian correlation coefficient was similar to the Lagrangian coefficient and reported that for his data $D_p/u_*d = 0.20$.

From these and other experiments listed in Table 2.1, it is observed that, for dissolved tracers, the dimensionless mixing coefficient $\overline{\theta}$ ranges from 0.083 measured by Pien (41) in a laboratory flume to 0.73 measured by Glover (42) in the Columbia River. For floating particles, D_p/u_*d is approximately 0.20 for the listed experiments all of which were performed in laboratory flumes. Further discussion of the measured values of $\overline{\theta}$ will be presented in Chapter 5.

2.B. ANALYTICAL INVESTIGATIONS

2.B.1. The Concept of a Turbulent Mixing (or Exchange) Coefficient.

The turbulence transfer coefficient, which is basic to the diffusion equation, requires special attention. The exchange coefficient concept states that the turbulent flux of material is directly proportional to the local mean gradient of the scalar distribution. The constant of proportionality is the turbulent mixing (or exchange) coefficient E_{ij} defined by

$$-\overline{u_i u_j} = E_{ij}\left(\frac{\partial U_i}{\partial x_j} + \frac{\partial U_j}{\partial x_i}\right) \qquad (2.40)$$

where E_{ij}, the eddy viscosity or the turbulent transfer coefficient for momentum, is a second order tensor.

Prandtl proposed the mixing-length theory as a physical explanation justifying Eq. 2.40. Prandtl's theory for the one-dimensional case can be summarized as follows:

(i) $$-\overline{u'v'} = E_2 \frac{\partial u}{\partial y} , \tag{2.41}$$

where u' and v' are velocity fluctuations in the x and y directions respectively and E_2 = turbulent "diffusion" coefficient in the y-direction,

(ii) $$E_2 \propto \ell v_* \tag{2.42}$$

where ℓ and v_* are respectively a characteristic length and velocity of the eddies, and

(iii) $$v_* \propto \ell \left|\frac{du}{dy}\right| . \tag{2.43}$$

The limitations of Prandtl's proposal become evident when postulates 2.41, 2.42, and 2.43 are compared to reality. Eq. 2.41, for example, assumes that turbulent transfer is affected by excursions of length ℓ, small in comparison to the characteristic width of the cloud of material being mixed. However, Batchelor (44) found, from velocity measurements of two-dimensional wakes and jets, that ℓ was of the order of the flow dimensions.

According to Batchelor (44), Prandtl's theory predicts that $\overline{u'^2}$, $\overline{v'^2}$, and $\overline{w'^2}$ can be represented by a single curve which depends on $(du/dy)^2$ and becomes zero where $du/dy = 0$. However, measurements by Townsend (45) showed that there was no single repre-

sentative curve and that turbulence intensities were appreciably greater than zero along the axis of a wake where the mean velocity gradient was zero. Townsend's (45) measurements also showed that there were regions within the wake where $\overline{u'^2}$ would be transferred up a gradient--a direct contradiction of Prandt's theory which requires that transfer coefficients be positive. Furthermore Starr (46) has shown that, according to Eq. 2.41, a wide range of fluid systems exhibit negative eddy viscosities.

The mixing length theory also predicts that in the region of zero shear, the mixing coefficient is also zero--again a contradiction to the fact that transverse spread of material occurs even if the transverse velocity gradient is zero. Therefore neither the Reynolds analogy nor Prandtl's theory applies in the central region of a uniform open channel flow where $\tau \approx 0$.

The preceding objections thus preclude use of the exchange coefficient concept and Reynolds analogy to establish existence of the transverse turbulent mixing coefficient, D_z. Rather Batchelor's (33) mathematical result discussed in Section 2.A.3 will be applied. In a uniform open-channel flow, turbulence is homogeneous in a plane parallel to the channel bottom. Thus if the cross-wise distribution of tracer concentration on this plane is Gaussian, then there exists a characteristic transverse mixing coefficient D_z for that plane. Under this condition use of Eq. 2.16 is considered valid.

2.B.2. The Transverse Exchange Coefficient as Derived From the Convective-Diffusion Equation. Since the present study is confined to the central region of a steady uniform flow in an open

channel (essentially away from the sidewall boundary layers), it will be assumed that both D_y and D_z are independent of z. Thus Eq. 2.16 becomes

$$u(y) \frac{\partial C}{\partial x} = \frac{\partial}{\partial y}\left(D_y(y) \frac{\partial C}{\partial y}\right) + \frac{\partial}{\partial z}\left(D_z(x,y) \frac{\partial C}{\partial z}\right) \tag{2.44}$$

where $C = C(x,y,z)$.

Applying the moment technique of Aris (26), an equation for the second moment of C can be derived by multiplying each term of Eq. 2.44 by z^2 and integrating over z. For the left-hand side,

$$\int_{-\infty}^{\infty} z^2 u(y) \frac{\partial C}{\partial x} dz = \int_{-\infty}^{\infty} u(y) \frac{\partial (z^2 C)}{\partial x} dz$$

$$= u(y) \frac{\partial}{\partial x} \int_{-\infty}^{\infty} z^2 C \, dz$$

$$= u(y) \frac{\partial M_2}{\partial x} \tag{2.45}$$

where the second moment $M_2 = \int_{-\infty}^{\infty} z^2 C \, dz$. The first term of the right-hand side becomes

$$\int_{-\infty}^{\infty} z^2 \frac{\partial}{\partial y}\left(D_y \frac{\partial C}{\partial y}\right) dz = \frac{\partial}{\partial y} D_y \int_{-\infty}^{\infty} \frac{\partial}{\partial y} (z^2 C) \, dz$$

$$= \frac{\partial}{\partial y}\left(D_y \frac{\partial M_2}{\partial y}\right) . \tag{2.46}$$

Setting

$$III = \int_{-\infty}^{\infty} z^2 \frac{\partial}{\partial z}\left(D_z \frac{\partial C}{\partial z}\right) dz,$$

and integrating by parts twice, one obtains

$$III = z^2 D_z \frac{\partial C}{\partial z} \Big|_{-\infty}^{\infty} - 2\left[\int_{-\infty}^{\infty} D_z \frac{\partial (zC)}{\partial z}\, dz - \int_{-\infty}^{\infty} D_z C\, dz\right]. \quad (2.47)$$

Assuming therefore that

(i) the tails of the C-distribution are such that the material flux $= D_z(\partial C/\partial z) = 0$ as $z \to \pm \infty$,

(ii) the integral $\int_{-\infty}^{\infty} D_z \frac{\partial}{\partial z}(zC)\, dz$ converges so that $C \to 0$ as $z \to \pm \infty$,

and

(iii) $D_z \neq D_z(z)$,

Eq. 2.47 reduces to

$$III = 2\, D_z M_0 \quad (2.48)$$

where the zero moment $M_0 = \int_{-\infty}^{\infty} C\, dz$ is the total material at any level, y of a given station.

Thus, combining all terms

$$u(y) \frac{\partial M_2}{\partial x} = \frac{\partial}{\partial y}\left(D_y \frac{\partial M_2}{\partial y}\right) + 2\, D_z M_o \quad (2.49)$$

and if $M_0 \neq 0$, the transverse exchange coefficient D_z can be calculated by the relation

$$D_z(x,y) = \frac{1}{2}\frac{1}{M_0}\left[u \frac{\partial M_2}{\partial x} - \frac{\partial}{\partial y}\left(D_y \frac{\partial M_2}{\partial y}\right)\right] \quad (2.50)$$

This is the generalized transverse mixing coefficient D_z expressed in terms of the moments of the cross-wise concentration distribution.

2.B.3. The Transverse Mixing Coefficient as a Function of Depth. From Eq. 2.50, the dependence of D_z on depth at a given station can be derived if $u(y)$, $D_y(y)$ and the distributions of the moments are known. It has been shown experimentally that D_y is the parabola

$$\frac{D_y}{u_* d} = \kappa\eta(1 - \eta), \tag{2.51}$$

where the shear velocity u_* is expressed as

$$u_* = \sqrt{\tau_0 / \rho}$$

$$= \sqrt{grS_f}, \tag{2.52}$$

τ_0 = bottom shear stress, ρ = fluid density, r = the hydraulic radius, $\eta = y/d$, and S_f = energy slope.

Therefore substituting Eqs. 2.51 and 2.33 into Eq. 2.50, the normalized transverse mixing coefficient becomes

$$\theta = \frac{D_z}{u_* d} = \frac{1}{2}\frac{1}{M_0}\left\{\frac{u(\eta)}{u_*}\frac{\partial M_{2n}}{\partial \xi} - \kappa\frac{\partial}{\partial\eta}\left[(\eta-\eta^2)\frac{\partial M_{2n}}{\partial\eta}\right]\right\} \tag{2.53a}$$

$$= \frac{1}{2M_0}\left\{\frac{u_a}{u_*}\frac{\partial M_{2n}}{\partial\xi} + \frac{1}{\kappa}\ell n(e\eta)\frac{\partial M_{2n}}{\partial\xi}\right.$$

$$\left. - \kappa\frac{\partial}{\partial\eta}\left[(\eta-\eta^2)\frac{\partial M_{2n}}{\partial\eta}\right]\right\}, \tag{2.53b}$$

where u_a = depth integrated velocity at a given value of z, $\xi = x/d$, $M_{2n} = M_2/d^2$, and e = base of the natural logarithm.

The right-hand side of Eq. 2.53a or 2.53b delineates the

contributions of longitudinal convection and shear to the transverse mixing coefficient. The first term in Eq. 2.53a expresses the contribution due to translation velocity. The value of θ at any level η must be computed by using the flow velocity $u(\eta)$ at that level.

The combined effect of the vertical diffusivity D_y and the vertical distribution of M_2 is expressed in the last term of Eq. 2.53a. It shows that as long as $\partial M_{2n}/\partial\eta \neq 0$, this combined effect can be a dominating factor in the determination of θ. However for each of the three cases: $\eta = 0$, $\eta = 1$, and $\partial M_{2n}/\partial\eta = 0$, θ can be calculated without knowledge of the value of D_y.

Eqs. 2.53 provide a framework for evaluating θ as a function of η at any distance from the source. It requires only that the variations of M_2 and M_0 be known through measurements. The equations also demonstrate that even at large distances where $\partial M_{2n}/\partial\eta = 0$, θ is constant with depth only when $\partial M_{2n}/\partial\xi$ varies with η in a manner that compensates for the shear effect. If $\partial M_{2n}/\partial\eta = 0$, and $\partial M_{2n}/\partial\xi$ = a constant at all η, θ at any section assumes the shape of the velocity profile at that station.

2.B.4. Method of Calculating the Transverse Mixing Coefficient. Eq. 2.53a is the basis for the determination of θ. For the general variation of θ, each term of the right side can be calculated numerically given the distributions of the pertinent functions M_0 and M_{2n}. Numerical evaluation of the last term requires the calculation of the second derivative $\partial^2 M_{2n}/\partial\eta^2$ in which the errors might be unduly large if $\Delta\eta$ is not small enough. In the present study, a

method of fitting polynomials by the least square to the experimental points was used to circumvent this problem. This is discussed further in Section 5.C.

The depth integrated value of θ can be evaluated from Eq. 2.53a by the operation

$$\overline{\theta} = \frac{1}{2}\int_0^1 \frac{1}{M_0}\left\{\frac{u(\eta)}{u_*}\frac{\partial M_{2n}}{\partial \xi} - \kappa \frac{\partial}{\partial \eta}\left[(\eta-\eta^2)\frac{\partial M_{2n}}{\partial \eta}\right]\right\} d\eta. \quad (2.54)$$

If M_0 is differentiable at least once with respect to η, the last term of Eq. 2.54 is zero. Assuming further that "material" is uniform over the depth so that $M_0 \neq f(x,y)$, and that the rate of growth of the second moment with distance is also uniform with depth so that $\partial M_{2n}/\partial \xi \neq g(y)$, then

$$\overline{\theta} = \frac{1}{2}\,\overline{u}_n \frac{\partial}{\partial \xi}\int_0^1 \frac{M_{2n}}{M_0}\, d\eta$$

$$= \frac{1}{2}\,\overline{u}_n \frac{\partial \overline{\sigma_n^2}}{\partial \xi} \quad (2.55)$$

where $\overline{u}_n = u_a/u_*$, and $\overline{\sigma_n^2}$ is the depth-mean variance of the cross-wise concentration distribution normalized by d^2.

Eq. 2.55 is similar to Taylor's (28) Eq. 2.25 for mixing in a field of homogeneous turbulence. However, while Taylor's result was derived on the assumption of homogeneity of the entire flow field, Eq. 2.55 maintains that indeed there is a depth variation of turbulence characteristics but that this variation can be erased by integration under the conditions specified. The errors accrued as a result of the assumptions leading to Eq. 2.55 will be discussed with

reference to experimental measurements in Section 5.C.2.

2.B.5. The Combined Effect of Shear and Vertical Mixing on Initial Distributions. A characteristic feature of a plume mixing in a turbulent shear flow is that near the source the vertical distribution of material within the plume is markedly skewed. This is due to the fact that D_y and u are nonuniform with depth.

The phenomenon is illustrated in Figure 2.2. It is assumed that the velocity profile is logarithmic (as in Eq. 2.33) and that D_y varies as a parabolic function of η (as in Eq. 2.51). The source is located at $\eta_h = 1/e$. Initially the tracer is concentrated at the source level and represented mathematically as a Dirac delta function.

Immediately after release, the source material is stretched over some vertical distance by vertical mixing. Since D_y is parabolically distributed as a consequence of shear and $\eta_h < 0.50$, vertical transport is more pronounced above than below the level of tracer release. The result is that a given amount of material will be spread out over a larger distance above than below η_h. As a consequence, the level η_m of maximum material concentration a short distance downstream of the source is smaller than η_h the level of tracer injection.

As ξ increases the process is repeated with the result that η_m continues to decrease giving rise to a skewed material distribution shown in stage (i) of Figure 2.2(b). Eventually the level of peak material concentration reaches the bed and $\eta_m = 0$ at a characteristic distance ξ_o. The resulting distribution is shown in stage (ii) of

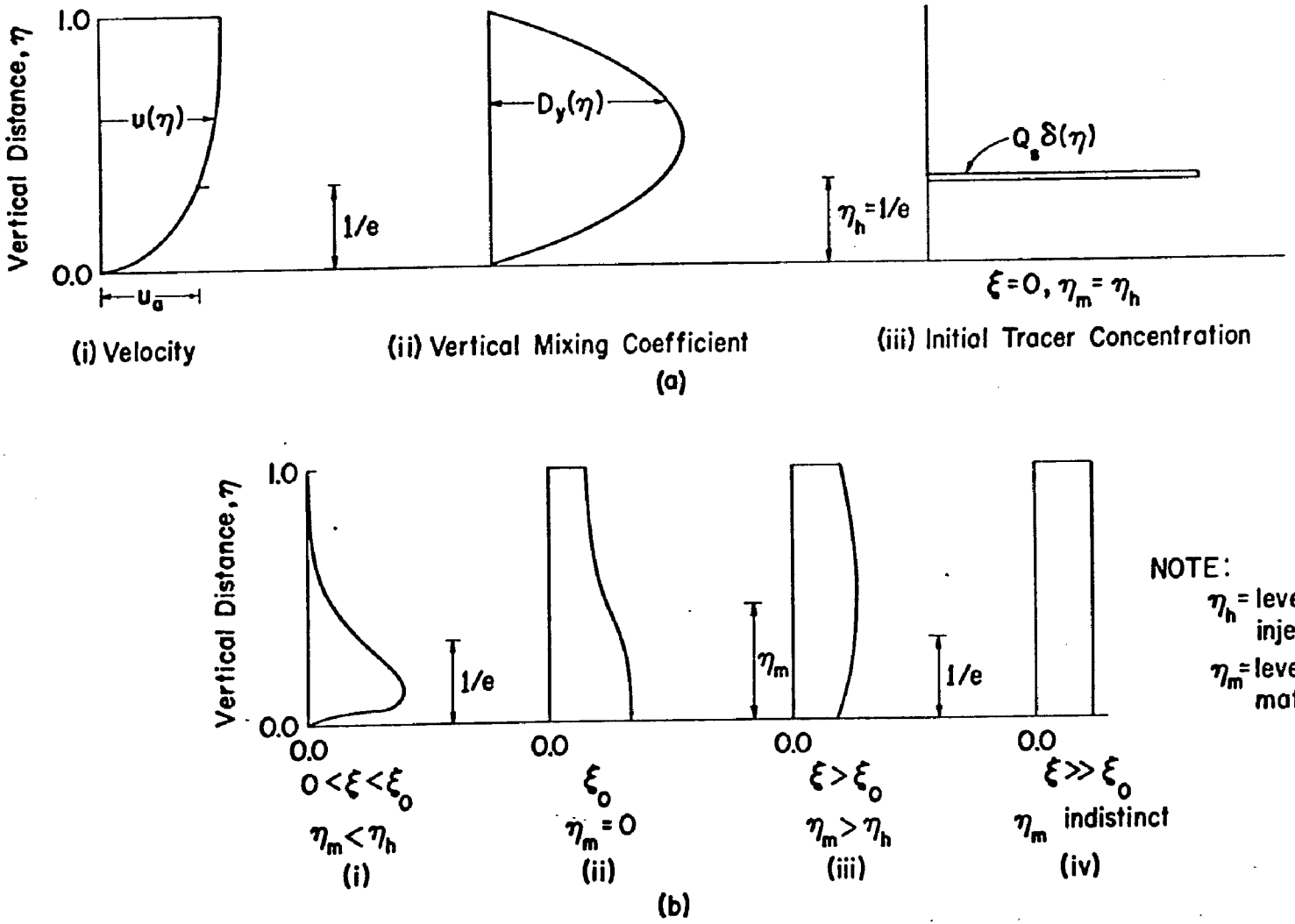

Fig. 2.2. Development of the vertical profile of material within the plume with increasing distance from the source: near-source plume behavior

Figure 2.2(b). As ξ increases further, the forcing functions and the location of the source shown in Figure 2.2(a) would require theoretically that η_m remain at the flow bed until material distribution is uniform with depth as shown in stage (iv) of Figure 2.2(b). In reality η_m may recover from zero to a value which could even be greater than η_h before stage (iv) is attained. This "bouncing" effect may be due to secondary current or other irregularities of the flow.

The distributions shown in Figure 2.2 are certainly dependent on the level of tracer injection η_h. If η_h is near unity, for example, η_m will initially rise to the water surface before material becomes uniformly distributed over the flow depth at large ξ. The "bouncing" effect could again be measured.

The initial distribution of material was numerically calculated at several ξ using the forcing functions of Figure 2.2(a). Various values of η_h were used. The theoretical results were compared with measurements in the flume as discussed in Section 5.E.

2.C. EXPERIMENTAL OBJECTIVE

2.C.1. General. All experiments relating to the first phase of this study were designed to calculate parameters derived from time-averaged values of tracer concentrations. In general, a tracer was continuously injected at ambient velocity from a small round injector into a uniform open-channel flow at a convenient depth at the flume centerline. Tracer concentrations were measured in situ at selected stations downstream of source and at various flow levels by conductivity probes. The output was conveniently stored on a

strip chart or magnetic tape for proper data retrieval and development of concentration profiles. Time averaging of the concentration record was accomplished either graphically or by numerical calculation.

2.C.2. Calculation of the Transverse Mixing Coefficient. A principal objective of the experiments was to determine the mixing coefficient D_z both as a depth-averaged value and as a space variable. For calculating $\overline{\theta}$ a form of Eq. 2.55 was used. The variance of the cross-wise concentration distribution was calculated by the relation

$$\sigma^2(x,y) = \frac{\int_{-\infty}^{\infty} z^2 C \, dz}{\int_{-\infty}^{\infty} C \, dz} - \left(\frac{\int_{-\infty}^{\infty} zC \, dz}{\int_{-\infty}^{\infty} C \, dz} \right)^2 \qquad (2.56)$$

for given values of x and y. Then the depth average was determined by the summation:

$$\overline{\sigma^2}(x) = \frac{1}{J} \sum_{i=1}^{J} \sigma^2(x;y_i) \qquad (2.57)$$

for a fixed x, where J is the number of levels where the cross-wise concentration profiles were established by measurement. The maximum growth rate of $\overline{\sigma^2}$ for large ξ was calculated from a plot of $\overline{\sigma^2}$ versus x and $\overline{\theta}$ determined by the equation

$$\overline{\theta} = \frac{1}{2} \frac{\overline{u}}{u_* d} \frac{d\overline{\sigma^2}}{dx} . \qquad (2.58)$$

Values of $\overline{\theta}$ were then calculated for various uniform flow configurations in two separate laboratory flumes in an attempt to verify past measurements and to add more information to the meagre values reported in the literature. For one series of experiments, the turbulence was intensified by placing a layer of stones on the bottom of the flume. For the rest of the experiments the flume bottom was essentially hydraulically smooth.

Determination of $\theta(\xi;\eta)$ as a function of ξ and η consisted in numerically evaluating each term of a modified form of Eq. 2.53b. The variance σ^2 was calculated at fixed values of x and y. At a given station, σ^2 was plotted against y and a curve fitted to the points. Thus for that station ξ_1, for example, θ was calculated by

$$\theta(\xi_1;\eta) = \frac{1}{2}\left\{\left[\frac{\overline{u}}{u_*} + \frac{1}{\kappa}\ell n(e\eta)\right]\frac{\partial}{\partial\xi}\left(\frac{\sigma^2}{d^2}\right) - \kappa\frac{\partial}{\partial\eta}\left[\eta(1-\eta)\frac{\partial}{\partial\eta}\left(\frac{\sigma^2}{d^2}\right)\right]\right\} \qquad (2.59)$$

From these calculations, the general change in the shape of the depth variation of θ with increasing ξ was developed.

2.C.3. Determination of Other Parameters.

(a) Attenuation of peak concentration. The decay of the maximum mean tracer concentration C_{max} with ξ was measured at fixed levels η. Owing to the nonuniform vertical distributions of the vertical diffusivity, flow velocity, and the transverse mixing coefficient with η, and the fact that the source is small, the decay rate of C_{max} with ξ is vastly different at various η near the source. These rates

were established from measurements for four values of η_h, the injection level.

At large values of ξ, curves of C_{max} attenuation with ξ at various levels essentially collapse into one. Thus if the transverse concentration profiles are assumed identical at all levels, the mixing process can be described as one-dimensional diffusion with a characteristic transverse mixing coefficient $\overline{D}_z$ expressed according to Eq. 2.58. The fundamental solution is given by

$$C(x,z) = C_{max}(x) e^{-z^2/2\overline{\sigma^2(x)}} \tag{2.60}$$

where $C_{max}(x)$ is the peak value of C assumed located along $z = 0$. The source strength Q_s is defined by

$$Q_s = u_o C_o A_o \tag{2.61}$$

$$= \int_{-\infty}^{\infty} \int_{o}^{d} u(y) C(x,y,z)\, dy\, dz \tag{2.20}$$

$$= \text{constant, by continuity}$$

where u_o, C_o, and A_o are, respectively, the injection velocity of the tracer, the initial tracer concentration, and the cross-sectional area of the injector. Thus by integration of Eq. 2.20, it is found that

$$C_{max}(x) = \frac{Q_s}{\sqrt{2\pi}\,\sigma(x)\,\overline{u}\,d}\ , \tag{2.62}$$

where $\sigma(x) = \sqrt{\overline{\sigma^2(x)}}$, and it is assumed that $\overline{u} = u_a$. Hence, $C_{max}(x) \sim [\sigma(x)]^{-1}$ which predicts that if Taylor's one-dimensional

mixing indeed occurs, the maximum tracer concentration would attenuate as the (- 1/2)-power of x. This relationship was verified by measurements in the present study.

Eq. 2.62 also offers a method of calculating the depth-averaged coefficient $\overline{D}_z$ given a value of C_{max} at a known distance downstream of the source and assuming a linear growth of the variance. Such calculations were made and compared to $\overline{D}_z$ evaluated by the moment method of Section 2.C.2.

(b) Iso-concentration maps. Concentration values were measured at sufficient points to permit complete mapping of the plume on both cross-sectional and cross-wise planes. The iso-concentration contours developed were used to visualize the geometric features of the mixing process. Concentration maps were also constructed on the vertical plane through the plume axis. This provided a distribution of the areas of high concentration levels on the axial plane.

(c) Other related parameters. From the experiments, the variation of M_0 with x and y was determined.

Velocity measurements were made to verify the assumed logarithmic distribution in the vertical, to establish isovels within the flow and thus delineate zones of the wall boundary layer, and to calculate the discharge through various flume cross sections.

2.C.4. Summary of the Experimental Objective (Phase I).

A plume was generated by a continuous point source in an open-channel flow. Time-averaged concentration values were measured at various levels of the flow for selected stations. From these,

cross-wise concentration profiles were developed and θ calculated both as a local variable and as a depth-averaged constant. Near source characteristics of the plume were measured and compared to theoretical predictions. Asymptotic plume behavior was also investigated. Iso-concentration contours were plotted on cross-sectional, transverse and axial planes. Material distribution within the plume was established and velocity measurements made.

CHAPTER 3

PAST STUDIES, ANALYTICAL INVESTIGATIONS, AND EXPERIMENTAL OBJECTIVE (Phase II)

The second phase of this study deals with the temporal fluctuations of tracer concentration at various points within the plume. Although some theoretical models have been proposed for describing this process, experimental verification is extremely scarce. This chapter reviews the pertinent work thus far reported in the literature, presents some analytical ramifications, and outlines the experimental objective of phase II.

3.A. PAST STUDIES

3.A.1. Conservation Equation for Mean-Square Concentration Fluctuations (msf). Using a method introduced by Csanady (15), a conservation equation is derived for the mean square concentration fluctuations (msf or $\overline{\phi'^2}$) at a fixed point. Essentially the time mean conservation equation is subtracted from the instantaneous equation to obtain an expression for the fluctuations of velocity and concentration. Thus, subtracting Eq. 2.8 from Eq. 2.5 one obtains:

$$\frac{\partial \phi'}{\partial t} + U_i \frac{\partial \phi'}{\partial x_i} + u_i' \frac{\partial \tilde{\phi}}{\partial x_i} + u_i' \frac{\partial \phi'}{\partial x_i} - \frac{\partial}{\partial x_i} (\overline{u_i' \phi'}) = \epsilon_m \frac{\partial^2 \phi'}{\partial x_i^2} \qquad (3.1)$$

where ϕ' = fluctuation of scalar concentration from the mean value Φ.

For an incompressible flow where $\partial U_i / \partial x_i = 0$,

$$\frac{\partial u_i'}{\partial x_i} = 0. \tag{3.2}$$

If Eq. 3.1 is multiplied by $2\phi'$ and Eq. 3.2 applied, the resulting relationship can be averaged in the sense of Eqs. 2.7 to give the following conservation equation for msf:

$$\frac{\partial \overbrace{\phi'^2}}{\partial t} + U_i \frac{\partial \overbrace{\phi'^2}}{\partial x_i} = -2\overbrace{u_i'\phi'}\frac{\partial \overbrace{\phi}}{\partial x_i} + \frac{\partial}{\partial x_i}\left(\epsilon_m \frac{\partial \overbrace{\phi'^2}}{\partial x_i} - \overbrace{u_i\phi'^2}\right) - \Psi \tag{3.3}$$

where Ψ, the rate of dissipation of msf, is shown by Batchelor et al. (47) to be related to the molecular diffusivity, ϵ_m by

$$\Psi = -2\epsilon_m \overbrace{\frac{\partial\phi'}{\partial x_i}\frac{\partial\phi'}{\partial x_i}}. \tag{3.4}$$

Hinze (48) postulated that if velocity and concentration fluctuations are generated simultaneously at a grid of a wind tunnel, Ψ can be expressed as

$$\Psi = \frac{12\epsilon_m}{\lambda_\phi^2}\overbrace{\phi'^2} \tag{3.5}$$

where λ_ϕ is a concentration microscale. For this case, as in the decay of kinetic energy behind a grid, $\lambda_\phi^2 \sim \epsilon_m t$. Hence

$$-\frac{d\overbrace{\phi'^2}}{dt} = \frac{3}{2}\frac{\overbrace{\phi'^2}}{t} \tag{3.6}$$

where the time, $t = x/\bar{u}$, is zero at the grid.

For a continuous plume generated by a point source into a steady uniform flow Eq. 3.3 reduces to

$$u\frac{\partial\overline{\phi'^2}}{\partial x_i} = -2\overline{u_i'\phi'}\frac{\partial\overline{\phi}}{\partial x_i} + \frac{\partial}{\partial x_i}\left(\epsilon_m\frac{\partial\overline{\phi'^2}}{\partial x_i} - \overline{u_i'\phi'^2}\right) - \Psi \qquad (3.7)$$

where $u \equiv U_1$ and $U_2 = U_3 = 0$. Thus assuming that (i) the gradient-diffusion relationship is valid for the flux of concentration and of msf, (ii) the marked-particle hypothesis can be applied (i.e. ϕ is replaced by c), and (iii) the plume is "slim," the following equations result:

$$\overline{u_i'c'} = -D\frac{\partial C}{\partial x_i}, \qquad (3.8)$$

$$\overline{u_i'c'^2} = -D_s\frac{\partial\overline{c'^2}}{\partial x_i}, \qquad (3.9)$$

and

$$u\frac{\partial s}{\partial x} = 2D\left[\left(\frac{\partial C}{\partial y}\right)^2 + \left(\frac{\partial C}{\partial z}\right)^2\right] + D_s\left(\frac{\partial^2 s}{\partial y^2} + \frac{\partial^2 s}{\partial z^2}\right) - \Psi \qquad (3.10)$$

where D and D_s are diffusivities for concentration and msf respectively; $s \equiv \overline{c'^2}$ is the mean square of the marked-particle concentration fluctuation; C is time-averaged concentration; and the axes x,y, and z are oriented as shown in Figure 2.1.

Csanady postulated that Ψ for the case of the continuous point source may be determined by the relation

$$\Psi = \frac{s}{T} \qquad (3.11)$$

where T is a decay-time scale which can be estimated. Assuming self-similarity for s and C, and equating the diffusivities, he obtained a theoretical distribution for s for the case of radial symmetry where the C-distribution is Gaussian along the x and y

directions. There was fair agreement between his calculated curves and the experimental measurements made by Becker et al. (49) for a continuous plume in the core region of a fully developed pipe flow. The experimental data also showed that the transverse s-profiles were self-similar at different values of x and that the decay rate of msf for the pipe flow was twice the rate for grid-generated turbulence.

3.A.2. The Fluctuating Plume Model. The fluctuating plume model, presented by Gifford (16), is a statistical alternative for predicting the properties of point concentration fluctuations. This model, illustrated in Figure 3.1 for the one-dimensional case, essentially assumes that the plume emitted by a continuous point source in a uniform wind is a superposition of an infinite number of elementary disks as in Figure 3.1(b). Each element is allowed to grow in the z direction as diffusion time increases but the elemental thickness, dx is always constant and equals u dt thus assuming negligible diffusion in the longitudinal direction. The centroid of the material distribuiton within the disk wanders back and forth in the z direction in a random manner.

Gifford represented the instantaneous concentration of material at any point within the disk as

$$\frac{d}{Q_s} = f(z - K_z, t) \qquad (3.12)$$

where K_z is the displacement of the centroid from the plume axis and is a function of t, and Q_s is the amount of material in the disk which is assumed to have originated at $x = z = 0$ and $t = 0$. The concen-

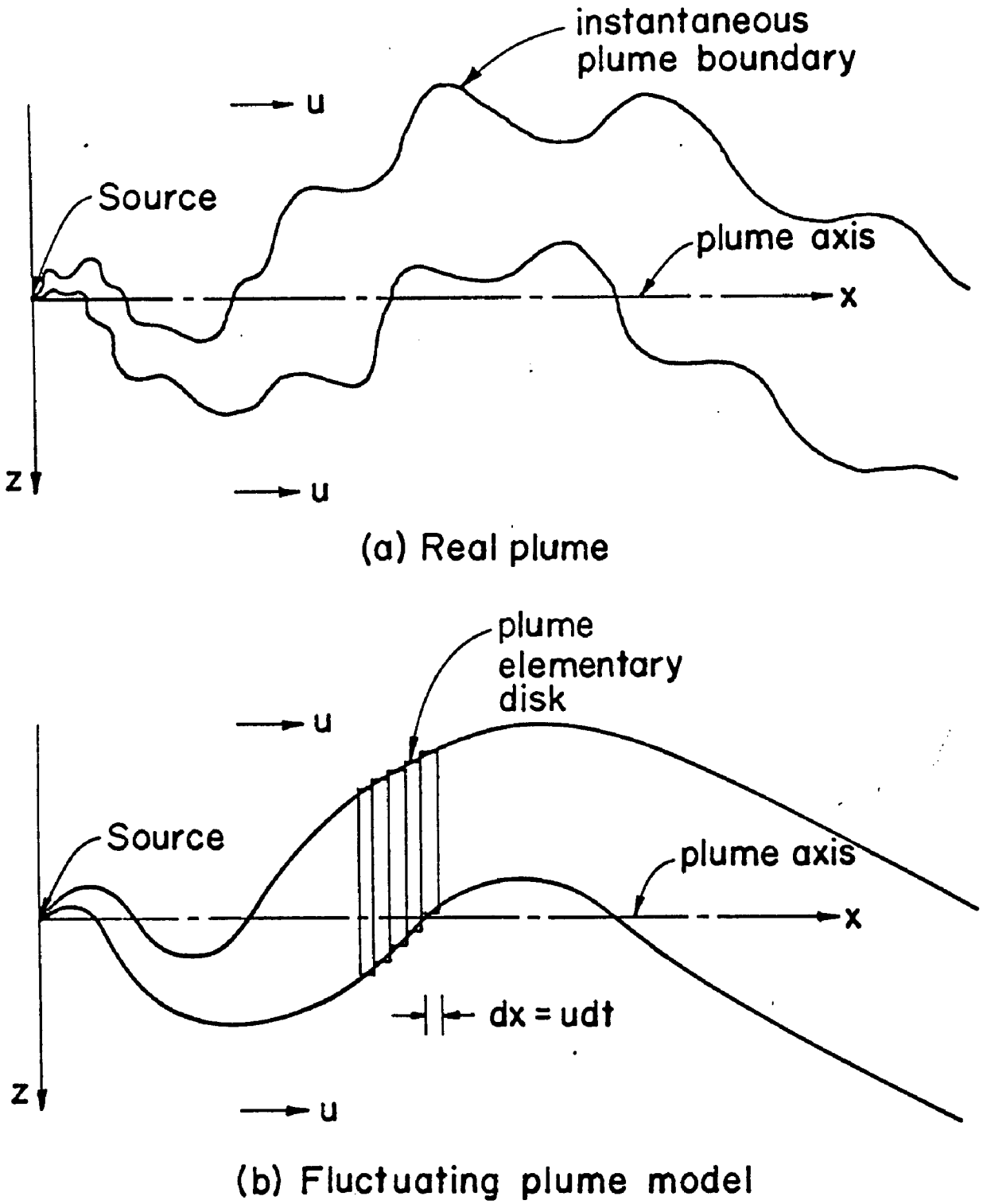

Fig. 3.1. Gifford's one-dimensional fluctuating plume model

tration has been integrated over the flow depth. Over many realizations, the mean of the instantaneous concentration distribution is given by

$$\frac{C}{Q_s} = \int_{-\infty}^{\infty} f(z - K_z, t) g(K_z)\, dK_z \qquad (3.13)$$

where $g(K_z)$ is the frequency function describing the variation of K_z over the trials.

If the functional form of f is fixed during the ensemble of trials, Eq. 3.13 can be regarded as a convolution transform for which

$$\sigma_M^2 = \sigma_f^2 + \sigma_g^2 , \qquad (3.14)$$

where σ_M^2, σ_f^2, and σ_g^2 are, respectively, the variances of the functions C/Q_s, f, and g. Assuming that the transverse distribution of the mean concentration is Gaussian and that the fluctuation of the instantaneous concentration distribution is random so that $g(K_z)$ is also Gaussian, Eq. 3.13 becomes a Weierstrass transform. For this relationship the inversion theorem predicts that f is also Gaussian.

Utilizing the fluctuating plume model, Gifford predicted the expected frequency distribution of the concentration fluctuations at a fixed point within the cloud. He further established that along the plume axis, the peak-to-average ratio P_a is represented by

$$P_a = (\sigma_f^2 + \sigma_g^2)/\sigma_f^2 , \qquad (3.15)$$

The "peak" refers to the maximum f experienced at a fixed point as the plume fluctuates back and forth over a long interval of time.

3.A.3. Previous Measurements of Point Concentration Fluctuation Parameters. Table 3.1 summarizes the literature on measured parameters related to temporal fluctuations of a scalar property at a point within a turbulent flow field. Only the studies by Gibson and Schwarz (50) and Lee and Brodkey (51) were conducted in a water medium. No measurement in an open-channel shear flow has been reported.

The scarcity of experimental (and in fact theoretical) information is due, not to the immateriality of these fluctuation parameters, but to the difficulty of defining and measuring meaningful parameters useful for practical purposes and then formulating pertinent equations. For example, it is extremely difficult to define a peak for a random variable without some qualification especially with regard to the length of the observation time. In practice one usually specifies a "probable" peak which is assumed to equal the mean value over an "adequate" sampling period plus twice the standard deviation of the fluctuation both of which must then be determined. Even when the parameters are well-defined, pertinent equations are complicated by anisotropy and nonhomogeneity just as in the time-averaged relationships but with the added terms which account for interactions between velocity and scalar fluctuations, and for dissipation as shown in Eq. 3.3.

There is also the problem of proper instrumentation. In measuring fluctuations, the frequency response curve of the detecting mechanism must be flat from zero to a point beyond the characteristic frequency of the fluctuation field where the spectral density is very

Table 3.1. Summary of previous measurements of concentration fluctuations at fixed points

Source	Environment	Source † Height (above ground level) m	Tracer	Sampling Frequency samples/sec	Test Reach m	Parameter Investigated	Result	Comment
Lowry et al (52)	atmospheric turbulence Brookhaven National Lab.	108.2	oil-fog	0.1	1620	peak-to-average ratio, P_a at ground level	P_a decays as x^{-1}	no asymptotic value of P_a was attained within the test reach.
Smith (54)	atmosphere under stable, unstable and transitional conditions	108.2	oil-fog aerosol collected on molecular filters	continuous sampling	6200	isolines of ground-level concentration	maximum concentration located at x = 0.5 km	also found that P_a decreased with x
Gosline[1]	atmosphere at various stability conditions	24.4	NO_2	0.1	244	frequency, f of various concentration levels, c	f decreases with increase of c	large scatter of data
Gifford (16) data by Wanta and Gartrell	atmospheric turbulence	76.2	N/A [2]	N/A	5632	P_a at ground level	P_a decays initially as x^{-1} and then remains constant after x ≈ 3.2 km	asymptotic value of $P_a \approx 2.0$ considerable scatter of data
Gifford [3] (53) data by Hilst	atmospheric turbulence (stable condition)	60.0	flourescent pigment	N/A	200	P_a at source height	$P_a \approx 2.0$ for x values between 50 50 m and 200 m from the source	P_a values are considerably higher at ground levels for same x
Becker et al [4] (49)	fully developed air stream in a pipe	source at pipe centerline	oil-fog	continuous record	2 to 12 pipe diameters	radial distribution of msf [5]	msf profiles are self-similar for various stations	profiles deviated from the theoretical solutions by Csanady (1967) near the pipe axis
Gibson and Schwarz (50)	water tunnel with grid-generated turbulence	source over the entire grid section	NaCl	continuous record	2	decay of msf with x	msf decays as $x^{-3/2}$ (equation III-6 verified)	both velocity and scalar fluctuations are generated at the grid
Lee and Brodkey (51)	turbulent water flow in a 7.8-cm pipe	source at pipe centerline	Gentian violet	continuous record on wave analyzer	3	(i) Decay of msf with x (ii) radial distribution of rms value of c'	(i) msf decays exponentially with x (ii) rms remains essentially constant within the core region	Decay of msf is different from the -3/2 power law for isotropic turbulence. Radial rms profiles are self-similar for various x.

NOTES:

[1] Reported by Gifford (16)

[2] Not available.

[3] Other measurements of peak-to-mean concentration ratios are reported by Gifford (53)

[4] Reported by Csanady (15)

[5] msf is mean square concentration fluctuation.

† Source located at x = 0.0 m.

small. Hence for very high Reynolds number flows, specially-constructed probes (see for example Gibson and Schwarz (50)) must be used to detect the high frequency fluctuations. This is especially necessary if peak values are sought because the peaks are usually associated with the high frequency Fourier components of the signal.

Most measurements made in the atmosphere relate to the peak-to-average concentration ratio, P_a, for elevated sources, under various atmospheric stability conditions. As expected, there is considerable scatter in the data plots but some gross trends can be detected. Measurements by Lowry et al. (52) and Wanta and Gartrell (Gifford (16)), indicated that near the source P_a at ground level decayed as x^{-1}. Data by Wanta and Gartrell also showed that P_a eventually attained an asymptotic value of 2.0 beyond $x = 3.2$ km from the source. Hilst's measurements (Gifford (53)) showed that for x between 50 m and 200 m, P_a at source height was essentially constant and equal to 2.0. The measurements also demonstrated that for the same values of x, P_a was considerably larger at the ground than at the source level.

Experiments by Gibson and Schwarz (50) confirmed Hinze's hypothesis that msf decayed as $x^{-3/2}$ for isotropic turbulence where velocity and scalar fluctuations were generated at the same flow section. The measurements were made in a water tunnel within a test section 15 cm by 15 cm and 2 m long. The sodium chloride tracer was introduced at the grid which also generated the turbulence.

For turbulent shear flow in a pipe 7.8 cm in diameter, Lee and Brodkey (51) experimentally demonstrated that msf decayed

exponentially with x and that at a fixed section the radial distribution of the rms for c' was flat-topped near the pipe axis. They also showed that the rms profiles were self-similar at various values of x. Pertinent details of this and other experiments are given in Table 3.1.

3.A.4. Summary of Previous Studies (Phase II). Relatively little work has been done in studying point concentration fluctuations in turbulent mixing problems. For theoretical analyses, two models for continuous plumes have been advanced: (i) a phenomenological model describing the conservation of the mean square fluctuations for concentration expressed in Eq. 3.10, and (ii) Gifford's fluctuating plume model illustrated in Figure 3.1.

Experimental verification is meagre and confined mainly to measurements of peak-to-average concentration ratios, P_a, in tracer plumes in the atmosphere. These atmospheric observations show that near the source $P_a \propto x^{-1}$ and far away, P_a attains an asymptotic value of about 2.0. One measurement in a water tunnel indicates that msf decays as $x^{-3/2}$ for grid-generated turbulence while another predicts that msf decays exponentially with x for pipe flows. Experiments also show that for both air and water flows in a pipe, the radial distribution of msf is self-similar.

3.B. ANALYTICAL INVESTIGATIONS

3.B.1. Relationship Between Variances for the Generalized Fluctuating Plume.

A plume which varies with both y and z and fluctuates according to Gifford's model is considered. Let $f(x_1;y,z,t)$ be the instantaneous concentration distribution at the fixed station x_1 at the instant t. The centroid of f is located at $z_c(x_1;y,t)$ and its variance is $\sigma_f^2(t)$ so that f is represented explicitly as

$$f = f[x_1;y,(z-z_c);\sigma_f^2(t)] . \tag{3.16}$$

The centroid of f is calculated by

$$z_c(x_1;y,t) = \int_{-\infty}^{\infty} zf\, dz \Big/ \int_{-\infty}^{\infty} f\, dz, \tag{3.17}$$

and the variance by

$$\sigma_f^2(x_1;y,t) = \int_{-\infty}^{\infty} (z - z_c)^2 f\, dz \Big/ \int_{-\infty}^{\infty} f\, dz. \tag{3.18}$$

For a large number of realizations, the ensemble average can be replaced by simple integration. Thus the mean concentration at fixed x_1 becomes

$$C(x_1;y,z) = \lim_{T\to\infty} \frac{1}{T} \int_0^T f\, dt. \tag{3.19}$$

The centroid $z_o(x_1;y)$ and variance $\sigma_M^2(x_1;f)$ of C are represented by

$$z_o(x_1;y) = \int_{-\infty}^{\infty} zC\, dz \Big/ \int_{-\infty}^{\infty} C\, dz, \tag{3.20}$$

and

$$\sigma_M^2(x_1;y) = \int_{-\infty}^{\infty} (z - z_o)^2 C \, dz \Big/ \int_{-\infty}^{\infty} C \, dz. \tag{3.21}$$

Therefore the variance of the centroidal oscillation becomes

$$\sigma_g^2 = \lim_{T\to\infty} \frac{1}{T} \int_0^T (z_c - z_o)^2 \, dt. \tag{3.22}$$

Expanding Eq. 3.21, one obtains

$$\sigma_M^2(x_1;y) = \frac{\int_{-\infty}^{\infty} (z - z_o)^2 \frac{1}{T} \int_0^T f \, dt \, dz}{\int_{-\infty}^{\infty} \frac{1}{T} \int_0^T f \, dt \, dz}$$

$$= \frac{\frac{1}{T} \int_0^T \int_{-\infty}^{\infty} (z' + z_c - z_o)^2 f \, dz \, dt}{\frac{1}{T} \int_0^T F(y,t) \, dt}, \tag{3.23}$$

where

$$F(y,t) = \int_{-\infty}^{\infty} f \, dz, \text{ and } z' = z - z_c .$$

Since $z_o(x_1;y)$ can also be calculated by

$$z_o(x_1;y) = \lim_{T\to\infty} \frac{1}{T} \int_0^T z_c \, dt,$$

it follows that

$$\int_{-\infty}^{\infty} \frac{1}{T} \int_0^T 2z'(z_c - z_o) f \, dt \, dz' = 0.$$

Thus it is found by substitution into Eq. 3.23 that at a given station downstream of the source,

$$\sigma_M^2(y) = \lim_{T\to\infty} \frac{\int_0^T F(y,t)\sigma_f^2(t)\,dt}{\int_0^T F(y,t)\,dt} + \frac{\int_0^T F(y,t)[z_c(y,t) - z_o(t)]^2\,dt}{\int_0^T F(y,t)\,dt} \tag{3.24}$$

If $f(y,t)$ is invariant with time,

$$\sigma_M^2(t) = \overbrace{\sigma_f^2(y,t)} + \sigma_g^2(y)\,, \tag{3.25}$$

where $\overbrace{\sigma_f^2(y,t)}$ is the ensemble average of the variance of the instantaneous concentration distribution f at the level y taken over a large number of trials.

Eq. 3.25 demonstrates that the relationship between variances for the fluctuating plume which varies in both the transverse and vertical directions is similar to the relationship developed by Gifford for a plume which varies only in the transverse direction. In the more general case of two-dimensional variation, the variance of the instantaneous distribution does not have to be constant with time as Gifford's model assumed. The only requirement is that the total amount of material within the cloud at any given level, y, remain constant with time.

This latter condition is realized physically if f is defined as the depth-mean value of the instantaneous concentration distribution. Therefore $F(y,t)$ may be replaced by $F_1(t)$ defined by

$$F_1(t) = \int_{-\infty}^{\infty} \frac{1}{d}\int_0^d f\,dy\,dz\,. \tag{3.26}$$

For the continuous point source in a steady uniform channel flow, $F_1(t) = Q_s/\bar{u}d$. Mass conservation requires that $F_1(t)$ be constant

with time. Thus Eq. 3.25 is exact as long as the lateral instantaneous concentration distribution is averaged over the flow depth.

3.B.2. The Concept and Application of the Intermittency Factor. The development in the preceding section shows that for proper use of the fluctuating plume model, the instantaneous concentration distribution should be integrated over the flow depth. This is readily accomplished by rapidly photographing the plume from a level above the flume at a fairly high frequency (depending on the expected fluctuation frequency of the plume). This technique presents a monstrous design and data-reduction problem. First, each photoframe must be analyzed, through appropriate calibration, to determine the concentration distribution at each instant of exposure in order to calculate the variance of the distribution and to locate its centroid. Hundreds of frames must be similarly analyzed to obtain a representative ensemble. Secondly, the relatively low sensitivity of generally available photo surfaces to existing dyes seriously limits the range of x over which reliable measurements can be made. In the preliminary investigation of the present study, it was found that the plume boundaries were hardly discernible beyond $x \approx 2$ m.

The concept of intermittency can be used to circumvent these problems and derive other parameters related to the fluctuating plume edge. Each plume edge at a given flow level y is defined as a boundary line running in the direction of the x-axis, along which tracer concentration equals a selected threshold concentration C_t. At a given x, the plume edge, which can be characterized as a plume

front, oscillates back and forth in the transverse direction. Therefore for fixed values of x and y, there exists a section along the z-direction where the threshold concentration C_t is exceeded only during a fraction of the total time of observation. This section will be termed an "intermittency region" (see for example Figure 3.4).

This idea was introduced by Townsend (10, 45) who, while attempting to verify Kolmogoroff's theory of local isotropy in the plane wake behind a cylinder, observed that away from the wake center the flow was only intermittently turbulent. He defined the intermittency factor, γ, as the fraction of time during which the flow was turbulent and calculated its value indirectly by measuring derivatives of velocity vectors. The concept has since been extended to axisymmetric jets and boundary layers by Corrsin and Kistler (11) who built a circuit which responded to vorticity and measured intermittency factors directly; to the plane jet by Bradbury (55) who determined γ both by direct measurements and from film recordings of hot-wire signals; and to an axisymmetric compressible wake by Demetriades (12) who used a modified version of Bradbury's circuit to directly measure γ as it relates to compressibility.

A complete list of intermittency measurements made in a variety of flows is shown in Table 3.2. Some pertinent experimental details are also shown. It is evident from the table that the technique has not been used for the diffusing plume and that all measurements were conducted in wind tunnels.

In this study, the intermittency factor, I_f, at a fixed z, is defined as the fraction of the total sampling time during which the

TABLE 3.2 SUMMARY OF PREVIOUS MEASUREMENTS OF THE INTERMITTENCY FACTOR, γ [1]

Source	Flow Investigated	Experimental Arrangement	Reach of Measurement m	Parameter Measured	Determintation of γ
Townsend (10)	plane wake	a cylinder 0.953 cm in an air stream of velocity 1280 cm/sec	1.52	spatial derivatives of velocity	γ calculated from the flattening factor
Townsend (45)	plane wake	a cylinder 0.159 cm in an air stream of velocity 1280 cm/sec	1.51	δ - signal [2]	direct evaluation of γ as the mean value of δ
Klebanoff (13)	turbulent boundary layer	artificially thickened boundary layer in a wind tunnel	measurements at only one section 3.21 m from channel entrance	velocity fluctuation	γ calculated indirectly from the flattening factor
Corrsin and Kistler (11)	(a) turbulent boundary layer (b) round jet (c) plane wake	a wind tunnel with a working section 61 cm x 61 cm	2.59	δ - signal for vorticity	γ determined directly by a counter
Sandborn (57)	turbulent boundary layer	divergent wind tunnel with smooth walls	3.56	velocity fluctuation	γ calculated from flattening factor
Bradbury (55)	plane jet	38-cm wide air jet centrally placed in a tunnel 1.22 m wide.	0.66	(i) velocity fluctuation (ii) δ - signal	γ obtained directly by (i) visual examination of hot-wire signals, and (ii) integration of the δ - signal
Gartshore (56)	wall jet	air jet blown from a 0.63-cm slot parallel to wall of a wind tunnel	0.92	(i) velocity fluctuation (ii) δ - signal	γ determined from hot-wire and δ - signals
Fielder and Head (14)	turbulent boundary layers	wind tunnel with a flexible upper wall	not given	δ - signal using (i) differentiating circuit, and (ii) photo-probe	γ = mean value of δ
Demetriades (12)	axisymmetric compressible wake	0.396 cm diameter rod in air stream at Mach number 3	0.40	δ - signal	γ automatically calculated by the electrical circuit

NOTES:

[1] In all investigations listed here, γ is the ratio of the duration of turbulent motion to the total sampling period at a fixed point.

[2] The δ - signal is unity when motion is turbulent and zero when it is non-turbulent.

threshold concentration is exceeded at that point. The intermittency factor may thus be considered to indicate the fraction of time that the plume front is on one side or the other of the position z. Thus I_f is a probability distribution function expressed as

$$I_f(z) = \text{prob}\ [z < Z_f(t) \leq \infty]\ , \tag{3.27}$$

where $Z_f(t)$ is the instantaneous z-position of the front.

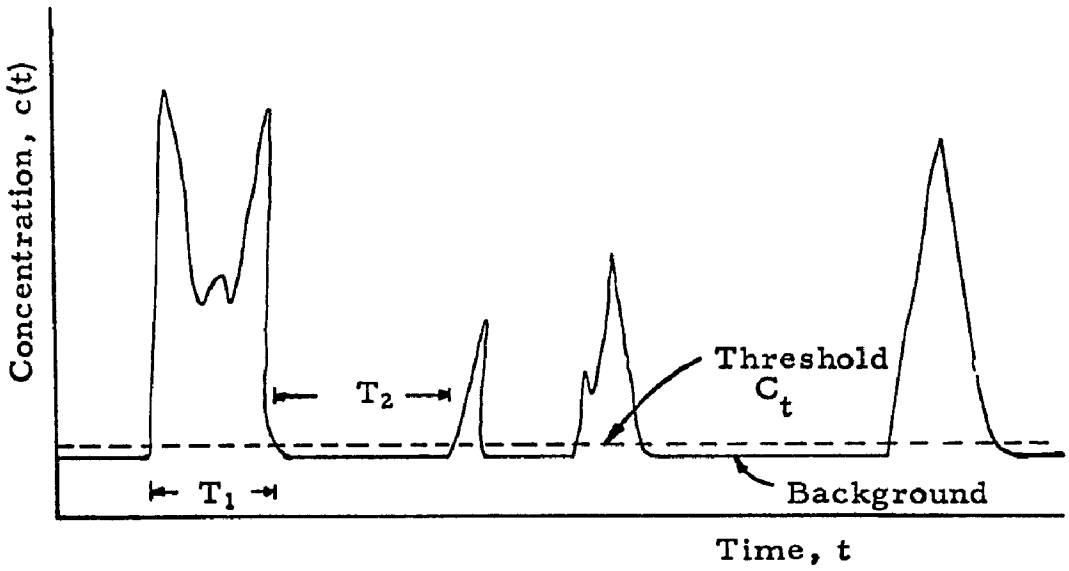

Fig. 3.2. Sketch of a typical concentration record at a fixed point as a function of time.

If, as shown in Figure 3.2, T_1 is the period during which $c(t) > C_t$, and T_2 the period when $c(t) \leq C_t$ at a point z, then following the arguments of Corrsin and Kistler (11),

$$I_f(z) = \tau_1/(\tau_1 + \tau_2)\,, \tag{3.28}$$

where

$$\tau_1 = \lim_{T_m \to \infty} \int_0^{T_m} T_1 p_1(T_1)\, dT_1 , \tag{3.29}$$

$$\tau_2 = \lim_{T_m \to \infty} \int_0^{T_m} T_2 p_2(T_2)\, dT_2 , \tag{3.30}$$

$p_1(T_1)$ and $p_2(T_2)$ are, respectively, the probability densities for T_1 and T_2, and T_m is the total sampling period. Therefore, by defining an intermittency function, $h(z,t)$, for the fixed point z such that

$$h(z,t) = \begin{cases} 1, \text{ if } c(z,t) > C_t \\ 0, \text{ if } c(z,t) \leq C_t, \end{cases} \tag{3.31}$$

the intermittency factor becomes

$$I_f(z) = \lim_{T_m \to \infty} \frac{1}{T_m} \int_0^{T_m} h(z,t)\, dt. \tag{3.32}$$

Examples of the intermittency function, $h(z,t)$ for selected values of the threshold concentration C_t are shown in Figure 3.3 for a sinusoidal signal, and a typical point concentration fluctuation.

Eq. 3.32 provides a method for directly calculating the intermittency factor from in situ measurements using appropriate detectors or probes. Unlike photography, this technique permits detailed measurements within the plume and over a considerably longer reach of the flow. If depth variation of plume parameters is negligible, a rake of several probes could simultaneously measure the instantaneous plume much like photography and the data directly fed

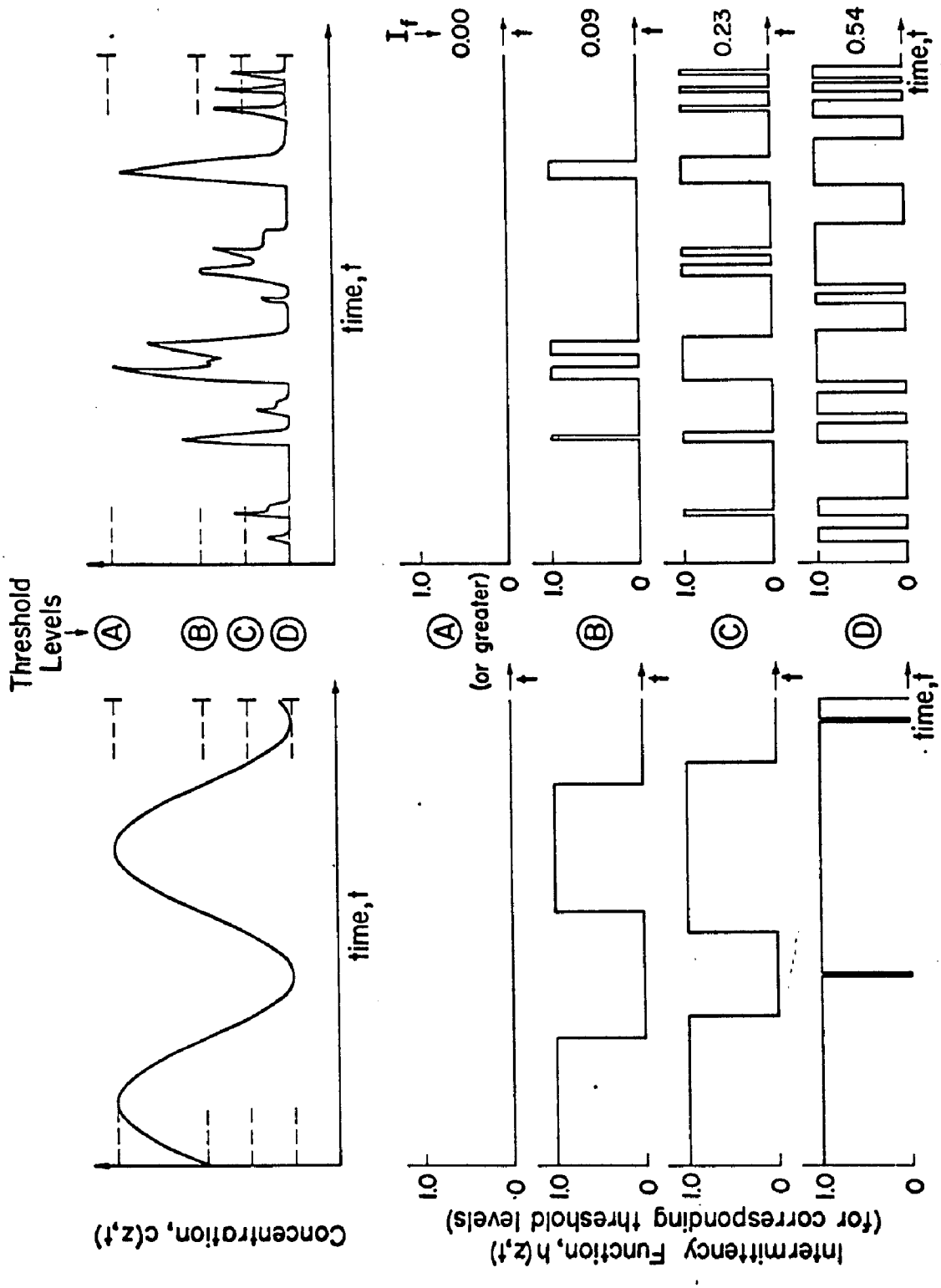

Fig. 3.3. Forms of the intermittency function, $h(z,t)$ at a fixed point z for selected threshold levels

into a computer for determination of any desired parameters.

From intermittency measurements, the distribution of the intermittency factor across the plume is determined. As shown in Figure 3.4, $I_f(z)$ attains and remains at a value of unity over the central core of the plume, and then decreases to zero at the extreme limits of the plume front. Thus a typical plume section is characterized by three regions: (i) a central core of continuous record above the threshold, C_t, (ii) a region of intermittency, and (iii) an outer zone where the threshold concentration is never attained. It must be noted that the central core does not always exist at all values of x. It should also be pointed out that I_f is not a function of z only, as Figures 3.3 and 3.4 imply. Rather, $I_f \equiv I_f(x,y,z)$, and $h \equiv h(x,y,z;t)$.

The preceding treatment has considered both x and y fixed. In reality, therefore, one should replace $I_f(z)$ by $I(x_1,y_1;z)$, and $h(z,t)$ by $h(x_1,y_1;z,t)$, where x_1 and y_1 are fixed values of x and y respectively.

Since I_f is a distribution function, then assuming it is differentiable, there exists a corresponding probability density function i_f for the position of the front such that

$$i_f(x_1,y_1;z) = \frac{\partial I_f}{\partial z}(x_1,y_1;z) \tag{3.33}$$

at the station x_1 and level y_1. Thus the z-location of the mean position of the front of C_t (for one side of the plume axis) becomes

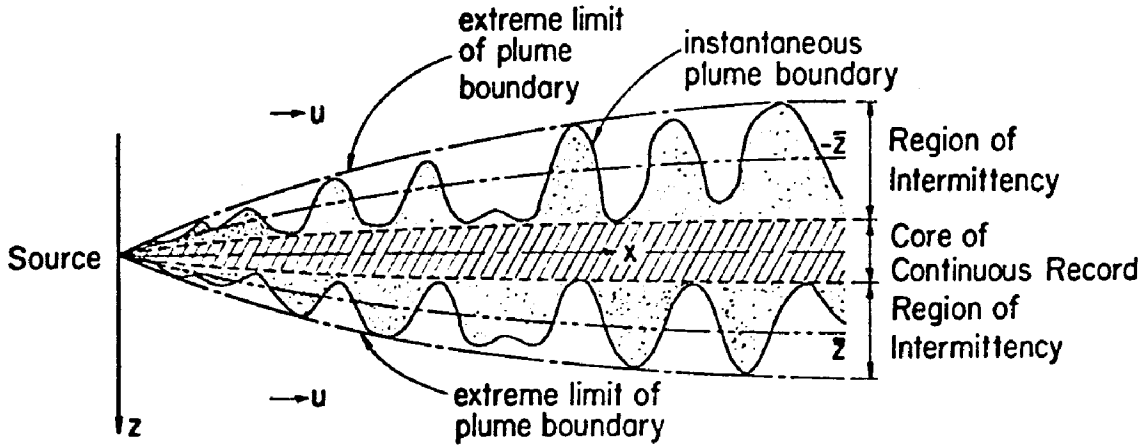

(a) Geometric Features of the Physical Model (plan)

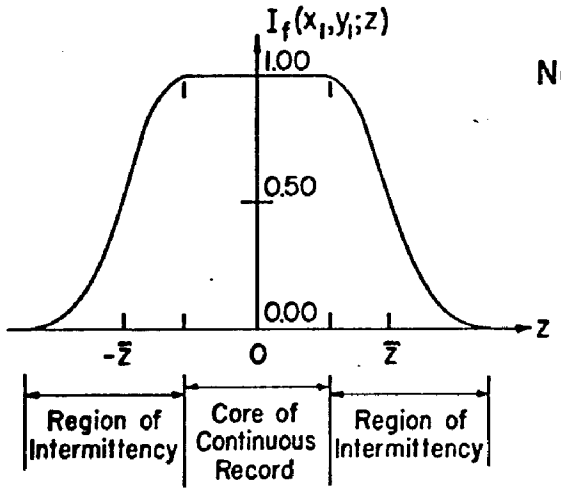

Note:

$I_f(x_i,y_i;z)$ = Intermittency Factor at section x_i and level y_i.

$\bar{z}$ = Mean position of the plume front.

(b) Distribution of the Intermittency Factor Across the Plume

Fig. 3.4. The intermittency factor model for cross-wise plume variation

$$\tilde{Z}(x_1, y_1) = \frac{\int_0^\infty z i_f(x_1, y_1; z)\, dz}{\int_0^\infty i_f(x_1, y_1; z)\, dz}, \tag{3.34}$$

and the corresponding variance, σ_I^2 of the intermittency region is expressed as

$$\sigma_I^2(x_1, y_1) = \frac{\int_0^\infty [z - \tilde{Z}(x_1, y_1)]^2 i_f(x_1, y_1; z)\, dz}{\int_0^\infty i_f(x_1, y_1; z)\, dz}. \tag{3.35}$$

It is noted that, from the definition of I_f,

$$\int_0^\infty i_f(x_1, y_1; z)\, dz = 1, \tag{3.36}$$

if the central core of continuous record exists at the station under consideration.

3.B.3. Characteristics of the Region of Intermittency. If the distribution function characterizing the temporal variation of the plume front is self-similar (as one would suspect), then a description of the region of intermittency will be complete if the following parameters are specified:

(i) the shape of $I_f(z)$ as a function of z,

(ii) the mean position of the front, $\tilde{Z}$,

(iii) a characteristic transverse length.

Figure 3.5 illustrates three examples of fluctuation models which could conceivably describe the motion of the plume front from the

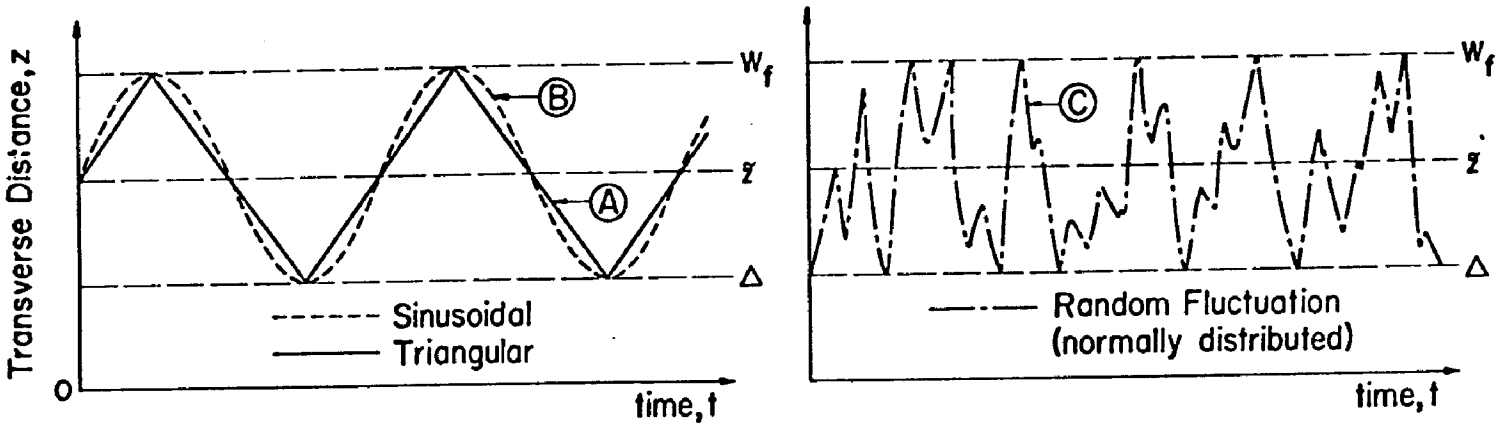

(a) Plume Front Oscillation Models

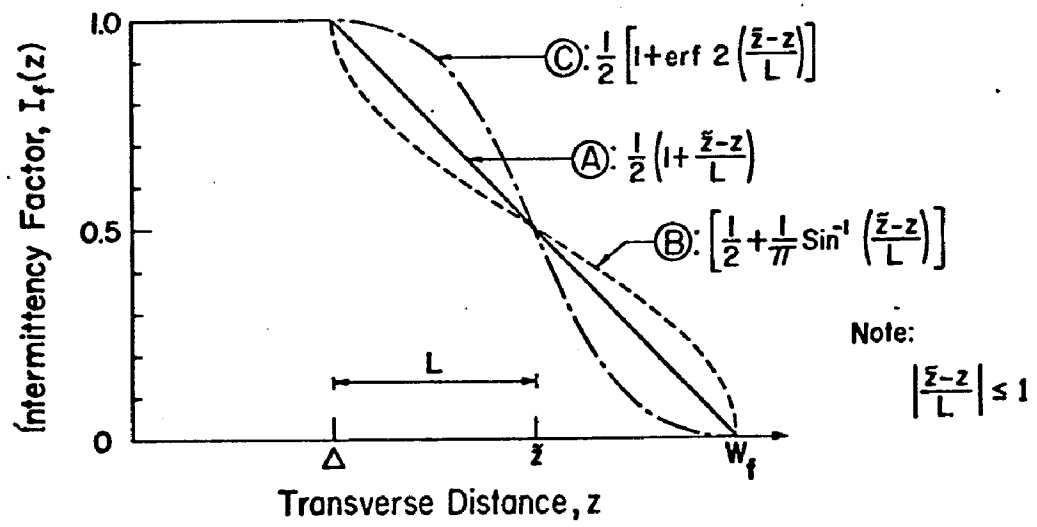

(b) Corresponding Distribution of the Intermittency Factor, $I_f(z)$ (as $t \to \infty$)

Fig. 3.5. Transverse distributions of the intermittency factor for selected plume front oscillation models

edge of the inner core at $z = \Delta$, to the extreme limit, W_f, of the front position. The front could propagate linearly from Δ to W_f and back, or oscillate as a sinusoidal function of time, or fluctuate randomly within the intermittency region as shown in Figure 3.5(a). For each model, the corresponding distribution of the intermittency factor (the distribution function) achieved as t becomes large is derived and plotted in Figure 3.5(b). For the triangular oscillation, (assuming that $I_f(z) \equiv I_f(x_1, y_1; z)$)

$$I_f(z) = \frac{1}{2}\left(1 + \frac{\overline{Z} - z}{L}\right); \tag{3.37}$$

for the sinusoidal model,

$$I_f(z) = \frac{1}{2} + \frac{1}{\pi} \sin^{-1}\left(\frac{\overline{Z} - z}{L}\right); \tag{3.38}$$

and for the normally distributed random fluctuation,

$$I_f(z) = \frac{1}{2}\left[1 + \text{erf } 2\left(\frac{\overline{Z} - z}{L}\right)\right]; \tag{3.39}$$

where L is the characteristic half-width of intermittency region,

$$\text{erf } \alpha = \text{error function of } \alpha$$

$$= \frac{2}{\sqrt{\pi}} \int_0^{\alpha} e^{-x^2}\, dx, \tag{3.40}$$

and the equations are valid for $\left|\frac{\overline{Z} - z}{L}\right| \leq 1$. In all cases

$$I_f(z) = \begin{cases} 1.0, & 0 \leq |z| \leq \Delta \\ 0.0, & |z| \geq W_f \end{cases} \tag{3.41}$$

Thus if self-similarity of $I_f(z)$ holds true, the shape of the intermittency function at every section will depend on the mode of the frontal oscillation. If this space-time motion is analytically representable, then so is the characteristic transverse distribution of the intermittency factor.

The mean front position, $\bar{Z}$ essentially locates the region of intermittency at any station. If the frontal fluctuation is symmetrical about its mean position, then $\bar{Z}$ coincides with the 50^{th} percentile where $I_f = 0.50$. The width of the intermittency zone can be characterized by L as shown in Figure 3.5(b). However, if the distribution function approaches its extremes asymptotically, the variance, σ_I^2 becomes a more appropriate length characteristic. In such a case, the limits $z = \Delta$, and $z = W_f$ would have to be determined experimentally or assumed to be located at some factor of the standard deviation σ_I.

3.C. EXPERIMENTAL OBJECTIVE

3.C.1. General. The second phase of this study differs from the first mainly in the method of data analysis. In general tracer concentration was continuously measured in situ by conductivity probes. The resulting signals were digitized at a selected rate and stored on magnetic tape for computer analysis. In the early experiments conducted in a flume 85 cm wide, intermittency factor calculations were made from analog records on strip charts by choosing a proper threshold concentration and directly reading off on the charts the periods when this value was exceeded. Analysis of other in situ

measurements for this second phase was done by computer programming.

A photo study was undertaken to verify the analytical results of the fluctuating plume model. A movie camera was mounted above the water surface and the plume photographed at several stations downstream of the source. The plume edges were located using a photo analyzer. The variances $\overline{\sigma_f^2}$ and σ_g^2 of the fluctuating plume model were determined by assuming that the instantaneous plume width at the instant t equaled $4\sigma_f(t)$, and that the instantaneous plume centroid was centered halfway between the observable plume edges.

3.C.2. Determination of the Characteristics of the Plume Front Oscillation.

a. The intermittency factor, $I_f(z)$. As explained earlier, the plume front (for fixed x_1, y_1) is the locus of the point along the z-direction where the concentration equals the threshold. All calculations relating to the space-time motion of the front were made by use of the intermittency factor concept. Except where otherwise stated, the intermittency phenomenon will be assumed symmetrical about the plume axis. Therefore only one side of plume will be considered in the presentation that follows.

From digitized data, the intermittency factor at the point z for fixed x_1, y_1 was calculated numerically by

$$I_f(z) = \frac{1}{N} \sum_{i=1}^{N} h(z, i), \qquad (3.42)$$

where $h(z, i)$ is the value of the intermittency function at the i^{th} time

digit and there are N samples within the sampling period. By placing probes at other values of z, the z-distribution of $I_f(z)$ was established for the station x_1 and the flow level y_1.

b. Geometric parameters. The geometric characteristics of the plume front model were derived by the relationships below. The mean position of the front, $\overline{\overline{Z}}$ was calculated by

$$\overline{\overline{Z}} = \sum_{i=1}^{M} z_i \left(\frac{\Delta I_f}{\Delta z}\right)_i (\Delta z)_i \Bigg/ \sum_{i=1}^{M} \left(\frac{\Delta I_f}{\Delta z}\right)_i (\Delta z)_i$$

$$= \sum_{i=1}^{M} z_i (\Delta I_f)_i \Bigg/ \sum_{i=1}^{M} (\Delta I_f)_i \,, \qquad (3.43)$$

where M is the total number of points where I_f was measured. As usual if the inner core of continuous record exists,

$$\sum_{i=1}^{M} (\Delta I_f)_i = 1.00.$$

By employing the definition of Eq. 3.35 and the notation of Eq. 3.43, the variance, σ_I^2, of the intermittency region was evaluated by the relation

$$\sigma_I^2 = \frac{\sum_{i=1}^{M} z_i^2 (\Delta I_f)_i}{\sum_{i=1}^{M} (\Delta I_f)_i} - \overline{\overline{Z}}^2 . \qquad (3.44)$$

The limit Δ of the inner core was located at the point where

$I_f(z)$ began to decrease from unity as $|z|$ increased. The outer extent W_f of the front was the value of z at which $I_f(z)$ first became zero with increasing $|z|$.

The intermittency measurements and calculations were then made at other stations (keeping y_1 fixed) downstream of the source. Consequently the rates of growth of the geometric parameters $\overline{\overline{Z}}$, σ_I^2, Δ, and W_f with diffusion time were ascertained. Universal growth rates for these functions were predicted for the smooth and rough bottom experiments from the experimental results. Similarly a representative curve for the distribution of $I_f(z)$ at all values of x (a result of self-similarity) was developed.

c. Frequency of "zero occurrence." Another useful characteristic of the frontal oscillation is the frequency at which the front sweeps by a given point. This is termed the frequency of zero occurrence or the zero frequency $\omega_0(z)$ defined as the rate at which the intermittency function, $h(z,t)$ at a point z (for fixed x_1 and y_1) varies from zero to unity or from unity to zero.

With a knowledge of $\omega_0(z)$, the time mean period $T_0(z)$ of the frontal oscillation at a fixed point z was calculated by

$$T_0(z) = 2I_f(z)/\omega_0(z) \quad (\omega_0(z) > 0). \tag{3.45}$$

The space mean values $\overline{\omega}_0(x)$ and $\overline{T}_0(x)$ were assumed to occur where $I_f(z) = 0.50$ and were termed, respectively, the characteristic frequency and period of the frontal oscillation at the particular station of measurement. If a convective velocity at the point where

$I_f = 0.50$ is denoted by u_c, then the characteristic longitudinal length scale $L_f(x)$ for the oscillation becomes

$$L_f(x) = u_c \overline{T}_0(x), \tag{3.46}$$

at the fixed level y_1. For a steady uniform flow in an essentially wide channel, u_c is constant so that both $L_f(x)$ and $\overline{T}_0(x)$ would grow at the same rate.

d. Probability densities $p_1(T_1)$, $p_2(T_2)$. Eq. 3.28 offers an alternate method for calculating $I_f(z)$. If the period over which C_t is exceeded is denoted by T_1 as shown in Figure 3.2 and termed the "duration of occurrence" (of excess) and T_2 is the "duration of non-occurrence," then $p_1(T_1)$ and $p_2(T_2)$ are the probability densities of occurrence and non-occurrence respectively.

The interest here is not to use Eq. 3.28 to evaluate $I_f(z)$, but to determine the shapes of the probability densities $p_1(T_1)$ and $p_2(T_2)$ for a better understanding of the characteristics of the intermittency function, $h(z,t)$. The periods of occurrence T_{1j}, and the periods of non-occurrence T_{2j} were determined from $h(z,t)$ (see for example Figure 6.1). Then convenient time intervals ΔT_1 for $p_1(T_1)$ and ΔT_2 for $p_2(T_2)$ were selected. The number of occurrences of T_1 within the period $T_{1j} + \Delta T_1$ was designated the density $p_1(T_{1j})$, and the occurrences of T_2 within the period $T_{2j} + \Delta T_2$ the density $p_2(T_{2j})$, as $j = 1,2,\ldots,N_1$ (or N_2), where N_1 (or N_2) is the total number of periods of occurrence (or non-occurrence). The densities were plotted as histograms such that

$$\sum_{j=1}^{N_1} p_1(T_{1j})\Delta T_1 = \sum_{j=1}^{N_2} p_2(T_{2j})\Delta T_2 = 1.0 \qquad (3.47)$$

In another set of calculations, the probability density $p(T)$ of both occurrence and non-occurrence was calculated by setting $\Delta T_1 = \Delta T_2 = \Delta T$ and the density $p(T_j) = \frac{1}{2}[p_1(T_{1j}) + p_2(T_{2j})]$ with $T_{11} = T_{21} = 0$. Thus

$$\sum_{j=1}^{N} p(T_j)\Delta T = 1.0 \qquad (3.48)$$

where N is the total number of periods.

The probability densities $p_1(T_1)$, $p_2(T_2)$, and $p(T)$ were determined at various stations and for values of z where $I_f \approx 0.50$.

3.C.3. Photo Analysis. The fluctuating plume model was studied by photographing the plume from an elevated point 2.13 m above the water surface at a rate of 24 frames per second. Assuming that

(i) the centroid of the instantaneous plume was located halfway between the plume edges,

(ii) the oscillation of the plume centroid was random,

and (iii) the transverse distribution of the mean concentration was Gaussian, then mathematically the instantaneous cross-wise profile was also Gaussian, and the plume width, $W(t)$, was essentially equal to $4\sigma_f(t)$ at any instant t. Thus by considering several frames, the following parameters were derived:

$$\overline{\sigma_f^2} = \frac{1}{n}\sum_{i=1}^{n}\left(\frac{W(i)}{4}\right)^2 \qquad (3.49)$$

and, from Eq. 3.22,

$$\sigma_g^2 = \frac{1}{n}\sum_{i=1}^{n}(z_c(i) - z_0)^2 \qquad (3.50)$$

where n is the total number of frames analyzed. From Eq. 3.25, the total variance σ_M^2 was evaluated. Ratios of the variances were thus calculated at various distances from the source.

3.C.4. Statistical Analysis of Point Concentration Variations. Concentration fluctuations at fixed points were also analyzed to determine the usual statistical variables and to relate calculated values to the variation of msf as outlined in Section 3.A.1. All statistical analyses used only digitized information so that with c(t) set as c(i), the mean concentration C was determined by

$$C = \frac{1}{N}\sum_{i=1}^{N} c(i) \qquad (3.51)$$

the deviation from the mean (or the temporal fluctuation) c'(i) by

$$c'(i) = c(i) - C\ ; \qquad (3.52)$$

the mean square (or intensity) of the concentration fluctuation s by

$$s = \frac{1}{N}\sum_{i=1}^{N} c'(i)^2\ ; \qquad (3.53)$$

the root mean square, σ_s, by

$$\sigma_s = s^{\frac{1}{2}} ; \tag{3.54}$$

and the temporal coefficient of variation, C_v, by

$$C_v = \sigma_s / C ; \tag{3.55}$$

where N is the total number of digital points of the concentration signal recorded over the total sampling period T_m and N is large.

The peak-to-average ratio P_a was calculated by the relation

$$P_a = c_p / C \tag{3.56}$$

where c_p is the largest value of $c(i)$ within the sampling period.

In some experiments, the frequency density, $g(c')$, for the fluctuation, c', was evaluated much like the probability densities $p_1(T_1)$ and $p_2(T_2)$. For $g(c')$, c' was assumed to range from $-2\sigma_s$ to $+2\sigma_s$ and the class interval was $\sigma_s/5$ thus giving a total of 20 intervals for each function $g(c')$. From c'_m, the value of c' where $g(c')$ was maximum, and c'_{me}, the location of the mean value of $g(c')$, the skewness factor, s_k, for $g(c')$ was calculated by

$$s_k = \frac{c'_{me} - c'_m}{\sigma_k} \tag{3.57}$$

where σ_k is the standard deviation of $g(c')$.

From the preceding calculations, the transverse variations of the parameters σ_s, C_v, and P_a were determined and compared with theoretical predictions. The shape of the frequency density, $g(c')$,

revealed the nature of the plume front oscillation. Characteristic frequencies of the concentration fluctuation were also established by power spectral analysis.

3.C.5. Summary of the Experimental Objective (Phase II).

The experimental objective of the second phase of this study is to analyze the temporal variation of tracer concentration as due to each one of the following three physical models:

(i) a fluctuating plume front,

(ii) a fluctuating plume,

and (iii) a random variation of point concentration within the plume. Using appropriate techniques, each model is applied to experimental measurements and theoretical predictions are examined in the light of the experiments.

CHAPTER 4

LABORATORY EXPERIMENTS (Phases I and II)

In this chapter, the details of the apparatus used for the laboratory experiments, the experimental procedure, and a reduction of data are presented. For in situ measurements, the apparatus and experimental procedure are the same for phases I and II. The differences in data reduction will be appropriately shown in the text.

4.A. APPARATUS FOR THE EXPERIMENTS

4.A.1. Flumes--Gross Characteristics. The experiments were conducted in two recirculating flumes designated as 85-cm and 110-cm flumes (the figures refer to their widths). Both flumes are located in the sub-basement of the W. M. Keck Laboratory of Hydraulics and Water Resources and run in a south to north direction with water flowing from south to north. The subsections below describe the gross characteristics of each flume and the roughening of the 110-cm flume bottom.

a. The 85-cm flume. An overall view of the 85-cm flume is shown in Figure 4.1. The cross section of the rectangular channel measures 30.5 cm deep and 85 cm wide. The channel length is approximately 18.3 m.

The channel, inlet box, and outlet tank are supported on a truss pivoted at a point near the downstream end of the flume, such that the channel bottom slope could be varied by use of a single pair of

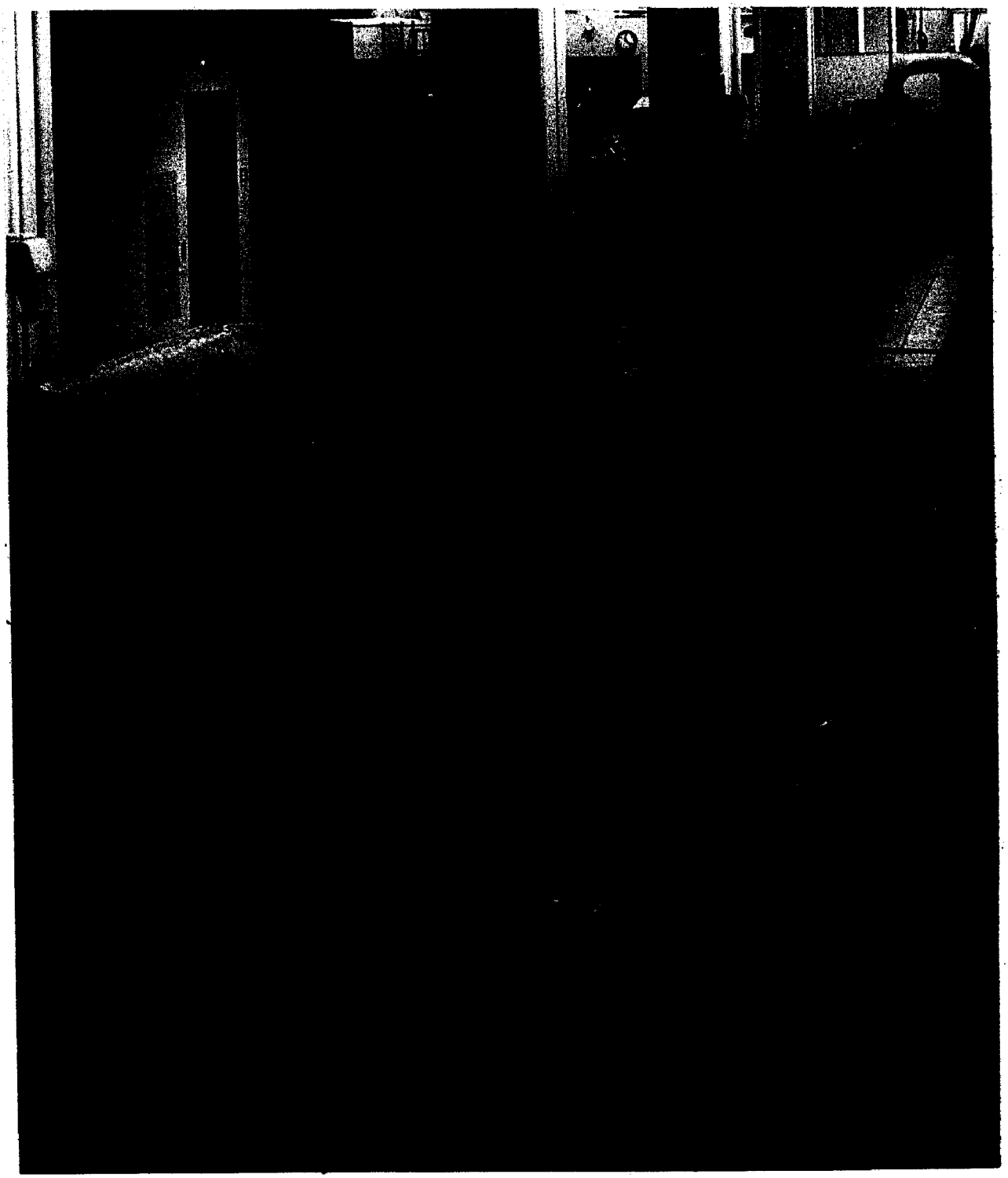

Fig. 4.1. Overall view of the 85-cm flume looking upstream (adapted from Fischer (2)).

power-driven jacks. The slope was calculated from the displacement registered by a vertical vernier gauge mounted 9.84 m upstream of the pivot supporting the channel. The slope gauge was calibrated to the nearest 0.001 inch (0.025 mm).

The water circulating pump, equipped with a 7-1/2 H.P. variable speed motor, delivers water from the outlet tank to the inlet box through an 8 inch (20.3 cm) pipe with an 8 × 5 inch Venturi meter (laboratory code Q-21) used for measuring water discharge. Water is discharged vertically downwards into the inlet box through an inlet pipe dipping freely into the box but not attached to it. A horizontal baffle within the inlet box, and a set of vertical screens at the downstream opening of the box were used to smoothen the discharge into the channel, and to achieve uniform flow conditions across the channel. For high Froude number experiments, a floating horizontal board was installed just downstream of the screens to reduce inlet wave distrubances.

The flume sides and bottom are made of steel plates except for a section of the west wall extending from 7.9 m to 14.6 m downstream of the inlet box which is glass. The rest of the channel interior is painted with a two-part epoxy coating of Pittsburgh Aquapon white paint.

On rails affixed to the top of each channel side is mounted an instrument carriage equipped with a variable speed electric motor, which provided a maximum carriage speed of about 300 cm/sec when desired. The carriage also supports an aluminum frame tower especially constructed to hold a camera and four 120-volt floodlight

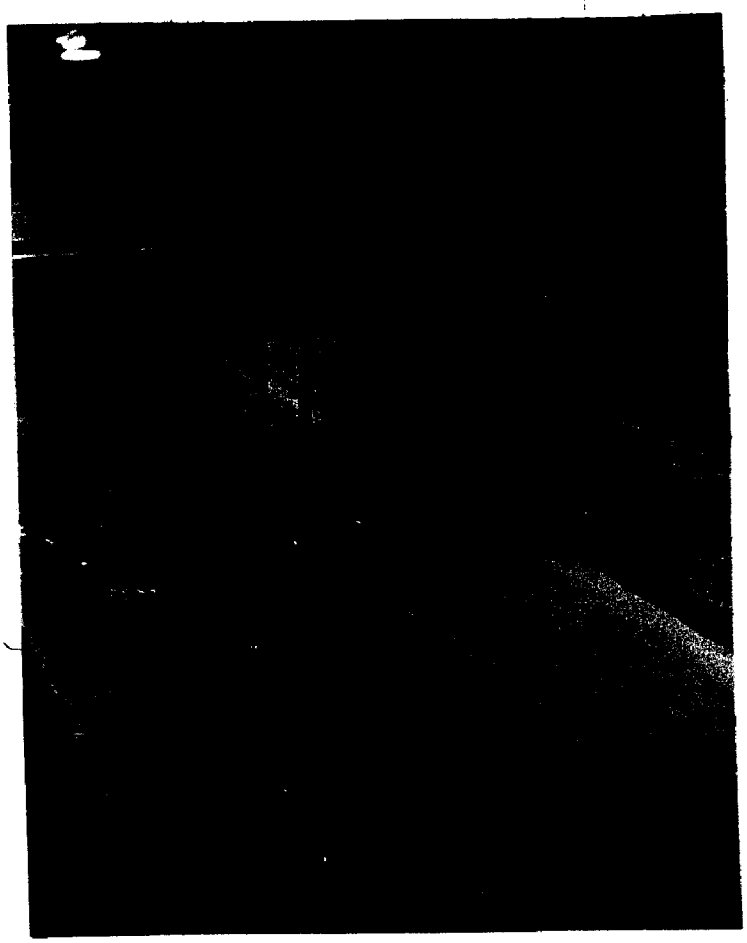

Fig. 4.2. The instrument carriage with probes placed in flume S1 during an experiment

bulbs used for photography.

As shown in Figure 4.2, point gage and the probes are mounted on the instrument carriage with gages equipped with verniers for measuring vertical displacements to within 0.1 mm. Transverse positions were measured to the nearest millimeter.

Two scales were used for measuring longitudinal distances: a steel tape fixed on top of the east channel wall, and a cloth tape

supported on two pairs of cross boards and maintained just above the water surface within the channel. Both tapes were calibrated to the nearest 0.5 cm. The steel tape was used for establishing carriage positions, and the cloth tape for scaling plume characteristics when the plume was photographed.

b. The 110-cm flume. The 110-cm flume, shown schematically in Figure 4.3, is 40 m long with a rectangular cross section 110 cm wide and 61 cm deep. A detailed description has been given by Vanoni et al. (58).

The flume rests on a central pivot and four pairs of screw jacks, two upstream and the other two downstream of the main pivot. The jacks are driven by electric motors and thus allow continuous tilting of the flume. Flume slope was calculated from the vertical displacement of a vernier gage stationed about 17 m upstream of the pivot. The vernier scale was read to the nearest 0.001 inch (0.0025 cm). By using a still water surface as a reference for calibration, it was found that the flume slope, S_o was related to the slope gage displacement by

$$S_o = (d_v - 3.023)/671.7 \qquad (4.1)$$

where d_v is the reading on the slope gage in inches.

The flume floor is made of hot rolled stainless steel plate, and the sides are glass except for a 3.05 m section near the inlet and a 2.14 m section near the outlet where the sides are of stainless steel plate. As in the 85-cm flume, an instrument carriage rests on steel

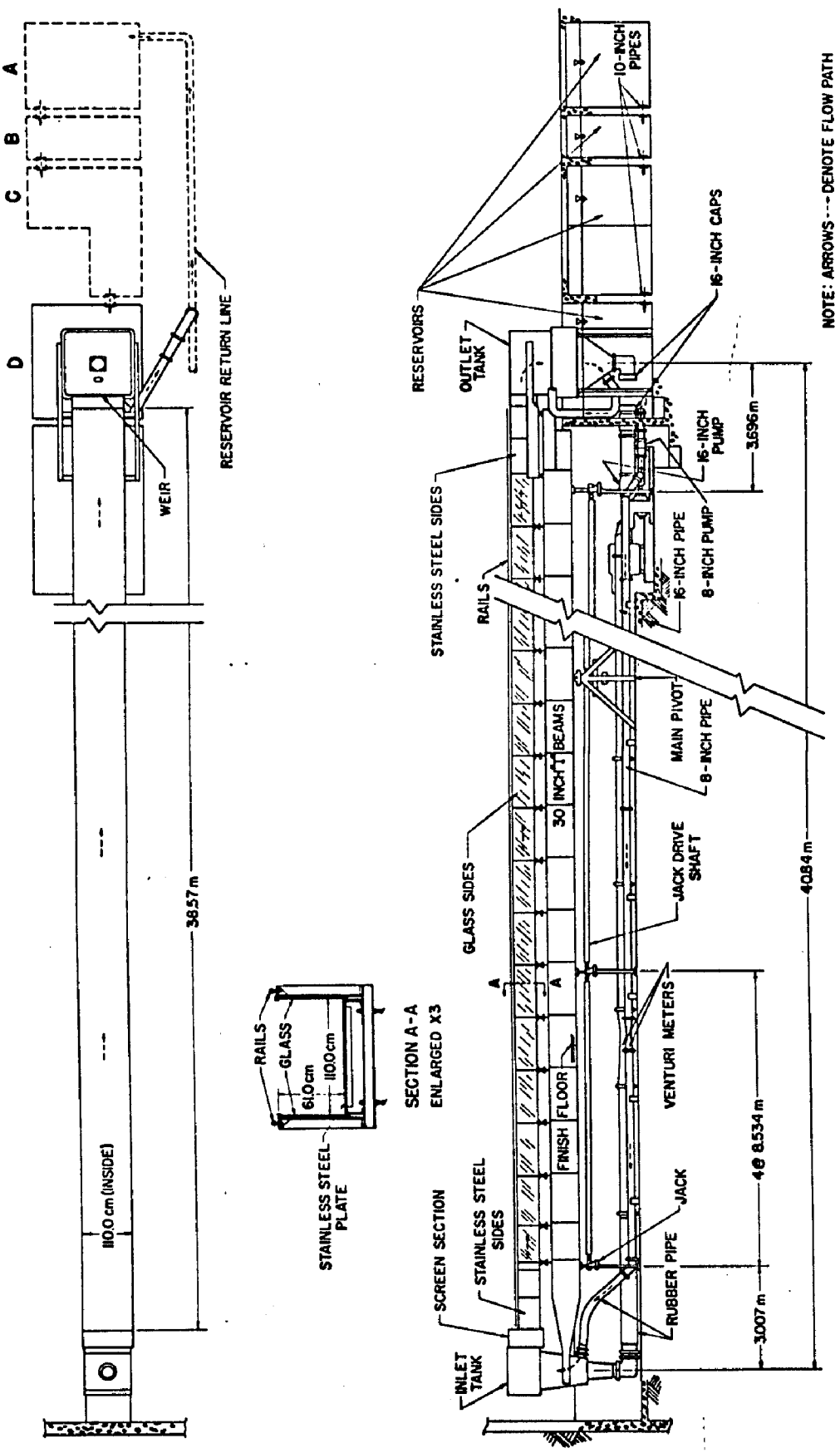

Fig. 4.3. Schematic of the 110-cm flume (adapted from Prych (39)).

rails and supports an aluminum channel to which point gage and probe holder brackets are attached.

The water is pumped to the inlet tank by a 10 H.P. variable speed pump through a return line of nominal diameter 8 inches. An 8 X 4 inch venturi meter (laboratory code Q-6) is installed in the line for discharge measurement. Water is released into the channel through horizontal wooden baffles in the inlet tank and a set of three vertical screens (about 3 mm mesh opening) placed just downstream of the inlet box. At the downstream end of the flume, the water flows over an adjustable sharp-crested weir into the outlet tank.

To maximize the total volume of water used and thus minimize the rise in the tracer concentration of the background during an experiment, four reservoirs (identified as A, B, C, and D in Figure 4.3) with a total capacity of about 63 m^3 are used essentially as dilution tanks. As shown in Figure 4.3, the flume water flows from the outlet tank to reservoir A furthest from the flume. From there the water discharges into the other reservoirs through 10 inch pipe connections, and is pumped finally into the 8 inch return line which connects reservoir D just under the outlet tank to the inlet tank.

c. Roughening of the 110-cm flume bottom. The bottom of the 110-cm flume was roughened by placement of crushed white decorative rock of nominal size of 3/4 inch supplied by Sunburst Rock Inc., Irwindale, California. The size distribution by sieve analysis, shown in Figure 4.4 was virtually Gaussian with a median size of 0.562 inch and a standard deviation of approximately 0.168 inch.

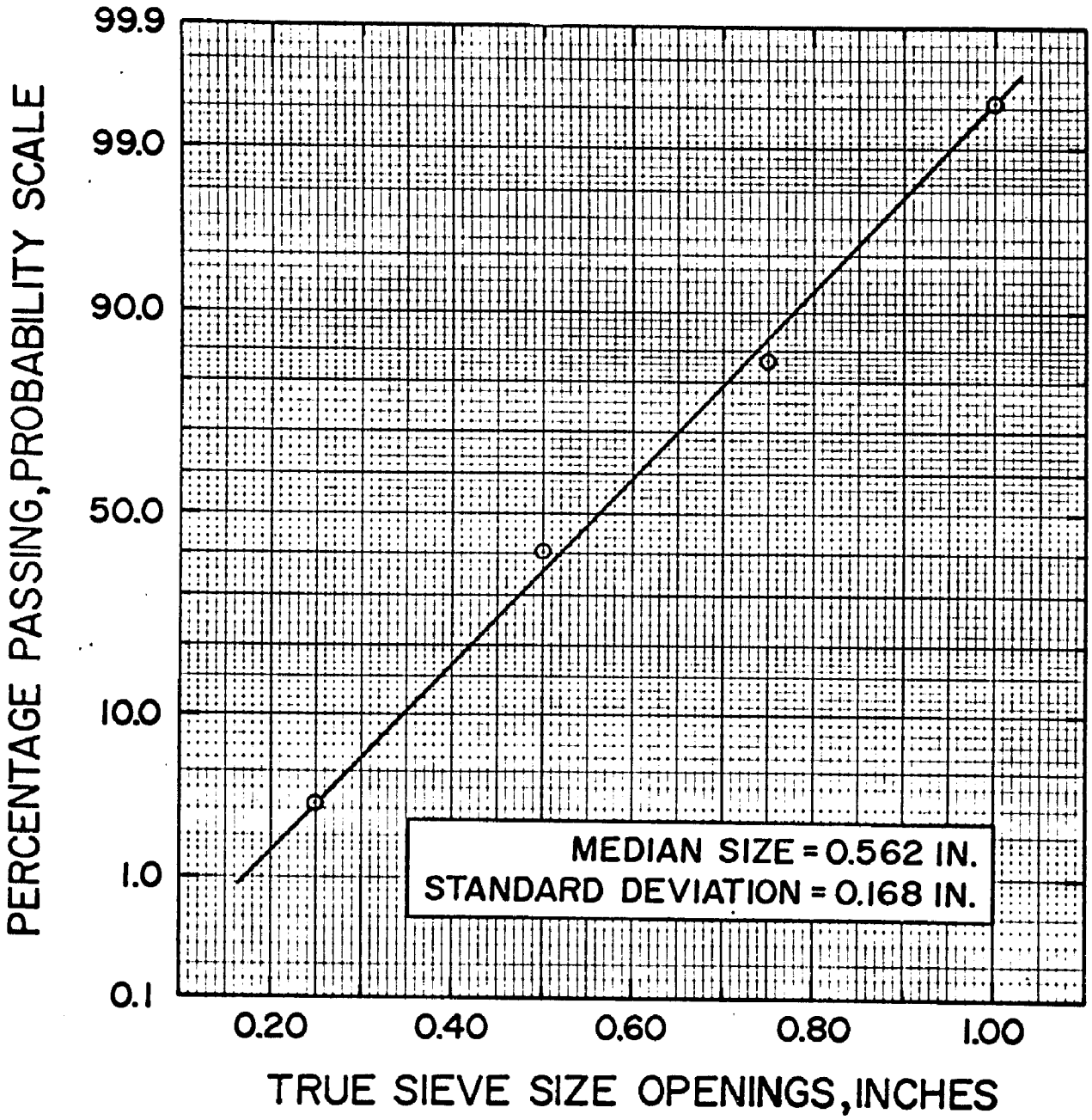

Fig. 4.4. Size distribution of the rocks used for roughening the 110-cm flume bottom

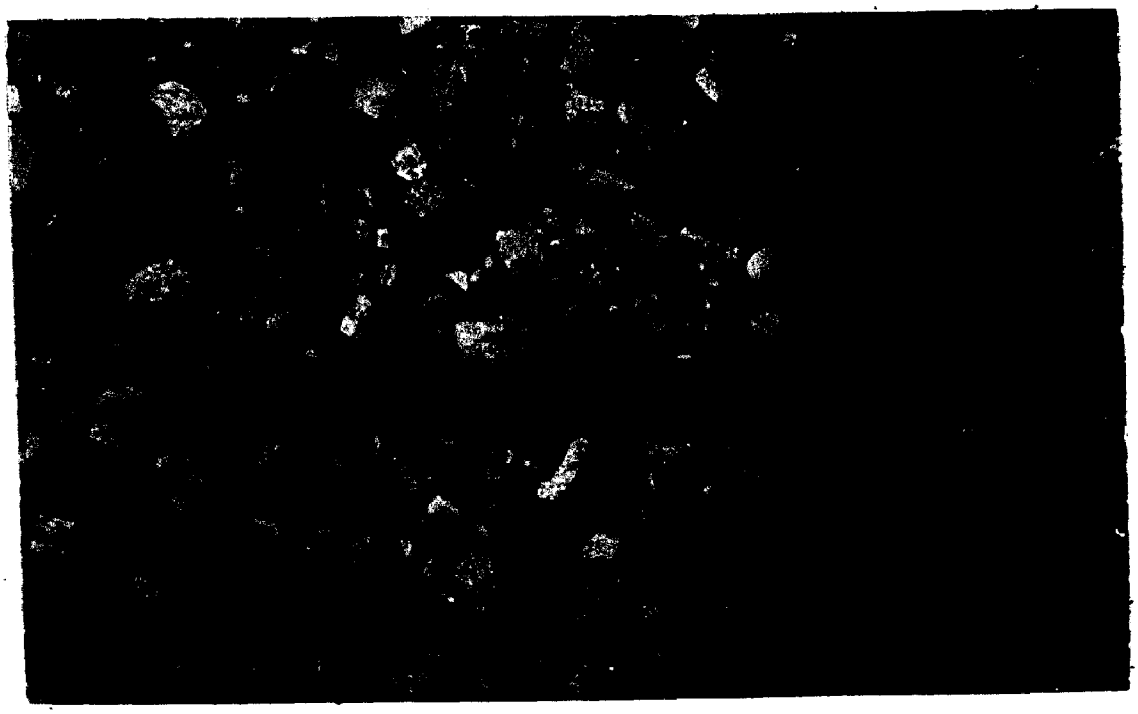

Fig. 4.5. Plan view of the rocks as placed on the flume bottom

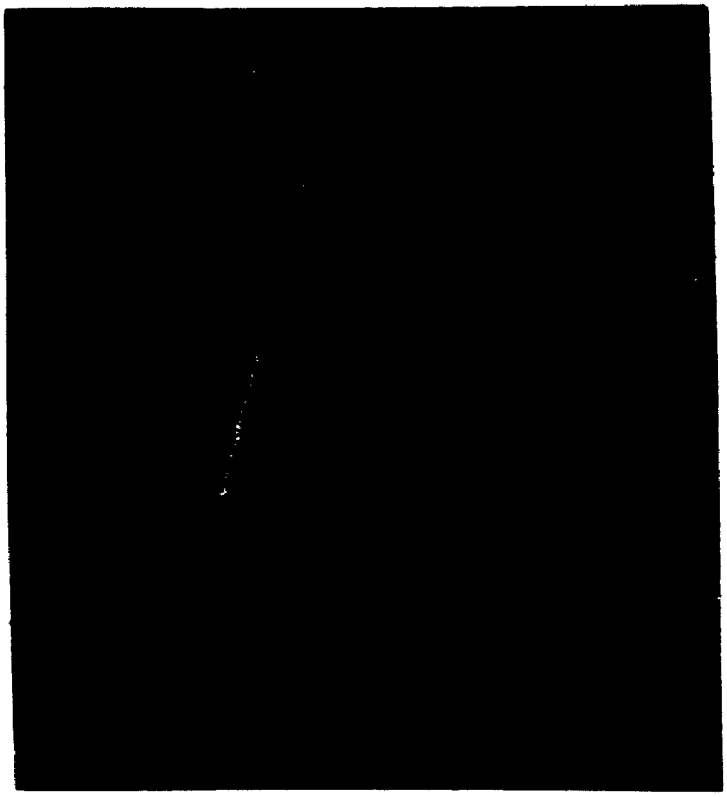

Fig. 4.6. Perspective view of the entire flume with the bottom covered with rocks

The stones were first washed to remove the fines, and then hand placed on the flume bottom to a one-layer thickness. They were packed to such tightness that removal of a stone exposed a flume bottom area equivalent to at most 100 per cent of the mean cross section of the stone. Figure 4.5 shows a plan view of the stones as placed on the flume bottom. Figure 4.6 is a perspective view of practically the entire flume bottom completely covered with stones.

The stone thickness at a point was determined by first recording the point gage reading at which the point gage first touched a stone, and then subtracting from this value the reading corresponding to the flume bottom elevation at that point. From point gage measurements, the mean stone thickness d_s for the entire flume was found to be 1.80 cm. For zero void ratio, d_s was calculated to be 1.11 cm. Flow depths were measured relative to the mean position of the top of the stones.

4.A.2. Concentration Detection Equipment.

a. The overall system. The concentration detection system for in situ measurements is shown in Figure 4.7. It consisted essentially of a conductivity probe which formed part of a Wheatstone bridge circuit. The other elements of the bridge were housed inside a grounded bridge box. Excitation of the bridge circuit was provided by a preamplifier-recorder system, which also amplified and recorded the output continuously on a strip chart, and simultaneously relayed it to an analog-to-digital (A/D) converter. The digitized information was recorded on magnetic tape by a synchronous tape

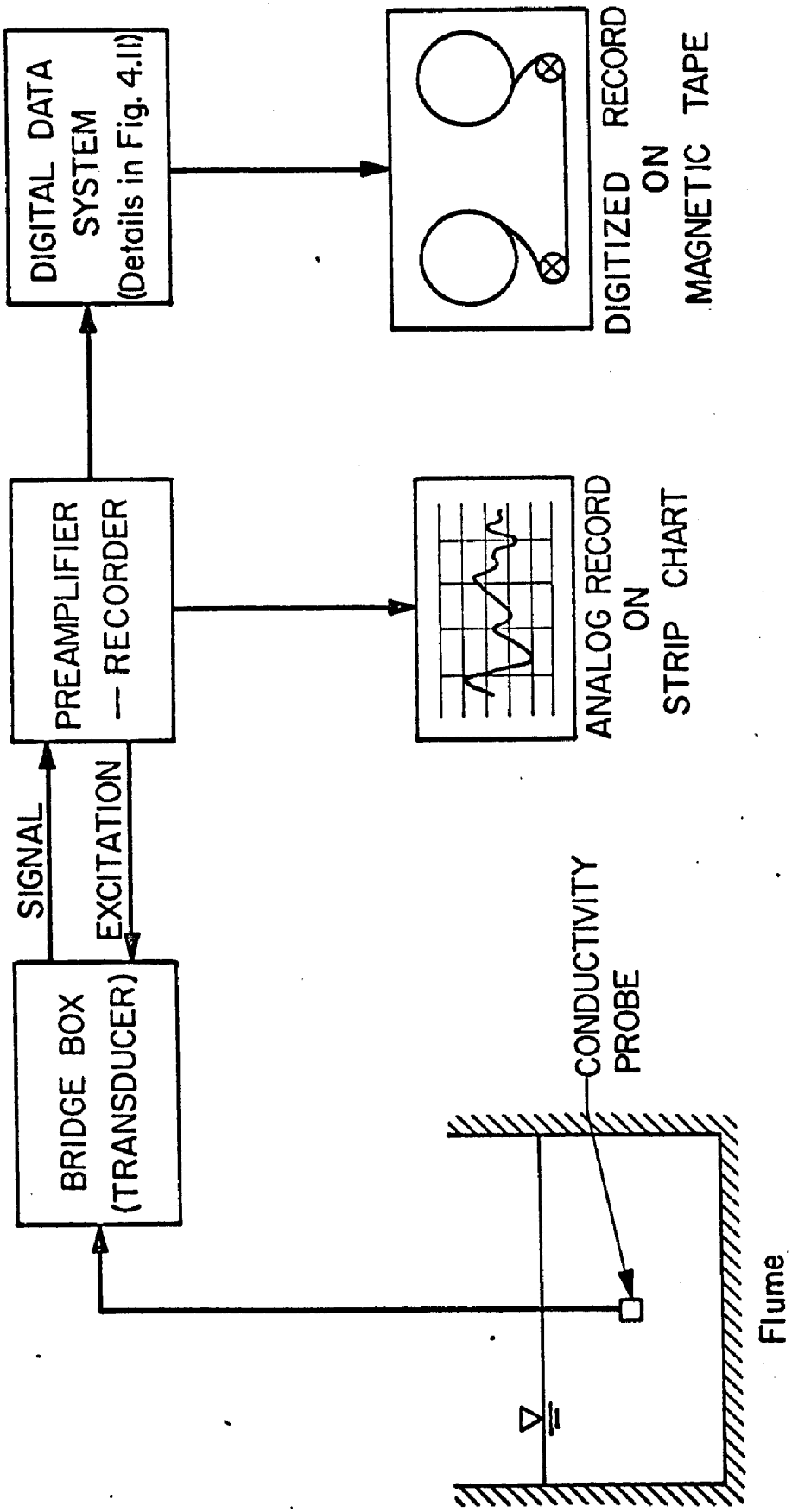

Fig. 4.7. Flow diagram of concentration detection system

recorder.

b. The conductivity probe. The conductivity probe used for in situ measurements is a modified version of the probes used by Fischer (2). It was designed to measure electrical conductivity (related to salt concentration) at the location of the probe electrodes. The design details of the probe are shown in Figure 4.8.

The probe, nominally 15 inches long, consisted of three platinum plate electrodes firmly set into a 7052 kovar sealing which blended into Corning 3320 canary glass. This sealed the lower end of a stream-lined 7740 Pyrex glass casing which tapered off at the top where it was glued to an amphenol connector with Reziweld epoxy. The casing was 1/32-inch thick.

Each electrode, 1/8 inch by 1/8 inch and 0.005 inch thick, was spot-welded to a two-inch long pure platinum wire. The copper wires leading to the amphenol connector were each silver soldered to the platinum wires. The central wire was insulated from the outer two, and the three wires were enclosed in a continuous metallic shield. The center lead was soldered to the center pin of the amphenol connector and the outer leads to the connector base.

The three electrodes were aligned such that the outer ones were 1/8 inch apart with the center plate exactly midway between them. Thus the generated electric field was confined to a small region within the outer plates in contrast to the large field which a conventional two-plate system would have induced. The three-plate arrangement therefore offered greater sensitivity and better response

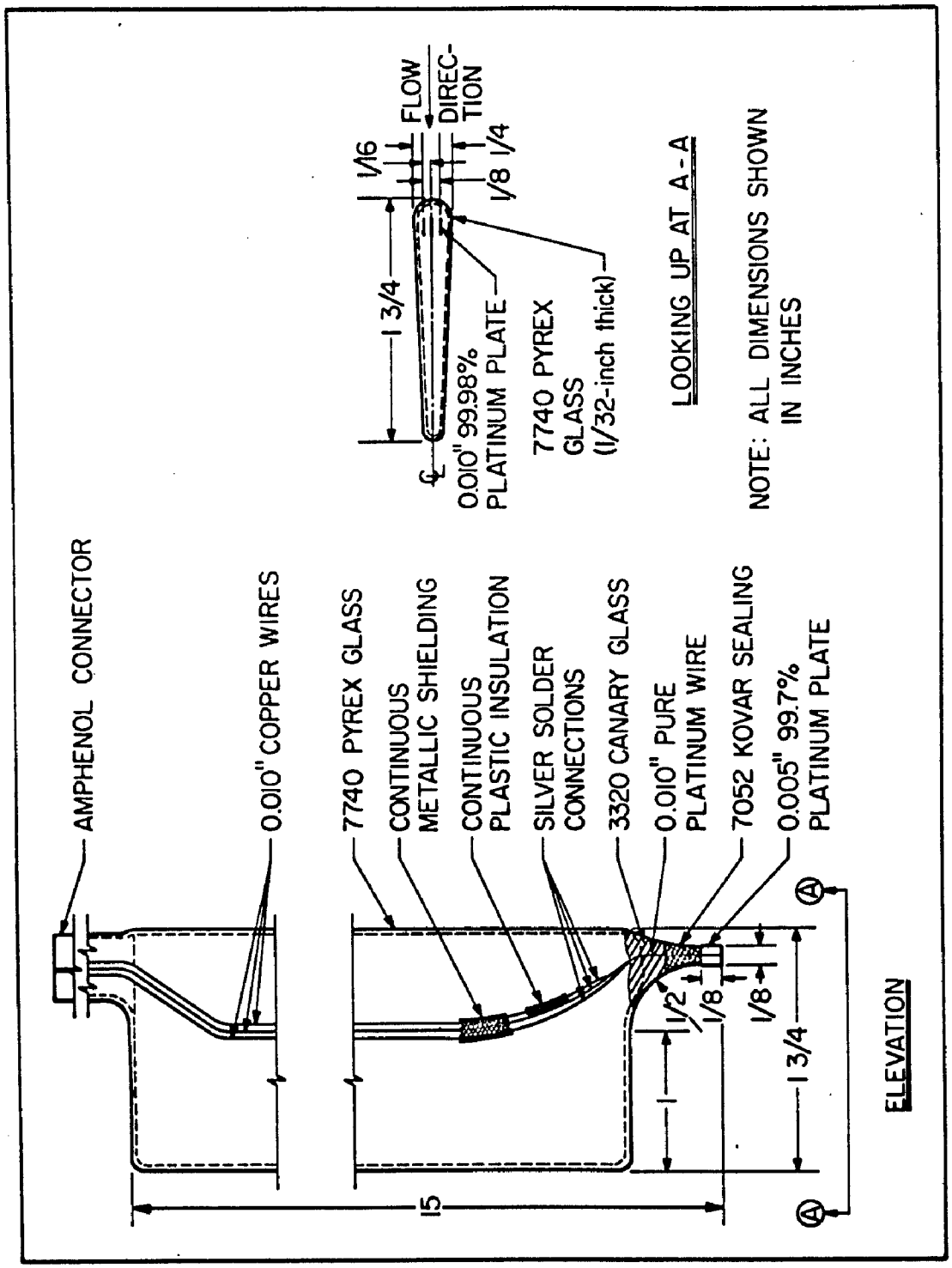

Fig. 4.8. Details of the conductivity probe

to concentration variations at a point than a dual electrode configuration.

Probe sensitivity was also enhanced by platinizing the electrodes in chloroplatinic acid and cleaning them frequently with chromic-sulphuric acid solution. During storage, the electrodes were immersed in distilled water.

c. Bridge circuit. The probe was connected to the bridge circuit by a two-conductor shielded cable (Belden 8402 or 8422) leading from the amphenol connector to a two-prong connector which was plugged into but insulated from the metallic bridge box. As shown in the block diagram of Figure 4.7, the recorder supplied the excitation voltage for the bridge and received the input signal of the probe via the bridge circuit.

The details of the elements of the full-bridge circuit and the external connections to the recorder are shown in Figure 4.9. The probe was connected across a 25-ohm resistor which could be replaced by a variable potentiometer in order to vary the probe sensitivity if desired. Increasing the potentiometer resistance at this point would decrease probe sensitivity, and vice versa. The 1K-ohm variable resistor on the opposite arm of the bridge offered immense flexibility in the initial balancing of the bridge circuit. All fixed resistors were 0.1% precision resistors having a low temperature coefficient. The potentiometers were Ohmite type AB.

The bridge was connected to the recorder via the signal and excitation circuits each of which was a two-conductor shielded cable.

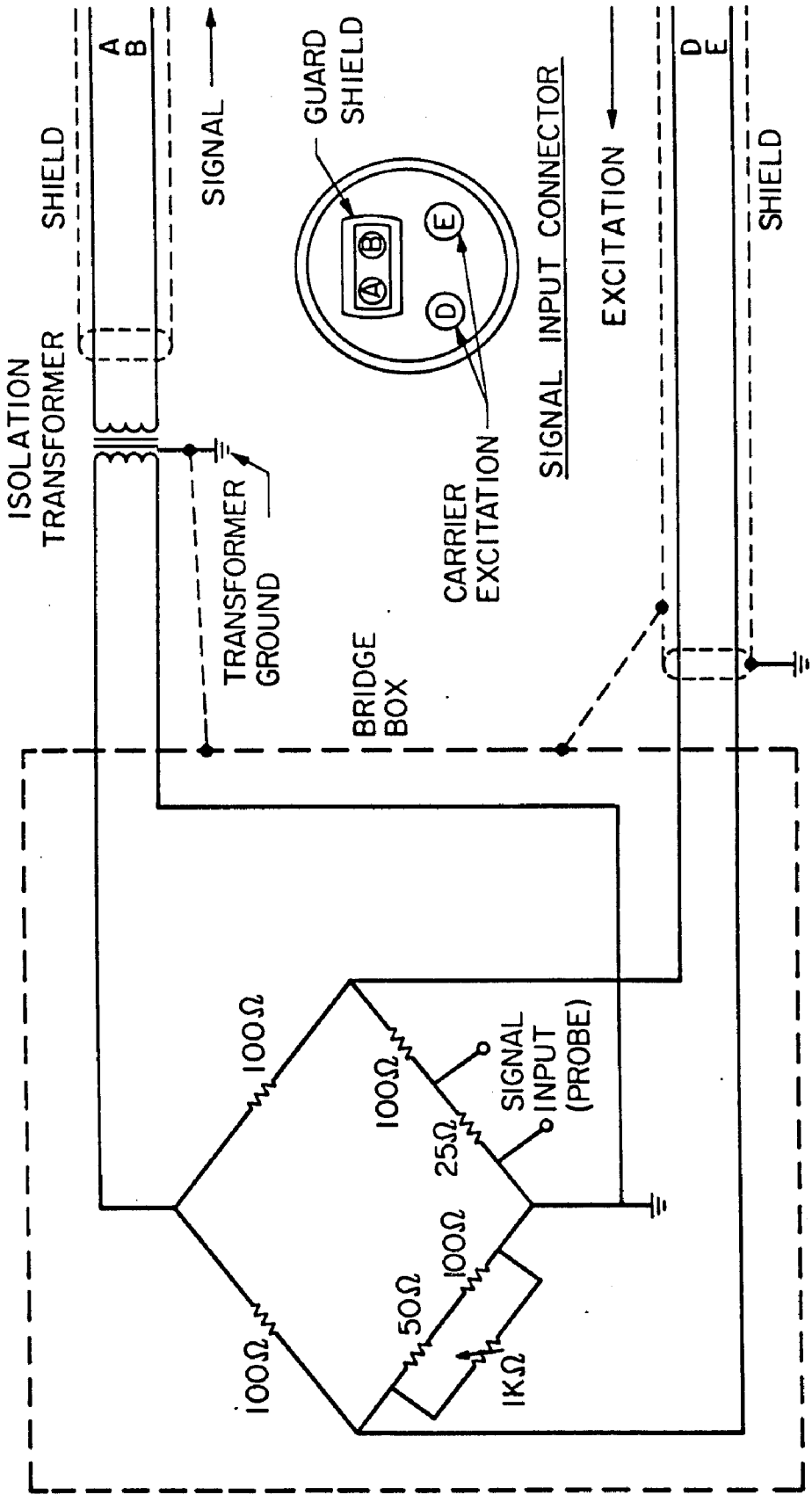

Fig. 4.9. Details of the bridge circuit and related external connections to the Sanborn analog recorder

The leads A, B and D, E of the bridge were connected to corresponding points within the signal input connector of the recorder shown as inset in Figure 4.9. The bridge box and the shields were grounded at the guard shield which also formed the signal ground.

When a probe was immersed in ionized water in a grounded flume, the potential difference between the flume and instrument grounds induced a current loop. Since the output of the recorder was single-ended (i.e. the output voltage was measured relative to the instrument ground potential), the ensuing loop voltage as well as the true signal was amplified, and the combined voltage erroneously recorded as the true output. In addition, when two or more probes were immersed in the water, cross loops developed between the probes. The result was signal coupling and interference between the probes. To eliminate the ground loop within each transducer circuit and the interference between probes, an isolation transformer was installed in the signal circuit of every bridge circuit as shown in Figure 4.9. A United Transformer Corp. transformer No. UTC A-18 proved very effective, and was used in the present study.

d. Analog recording system. A transistorized Hewlett-Packard recording system (Series 7706A) operating in conjunction with a carrier preamplifier (Series 8805A) was used. The recorder had a capacity of six channels each of which was connected to a carrier preamplifier. A single oscillator provided about 5 volts of excitation voltage output alternating at 2400 Hz for each preamplifier. The amplifier also amplified, demodulated, and further amplified the

input signal from the bridge circuit. The output, which was within ± 3 volts DC across 1000 ohms, was fed directly to the recorder. For each channel, a heated stylus was activated to simultaneously impress on a temperature sensitive paper (permapaper) a deflection proportional to the amplifier output. The permapaper was driven by a motor at a selected constant speed, thus allowing the signal output to be continuously recorded on the strip chart. An averaging switch permitted the output to be continuously averaged over a 1-sec period if desired.

e. Analog-to-digital (A/D) data acquisition system. In experiments where the analog information was digitized, the signal output was fed directly to an analog-to-digital (A/D) data acquisition system from the output jack of the carrier preamplifier--thus completely bypassing the analog recorder. A photograph and a flow diagram of the A/D system are, respectively, shown in Figures 4.10 and 4.11.

The A/D system (series 1103) manufactured by Digital Data Systems, Northridge, California, accepted eight channels of analog voltages which ranged to a maximum of ± 10 volts. The channels were sampled by an analog multiplexer which scanned the eight channels in about 4.4 milliseconds. The sample-and-hold amplifier, receiving the sampled voltage, had an aperture of 0.17 microseconds. This represents the period over which the input voltage was digitized. Both the scanning rate and the aperture were constants for the system.

However, the sampling rate, which denotes the rate at which

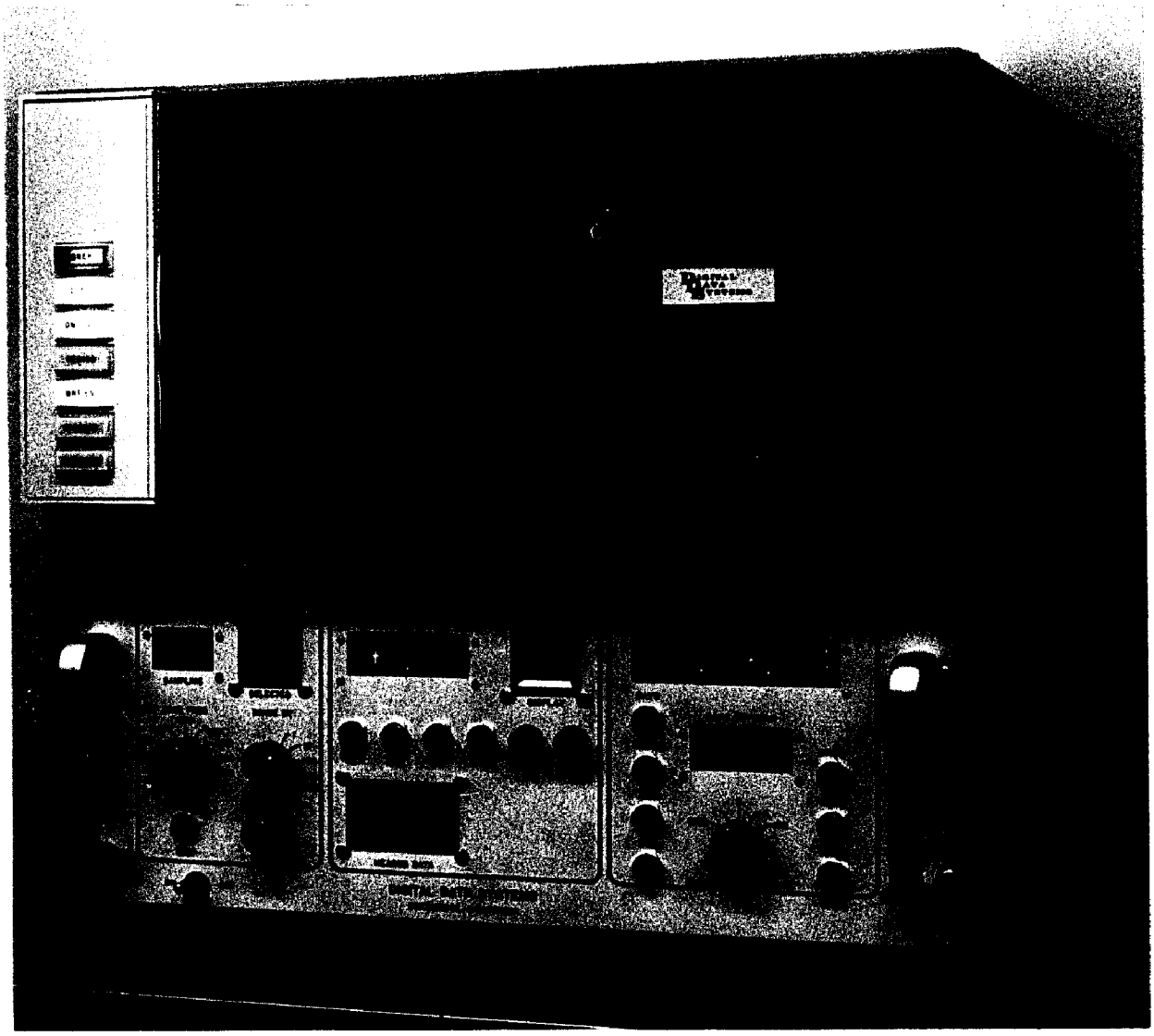

Fig. 4.10. Data acquisition system for digitizing analog records and storing the digitized output on tape

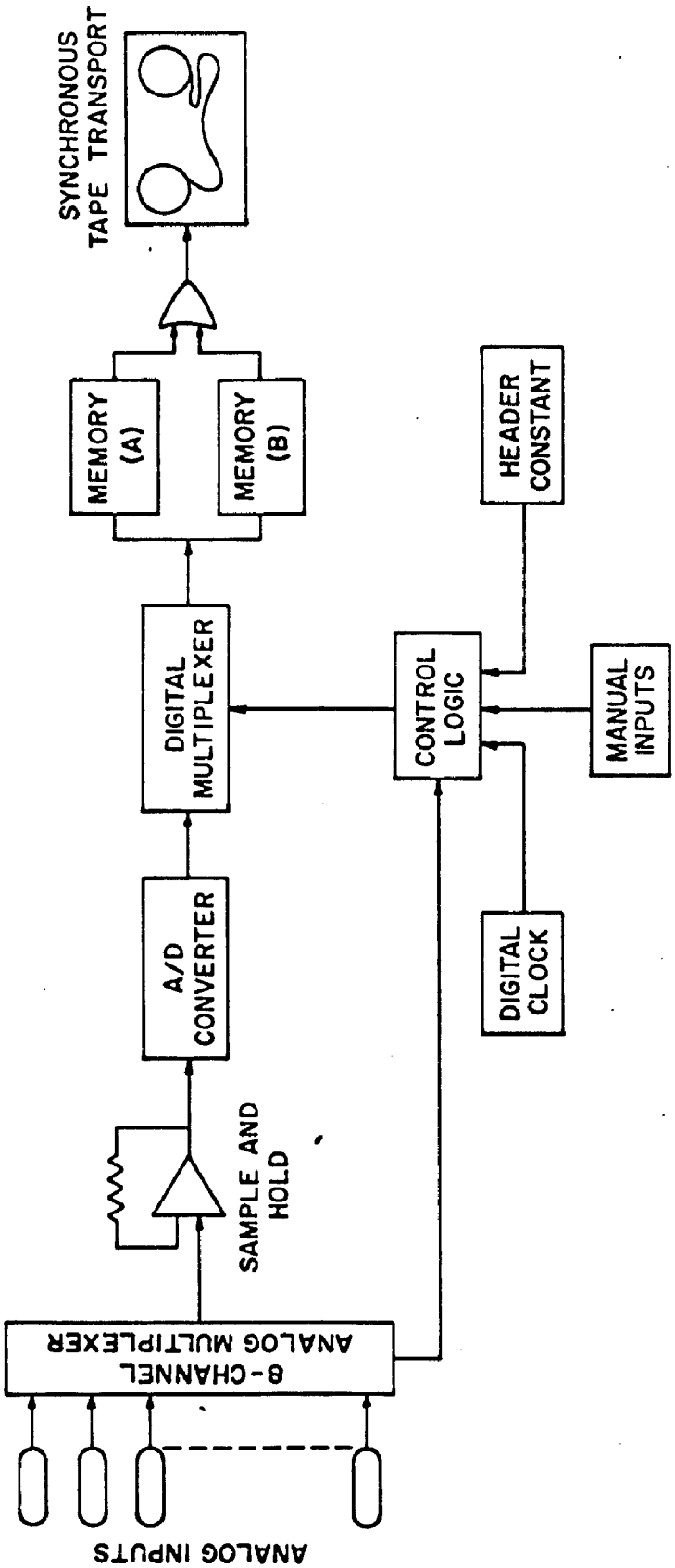

Fig. 4.11. Flow diagram of the digital data system

the analog voltage was digitized, was selected by the operator by use of the BASE FREQ and DIVIDE BY controls. The maximum sampling rate was 1600 samples per second (s/sec) for one channel. Thus if eight channels were being used, the maximum rate was 200 s/sec per channel.

Sampled voltage was fed to the A/D converter where it was converted to a binary signal and then to binary-coded-decimal (BCD). Meanwhile the header data received by the control logic were coded appropriately. The header data consisted of (i) identification information from the analog multiplexer, (ii) digital clock data, (iii) a four-digit number termed the header constant, and (iv) manual identification inputs. The BCD of the converter and the header data from the control logic were received by a digital multiplexer and transferred to one of two memory units for storage. Each unit has a capacity of 1024 tape characters.

Since the system utilized a synchronous tape transport, as opposed to an incremental recorder, data were first collected in one memory unit at the sampling rate, and then transferred to the tape at the maximum transport rate of the recorder. Meanwhile the other memory unit accepted data from the digital multiplexer while data in the full unit were being recorded on tape. Thus no information was lost while digitized data were being recorded on tape.

Digitized information was packed on the magnetic tape in a language and format compatible with the IBM 360/75 high speed computer. Data from a set of measurements, such as concentration monitored at a fixed point over a given length of time, were stored on

tape as a file. The files were separated from each other by END OF FILE marks. Each file was composed of records separated from one another by INTER RECORD GAPS. A record length was 1024 tape characters, and comprised the storage of each memory unit. In each record, the first sixteen tape characters identified the header data from the control logic, the remaining 1008 characters were digitized data. Since voltages were recorded as 3-digit values, each sample consisted of three tape characters; thus 336 samples were stored in every record.

By use of appropriate subroutines, the recorded information was conveniently retrieved by the IBM 360/75 computer; thus digitized concentration data were available for reduction and analysis by the main computer program.

4.A.3. Velocity Measuring Device. Water velocities were measured with a 1/8 inch (0.32 cm) diameter Prandtl pitot static tube with a dynamic head opening of 0.107 cm. The pressure difference between the static and dynamic heads was measured by a pressure transducer built by the Pace Manufacturing Co., Los Angeles, California. The pressure difference deflected a 0.0102 cm diaphragm which in turn induced a voltage that was measured by a Sanborn analog recorder.

The transducer was calibrated by inducing pressure differences across the diaphragm, and measuring the pressure differential in manometer pots equipped with micrometer scales. Pressure heads were recorded to within 0.00025 cm. Calibrations made before and

at the end of an experiment agreed to within two per cent.

The velocity was obtained by positioning the pitot tube at the desired point within the flow field, and recording the output on the strip chart of the Sanborn recorder for about 30 seconds. Since the output was averaged over a one-second time constant by the recorder, variations about the mean value were generally less than 15% of the total stylus deflection from zero. The mean deflection was obtained by placing a straight line on a transparent scale over the record, and estimating an average value by eye.

4.A.4. The Tracer Injection System. Figure 4.12 is a sketch of the tracer injection system. The tracer was a sodium chloride solution colored blue with dye primarily for visual effects. The solution density was restored to approximately unity by addition of methanol. The tracer was stored in a five-gallon constant head tank placed on a support base about 2.5 m above the flume bottom at the injection station.

With a plug valve completely open, tracer flow rate was controlled by use of a metering valve, and measured by a precision flowrator which used a floating ball as a flow rate indicator. The tracer flowed through a Poly-flo connector to a copper tube which was soldered to a stainless steel injector. The internal diameter of the injector was 0.267 cm, and the tracer was injected at ambient velocity parallel to the water flow. The vertical position of the injector was determined to within 0.001 ft (0.030 cm) by a vertical displacement scale mounted to the instrument carriage. The injector was always

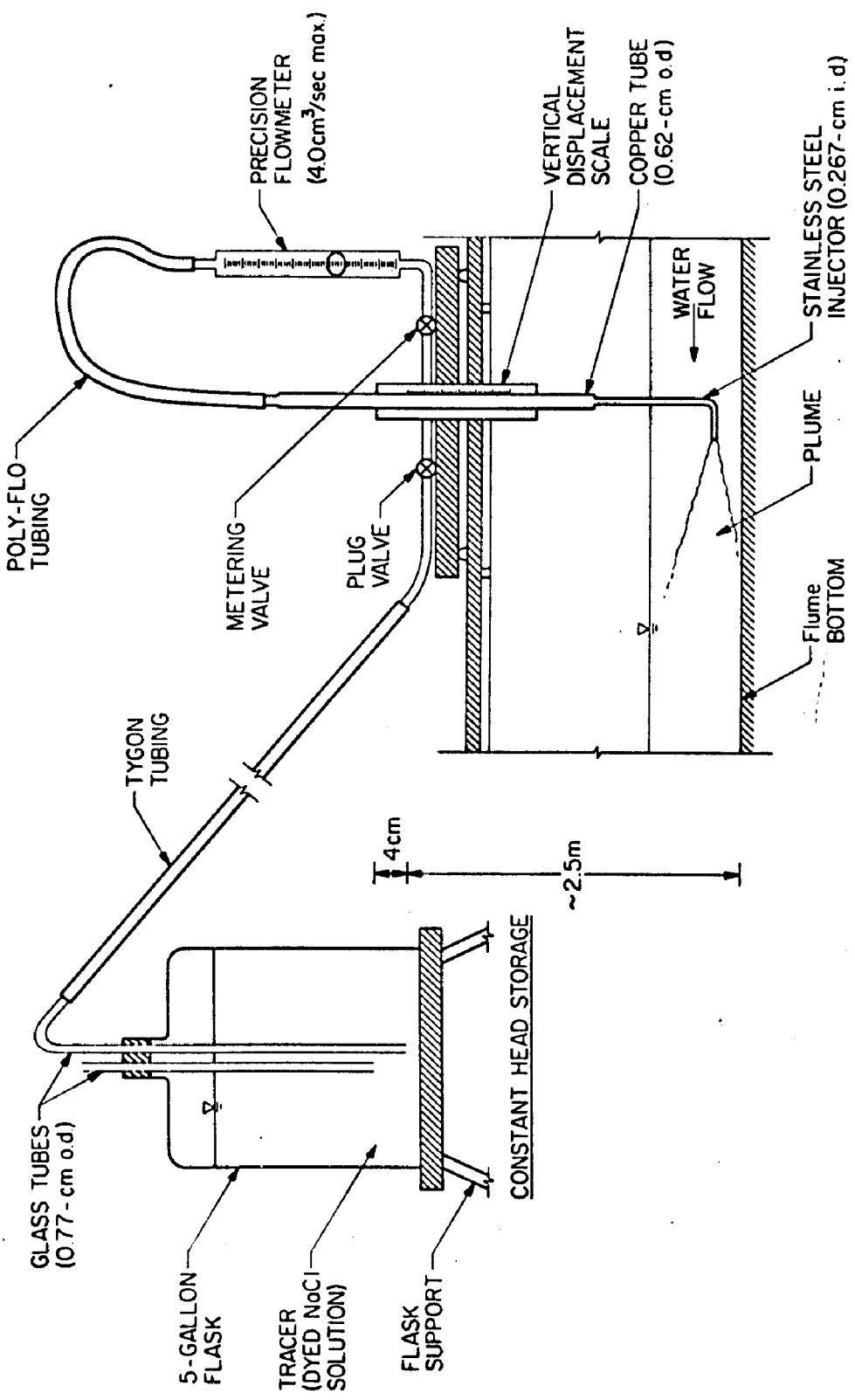

Fig. 4.12. Sketch of the tracer injection system

located at the flume center line.

The flowmeter was calibrated by keeping the plug valve wide open and, using the metering valve for control, recording tracer discharge for various flowrator readings. With the injector cross-sectional area known, the mean tracer flow velocity was calculated, and a curve of tracer velocity versus flowrator reading was developed. It was found that within the range of the change in tracer temperature experienced from one experiment to another and within the sensitivity of the flowmeter, a single calibration curve was adequate for a set of experimental runs. A new curve was developed only when any section of the injector system was altered.

During an experiment, the injection velocity, which closely equaled the local water flow velocity, was first determined. The corresponding flowrator reading was then obtained from the calibration curve. With the injector set at the desired depth, and the plug valve wide open, the flowrator was set at the required reading using the metering valve. Tracer flow was subsequently controlled only by completely opening or closing the plug valve.

4.A.5. Photo Analysis Equipment. The motion picture of the fluctuating plume was taken by a Bolex camera motorized to operate at exactly 24 frames per second. The developed negative was stored in reels each with 30.5 m of film.

The film was analyzed by projecting the picture on the screen of a film scoring viewer. The film could be projected automatically at a selected speed, or manually one frame at a time. With the

picture on the screen, a cross-hairline was manually used to determine the crosswise positions of the edges of the plume at that particular instant of exposure. A transverse scale located in the picture field was used to calibrate the scale on the screen. Transverse displacements in the flume were determined to within 1 mm.

Since the motion picture studies were conducted in the 85-cm flume, the longitudinal tape located within the channel was used to measure values of x. Elapsed time was measured either by a ten-second sweep clock in the camera view or by counting the film frames.

4.B. EXPERIMENTAL PROCEDURE

4.B.1. Identification Code for Flumes and Experiments.

Since experimental numbers will be used in this section as examples to illustrate typical measurements or operations, it is necessary that the code for identification of the flumes and the experiments be explained. A summary of the classification is shown in Table 4.1.

The flume identification code consists of a letter-figure combination with the letter referring to the roughness of the flume bottom, and the figure to a particular flume. The letter S indicates that the flume bottom was hydraulically smooth during the experiments, and R means that the flume bottom was roughened with rocks. The 85-cm flume is identified by the figure 1, and the 110-cm flume by 2. Thus, the code S2 refers to an experiment performed in the 110-cm flume with the flume bottom hydraulically smooth.

All experiments were grouped in "series" each consisting of

Table 4.1. Classification of flumes and experiments

SERIES	Flume	Flume Bottom Roughness	Flume Identification Code	Data Digitized?	Mode of Analysis
500	85-cm	Smooth	S1	no	Time-averaged calculations only
600	85-cm	Smooth	S1	no	Time-averaged and intermittency analysis
700	110-cm	Smooth	S2	no	Same as in Series 600
800	110-cm	Smooth	S2	yes	Time-averaged, intermittency, and statistical analyses from digitized data
900	110-cm	Smooth	S2	yes	Cross-correlation analyses
400	110-cm	Rough	R2	yes	Same as in Series 800
300	85-cm	Smooth	S1	no	Fluctuating plume studies using motion pictures

one or more experiments referred to as "runs." The first digit of a run number refers to the series, the second and third digits to the experiment number within the series. For example, RUN 512 denotes experiment 12 in the 500 series. Each run, except in Series 300, consisted of an entire experiment beginning with uniform flow establishment and concluding with concentration measurements.

If velocity measurements were also made and velocity contour maps subsequently developed, the letter V was affixed to the run number. For example, run numbers 506V, 708V, and 404V indicate that velocity maps were developed for the corresponding runs 506, 708, and 404.

Velocity contours were developed in Series 500 for the 85-cm flume with the smooth bottom, in Series 700 for the 110-cm flume also with smooth boundaries, and in Series 400 for the 110-cm flume with the bottom roughened with rocks.

4.B.2. Typical in situ Measurement

a. Establishment of uniform flow and calculation of hydraulic parameters. By adjusting discharge and flume slope, the water depth was set at a desired value. Uniform flow conditions were assumed to prevail when the flow depths at various stations agreed to within ± 0.02 cm.

In the 85-cm flume the energy slope S_f was determined by fitting a straight line to the plot of the difference between the still water level and the flowing water surface elevation versus x. The slope of this line was used as the energy slope. Since the deviations of the flow depth at various stations from the mean depth were

generally small and random, corrections for differences in the velocity head did not significantly alter the value of S_f thus calculated. A typical energy slope determination is shown in Figure 4.13. In general S_f was different from the flume bottom slope by between 1% and 10%.

The flume rails of the 110-cm flume were so precisely positioned that the slope of the rails was exactly the same as the flume slope S_o determined by Eq. 4.1. The value of S_o at the condition of uniform flow was used as the energy slope. Velocity head corrections were made for the smallest flow depths.

The normal depth, d, used for subsequent calculations is the mean value of the flow depths measured at the various stations for the uniform flow condition. For experiments where the flume bottom was rough, the mean stone thickness used was 1.66 cm, i.e. 92.3% of the thickness calculated from point gage measurements. This correction was obtained from velocity measurements. The depth y = 1.66 cm above the flume bottom represented the average height at which flow velocity was effectively zero.

The mean velocity, $\bar{u}$ was evaluated by the relation

$$\bar{u} = Q/A, \tag{4.2}$$

where Q is the discharge, and A the flow cross-sectional area; the mean shear velocity, u_* by

$$u_* = \sqrt{grS_f}\ , \tag{4.3}$$

where r is the hydraulic radius; the friction factor, f_* by

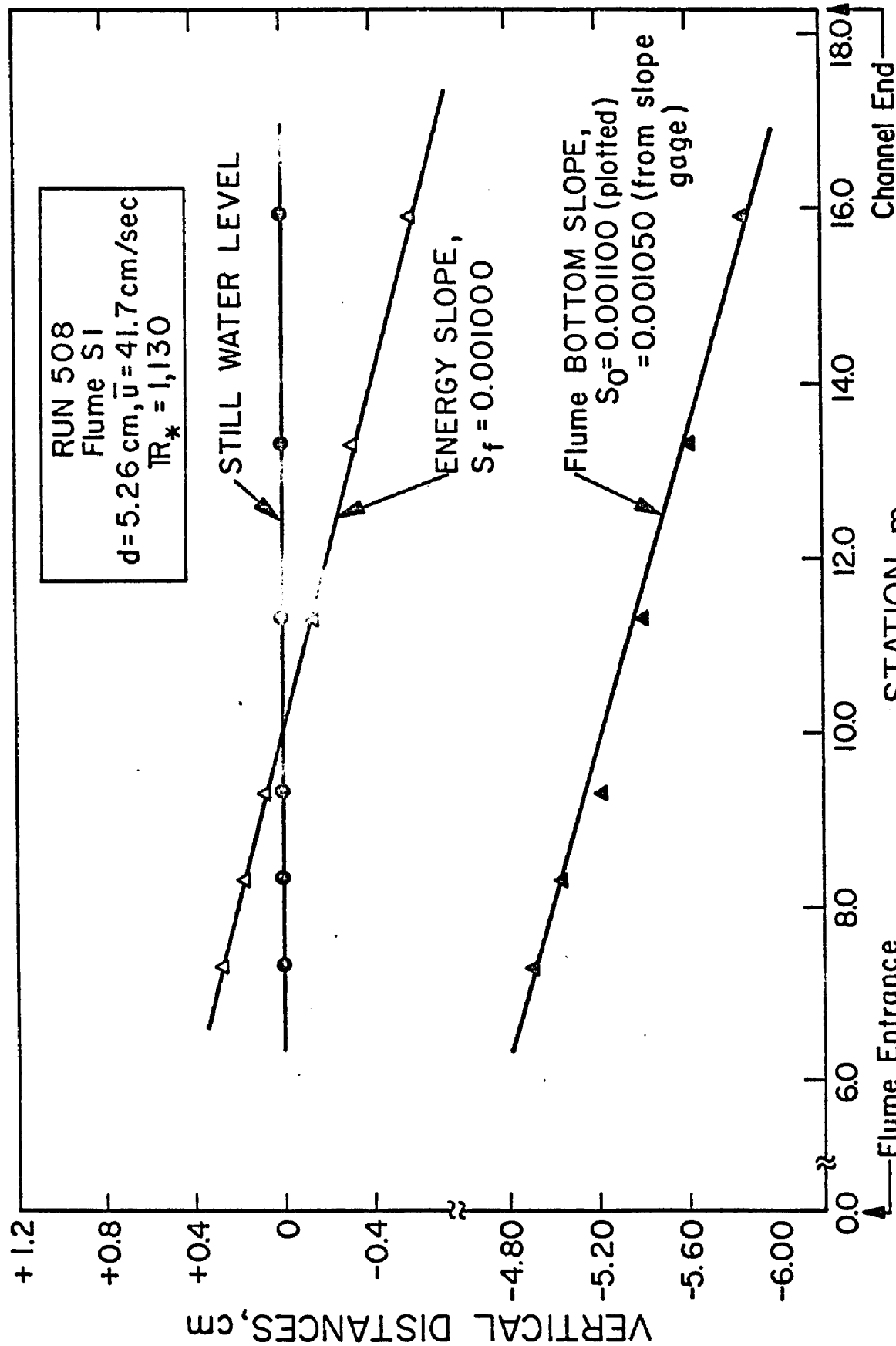

Fig. 4.13. Determination of the energy slope S_f in the 85-cm flume; RUN 508

$$f_* = 8\left(\frac{u_*}{\bar{u}}\right)^2 ; \tag{4.4}$$

the Froude number, $\mathbb{F}$ by

$$\mathbb{F} = \frac{\bar{u}}{\sqrt{gd}} ; \tag{4.5}$$

the Reynolds number, $\mathbb{R}$ by

$$\mathbb{R} = \frac{4\bar{u}r}{\nu} \tag{4.6}$$

where ν is the kinematic viscosity at the measured water temperature for the particular run; and the friction Reynolds number, $\mathbb{R}_*$ by

$$\mathbb{R}_* = \frac{u_* d}{\nu} . \tag{4.7}$$

When velocity measurements were made, the von Kármán constant, κ was determined from the slope of the velocity profile by the relation

$$\kappa = 2.30\, u_* \frac{\log_{10} \frac{y_2}{y_1}}{u_2 - u_1} \tag{4.8}$$

where u_2 and u_1 are the mean velocities at y_2 and y_1 respectively. For experiments in the flume with the rough bottom, the bed shear velocity, u_{*b} was calculated by the side-wall correction method of Vanoni and Brooks (59).

b. Tracer preparation. A tracer batch was made by dissolving approximately 613 gm salt (NaCl), 2.58 kg methanol (Tech grade),

and 20.30 gm 7-K blue dye in 11.13 kg laboratory water. The resulting solution consisted of approximately 4.34% NaCl, 18.32% methanol, and 0.14% dye by weight. The sodium chloride was used as the primary ionizing agent, the methanol was added to restore the specific gravity of the tracer solution to approximately unity, and the dye was introduced essentially for visual observation. The tracer batch was usually immersed in a reservoir of flume water for at least 24 hours so that, during an experiment, tracer and flume water temperatures were approximately equal. It was found that generally the specific gravity of the flume water was slightly greater than that of the solution with a discrepancy of about 0.02% in most cases.

Since tracer conductivity was the distinguishing property to be detected during the experiments, the conductivities of the constituents of the tracer solution were measured with one of the probes. Table 4.2 summaries the results. It is evident that the Tech grade methanol was essentially non-ionized, and that both the NaCl and the blue dye had the same order of specific conductivities (at 1% solution about twenty times the value for the flume water). Since the amount of NaCl used in the tracer solution was 31 times that of the dye, and their conductivities were in the ratio of 3.52 NaCl to 1 of dye, it meant that the conductivity, above the flume water background, measured during the experiments was due essentially to both NaCl and the dye in the ratio of 109 to 1. This ratio assumes that the turbulent mixing characteristics of NaCl and the dye were the same, and that there was a linear relationship between conductivity and concentration for each constituent.

Table 4.2

Relative Conductivities of the Constituents of the Tracer Solution

Solute	Solvent	Concentration by weight, %	Equivalent Conductivity Relative to Zero Load* Arbitrary Units
None	Distilled Water†	0	1.0
Natural Salts	City Water Supply	unknown	~236
NaCl	Distilled Water	1	8.88×10^3
7-K blue dye	Distilled Water	1	2.50×10^3
Methanol (Tech Grade)	Distilled Water	1	1.7

Notes:
*Zero Load occurred when the probe was left in air with the electrodes dry.
†The distilled water was essentially de-ionized.

Just prior to the beginning of experimental measurements, the specific gravities and temperatures of the tracer solution and the flume water were measured. If these values agreed to within acceptable limits, the tracer storage flask was set up as shown in Figure 4.12. The solution was supplied to the injector at a constant rate from the constant head reservoir.

c. Calibration of probes. The purpose of the probe calibration was (i) to determine if, within the limits of the concentration values to be measured during the experiments, there was a consistent (and perhaps linear) relationship between NaCl concentration and recorder deflection (or conductivity), (ii) to evaluate the proportionality constant for each probe, and (iii) to check for the existence of ground loops in the bridge circuits. The probes were separately immersed in standard solutions having known concentrations of NaCl. Corresponding deflections of the analog recorder were measured. Plots of recorder deflection versus NaCl concentration were developed as shown in Figure 4.14 for RUN 709. The calibration curves for the various probes were linear and converged to a single point.

The probes were also immersed separately into a glass beaker of a sample of flume water, and then together into the flume water in the flume, to check for ground loops and interactions between probes. There was no measurable difference between the recorder deflections for the flume water in the beaker and the same in the flume. This indicated complete elimination of ground loops by the isolation transformer.

Calibration curves developed for various experiments were virtually identical for the same probes and preamplifiers. During any given experiment, the variation of flume water temperature was less than 1° C; thus a set of calibration plots recorded at the beginning of a run was used for measurements during the entire run.

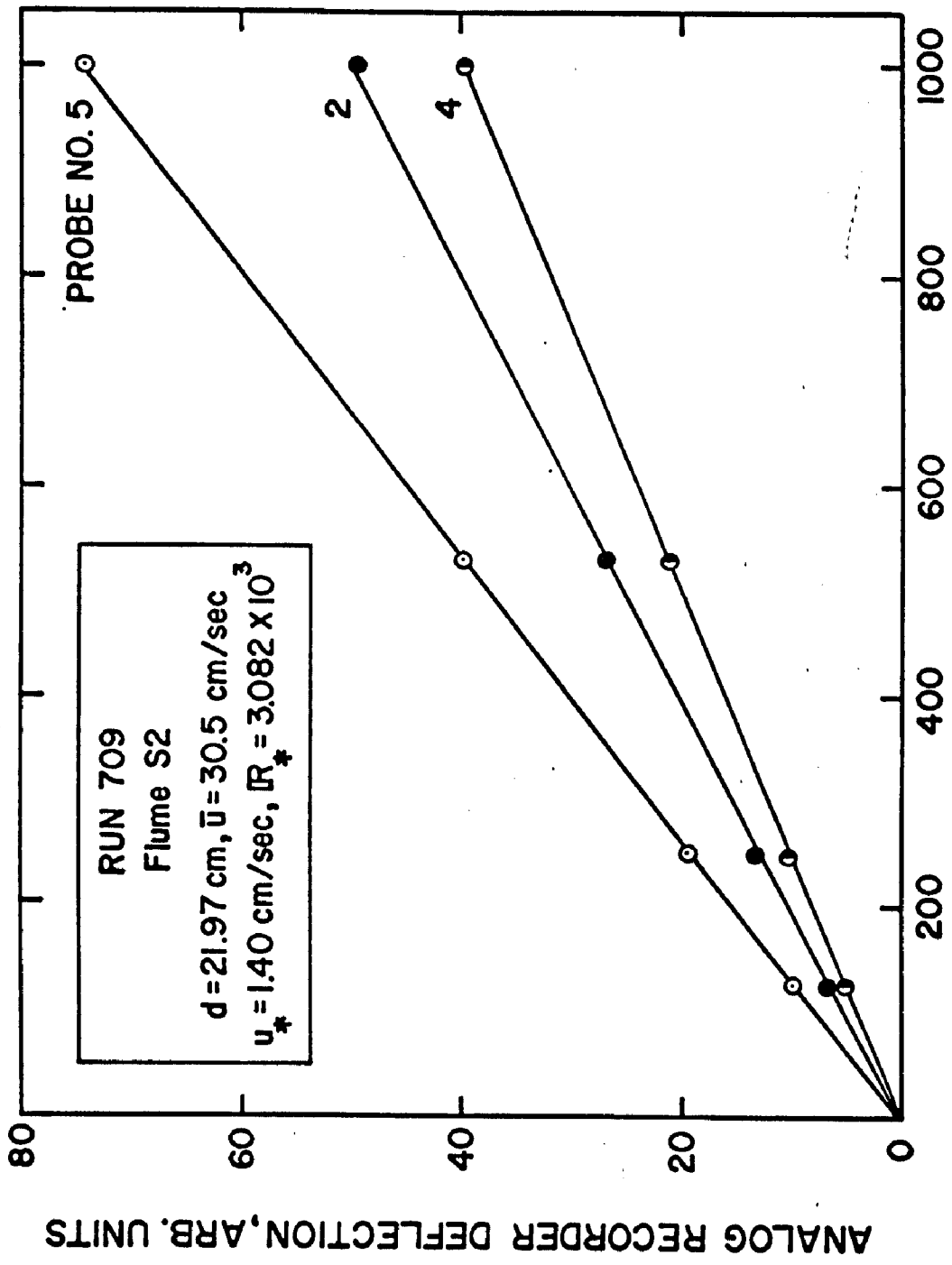

Fig. 4.14. Calibration curves for the conductivity probes

d. A typical run. A typical run in which data were recorded on the strip chart and also digitized by the A/D converter, will be outlined. First the stations and the flow levels at which measurements would be made were determined. In most experiments six stations and four levels located at $y/d = 0.850$, 0.632, 0.368, and 0.095 were used.

The tracer injector was placed usually at $y/d = 1/e$ (= 0.368) and about 15 meters from the flume entrance for the 110-cm flume. In the 85-cm flume, the injector was stationed approximately 9 m from the channel entrance. The tracer injection velocity was set at the mean flow velocity, $\bar{u}$.

The probes were calibrated and placed in the flume. Usually three probes were used. If the flume water conductivity was excessive, the output voltage of the recorder was reduced to a convenient level with a zero suppression control. A sine wave was always generated by a function generator, observed on an oscilloscope during the entire run, and fed to the first channel of the A/D converter. This offered a check on the integrity of the data recorded on the other channels.

The probes were placed at the first level of measurement (usually the level of tracer injection) at the station nearest the tracer source. They were then set at the desired values of z (transverse position) and the background concentration recorded for about 10 seconds. Then the tracer was injected continuously at the constant velocity, $\bar{u}$, and tracer concentration recorded for about 30 seconds after allowing an initial period of process establishment. Tracer supply was then shut off, and the probes moved to the next set of z

values. The procedure was then repeated. Adjacent probes were overlapped at one point as a check on the conversion constants used for inter-relating various probe measurements.

After the measurements were completed at the first station, the probes were moved downstream to the next station until all stations were covered. The probes were then set at another level, and measurements made; this time moving upstream from one station to the next. The process was then repeated moving downstream for the third level and upstream for the fourth.

If the data were not digitized, an averaging switch was used to automatically average the signal recorded on the strip chart over a one-second period. This essentially smoothed the record, and facilitated the measurement of the time-mean concentration which was obtained by simply laying a straight edge on the record, and averaging by eye.

When data were digitized, all calculations were made from the magnetic tape, and the analog record, which was not averaged, provided only a check on the digitized information. At the end of the experiment, all the header data for the entire experiment, including the number of records in every file, were first retrieved. The result was compared to a log which was drawn up during the experiment. Then the mean value of the background concentration for each measurement was calculated. With these values and the conversion factors for the probes now available, the entire experimental measurements were analyzed.

For any fixed point, the instantaneous tracer concentration,

c(i) due to the point source of tracer was computed by the relation

$$c(i) = \frac{Ka_t}{20}(c_d(i) - C_b) \qquad (4.9)$$

where K, the conversion factor, is the ratio of slope of the calibration line for probe number 5 to that for the particular probe detecting the concentration, a_t is the attenuation value for the analog channel connected to the particular probe, C_b is the average background concentration, and $c_d(i)$ is the i^{th} concentration value recorded on tape for the particular channel within the sampling period. With Eq. 4.9, therefore, concentration values for all probes were calculated relative to probe 5 set at attenuation 20, thus giving a truncation level of approximately 0.3 ppm equivalent conductivity of NaCl (i.e. 7×10^{-4}% of initial NaCl concentration).

4.B.3. Photo Studies. The photo studies were conducted in the 85-cm flume for only one uniform flow depth, d = 17.0 cm. To photograph the fluctuating plume, the motion picture camera was mounted on the instrument carriage with the camera lens 2.13 m above the water surface on the flume center line. The camera made 24 exposures per second.

The plume was photographed at eight stations located 0.55, 0.70, 0.85, 0.95, 1.10, 1.28, 1.46, and 1.62 m downstream of the source. At each station, 33 seconds of data were collected.

For each frame, the z values of the plume boundaries were measured, and the difference between them used as the plume width at that instant of exposure. Readings were made at an interval of 4 frames (i.e. 1/6-sec). This was considered adequate because

the expected characteristic frequency of the plume meander was of the order of one Hz.

4.B.4. Velocity Measurements and Results. Water flow velocities were measured primarily to (i) obtain velocity profiles, (ii) compute the von Kármán constant, κ, and (iii) develop velocity contours as a check on the two-dimensionality of the flow. As a secondary objective, velocity measurements were made to compute flow discharge by integration of the velocity distribution in the cross section.

The velocity profiles were logarithmic, and of the form expressed by Eq. 2.33. Examples of profiles measured during RUN 706V for which d = 2.75 cm are shown in Figure 4.15. The transverse positions z where the measurements were made and the values of the von Kármán constant κ are also included for the two stations x = 400 cm and x = 1900 cm. It is evident from Figure 4.15 and the summary of hydraulic data of Table 5.1 that $0.30 \leq \kappa \leq 0.43$.

Velocity contours were plotted during RUN 506V in flume S1 for d = 2.95 cm, and during RUNS 706V and 708V in flume S2 for the hydraulically smooth bottom with d = 2.75 cm and 17.31 cm respectively. With flume 2 roughened on the bottom with rocks, velocity contours were mapped during RUN 404V where d = 10.36 cm. Contours obtained for RUNS 404V and 708V are shown in Figure 4.16 with one station of each run selected as an example.

Both Figures 4.15 and 4.16 indicate that within the central region of the flume where concentration measurements were confined,

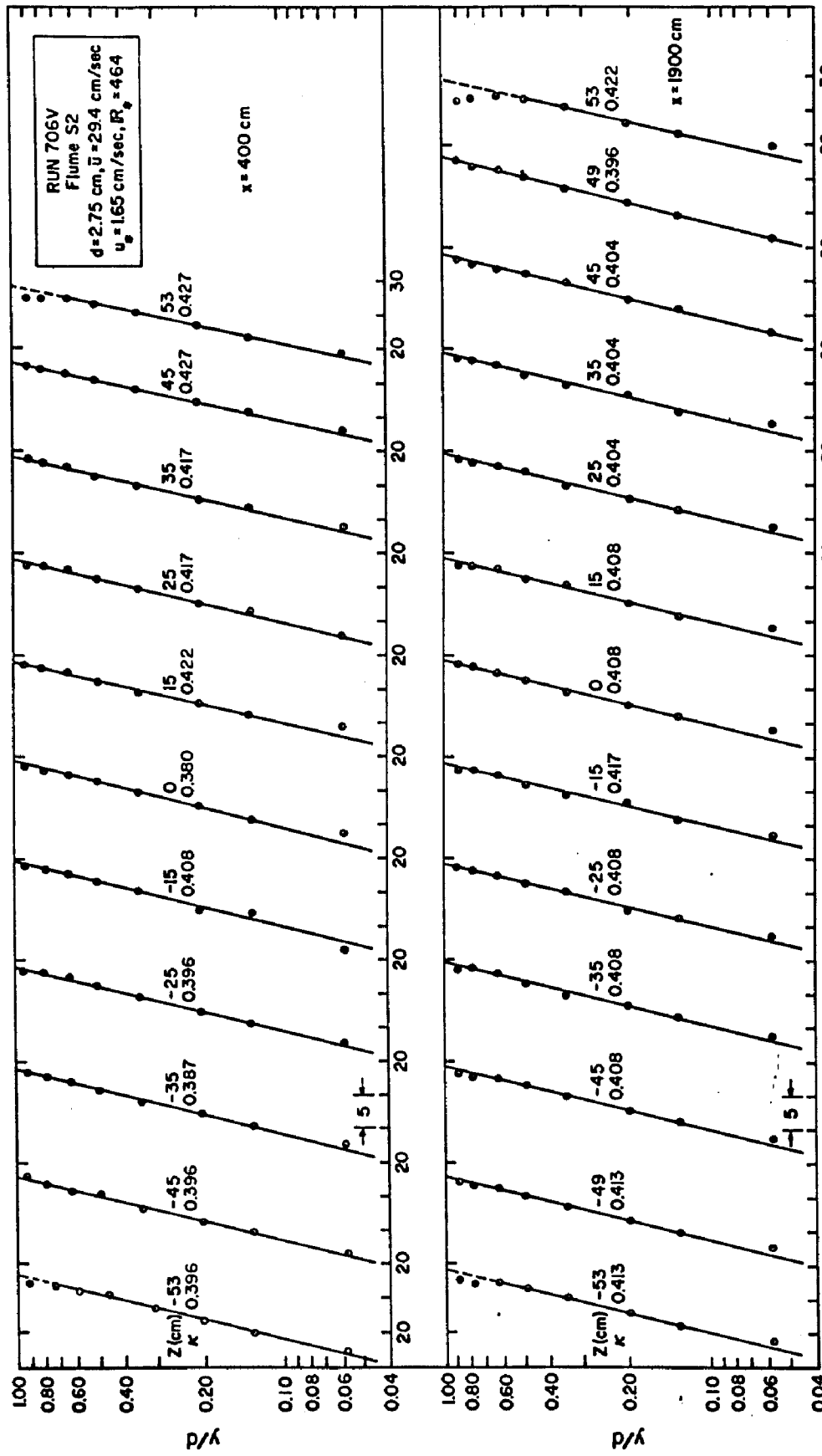

Fig. 4.15. Velocity profiles at two stations and several sections in flume S2; Run 706V

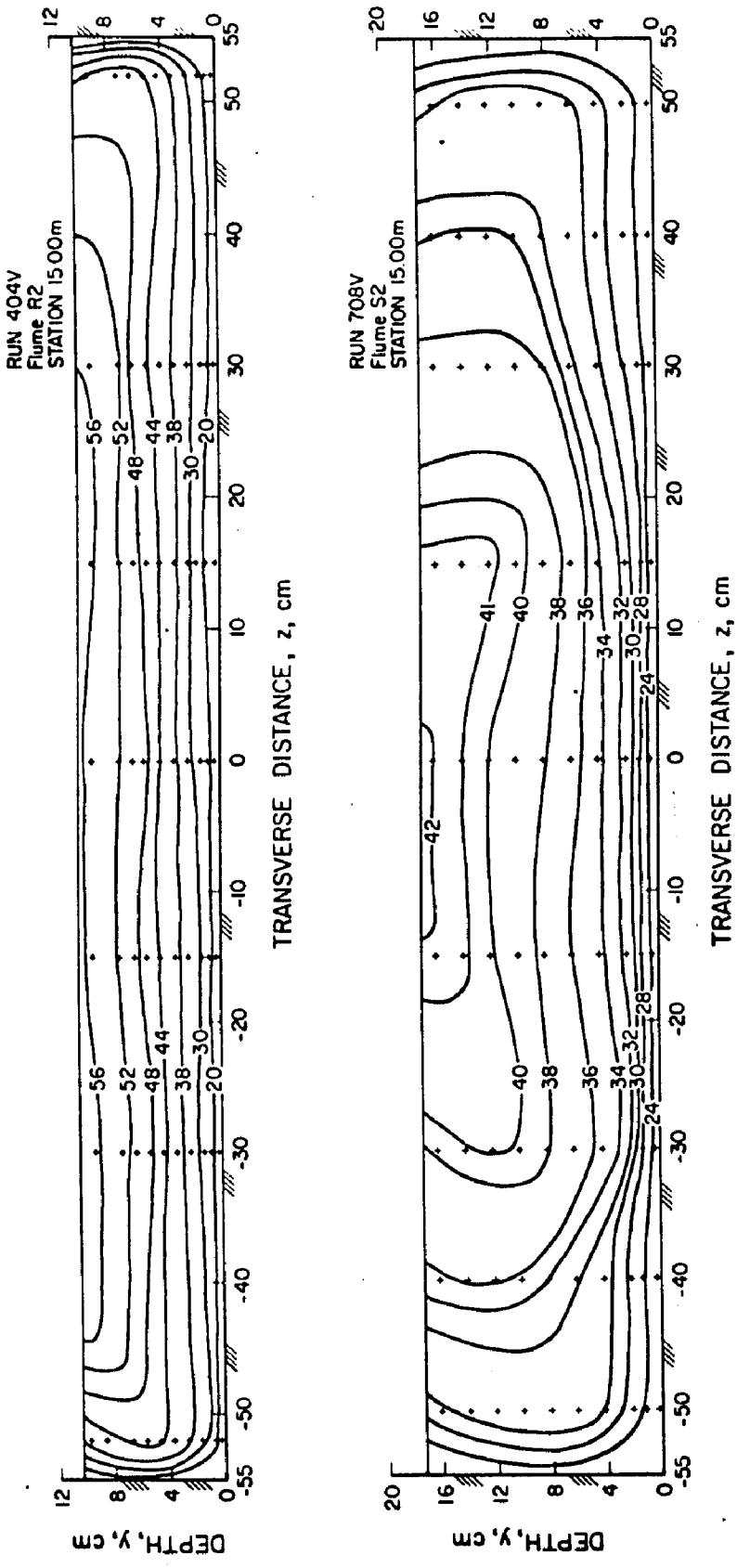

Fig. 4.16. Velocity contours at a station 15 m from the flume entrance for RUNS 404V and 708V. Cross-marks indicate points where velocities were measured. Velocities on isovels in cm/sec.

the flow was essentially uniform across the flume except perhaps for RUN 708V where the aspect ratio, d/W was largest. In particular, it was found that within the central 80% of the flume, the maximum deviation of u_a, the depth integrated velocity at a given z, from its cross-wise mean value was 3.1, 0.7, 6.4, and 3.5% for RUNS 506V, 706V, 708V, and 404V respectively.

It was found that the discharge calculated by integration of velocities over fixed cross sections was always less than the metered discharge by less than 3%. This discrepancy was accrued in the integration of the velocity distribution near the flume walls. The metered discharge was therefore considered a better measure of the mean flow and was used for calculation of the mean velocity $\bar{u}$ as expressed in Eq. 4.2.

4.B.5. Probe Response to High Frequency Loading. To measure concentration fluctuations, it was necessary to determine probe response to a rapidly changing load. Manufacturer specifications for the response of the recorder system could not be used because the response of the conductivity probe depends on the transducer used and the cell volume surrounding the electrodes (see, for example, Gibson and Schwarz (50), or Lamb, Manning, and Wilhelm (60)). For a given transducer, the larger the electrodes, the slower is the response.

In this study, the probe response was determined by subjecting the probes to a nearly instantaneous load, and recording the resulting transient response of each probe on the magnetic tape. The probes

were placed in a tank of salt water such that initially the lower tips of the electrodes were about 1 mm above the water surface with the probe axes inclined at about 73° to the horizontal. Using a laboratory "tsunami generator," the water level was raised rapidly so that the electrodes were completely immersed in 6.4 milliseconds. Once immersed, the electrodes were left in the water at least until the final deflection of the recorder was attained. Simultaneously the output of each probe was digitized at 800 samples/sec, and recorded on the magnetic tape.

The transient response curves of the probes, as recorded on tape, are plotted in Figure 4.17(a). The input (or excitation) which was approximately linear is also shown. The relative amplitude of the ordinate is the ratio of the concentration at any time to the final concentration value after an infinitely long time. Also included in Figure 4.17(a) is the rise time, r_t, due to the excitation load. The rise time was defined as the time to attain final deflection, as measured by the best straight-line approximation to the initial rise of the transient curve. Values of r_t were 14.9, 13.2, and 11.0 millisecs for probes 5, 4, and 6 respectively.

The frequency response of the system is the relation between the relative amplitude of the output and the frequency of a cyclic loading imposed on the probe. Since this relationship could not be physically determined directly, it was calculated from the known input signal and the corresponding transient response curves shown in Figure 4.17(a). A method proposed by Walters and Rea (61) was used.

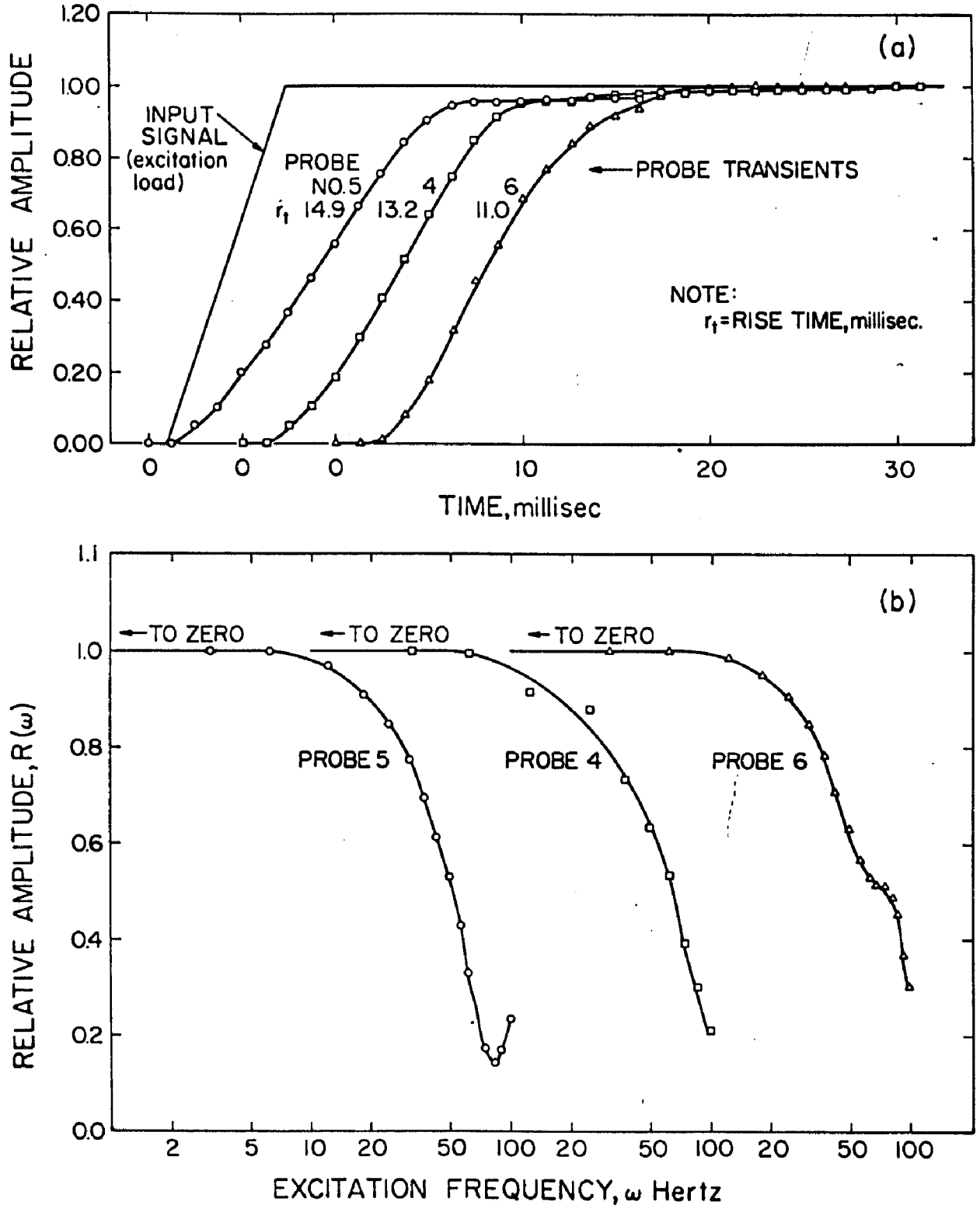

Fig. 4.17. Response of the conductivity probes to high frequency loading showing (a) the transient response curves, and (b) the corresponding frequency response

The input and transient response functions were represented as Fourier series. A common fundamental period, T_p was chosen for both functions such that the transient had damped to its final amplitude at a time less than $T_p/2$. The Fourier coefficients, I(n), of the input series and J(n) of the output series were then calculated, and the transfer function $R(n)e^{i\phi(n)}$ determined by the relation

$$R(n)e^{i\phi(n)} = \frac{J(n)}{I(n)} , \qquad (4.10)$$

where R(n) is the amplitude ratio and $\phi(n)$, the phase shift of the transfer function for the n^{th} multiple of the fundamental frequency, ω_f, and i is $\sqrt{-1}$. The multiple n takes values 0, ±1, ±2, ... Thus $R(\omega)$ and $\phi(\omega)$ can be evaluated as functions of the real and imaginary parts of J(n) and I(n) with $\omega = n\omega_f$.

Figure 4.17(b) shows the frequency response curves calculated for the input signal and corresponding transients of Figure 4.17(a). For the three probes, the response was flat at $R(\omega) = 1.0$ for the excitation frequency $\omega \leq 6.3$ Hz. Beyond this point, the curves decreases monotonically such that the relative amplitude, $R(\omega)$ was down about 3 decibels at approximately $\omega = 30$ Hz. Near $\omega = 100$ Hz, the curves became oscillatory.

The limitations of the probes in measuring high frequency signals become apparent. The probes would respond to fluctuations up to a maximum frequency of 6.3 Hz without modulation of the amplitude of the input signal. For higher frequencies, the probe output would indicate a reading reduced according to the curves of Figure

4.17(b). Since the expected characteristic frequency of the concentration variations with time was in the order of 1 Hz (from preliminary observations on the analog recorder), the probe response was considered adequate for the intermittency and statistical analyses of the concentration fluctuations. Data were digitized at 60 samples/sec so that the cut-off frequency was 30 Hz. This provided a suitable sampling rate as will be shown in the next section.

4.C. REDUCTION OF DATA

4.C.1. Recorded Concentration Data. Figure 4.18(a) shows examples of concentration measurements recorded on the strip chart of the analog recorder. Corresponding records digitized at 60 samples/sec by the A/D converter are also plotted in Figure 4.18(b) for comparison. The mean background concentration was used as zero reference. The high frequency (30 Hz) fluctuation shown in the plot of the digitized record is a 0.01-volt background noise. This noise is not apparent in the analog record because it was filtered off by the inertia of the recorder stylus.

Comparison of the analog and digitized records reveals that all peak values indicated on the analog recorder were also recorded on tape. This was expected because the response of the stylus of the analog recorder was slower than the response at the output jack leading to the A/D converter. Thus, in general, the A/D converter, operating at 60 samples/sec, furnished an excellent record of the variation of the tracer concentration.

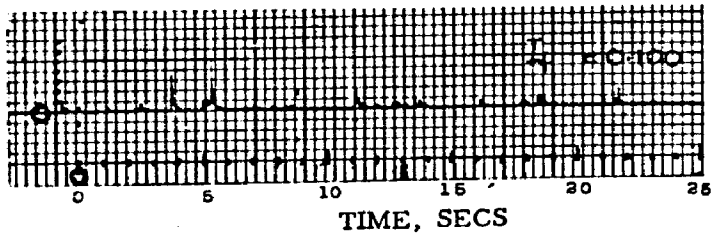

a (i) Analog record for z = 5 cm

RUN 806

d = 2.77 cm

$R_* = 470$

$\frac{x}{d} = 28.9$

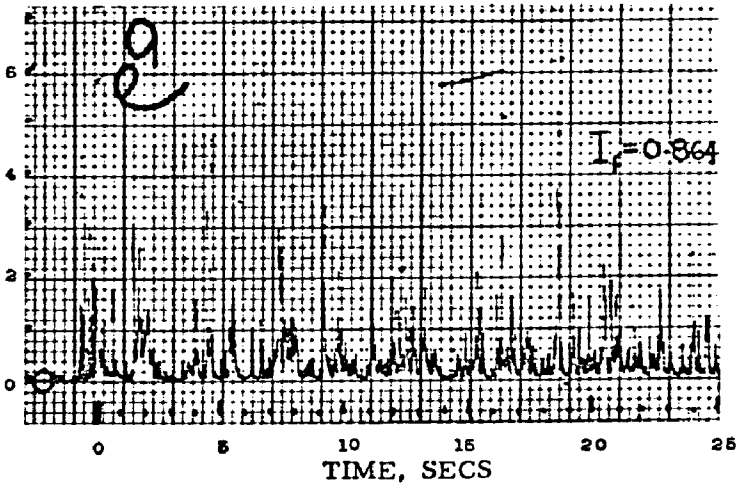

a (ii) Analog record for z = -5 cm

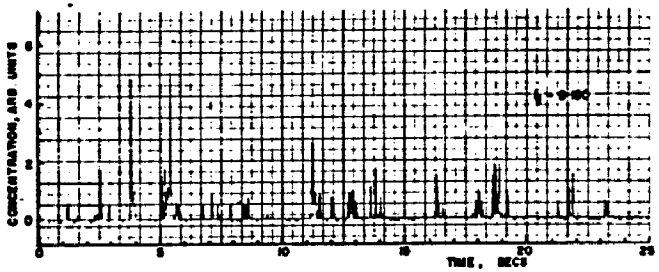

b (i) Corresponding digitized record for z = 5 cm

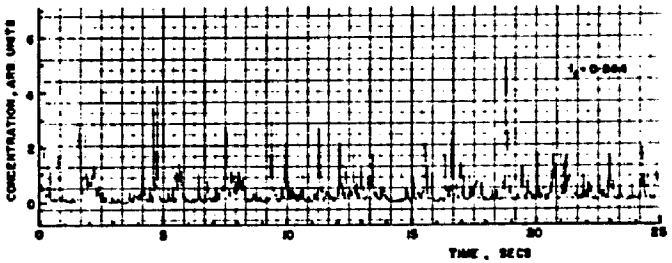

b (ii) Corresponding digitized record for z = -5 cm

Fig. 4.18. Typical concentration data at two points as recorded by the analog recorder shown in a(i) and a(ii). The same data digitized by the A/D converter at 60 samples/sec are correspondingly plotted in b(i) and b(ii); RUN 806

4.C.2. Effects of Sampling Period and Sampling Rate on Calculated Parameters.

a. Effects on the time-mean concentration. The sampling period T_m is the total length of time over which concentration used for subsequent analyses was measured at a fixed point. The time-mean concentration C is the average over the sampling period T_m. The value of C is thus a function of the length of T_m, and theoretically would approch a limiting value as T_m becomes infinite. In practice, however, the samples must be truncated at a finite T_m such that for periods longer than T_m, C is essentially invariant. Ogura (62) showed that the deviation of C from the asymptotic value increases with the size of the largest eddy effecting mixing. Thus the greater the flow depth the longer is the sampling period required to obtain a representative value of C.

Measurements were made to determine an appropriate value of T_m. RUN 804 for which d (= 10.84 cm) was larger than most of the other experiments was chosen. Concentration data digitized at 60 samples/sec were recorded for one minute, and C evaluated numerically with T_m increasing from 4 to 56 seconds. The result is shown in Figure 4.19. The relationships were developed for x/d = 7.4, 16.6, 35.0, 71.9, and 108.8 at values of z where the intermittency factor $I_f \approx 0.50$ for each case. All points were located at $\eta = 0.368$, the level of tracer injection. The intermittency factor was calculated with the threshold concentration equal to the mean background concentration. From Figure 4.19, it was concluded that for experiments where $d \leq 10.84$ cm, T_m = approximately 25 seconds

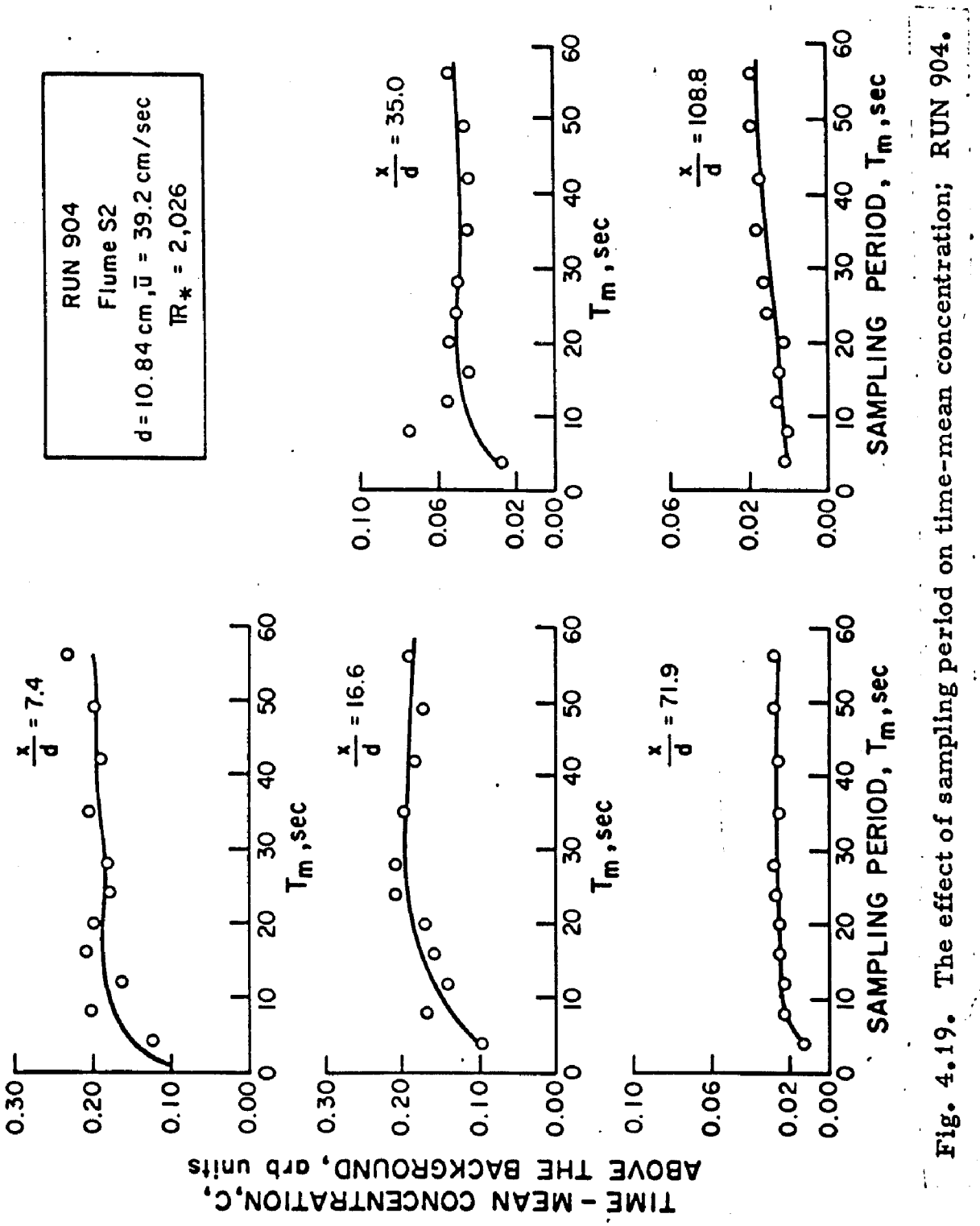

Fig. 4.19. The effect of sampling period on time-mean concentration; RUN 904.

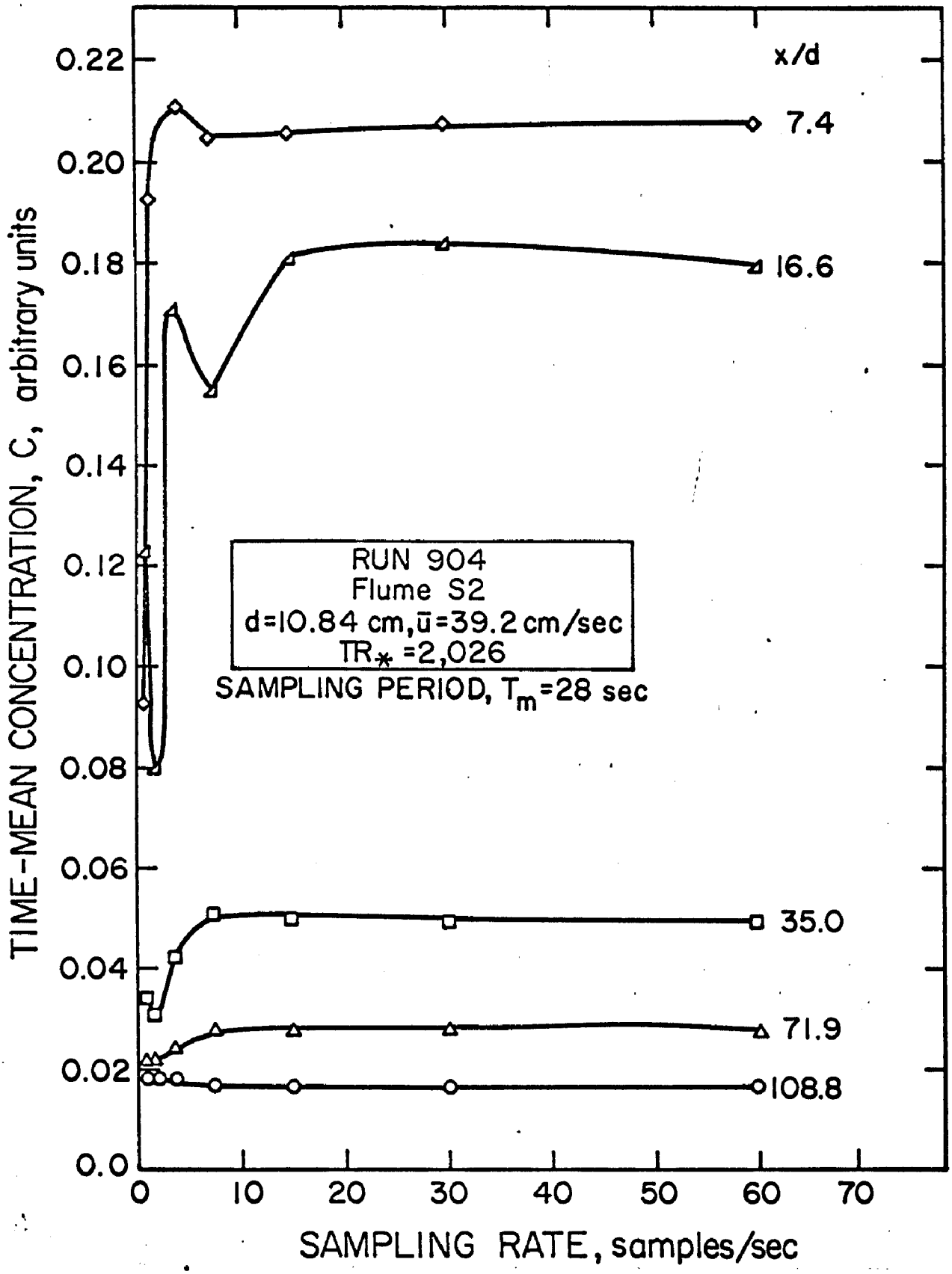

Fig. 4.20. The effect of sampling rate on time-mean concentration; RUN 904

was adequate for determining C.

Figure 4.20 illustrates the effect of sampling rate S_r on computed C for the same values of x/d and z as in Figure 4.19. and T_m = 28 secs. The plots show that for this sampling period, a consistent value of C was obtained for S_r greater than 15 samples/sec for all points investigated.

b. Effects on the intermittency factor, I_f. Figure 4.21 illustrates the effect of sampling period, T_m on the intermittency factor I_f at various x/d. The points chosen for analysis are exactly the same as in Figure 4.19. The figure shows that a fairly stable value of I_f was achieved for $T_m \geq 22$ secs. As expected, the deviation from the mean value of I_f at large T_m was greatest at higher values of x/d where the signal-to-noise ratio was lowest. Indeed for x/d = 108.8, a constant value of I_f was not actually attained within T_m = 56 secs. This meant that a large scatter in the plots of $I_f(z)$ versus z would be realized at large x/d unless longer records were utilized.

The effect of sampling rate on I_f is shown in Figure 4.22. The points analyzed are the same as those in Figure 4.19. The graphs show that for T_m = 28 secs, an essentially constant I_f was achieved beyond $S_r \approx 18$ samples/sec at all stations.

c. Choice of the sampling period and the sampling rate. The effects of T_m and S_r on other statistical parameters were determined for RUN 804. On the basis of the analyses, a sampling period of at least 28 secs for $d \geq 10.84$ cm was used. For lower values of d,

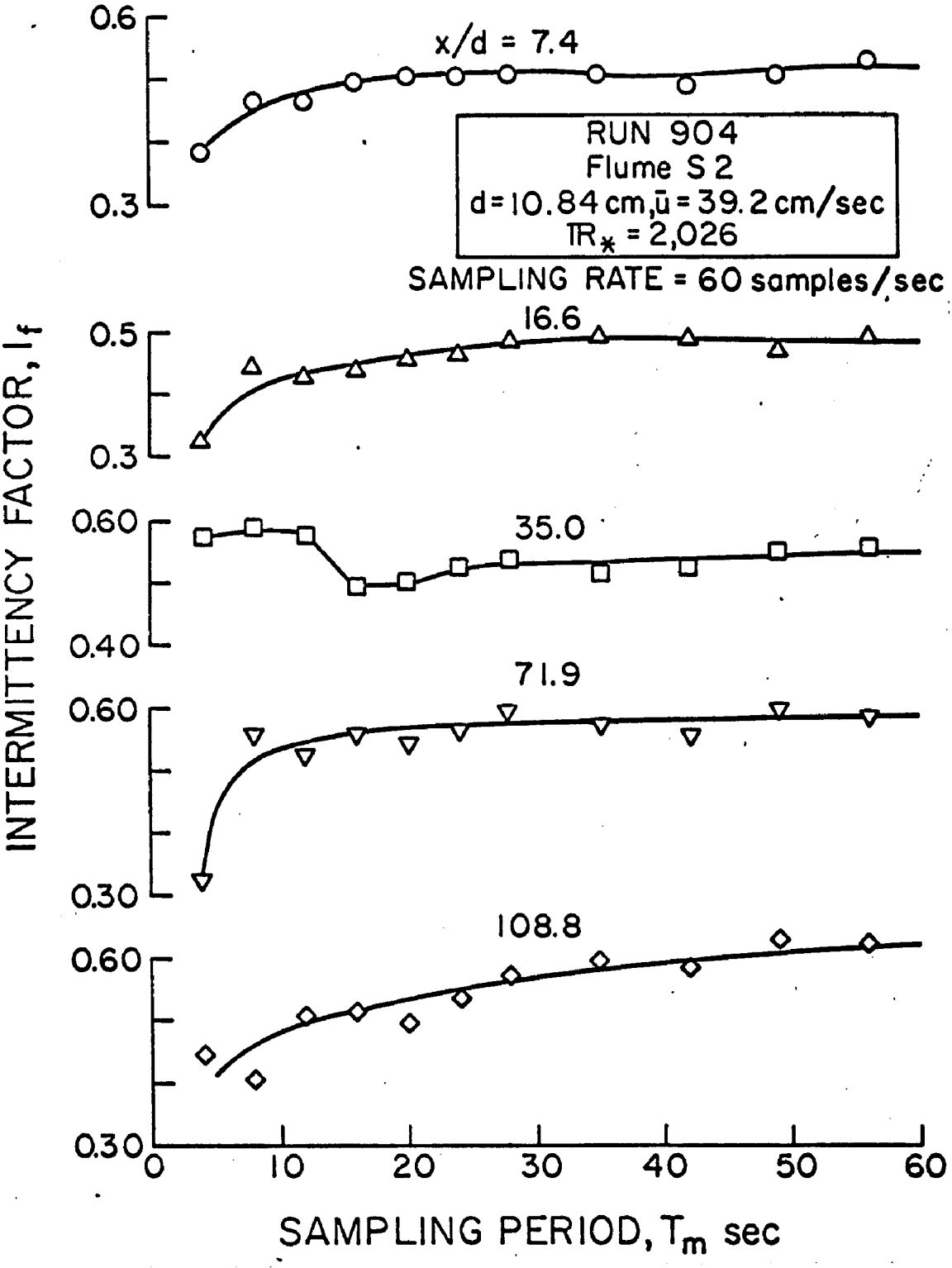

Fig. 4.21. The effect of sampling period on the intermittency factor; RUN 904

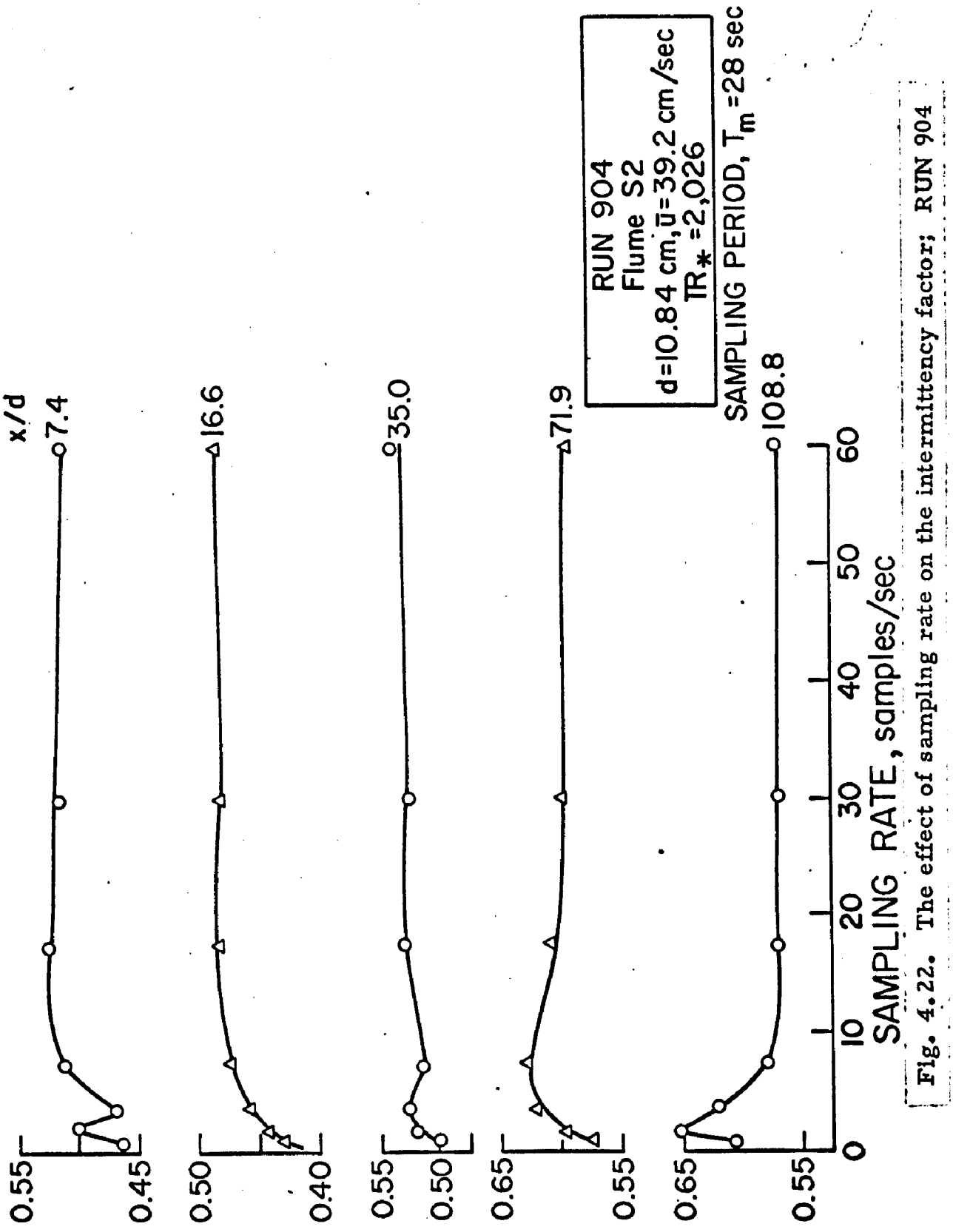

Fig. 4.22. The effect of sampling rate on the intermittency factor; RUN 904

T_m was set at 25 secs. In all experiments, S_r was 60 samples/sec. At this rate, all fluctuations with frequencies equal to or less than 30 Hz would be recorded on tape. The maximum eddy size whose effects were measured would have a frequency of $1/T_m$ ($\approx$ 1/25 Hz).

4.C.3. Choice of the Threshold Concentration C_t for Determination of the Intermittency Factor, I_f. It is immediately apparent from Figure 3.3 that the value of I_f at any fixed point depends greatly on the threshold level C_t used. This is especially true in regions far from the source where the signal-to-noise ratio is smallest. To illustrate the influence of C_t on I_f at a fixed point, a 56-second record in RUN 804 was analyzed for x/d = 7.4, 16.6, 35.0, 71.9, and 108.8, all at the level η = 0.368. For each station z was chosen such that the asymptotic value of I_f relative to the background concentration was approximately 0.5. At each point I_f was calculated for various ratios of the threshold concentration to the local time-mean concentration C_t/C. The result is shown in Figure 4.23. For clarity, only three stations are plotted. It is observed that I_f rose suddenly to 1.0 for $C_t/C < 0.0$, and decayed gradually as C_t/C increased beyond zero. At $C_t/C = 0$, the concentration equalled the mean background concentration.

The resulting modification of the transverse distribution of I_f by the choice of C_t/C is shown in Figure 4.24 for RUN 804 with x/d = 7.4. The plots again indicate that substantial changes could be introduced without a proper choice of C_t.

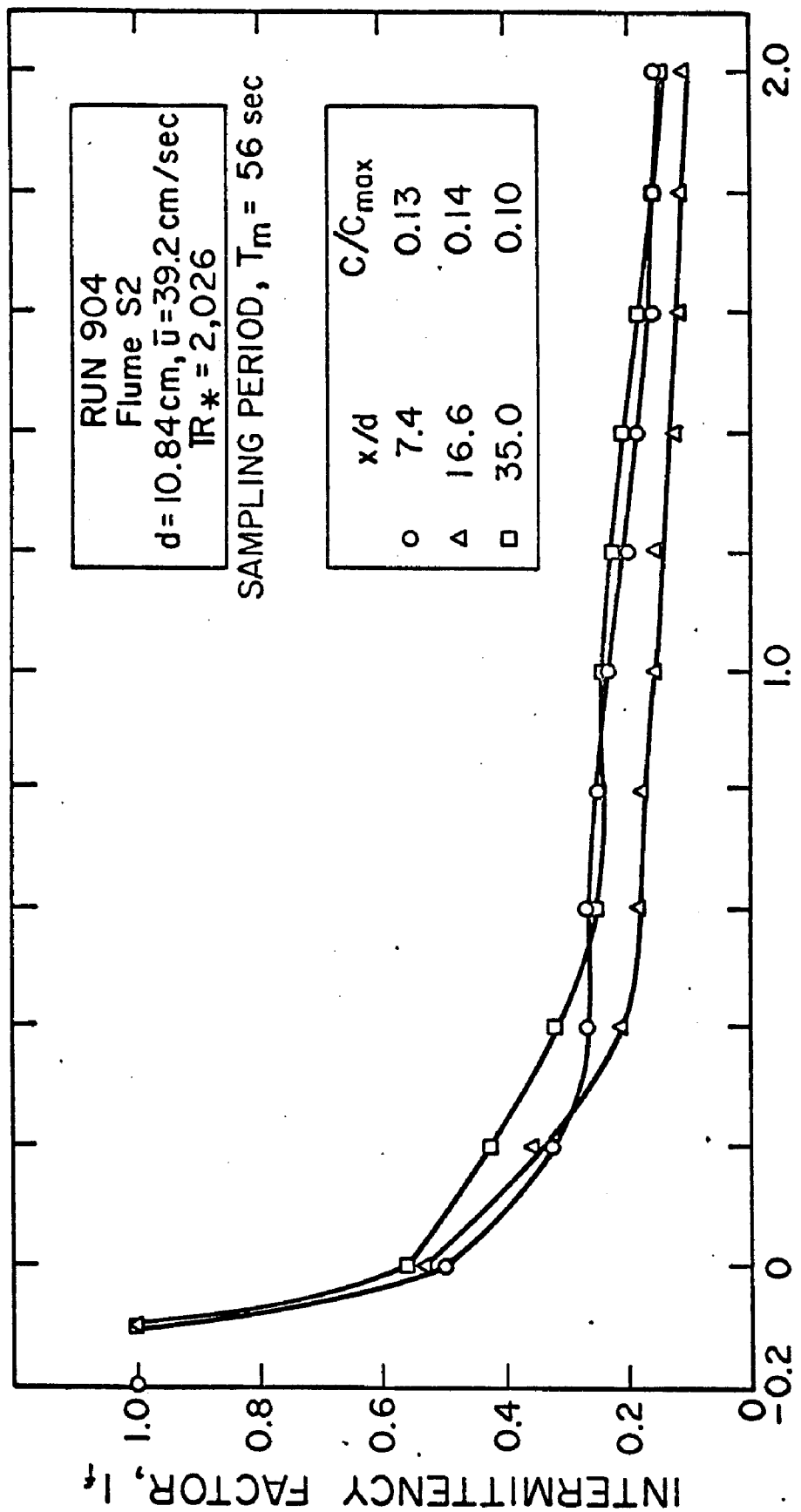

Fig. 4.23. The effect of the choice of threshold concentration C_t on the intermittency factor. Each curve applies to a fixed point, and C_t is normalized by the local mean concentration; RUN 904

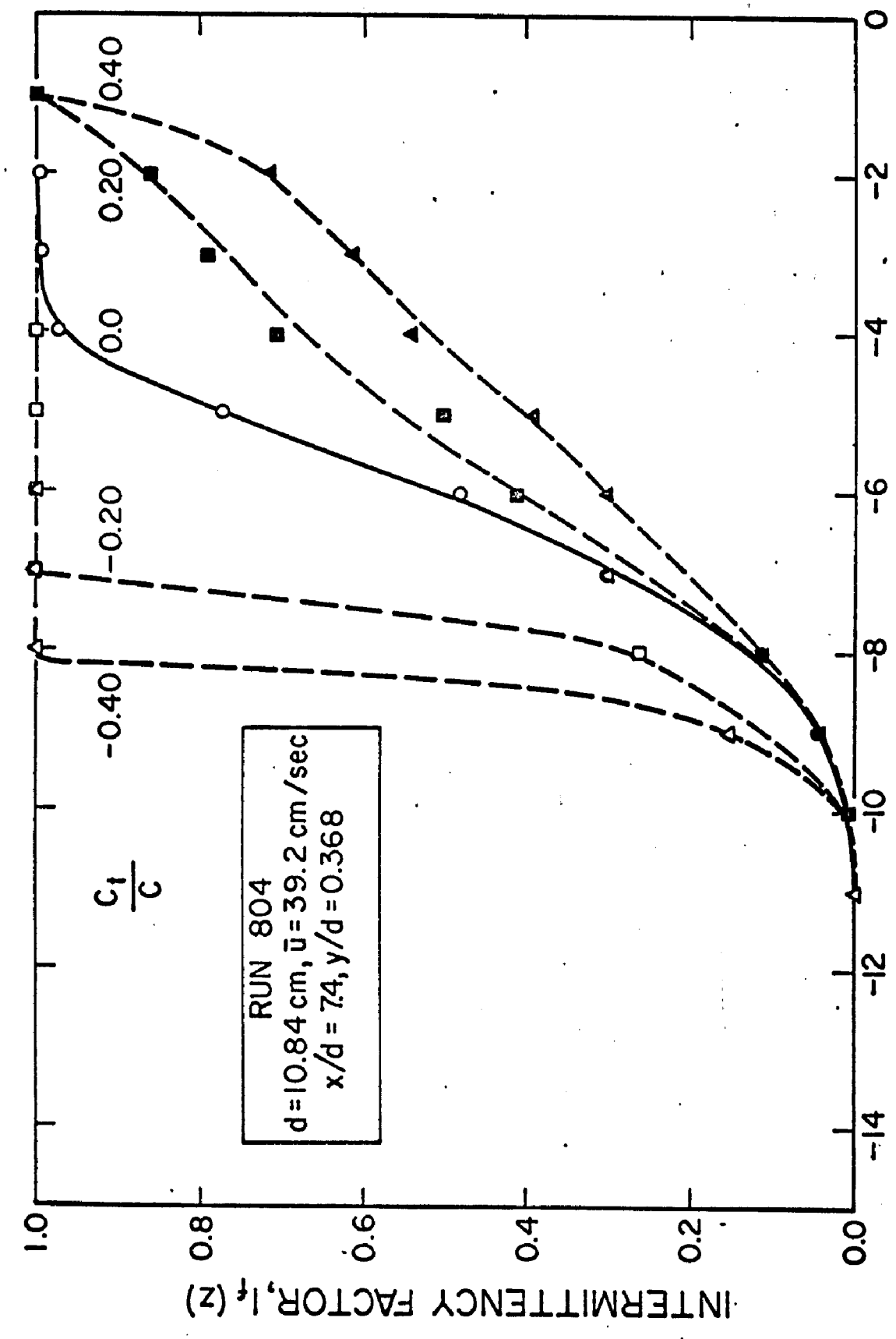

Fig. 4.24. Modification of the transverse distribution of the intermittency factor by the choice of the threshold concentration; RUN 804

In the computer program used for calculating I_f, C_t was chosen to be slightly above the mean background to effectively eliminate the background noise. Thus in all calculations of I_f, the threshhold concentration was set essentially equal to the background concentration.

CHAPTER 5

PRESENTATION AND DISCUSSION OF EXPERIMENTAL RESULTS (Phase I)

This chapter summarizes the hydraulic data for all experiments and presents the results of measurements relating to time-averaged concentration. Each result (or set of results) is discussed according to the objectives outlined in Chapter 2.

5.A. HYDRAULIC DATA

Table 5.1 is a complete summary of the hydraulic data for all experiments related to both Phases I and II. The experiments are grouped in an increasing order of flow depths which ranged from 1.52 to 21.97 cm.

Column 1 lists the experimental runs, and Column 2 the phase of the study undertaken: Phase I refers to time-averaged concentration measurements, and Phase II to concentration fluctuation analyses. Column 3 identifies the flumes as explained in Table 4.1. Columns 4 through 7 are explained as indicated. The shear velocities shown in Column 8 were calculated according to Eq. 4.3. However, the bed shear velocity was used for experiments conducted in the flume roughened with rocks. Friction factors entered in Column 9 were determined using values of the shear velocity given in Column 8.

The von Kármán constant κ, tabulated in Column 10, was calculated for only one run in each set of hydraulically similar experi-

Table 5.1. Summary of hydraulic data

RUN	Phase of Study [1]	Flume Identif. Code [2]	Normal Depth d cm	Hydraulic Radius r cm	Mean Velocity $\bar{u}$ cm/sec	Energy Slope, S_f ($\times 10^3$)	Shear Velocity, [3] $u_* = \sqrt{g r S_f}$ cm/sec	Friction Factor [4] $f_* = 8\left(\frac{u_*}{\bar{u}}\right)^2$ ($\times 10^2$)	von Kármán Constant, κ	Froude Number $F = \frac{\bar{u}}{\sqrt{gd}}$	Kinematic Viscosity, ν cm^2/sec ($\times 10^2$)	Reynolds Number $R = \frac{4\bar{u}r}{\nu}$ ($\times 10^{-4}$)	Friction Reynolds Number, [4] $R_* = \frac{u_* d}{\nu}$ ($\times 10^{-3}$)	Level of Tracer Injection η_h	RUN
1	2	3	4	5	6	7	8	9	10	11	12	13	14	15	1
507	I	S1	1.52	1.47	31.2	3.110	2.12	3.69	0.364	0.808	0.992	1.85	0.325	0.368	507
705	I	S2	1.69	1.64	32.8	2.467	1.99	2.95	-	0.805	0.960	2.24	0.351	0.368	705
805	II	S2	1.69	1.64	33.5	2.464	1.99	2.83	-	0.828	0.980	2.24	0.343	0.500	805
707	I	S2	2.74	2.61	50.4	2.735	2.65	2.21	0.347	0.972	0.979	5.37	0.741	0.368	707
706	I	S2	2.75	2.62	30.0	1.063	1.65	2.43	0.408	0.578	0.980	3.21	0.464	0.368	706
807	I, II	S2	2.76	2.63	49.5	2.735	2.66	2.30	-	0.951	0.978	5.32	0.750	0.368	807
806	I, II	S2	2.77	2.64	29.7	1.064	1.66	2.50	-	0.570	0.978	3.20	0.470	0.368	806
506	I	S1	2.95	2.76	27.1	0.910	1.57	2.68	0.374	0.504	0.992	3.01	0.464	0.368	506
703	I	S2	3.46	3.26	32.0	0.973	1.76	2.43	-	0.549	0.961	4.34	0.635	0.368	703
504	I	S1	3.47	3.21	29.9	0.631	1.41	1.78	0.341	0.512	0.980	3.92	0.499	0.368	504
505	I	S1	3.57	3.29	37.2	1.040	1.83	1.94	0.363	0.629	0.975	5.03	0.671	0.368	505
503	I	S1	3.93	3.60	33.1	0.779	1.66	2.01	0.381	0.533	0.980	4.86	0.665	0.368	503
501	I	S1	4.25	3.86	32.9	0.811	1.75	2.27	0.375	0.510	0.975	5.21	0.764	0.322	501
509	I	S1	5.25	4.67	42.6	1.110	2.26	2.24	-	0.594	0.992	8.03	1.193	0.368	509
511	I	S1	5.25	4.67	42.8	0.943	2.08	1.89	-	0.596	0.953	8.39	1.145	0.051	511
512	I	S1	5.25	4.67	42.5	1.030	2.17	2.09	-	0.592	0.960	8.27	1.188	0.850	512
508	I	S1	5.26	4.68	41.7	0.990	2.13	2.09	0.375	0.581	0.992	7.87	1.130	0.368	508
510	I	S1	5.26	4.68	42.4	0.978	2.12	2.00	-	0.590	1.005	7.90	1.109	0.632	510
600	II	S1	5.26	4.68	42.3	1.005	2.15	2.06	-	0.589	0.991	7.99	1.140	0.368	600
601	II	S1	5.26	4.68	42.3	0.990	2.13	2.03	-	0.589	1.011	7.83	1.109	0.368	601
802	I, II	S2	5.36	4.88	43.7	0.981	2.17	1.97	-	0.602	0.990	8.62	1.173	0.368	802
702	I	S2	5.41	4.93	43.5	0.981	2.18	2.01	0.373	0.598	0.982	8.74	1.200	0.129	702
701	I	S2	5.53	5.02	42.0	0.981	2.20	2.19	0.372	0.570	0.969	8.71	1.254	0.391	701
405	I, II	R2	6.81	6.06	35.9	3.837	5.01	15.61	-	0.439	1.007	8.64	3.388	0.368	405

(Continued)

Table 5.1 (Continued)

RUN	Phase of Study [1]	Flume Identif. Code [2]	Normal Depth d cm	Hydraulic Radius r cm	Mean Velocity $\bar{u}$ cm/sec	Energy Slope, S_f $(\times 10^3)$	Shear Velocity, [3] $u_*=\sqrt{gr\,S_f}$ cm/sec	Friction Factor [4] $f=8\left(\frac{u_*}{\bar{u}}\right)^2$ $(\times 10^2)$	von Kármán Constant, κ	Froude Number $F=\frac{\bar{u}}{\sqrt{gd}}$	Kinematic Viscosity, ν cm^2/sec $(\times 10^2)$	Reynolds Number $R=\frac{4\bar{u}r}{\nu}$ $(\times 10^{-4})$	Friction Reynolds Number, [4] $R_*=\frac{u_* d}{\nu}$ $(\times 10^{-3})$	Level of Tracer Injection η_h	RUN
1	2	3	4	5	6	7	8	9	10	11	12	13	14	15	1
407	I, II	R2	8.66	7.48	41.0	3.189	5.12	12.50	-	0.445	1.018	12.05	4.356	0.368	407
404	I, II	R2	10.36	8.72	42.8	2.597	5.05	11.15	0.324	0.425	1.052	14.19	4.973	0.368	404
606	II	S1	10.70	8.55	42.6	0.454	1.95	1.68	-	0.416	0.945	15.43	2.210	0.368	606
607	I, II	S1	10.70	8.55	41.8	0.429	1.90	1.65	0.333	0.408	0.955	14.95	2.125	0.368	607
704	I	S2	10.81	9.03	39.2	0.390	1.86	1.80	0.357	0.381	0.978	14.58	2.055	0.368	704
804	II	S2	10.84	9.06	39.2	0.390	1.86	1.80	-	0.380	0.996	14.25	2.026	0.368	804
904	II	S2	10.84	9.06	39.2	0.390	1.86	1.80	-	0.380	0.996	14.25	2.026	0.368	904
300	II	S1	17.00	12.10	35.4	0.210	1.58	1.60	-	0.274	1.020	16.80	2.634	~1.00	300
406	I, II	R2	17.07	13.03	35.3	0.853	3.64	8.49	-	0.273	1.087	16.92	5.716	0.368	406
708	I	S2	17.31	13.17	34.9	0.213	1.66	1.81	0.332	0.268	0.961	19.13	2.988	0.368	708
808	I, II	S2	17.32	13.17	34.9	0.213	1.66	1.81	0.332	0.268	0.978	18.80	2.938	0.368	808
602	I, II	S1	17.34	12.32	36.5	0.242	1.71	1.75	-	0.280	0.978	18.38	3.038	0.368	602
603	I, II	S1	17.34	12.32	36.9	0.263	1.75	1.80	-	0.283	0.978	18.59	3.110	0.368	603
604	II	S1	17.34	12.32	36.9	0.263	1.75	1.80	0.388	0.283	0.953	19.07	3.181	0.368	604
605	I, II	S1	17.34	12.32	37.0	0.263	1.75	1.80	-	0.284	0.963	18.93	3.155	0.850	605
709	I	S2	21.97	15.70	30.5	0.127	1.40	1.68	-	0.208	0.997	19.21	3.082	0.368	709
809	I, II	S2	21.97	15.70	30.7	0.126	1.39	1.65	-	0.209	0.978	19.71	3.140	0.368	809

NOTES:

[1] Phase I is related to time-averaged concentration; phase II to temporal fluctuations of tracer concentration.

[2] For flume identification, S and R denote smooth boundaries and rough bottom respectively. Flume 1 is 85 cm wide, Flume 2 is 110 cm wide.

[3] For the 400 Series only, the listed values are for bed shear velocity calculated by a side-wall correction method: g=gravitational acceleration.

[4] For the 400 Series only, f applies only to rough bed.

ments. For example, a κ-value of 0.375 measured for RUN 508 was used for RUNS 509, 510, 511, 512, 600, and 601 which were essentially identical to RUN 508.

As indicated in Columns 11, 13, and 14, all flows were subcritical and turbulent. The Froude number varied from a high value of 0.972 for $d = 2.74$ cm to a low of 0.208 for $d = 21.97$ cm. The Reynolds number $\mathbb{R}$ was greater than 1.8×10^4 in all experiments, and the minimum value of the friction Reynolds number $\mathbb{R}_*$ was 325.

Column 15 lists the level η_h at which tracer was injected. For most experiments, $\eta_h = 1/e = 0.368$, and the injection velocity was set at the mean water flow velocity. The injection level was specifically varied for the runs where the normal depth was approximately 5.25 cm in order to determine the effect of η_h on initial distributions of tracer just downstream of the source. In this set of runs, the following values of η_h were used: 0.368, 0.632, 0.850, and 0.051. The injection velocity in each case was adjusted to approximately equal the local water flow velocity.

5.B. TRANSVERSE DISTRIBUTIONS OF TIME-AVERAGED CONCENTRATION

Typical transverse distributions of the time-averaged concentration within the plume are shown in Figures 5.1, 5.2, and 5.3 for various normal depths. The runs shown were selected to cover measurements made at various levels of the flow with the flume bottom either smooth or roughened with rocks.

In Figures 5.1(a), (b), and (c), the measured concentration C

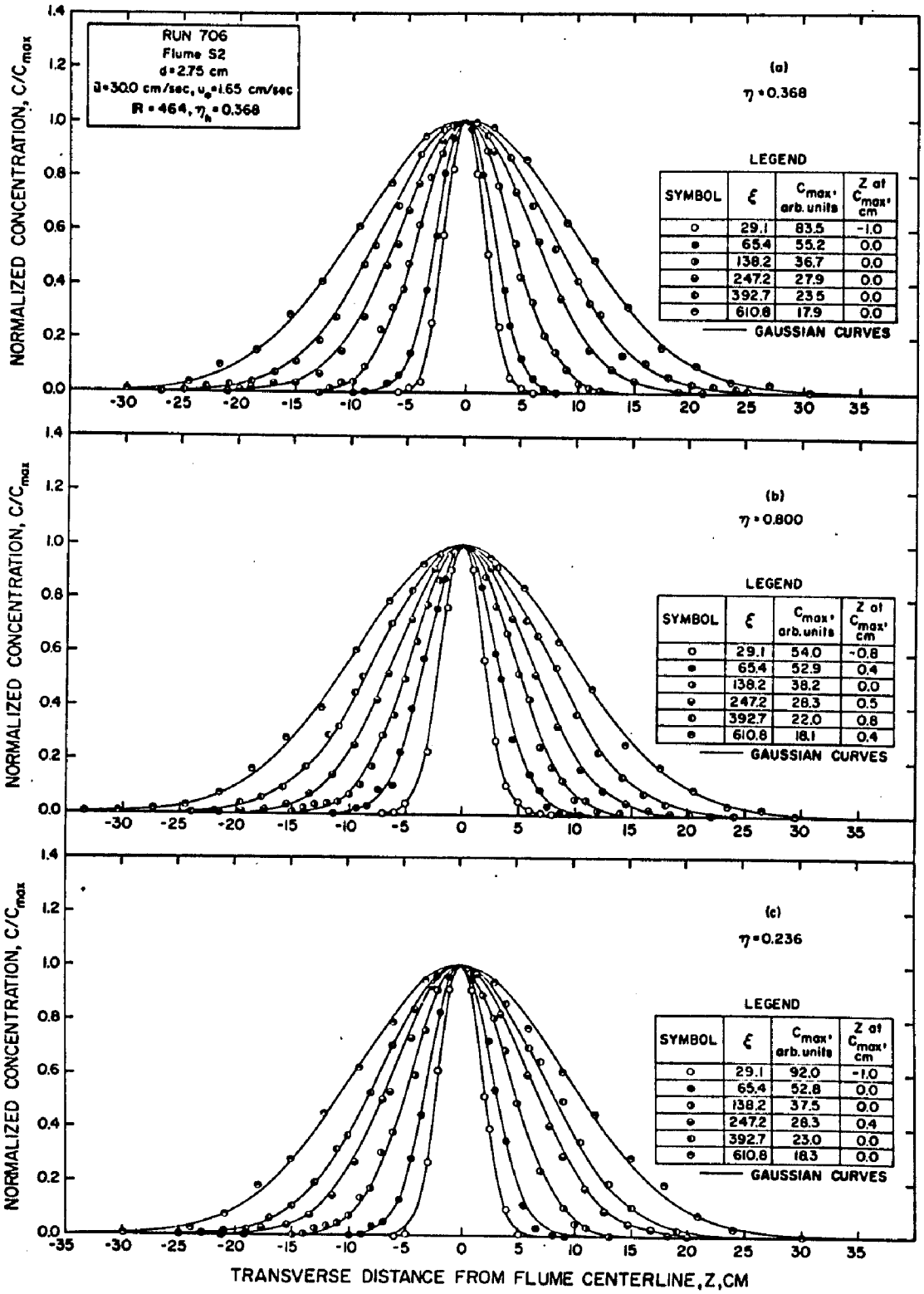

Fig. 5.1. Transverse distributions of the time-averaged concentration measured at various distances $\xi = x/d$ downstream of source, and at various levels of the flow: (a) $\eta = \eta_h = 0.368$, (b) $\eta = 0.800$, (c) $\eta = 0.236$; RUN 706

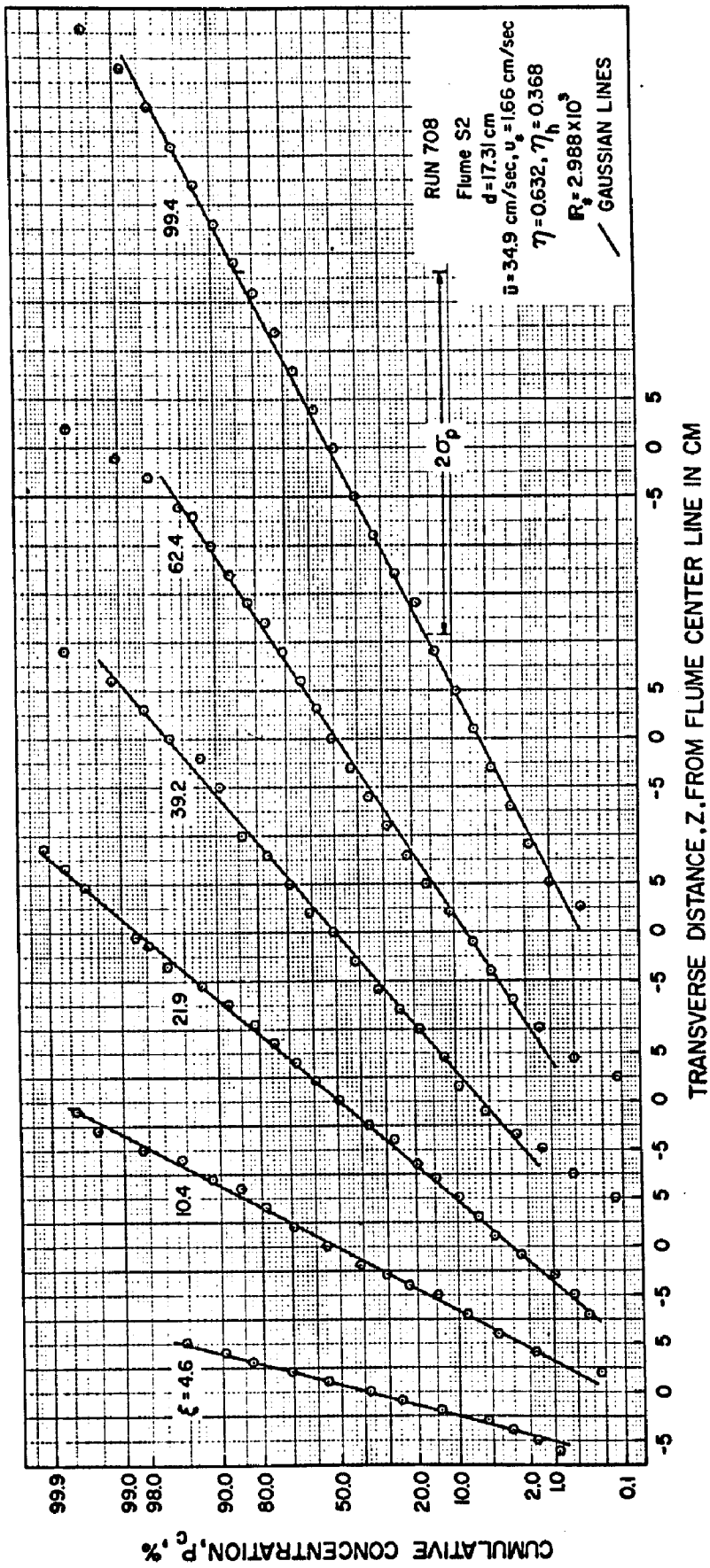

Fig. 5.2. Transverse distributions of the cumulative mean concentration measured at various distances ξ from the source and at the flow level $\eta = 0.632$. Plots on arithmetic probability paper; RUN 708

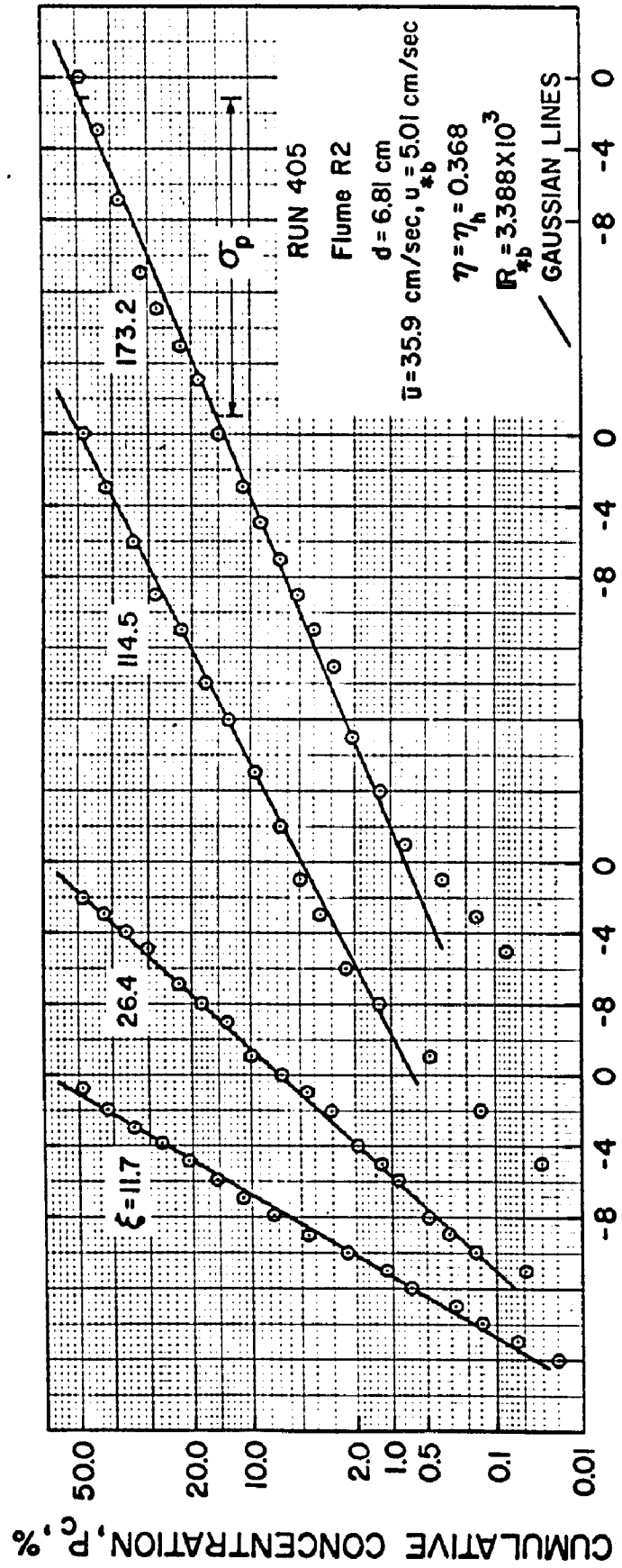

Fig. 5.3. Transverse distributions of the cumulative mean concentration measured at various distances ξ from the source and at the flow level η = 0.368. Plots on arithmetic probability paper; RUN 405

normalized by the maximum concentration C_{max} located at the mode of the concentration distribution is plotted against the transverse distance, z. All measurements plotted in this set of figures were made during RUN 706 in flume S2. The flow depth was 2.75 cm, the mean flow velocity 30.0 cm/sec and the friction Reynolds number $\mathbb{R}_* = 464$. Tracer was injected at $\eta_h = 0.368$.

In each set of graphs shown in Figure 5.1 (for example, Figure 5.1(a)), measurements made at a fixed level of the flow are plotted for various distances, ξ. The points shown are the measured values, and the fitted curves are Gaussian distributions each having a variance equal to that calculated numerically from the measured data, and a corresponding value of C_{max}. The legend explains the plotting symbols: the distances ξ at which the measurements were made, the actual values of C_{max}, and the transverse positions z at which C_{max} was located. Distributions at the levels $\eta = 0.368$, 0.800, and 0.236 are shown in Figure 5.1(a), 5.1(b), and 5.1(c) respectively.

To illustrate the form of the concentration distributions at higher values of $\mathbb{R}_*$, the cumulative concentration, P_c, was plotted against z on arithmetic probability scales for various ξ in Figure 5.2 for RUN 708 where $\mathbb{R}_* = 2.988 \times 10^3$, and in Figure 5.3 for RUN 405 where the flume bottom was rough and $\mathbb{R}_{*b} = 3.388 \times 10^3$. The variable P_c was calculated by the relation

$$P_c(x_1, y_1, z_j) = \left[\sum_{i=0}^{j} C(x_1, y_1, z_i) \Delta z_i \Big/ \sum_{i=0}^{N} C(x_1, y_1, z_i) \Delta z_i \right] \times 100, \quad (5.1a)$$

where x_1 and y_1 are fixed values of x and y; z_0 is the point beyond which, for increasing z, C first attains a non-zero value; z_{N+1} is the largest value of z at which C first becomes zero; $\Delta z_i = z_{i+1} - z_i$, $i = 0,1,\ldots,N+1$; and $j = 1,2,\ldots,N$. In cases where Δz_i is small (about 1 cm) and constant, and N was large, P_c was calculated simply by

$$P_c(x_1,y_1,z_j) = \left[\sum_{i=0}^{j} C(x_1,y_1,z_i) \Big/ \sum_{i=0}^{N} C(x_1,y_1,z_i)\right] \times 100 \ . \qquad (5.1b)$$

Straight lines representing Gaussian distributions were fitted to the plots. A representative standard deviation σ_p was determined for each distribution by the relation

$$\sigma_p = \tfrac{1}{2}(z_{84.1} - z_{15.9}), \qquad (5.2)$$

where $z_{84.1}$ and $z_{15.9}$ are, respectively, the values of z where the fitted Gaussian line intersects $P_c = 84.1$ and $P_c = 15.9$. As will be pointed out in the next section, σ_p^2 in general differed from the variance, σ^2, calculated directly from the measured data using Eq. 5.3.

The plots shown in Figures 5.1 through 5.3 demonstrate that the transverse distribution of the time-averaged concentration was very closely Gaussian at all levels of measurements and for ξ extending from 4.0 to 610.8 regardless of whether the flume bottom was smooth or roughened with rocks. Deviations from the fitted normal distribution occurred only at large values of $|z|/W$ where

the tails of the distributions were very near the flume wall. This is attributed primarily to the effects of the side-wall boundary layers generated next to the flume walls. Reflections from the side walls also contributed, to a lesser degree, to the deviations of measured C at the tails from the Gaussian distribution.

For a given experiment, the closeness of fit of experimental points to the normal distribution was not a function of either the distance downstream of source ξ or the level of concentration measurement η. The measured points appeared to fit best at the lowest and highest values of ξ, as shown in Figures 5.1 through 5.3. However, the deviations of the points from the Gaussian curve at intermediate ξ were still generally insignificant. It is thus concluded that the transverse distribution of C is Gaussian both very near the source ($\xi = 4.0$) and far away, and at all levels of the flow.

5.C. VARIANCE OF THE TRANSVERSE CONCENTRATION DISTRIBUTION

5.C.1. Calculation of the Variance. The variance σ^2 of the cross-wise distribution of tracer concentration for fixed x and y defined by Eq. 2.56, was calculated numerically by

$$\sigma^2(x_1, y_1) = \left(\sum_{i=1}^{N} SM_i \Big/ \sum_{i=1}^{N} A_i \right) - \left(\sum_{i=1}^{N} FM_i \Big/ \sum_{i=1}^{N} A_i \right)^2 \qquad (5.3)$$

where SM_i and FM_i are, respectively, the second and first moments of the trapezoid formed by the concentration values $C(z_i)$, $C(z_{i+1})$ and the points z_i, z_{i+1}, and A_i is the trapezoidal area

$$A_i = \tfrac{1}{2}[C(x_1, y_1, z_{i+1}) + C(x_1, y_1, z_i)](z_{i+1} - z_i) \ . \qquad (5.4)$$

In most experiments, values of C used in Eq. 5.3 were the measured concentration values. In some cases where the experimental data closely fitted a smooth curve, C was obtained as points on the experimental curve.

The variance σ^2 calculated by the moment method of Eq. 5.3 was compared with σ_p^2 determined from the arithmetic probability plots and evaluated by Eq. 5.2. The slopes of the straight lines, $d\sigma^2/dx$ and $d\sigma_p^2/dx$, fitted to the plots of σ^2 and σ_p^2 versus x, were also compared. The results are shown in Table 5.2. Four depths of flow were chosen: 2.75, 5.53, 10.70, and 17.31 cm with corresponding $\mathbb{R}_* = 464$, 1254, 2125, and 2988. For each run a different level of measurement η was selected as an example. The comparison was made at various ξ ranging from 4.0 to 611.0.

As shown in the table the discrepancy between σ^2 and σ_p^2 was generally non-zero but within 14%, and tended to increase with increasing $\mathbb{R}_*$. The errors between $d\sigma^2/dx$ and $d\sigma_p^2/dx$ were even smaller remaining within 8%. The moment method (i.e. σ^2) was used for the calculation of the mixing coefficients in all experiments except the 400 series where the probability method (i.e. σ_p^2) was used.

Table A.1 of the Appendix lists the calculated values of the variance σ^2 for experiments in which concentration was measured at more than two levels of the flow. In RUN 705 where d = 1.69 cm, the flow depth was too small to allow measurements at more than two

Table 5.2 Comparison of the variance σ^2 computed by the moment method and σ_p^2 derived from the probability method

RUN	ξ	σ^2 cm²	σ_p^2 cm²	Error % *	RUN	ξ	σ^2 cm²	σ_p^2 cm²	Error % *
1	2	3	4	5	1	2	3	4	5
706	29.1	2.95	2.89	-2.9	701	14.5	4.59	4.71	+2.6
	65.5	6.11	6.25	+2.3		32.5	12.89	13.19	+2.3
d=2.75 cm	138.1	16.84	16.40	-2.6	d=5.53 cm	68.7	29.88	29.18	-2.3
	247.5	36.06	36.00	-0.2		122.9	52.16	51.10	-2.0
R_* = 464	393.0	59.19	59.29	+0.2	R_* = 1,254	213.3	94.85	90.25	-4.8
	611.0	90.76	92.16	+1.5		303.7	140.28	140.30	+0.0
(η=0.368)	$\frac{d\sigma^2}{dx}$ = 0.0566 cm			+2.3	(η=0.855)	$\frac{d\sigma^2}{dx}$ = 0.0854 cm			-3.3
	$\frac{d\sigma_p^2}{dx}$ = 0.0579 cm					$\frac{d\sigma_p^2}{dx}$ = 0.0826 cm			
RUN	ξ	σ^2 cm²	σ_p^2 cm²	Error %	RUN	ξ	σ^2 cm²	σ_p^2 cm²	Error %
1	2	3	4	5	1	2	3	4	5
607	4.0	2.5	2.6	+4.0	708	4.6	5.6	6.4	+14.3
	8.7	9.1	8.8	-3.3		10.4	26.0	26.0	- 0.0
d=10.70 cm	18.0	15.2	16.4	+7.9	d=17.31 cm	21.9	64.7	65.6	+ 1.4
	36.7	43.3	39.8	-5.8		39.2	126.4	124.3	- 1.7
R_* = 2,125	50.7	54.8	58.2	+6.2	R_* = 2,988	62.4	195.0	216.1	+10.8
	69.4	80.7	77.8	-3.6		99.4	313.2	349.0	+11.5
(η = 0.095)	$\frac{d\sigma^2}{dx}$ = 0.109 cm			0.0	(η = 0.632)	$\frac{d\sigma^2}{dx}$ = 0.188 cm			+ 8.0
	$\frac{d\sigma_p^2}{dx}$ = 0.109 cm					$\frac{d\sigma_p^2}{dx}$ = 0.203 cm			

NOTE:

* The variance σ^2 is used as base.

levels. In the 400 series, where σ_p^2 was calculated, concentration was measured only at $\eta = 0.368$ and 0.632. The depth-averaged variance, denoted by AVG in the table, was determined as a simple average of the non-zero values of the variance at the various levels of measurement.

5.C.2. Growth of the Variance σ^2 With Distance x Downstream of Source. Figures 5.4 through 5.7 are plots of the variance σ^2 versus x, developed for various levels of the flow η. The bottom curve in each figure denoted as AVG is the plot of the depth-averaged variance $\overline{\sigma^2}$ versus x. The runs shown were selected as typical examples covering a wide range of flow depths and $\mathbb{R}_*$.

The plots of Figures 5.4 through 5.7 show that the variance grew linearly with x both at various levels of the flow and as a depth average. For every level, straight lines could be fitted to each plot for $x > 70$ cm provided tracer was detected at that station. Thus the plume width (estimated as a constant factor of σ) grew parabolically for $x \geq 70$ cm for all normal depths covered in this study. The parabolic growth is in accord with Taylor's (28) one-dimensional diffusion theory and is illustrated by concentration contours plotted in Figure 5.24.

The linear growth rates $d\sigma^2/dx$, however, varied with levels of measurement η as shown in Figures 5.4 through 5.7. The discrepancies ϵ between $d\sigma^2/dx$ at various levels η and the growth rate $d\overline{\sigma^2}/dx$ of the depth-averaged variance are listed in Table 5.3 for $d = 2.75$, 5.53, 10.70, and 17.31 cm. As indicated, the absolute value of the error varied from 0.0% measured in RUN 706 where

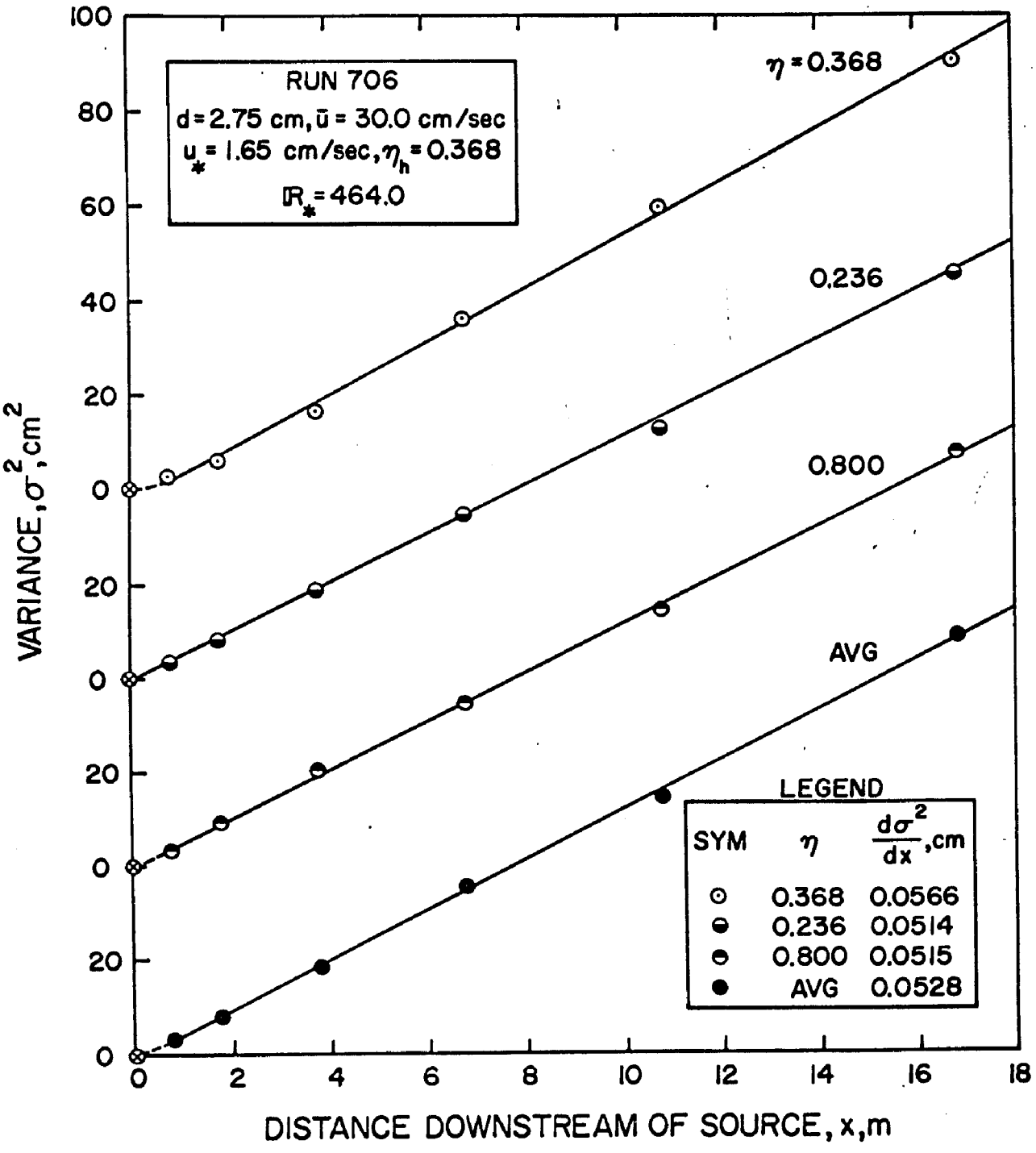

Fig. 5.4. Growth of the variance σ^2 with distance x at various levels of the flow η and as a depth average; RUN 706

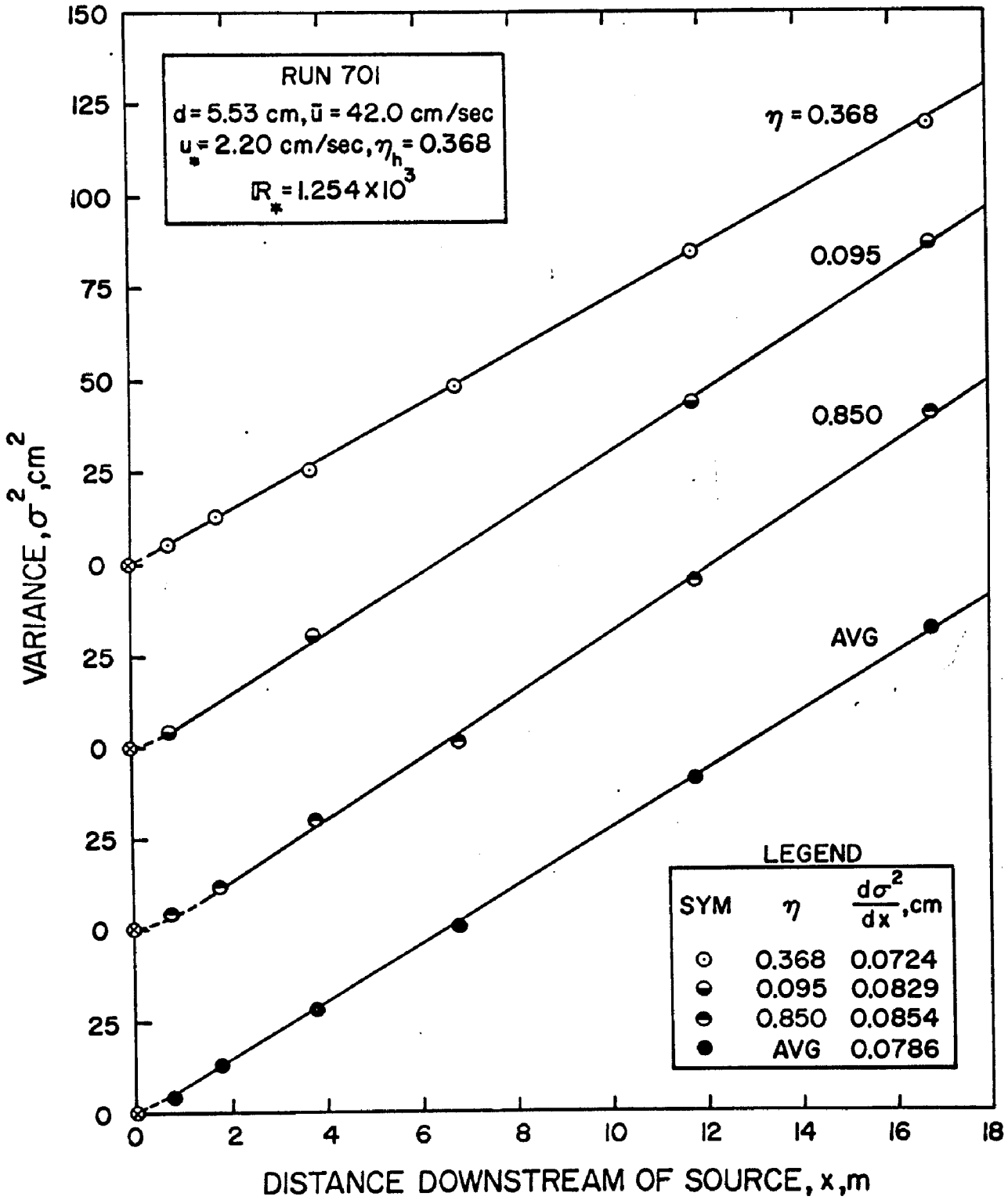

Fig. 5.5. Growth of the variance σ^2 with distance x at various levels of the flow η and as a depth average; RUN 701

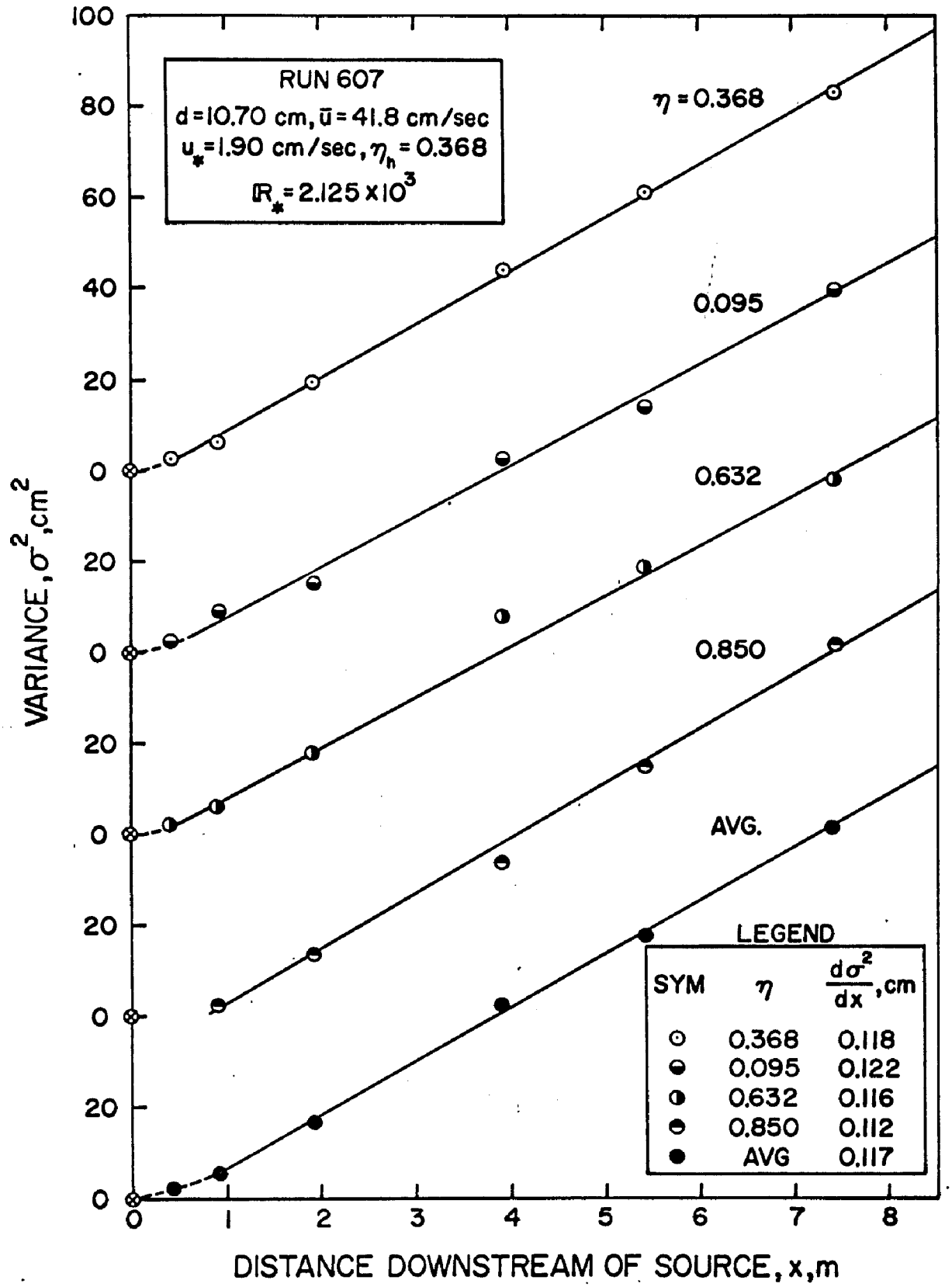

Fig. 5.6. Growth of the variance σ^2 with distance x at various levels of the flow η and as a depth average; RUN 607

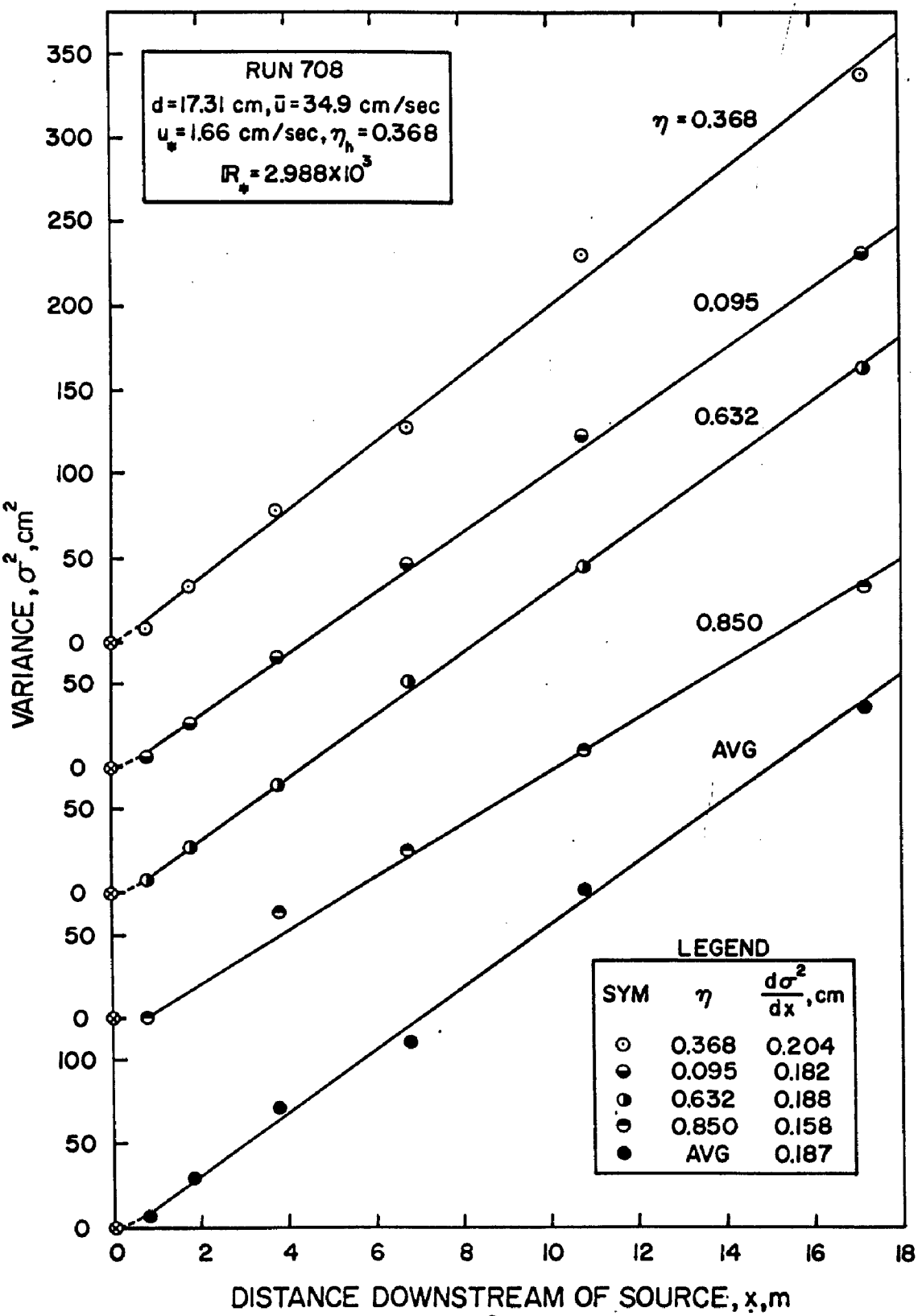

Fig. 5.7. Growth of the variance σ^2 with distance x at various levels of the flow η and as a depth average; RUN 708

Table 5.3

Comparison of $d\sigma^2/dx$ at Various Levels η and $\overline{d\sigma^2}/dx$, the Rate of Growth of the Depth-Mean Variance

RUN	d cm	η	$\frac{d\sigma^2}{dx}$ cm	$\frac{\overline{d\sigma^2}}{dx}$ cm	Error, ϵ %	Mean $\lvert\epsilon\rvert$ %
706	2.75	0.368	0.0566	0.0528	+7.2	
		0.236	0.0514		-2.6	
		0.800	0.0528		0.0	3.3
701	5.53	0.368	0.0724	0.0786	-7.9	
		0.095	0.0829		+5.5	
		0.850	0.0854		+8.6	7.3
607	10.70	0.368	0.118	0.117	+1.0	
		0.095	0.122		+4.3	
		0.632	0.116		-1.0	
		0.850	0.112		-4.3	3.5
708	17.31	0.368	0.204	0.187	+9.1	
		0.095	0.182		-2.7	
		0.632	0.188		+0.5	
		0.850	0.158		-15.5	9.3
In all cases the injection level $\eta_h = 0.368$.						

d = 2.75 cm to a maximum of 15.5% evaluated in RUN 708 where d = 17.31 cm. The mean value of the absolute error $|\epsilon|$ was about 5%.

5.D. THE TRANSVERSE MIXING COEFFICIENT

5.D.1. The Depth-Averaged Mixing Coefficient, $\overline{D}_z$.

a. Calculation of the depth-averaged mixing coefficient. It has been shown in subsection 2.B.4 that if the variance σ^2 of the transverse distribution of tracer concentration is invariant with depth, the depth-

averaged eddy coefficient of transverse mixing $\overline{D}_z$ can be calculated by Eq. 2.55. Without normalization, this equation reduces to

$$\overline{D}_z = \frac{1}{2} \overline{u} \frac{d\overline{\sigma^2}}{dx} , \qquad (5.5)$$

where $\overline{u}$ is the average velocity in the cross section, and $\overline{\sigma^2}$ is the depth-averaged value of σ^2.

In this study, Eq. 5.5 was used to calculate $\overline{D}_z$. As shown in Figure 5.8 for six runs other than those already included in Figures 5.4 through 5.7, plots of $\overline{\sigma^2}$ versus x were developed. Since $\overline{\sigma^2}$ grew linearly with x for $x > 70$ cm, straight lines were fitted to the plots and their slopes determined. Thus $\overline{D}_z$ was calculated by Eq. 5.5.

RUN 509 differed from RUN 511 only in the height of tracer injection, η_h. For RUN 509, $\eta_h = 0.368$ and for RUN 511, $\eta_h = 0.051$. As shown in Figure 5.8, $d\overline{\sigma^2}/dx$ is virtually identical for both runs indicating that $d\overline{\sigma^2}/dx$ and therefore $\overline{D}_z$ was not affected by the level of tracer injection, η_h.

Table 5.4 summarizes all calculated values of $\overline{D}_z$ including other related parameters. In addition to the hydraulic data shown in Columns 1 through 5, the table lists: the aspect ratio $\lambda = d/W$ in Column 6; the rate of growth of the depth-averaged variance $d\overline{\sigma^2}/dx$ in Column 7; the depth-mean coefficient $\overline{D}_z$ in Column 8; and the normalized coefficient, $\overline{\theta} = \overline{D}_z/u_* d$ in Column 9. For experiments in the flume with the rough bottom, u_* was replaced by the bed shear velocity u_{*b} in the normalization of $\overline{D}_z$.

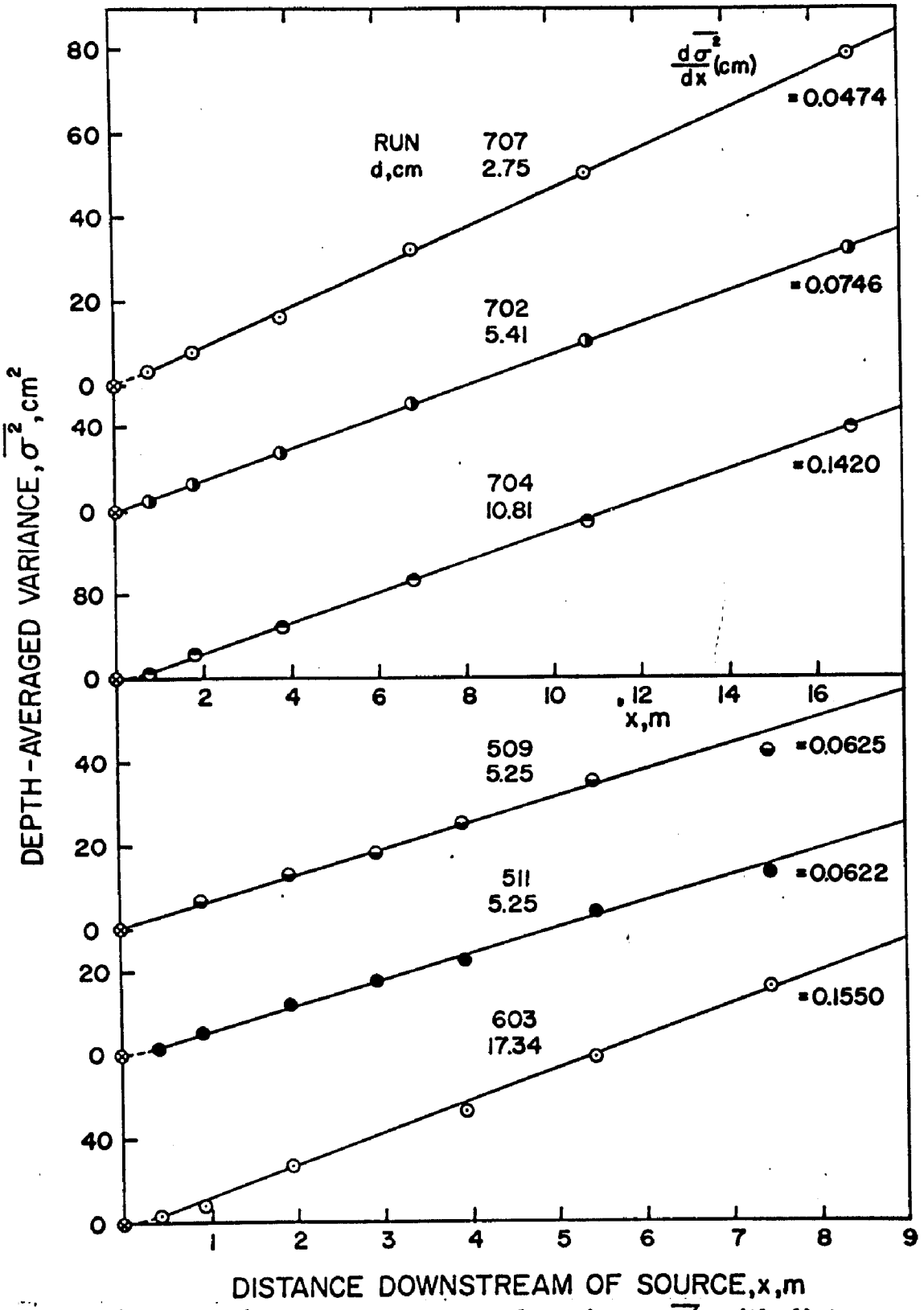

Fig. 5.8. Growth of the depth-averaged variance $\overline{\sigma^2}$ with distance x downstream of source for various normal depths; RUNS 707, 702, 704, 509, 511, 603

b. Variation of $\overline{\theta} = \overline{D}_z/u_*d$ with the aspect ratio $\lambda = d/W$. A similarity approach was used to develop a representation of the depth-averaged mixing coefficient as a universal function of the hydraulic parameters. The pertinent variables chosen were $\overline{D}_z$, u_*, d, and W. The choice of the independent variables, u_*, d, and W was justified by the following reasoning: the transverse mixing coefficient depends on essentially two parameters--turbulence intensity and the size scale of the eddies. The shear velocity u_* has been shown by measurements of Laufer (63) in a two-dimensional flow in a wind tunnel to equal approximately the rms value of the transverse velocity fluctuation. The turbulence scale in flows with upper and lower boundaries and side-wall confinements is limited not only by the flow depth but also by the separation distance between the side walls. A characteristic scale of the mixing process is, therefore, related to both d, the flow depth, and W, the flume width.

The other variables of the flow are either intrinsically part of the variables already selected or insignificant in describing the mixing process. For example, the mean velocity, $\overline{u}$ is important only in the transport of the marked fluid and has been utilized in the calculation of $\overline{D}_z$ in Eq. 5.5. The friction factor falls within the determination of u_*. Since the Reynolds number was very high in all experiments (minimum $\mathrm{IR} \approx 2 \times 10^4$), the turbulent Schmidt number $S_c = \overline{D}_z/\nu$ was also high--a typical value of $S_c \approx 300$. Thus the kinematic viscosity will be considered important only in establishing that the flow was indeed turbulent but will not be included as a variable.

With four variables: $\overline{D}_z$, u_*, d, and W, and two basic units: length and time, dimensional analysis yields the functional relationship

$$\frac{\overline{D}_z}{u_* d} = \Phi\left(\frac{d}{W}\right), \tag{5.6a}$$

which could be written as

$$\overline{\theta} = \Phi(\lambda), \tag{5.6b}$$

where Φ is an unknown function, $\overline{\theta} = \overline{D}_z/u_* d$, and $\lambda = d/W$ is termed the aspect ratio.

The results listed in Table 5.4 and plotted in Figure 5.9 support the preceding relationship. For example $\overline{\theta}$ remained essentially unchanged when the mean flow velocity $\overline{u}$ was almost doubled between RUNS 706 and 707 while λ was kept constant. That $\overline{\theta}$ was independent of the friction Reynolds number $\mathbb{R}_*$ or the friction factor f_* is vividly illustrated by several results. For example, when $\mathbb{R}_*$ was raised from 2.06×10^3 (RUN 704) to 4.97×10^3 (RUN 404) while λ was essentially unchanged ($\approx +4\%$ error), $\overline{\theta}$ increased by only 4%. Similarly when $\mathbb{R}_*$ was more than doubled between RUNS 708 and 406 while λ remained within 1% of each other, the change in $\overline{\theta}$ was only about 4%. However when $\mathbb{R}_*$ was virtually constant in RUNS 709 and 405 (error of +10% in $\mathbb{R}_*$), but λ was decreased by 70%, $\overline{\theta}$ was increased by about 32%. This clearly demonstrates a well defined sensitivity of $\overline{\theta}$ to λ and little relationship of $\overline{\theta}$ to $\mathbb{R}_*$.

Figure 5.9 also shows that $\overline{\theta}$ is not dependent on the flow depth d but on the aspect ratio λ. Each pair of experiments with essentially

Table 5.4 Summary of measured depth-averaged mixing coefficient $\overline{D}_z$ and related parameters.

RUN	Flume	Normal Depth d cm	Mean Velocity $\bar{u}$ cm/sec	Shear Velocity u_* cm/sec	Aspect Ratio § $\lambda=d/W$ (10^2)	$\frac{d\overline{\sigma^2}}{dx}$ † cm $(\times 10^2)$	Depth-averaged Mixing Coefficient † $\overline{D}_z$ (Eq. 5.5) cm^2/sec	Normalized Coefficient, * $\theta=\frac{\overline{D}_z}{u_* d}$	RUN
1	2	3	4	5	6	7	8	9	1
507	S1	1.52	31.2	2.12	1.79	4.06	0.63	0.197	507
705	S2	1.69	32.8	1.99	1.53	4.82	0.79	0.235	705
707	S2	2.74	50.4	2.65	2.49	4.74	1.19	0.164	707
706	S2	2.75	30.0	1.65	2.50	5.28	0.79	0.174	706
506	S1	2.95	27.1	1.57	3.47	5.80	0.79	0.166	506
703	S2	3.46	32.0	1.76	3.15	5.35	0.86	0.142	703
509	S1	5.25	42.6	2.26	6.17	6.25	1.33	0.112	509
511	S1	5.25	42.8	2.08	6.17	6.20	1.33	0.122	511
512	S1	5.25	42.5	2.17	6.17	6.72	1.43	0.126	512
508	S1	5.26	41.7	2.13	6.19	5.80	1.21	0.108	508
510	S1	5.26	42.4	2.12	6.19	6.87	1.45	0.130	510
702	S2	5.41	43.5	2.18	4.92	7.46	1.62	0.137	702
701	S2	5.53	42.0	2.20	5.03	7.86	1.65	0.135	701
405	R2	6.81	35.9	5.01	6.19	26.8	4.81	0.141	405
407	R2	8.66	41.0	5.12	7.87	29.4	6.03	0.136	407
404	R2	10.36	42.8	5.05	9.42	35.0	7.49	0.143	404
607	S1	10.70	41.8	1.90	12.58	11.7	2.09	0.103	607
704	S2	10.81	39.2	1.86	9.83	14.2	2.78	0.138	704
406	R2	17.07	35.3	3.64	15.52	38.2	6.74	0.108	406
708	S2	17.31	34.9	1.66	15.73	18.7	3.26	0.113	708
603	S1	17.34	36.9	1.75	20.39	15.5	2.86	0.094	603
709	S2	21.97	30.5	1.40	19.97	21.4	3.26	0.107	709

NOTES:

* Bed shear velocity was used for experiments in the 400 Series.

§ W = flume width.

† For the 400 Series, measurements were made at two levels: $\eta = 0.368$ and 0.632; $\overline{\sigma^2}$ is the depth-averaged variance of the transverse distribution of tracer concentration.

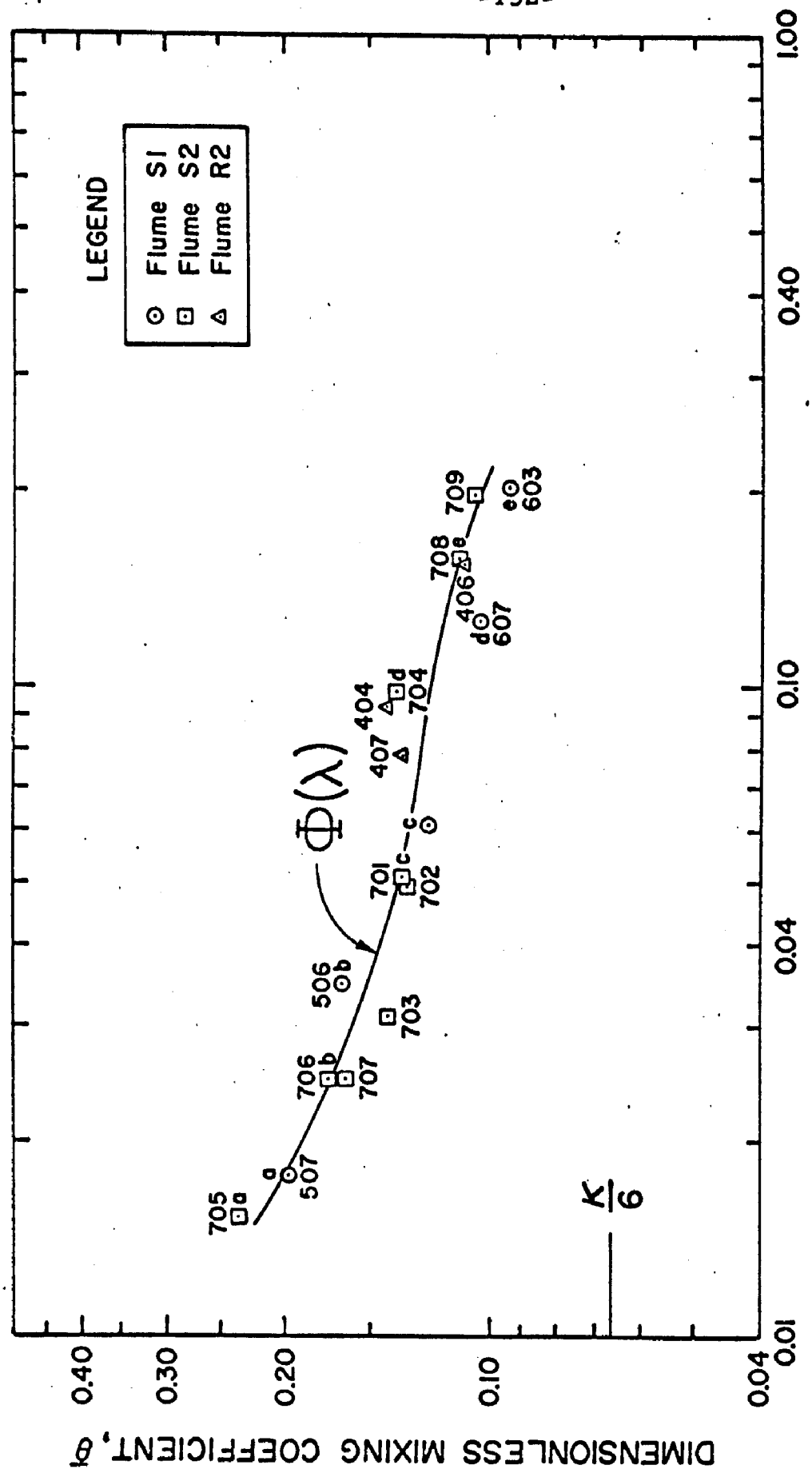

Fig. 5.9. Variation of the depth-averaged, dimensionless mixing coefficient $\bar{\theta}$ with the aspect ratio λ for experiments performed in this study. The average value of $\bar{\theta}$ for RUNS 508, 509, 510, 511, and 512 is plotted for $\lambda = 0.062$

equal flow depths but performed in separate flumes are marked a, b, c, d, and e. As shown in the plots, $\overline{\theta}$ for each pair was always lower for the higher λ.

That $\overline{D}_z/u_*d$ should decrease with d/W may be explained as follows. The larger the turbulence scale in the lateral direction, the greater is the transverse spreading of material cloud. Thus if the flow depth d is constant, $\overline{D}/u_*d$ increases as W increases since the lateral scale can increase further yet. Therefore, $\overline{D}_z/u_*d$ increases with decreasing $\lambda = d/W$, and decreases with increasing λ.

As $\lambda \rightarrow 1$, the analysis is no longer applicable because the flow becomes strongly three dimensional. As $\lambda \rightarrow 0$, the flume width, W, is no longer the characteristic transverse length and the dimensionless transverse coefficient $\overline{\theta}$ would be expected to approach a constant value. For all cases where measurements were made in this study, $\overline{\theta}$ was always greater than $\kappa/6$, the value of $\overline{D}_y/u_*d$.

c. Dependence of $\overline{\theta}$ on λ for experiments performed by other investigators. Figure 5.10 is a plot of $\overline{\theta} = \overline{D}_z/u_*d$ versus $\lambda = d/W$ for both the present study and the measurements made by other investigators. All experiments performed in the laboratory and reported by Prych (39), Sullivan (6), Elder (1), and Kalinske and Pien (30) lie very close to the curve $\Phi(\lambda)$ except in the range $0.07 < \lambda < 0.11$ where measured values of $\overline{\theta}$ plot above $\Phi(\lambda)$. No apparent reason could be found for this discrepancy. For experiments performed in the field

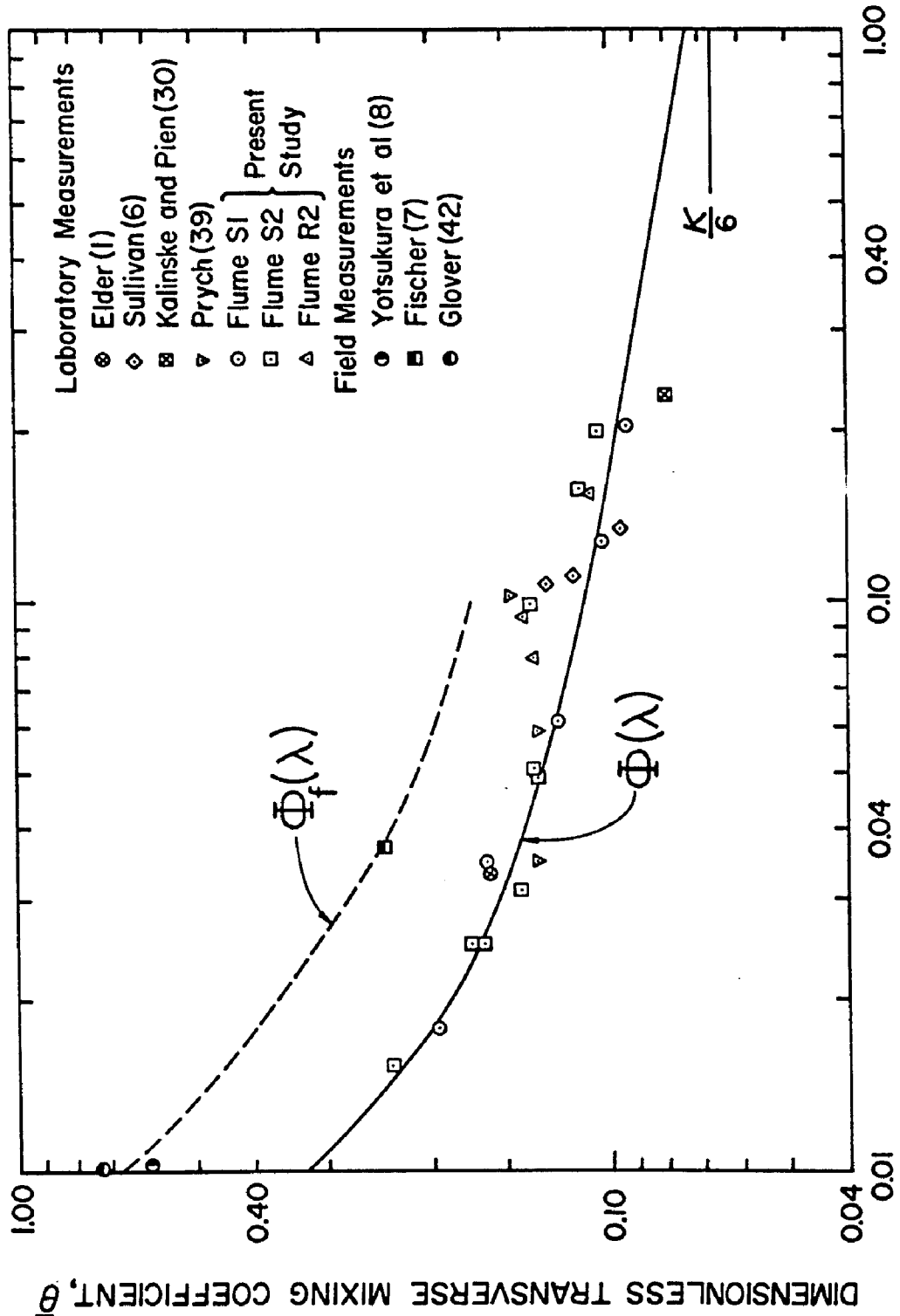

Fig. 5.10. Variation of the depth-averaged, dimensionless mixing coefficient $\overline{\theta}$ with the aspect ratio λ for all experiments performed in the present and past studies

and reported by Yotsukura et al. (8), Fischer (7), and Glover (42), $\overline{\theta}$ is approximately twice the value that $\Phi(\lambda)$ predicts. Indeed the field experiments tend to lie on a higher curve $\Phi_f(\lambda)$ which also decreases with λ.

The difference between laboratory and field experiments is due to accentuated mixing caused by the large secondary currents and strong lateral gradients in velocities generated by bends and non-uniform cross sections in natural streams. Fischer (64) showed experimentally that a short bend in a laboratory flume could increase $\overline{\theta}$ on the average about six times above the value in an identical straight channel. Further field measurements, however, are needed for a more complete understanding of irregular channels.

The present experiments agree with previous results but cover a wider range of the aspect ratio λ. In addition this study confirms the dependence of $\overline{D}_z/u_*d$ on λ.

5.D.2. Variation of the Transverse Mixing Coefficient With Depth Caused by Shear and the Non-Uniform Distribution of the Vertical Diffusivity With Depth. As a result of shear and the variation of the vertical diffusivity D_y with depth, the transverse mixing coefficient D_z varies with depth within the flow. Two methods were used to determine this variation.

The first utilized Batchelor's (33) result outlined in Chapter 2. Stated for the one-dimensional case, this proposition asserts that if on a plane of homogeneous turbulence, tracer distribution is Gaussian, then a mixing coefficient D can be defined such that

$$D = \frac{1}{2} \frac{d\sigma^2}{dt} \quad , \tag{5.7}$$

where σ^2 is the variance of the tracer distribution and t is time. For the uniform open-channel flow every transverse plane parallel to the flume bottom is a level of homogeneous turbulence. Measurements shown in Figures 5.1 through 5.3 demonstrate that at each level of measurement η, the transverse distribution of tracer concentration is Gaussian for all x. Therefore at each level one can define a transverse coefficient D_z expressed as

$$D_z(\eta) = \frac{1}{2} \frac{d\sigma^2}{dt}(\eta), \tag{5.8}$$

where σ^2 is now the variance of the transverse distribution of C at level η. Thus assuming that a space-time transformation is valid, Eq. 5.8 can be written as

$$D_z(\eta) = \frac{1}{2} u(\eta) \frac{d\sigma^2}{dx}(\eta) \quad , \tag{5.9}$$

where $u(\eta)$ is the flow velocity at the level η. By calculating $u(\eta)$ and $\frac{d\sigma^2}{dx}(\eta)$ at various η, a dimensionless coefficient

$$\theta_1(\eta) = \frac{u(\eta)}{2u_* d} \frac{d\sigma^2}{dx}(\eta), \tag{5.10}$$

is evaluated.

Figure 5.11 shows distributions of $\theta_1(\eta)$ for RUNS 511, 704, and 512. As shown in the legend, the injection levels, η_h, were respectively 0.051, 0.368, and 0.850 for RUNS 511, 704, and 512. The maximum variation of $\theta_1(\eta)$ from its depth mean value was 24%,

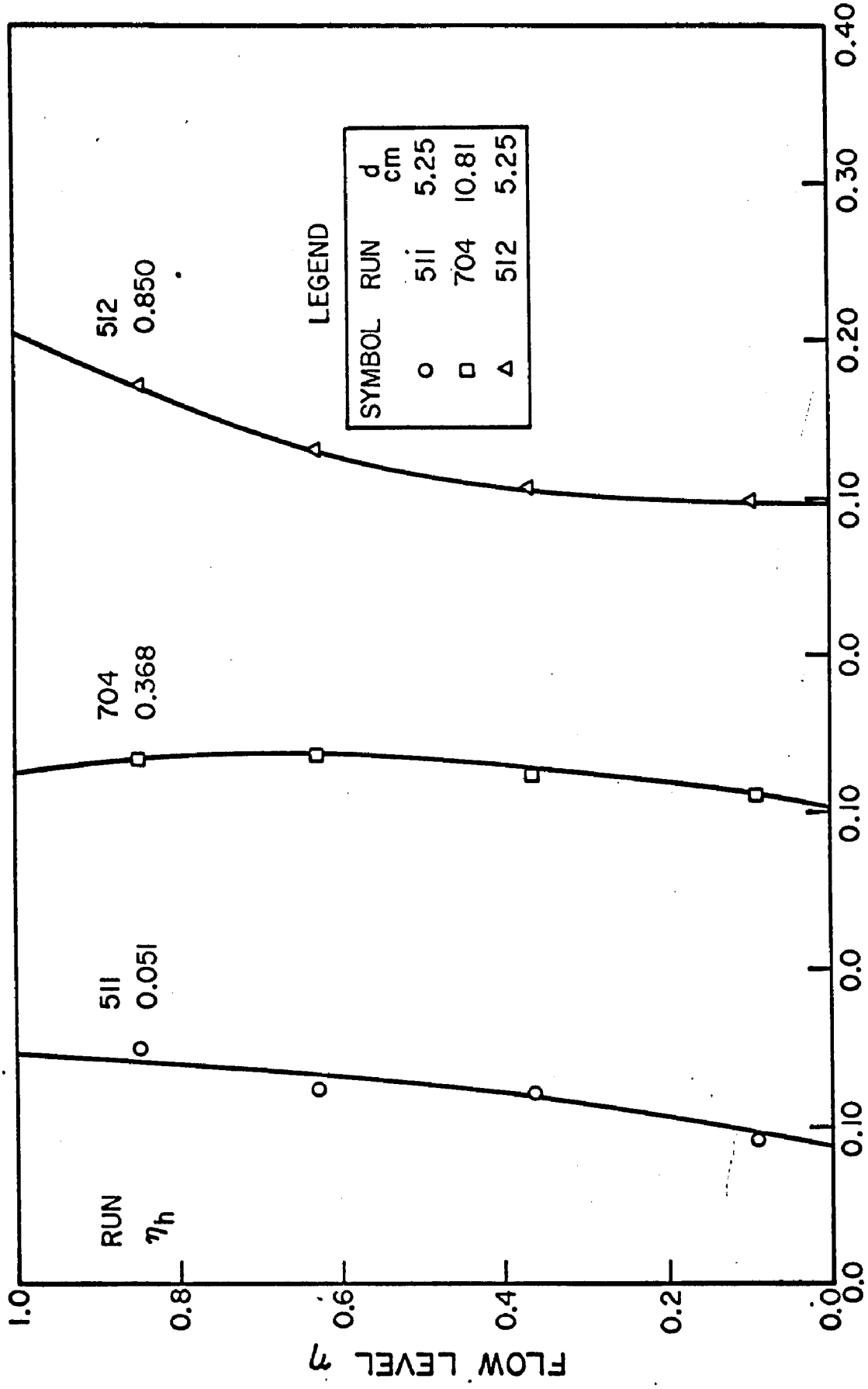

Fig. 5.11. Depth variation of the normalized transverse mixing coefficient θ_1 due to shear only; RUNS 511, 704, 512

21%, and more than 35% for RUNS 511, 704, 512 respectively. The large discrepancy in RUN 512 is due to the fact that when tracer is injected near the water surface where the flow velocity is high, both $u(\eta)$ and $\frac{d\sigma^2}{dx}(\eta)$ are high at large η. Thus $\theta_1(\eta)$ is much higher at large η than at the lower levels of the flow.

The second method for calculating the variation of D_z with depth is based on Eq. 2.59. This method considers the effects of both shear and the vertical variations of σ^2 and of the diffusivity D_y on D_z. As stated in Chapter 2, numerical calculation of the derivatives of σ^2 at a fixed η by incremental approximation was inadequate because of the generation of large numerical errors. Therefore, an analytical method was used.

First σ^2 was determined for various levels of measurement η and distances ξ from the straight lines fitted to the σ^2 versus x plots (for example, Figure 5.6). At each ξ, σ^2 was plotted against η. Using the plotted points a representative curve of σ^2 as a function of η was drawn. Then utilizing the method of least squares, polynomials of various degrees were fitted to points on this curve until the chi-square error was small (about 0.02). The resulting polynomial was used to represent the variation of σ^2 with η at the particular ξ. As further verification of the goodness of fit, σ^2 was re-calculated using the fitted polynomial and compared with the data points. Agreement was within 2% (for most points the error was zero).

A third degree polynomial was found adequate for the runs investigated and at all ξ. Thus σ^2 was expressed as

$$\sigma^2 = a_0 + a_1\eta + a_2\eta^2 + a_3\eta^3 . \qquad (5.11)$$

where the coefficients a_0, a_1, a_2, a_3 were determined for each ξ. Eq. 2.59 was then written in the form

$$D_z(\xi,\eta) = \frac{1}{2}\left\{\left[\bar{u} + \frac{u_*}{\kappa}\ell n\,(e\eta)\right]\frac{d\sigma^2}{dx}(\eta)\right.$$

$$\left. - \frac{\kappa u_*}{d}\left[(1 - 2\eta)\frac{\partial\sigma^2}{\partial\eta}(\xi) + (\eta - \eta^2)\frac{\partial^2\sigma^2}{\partial\eta^2}(\xi)\right]\right\} . \qquad (5.12)$$

Substituting Eq. 5.11 into Eq. 5.12 and normalizing by u_*d, it was found that at a given ξ

$$\theta(\eta) = \frac{D_z}{u_*d}$$

$$= \frac{1}{2u_*d}\left[\bar{u} + \frac{u_*}{\kappa}\ell n\,(e\eta)\right]\frac{d\sigma^2}{dx}(\eta)$$

$$- \frac{\kappa}{2d^2}\left[(1 - 2\eta)(a + 2a_2\eta + 3a_3\eta^2) + (\eta - \eta^2)(2a_2 + 6a_3\eta)\right] . \qquad (5.13)$$

Therefore,

$$\theta(\eta) = \theta_1(\eta) - \frac{\kappa}{2d^2}\left[a_1 + \eta(-2a_1 + 4a_2) + \eta^2(-6a_2 + 3a_3) + \eta^3(-12a_3)\right] . \qquad (5.14)$$

Hence $\theta(\eta)$ is composed of two parts: the first, $\theta_1(\eta)$, due to shear and the second due to the interaction of the vertical distributions of the variance σ^2 and vertical diffusivity, D_y.

Figures 5.12 and 5.13 show the measured distributions of $\sigma^2(\eta)$ and the corresponding $\theta(\eta)$ calculated by Eq. 5.14 at several

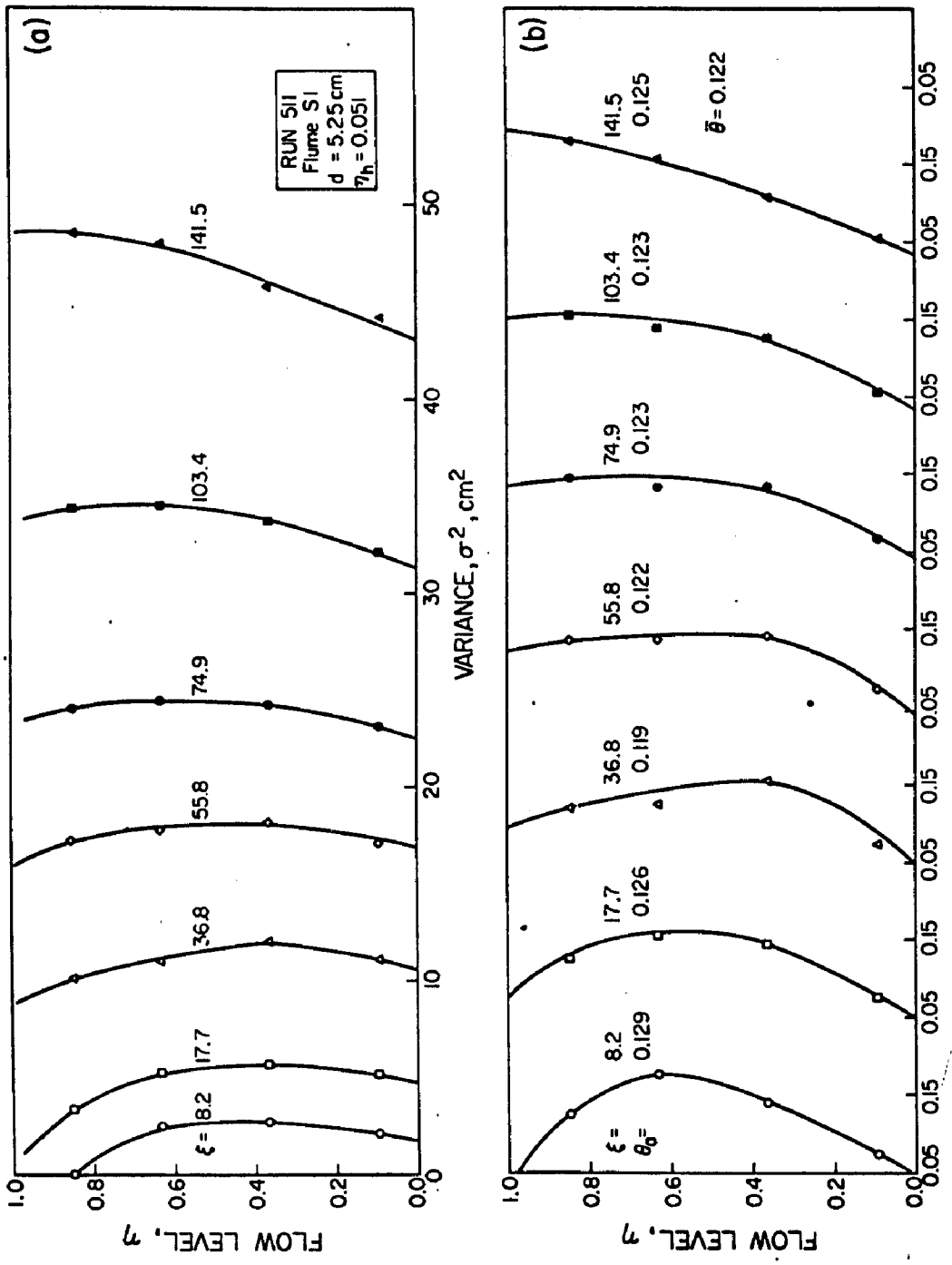

Fig. 5.12. Depth variation of the normalized transverse mixing coefficient θ due to shear and the interaction between the vertical distributions of the variance σ^2 and of the vertical diffusivity D_y; RUN 511

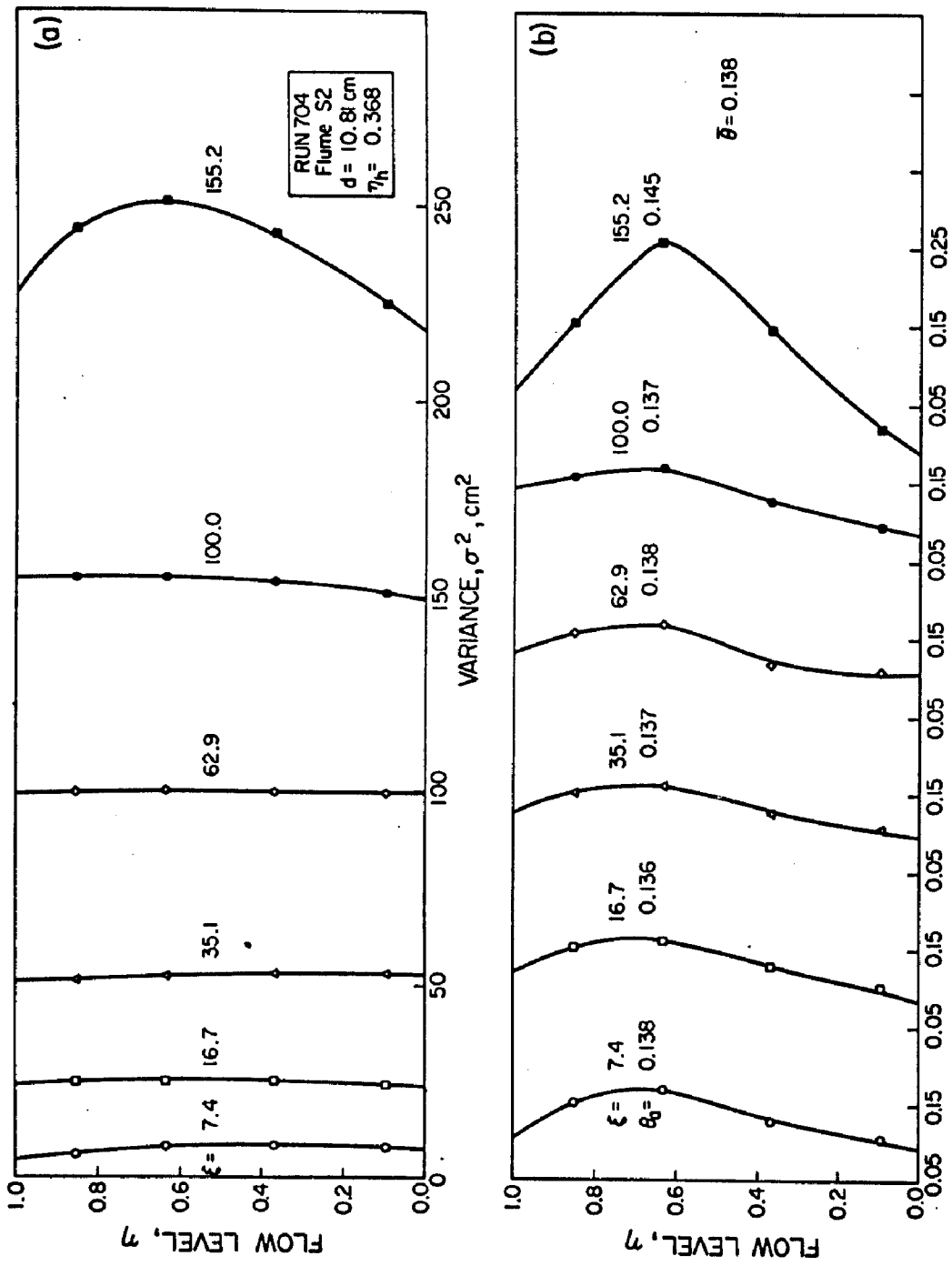

Fig. 5.13. Depth variation of the normalized transverse mixing coefficient θ due to shear and the interaction between the vertical distributions of the variance σ^2 and of the vertical diffusivity D_y; RUN 704

ξ. In Figure 5.12, the results for RUN 511 are shown. The flow depth was 5.25 cm and the injection level $\eta_h = 0.05$ (i.e. very close to the flume bottom). Although $\sigma^2(\eta)$ was similar at all ξ, the shape of $\theta(\eta)$ varied with ξ. Figure 5.12(b) shows that as ξ increased, $\theta(\eta)$ successively grew larger at higher values of η and decreased at low η with the position of maximum $\theta(\eta)$ increasing from $\eta = 0.632$ at $\xi = 8.2$ to $\eta = 1.0$ at $\xi = 41.5$. This was due to the fact that the curvature of $\sigma^2(\eta)$ decreased with increasing ξ. Hence as the curvature diminished, the shear effect θ_1 dominated over the second term of Eq. 5.14. Consequently at high η where θ_1 was large, θ was also large, while at small η where θ_1 was small θ was also small.

In Figure 5.13 where the flow depth was 10.81 cm and the injection level $\eta_h = 0.368$, the distributions of $\theta(\eta)$ were essentially similar at all ξ except at $\xi = 155.2$. This similarity was achieved because $\sigma^2(\eta)$ was approximately uniform with depth for all ξ except at $\xi = 155.2$. The highest value of θ was located around $\eta = 0.72$ at all ξ. For $\xi = 155.2$, however, maximum θ occurred at $\eta = 0.632$ where the curvature of $\sigma^2(\eta)$ was greatest.

The mean value of $\theta(\eta)$ denoted by θ_a was determined from the calculated θ at each ξ. The results are shown in Figures 5.12(b) and 5.13(b). These were compared to the depth-averaged coefficient $\overline{\theta}$ (also shown in the figures) evaluated for the particular runs by use of Eq. 5.5. Agreement between θ_a at various ξ and $\overline{\theta}$ was within 5% for all ξ.

As a summary, therefore, it is noted that the variation of the

transverse mixing coefficient with depth can be considered as due to either shear only or a combination of shear and the interaction of the vertical distributions of the variance σ^2 and vertical diffusivity D_y. In the first case a single distribution $\theta_1(\eta)$ can be determined for any given experiment using Eq. 5.10. In the second, $\theta(\eta)$ is evaluated for each ξ using Eq. 5.14. In general the shape of $\theta(\eta)$ varies with ξ depending on the vertical distribution of $\sigma^2(\eta)$ at corresponding ξ. However, if the variation of $\sigma^2(\eta)$ with depth is similar at all ξ, then with successive increment in ξ, $\theta(\eta)$ increases at high values of η and diminishes at low η. Indeed θ can attain a negative value which would mean that at the particular ξ the interaction between D_y and $\sigma^2(\eta)$ has dominated the effect of shear, and there is a resultant transfer of material vertically to adjacent layers. The depth mean value of θ calculated at each ξ agreed closely with $\overline{\theta}$ determined for the entire run using Eq. 5.5.

5.E. NEAR-SOURCE VERTICAL DISTRIBUTION OF TRACER DUE TO SHEAR AND THE VERTICAL DIFFUSIVITY

As outlined in Chapter 2 and illustrated in Figure 2.2, the vertical distribution of material within the plume is strongly skewed very near the source. This is due to the non-uniform vertical distributions of the flow velocity u, and of the vertical diffusivity D_y. To evaluate the resultant vertical distribution of the tracer concentration along any vertical plane parallel to the plume axis, one must solve Eq. 2.44. As explained earlier analytical solutions have proved inadequate.

A numerical solution,* however, has been performed for the case of a continuous line source placed laterally at any selected depth, η_h. Since the line source is a superposition of an infinite number of point sources along a lateral line, this solution is equivalent to the solution of Eq. 2.44 integrated with respect to z. The result is an elimination of the effect of D_z with Eq. 2.44 reduced to

$$u(y) \frac{\partial M_0}{\partial x} = \frac{\partial}{\partial y}\left(D_y \frac{\partial M_0}{\partial y}\right) . \tag{5.15}$$

where $M_0 = \int_{-\infty}^{\infty} C \, dz$. Eq. 5.15 was solved numerically with the logarithmic velocity distribution of Eq. 2.33, and the parabolic variation of D_y expressed in the form of Eq. 2.51. The initial condition was:

$$M_0(0,\eta) = \frac{Q_s}{\bar{u}d} \delta(\eta - \eta_h), \tag{5.16}$$

and the boundary conditions,

$$\frac{\partial M_0}{\partial \eta}(\xi,0) = 0 , \tag{5.17}$$

and

$$\frac{\partial M_0}{\partial \eta}(\xi,1) = 0 . \tag{5.18}$$

---

*Coudert, J. F., "A Numerical Solution of the Two-Dimensional Diffusion Equation in a Shear Flow with Variable Diffusion Coefficient--Case of a Steady Line Source in a Stream," W. M. Keck Lab. of Hyd. and Water Res., Tech. Memo. 70-7,. California Institute of Technology, Pasadena, California, 1970.

The numerical program has been applied to RUNS 509 and 510 where the injection levels η_h were, respectively, 0.368 and 0.632. Using the experimental values of η_h, $\bar{u}$, u_*, κ, and d for each run, theoretical values of

$$\overline{M}_0(\xi,\eta) = \frac{M_0(\xi,\eta)}{Q_s/\bar{u}d} \tag{5.19}$$

were calculated for values of ξ where measurements were made. From continuity,

$$\int_0^1 M_0(\xi,\eta)\, d\eta = 1.0. \tag{5.20}$$

The results of numerical calculations and the measurements are plotted in Figure 5.14. For each run the forcing functions $D_y(\eta)/u_*d$ and $u(\eta)/u_*$, and the theoretical distributions of $M_0(\xi,\eta)$ are drawn for successive distances ξ = 1.0, 8.2, 17.7, 36.7, 55.9, 75.1, 102.7, and 144.1. For comparison, points determined from experiments are plotted for the values of ξ where measurements were made.

Agreement between the numerical solution and the experimental measurements was very close. Both showed that the vertical distribution of $\overline{M}_0(\xi,\eta)$ was skewed for $0 < \xi \leq 17.7$, with the level of maximum $\overline{M}_0(\xi,\eta)$ rising with increasing ξ for RUN 510 where $\eta_h = 1 - 1/e = 0.632$, and falling with increasing ξ for RUN 509 where $\eta_h = 1/e = 0.368$. Beyond $\xi = 35.7$, there was very little vertical variation of $\overline{M}_0(\xi,\eta)$ (mean deviation $\approx 5\%$), and material

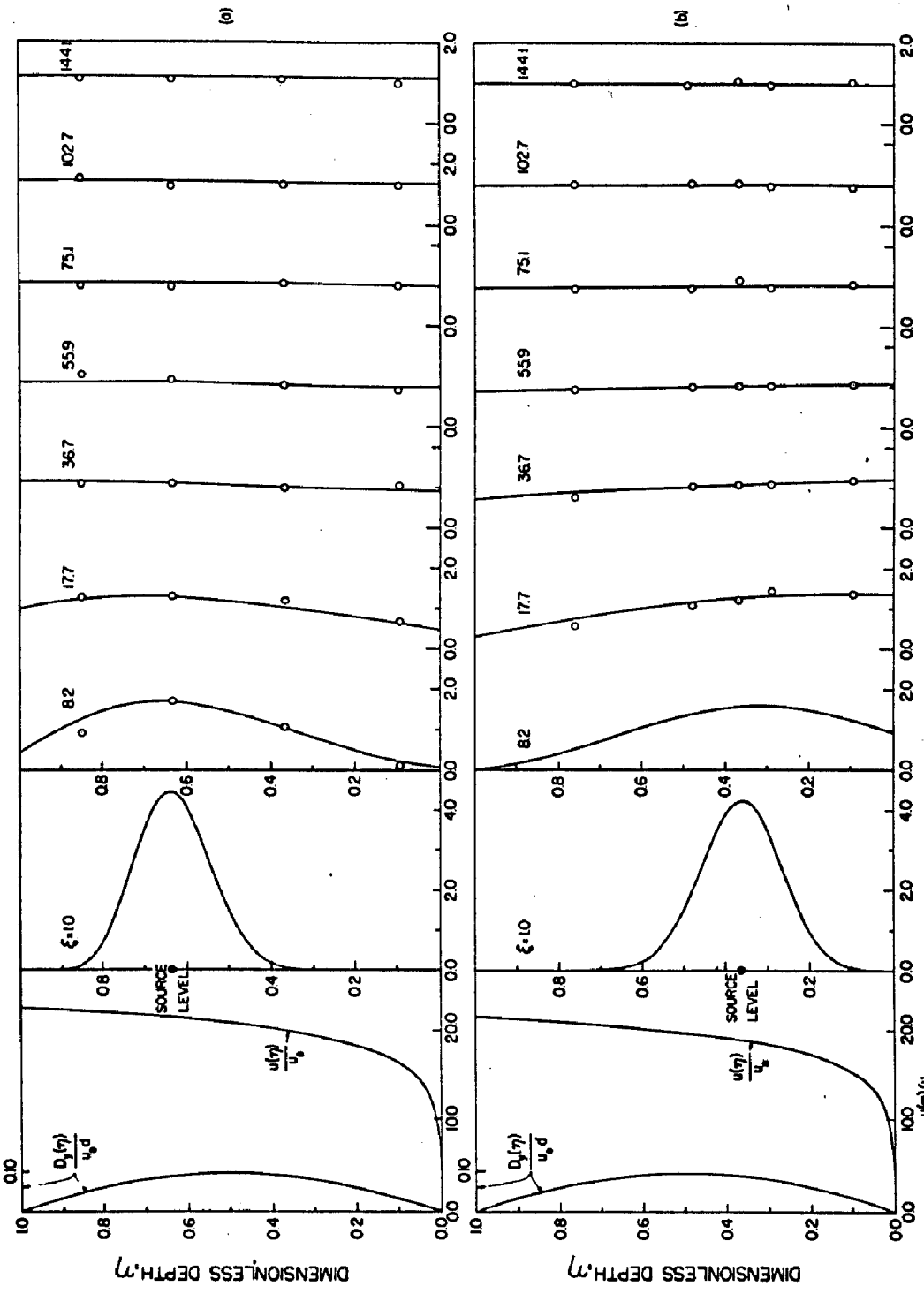

Fig. 5.14. Vertical distribution of material $\overline{M}_0(\xi,\eta) = M_0(\xi,\eta)/(Q_s/\overline{ud})$ for (a) RUN 510 and (b) RUN 509. The curves are theoretical solutions of Eq. 5.15 at various ξ. The plotted points were measured.

distribution was essentially uniform with depth for both runs.

Figure 5.15 shows the plots of curves describing the levels of maximum $\overline{M}_0(\xi,\eta)$ as calculated by the numerical analysis for four levels of tracer injection. Theoretically the point of maximum $\overline{M}_0(\xi,\eta)$ reached the water surface at $\xi \approx 9.0$ for $\eta_h = 0.850$, and at $\xi \approx 31.0$ for $\eta_h = 0.632$, and fell to the flume bottom at $\xi = 5.0$ for $\eta_h = 0.095$, and at $\xi = 19.0$ for $\eta_h = 0.368$. Thus the point of maximum $M_0(\xi,\eta)$ arrived at the flow bottom for small η faster than it rose to the water surface at high η. This is of course due to the fact that near the flume bottom, shearing is strong and $u(\eta)$ decreases rapidly with decreasing η. Thus near the bed both shear and the variation in vertical diffusivity combine to accelerate the fall in the center of mass of the plume. Near the water surface, however, $u(\eta)$ is nearly uniform with depth and the contribution due to shear is substantially reduced.

Figure 5.15 also shows plots of experimentally determined levels of maximum $M_0(\xi,\eta)$ for corresponding runs. It is evident that indeed there was a general trend in the direction predicted by theory. However after the locus of maximum values of $\overline{M}_0(\xi,\eta)$ reached the free surface or the lower solid boundary, it seemed to "bounce" back into the flow interior. This phenomenon was measured for all runs except RUN 512 ($\eta_h = 0.850$) where the level of maximum $\overline{M}_0(\xi,\eta)$ rose at a rate slower than theoretically predicted but once reaching the water surface remained there for larger ξ. The apparent bounce back feature is probably a result

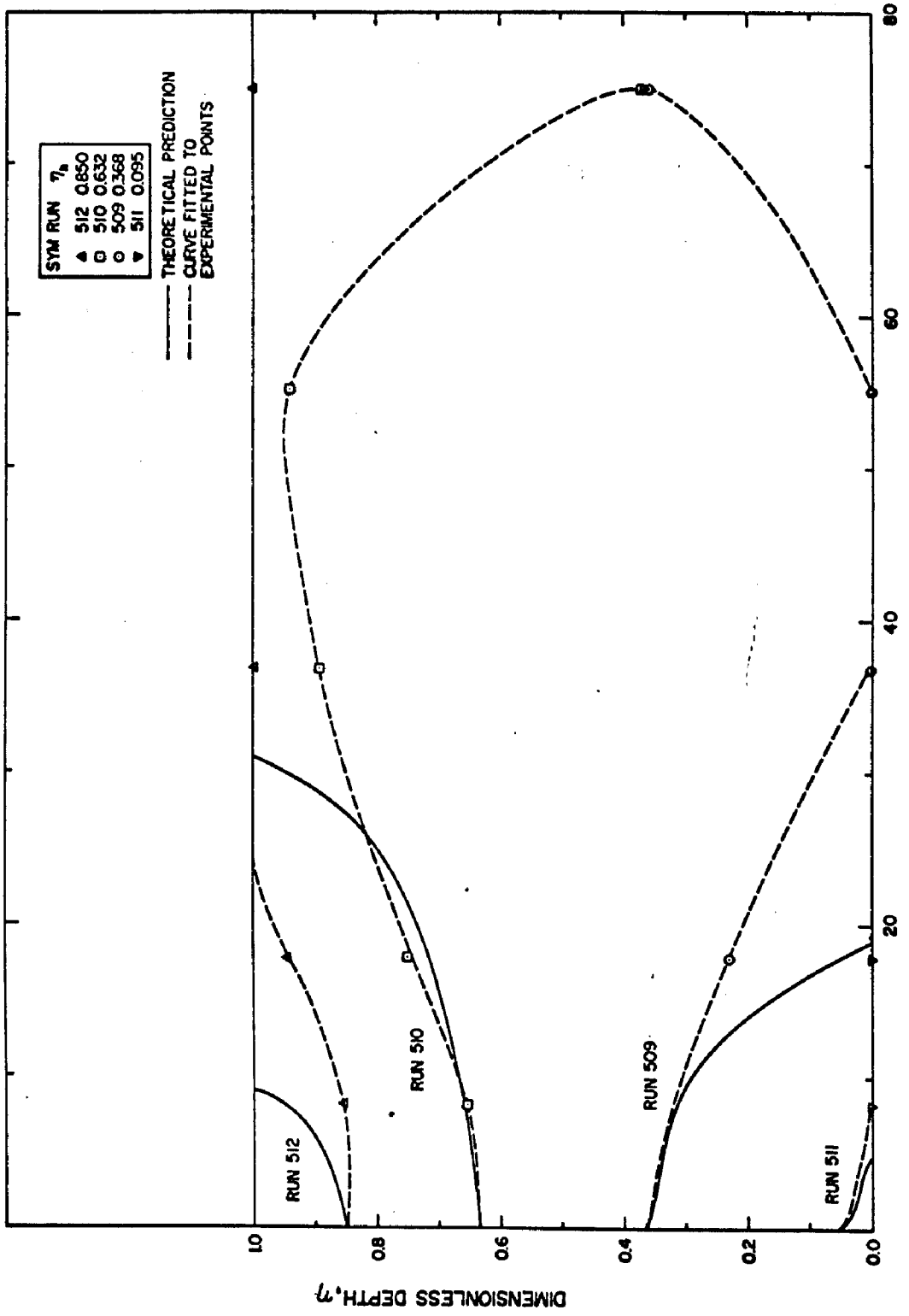

Fig. 5.15. Theoretical levels of maximum $\overline{M}_0(\xi, \eta)$ for four levels of tracer injection η_h. The plotted points were measured; RUNS 512, 510, 509, 511

of secondary current which at large ξ is strong enough to overcome the gradient $\partial\overline{M}_0/\partial\eta$ which approaches zero with increasing ξ. The phenomenon was also measured by Davar (9) for a plume generated by a point source of gases within the wall boundary layer of a wind tunnel.

5.F. DISTRIBUTION OF THE TRACER CONCENTRATION $C(\xi,\eta,0)$ ALONG THE AXIAL PLANE

F.5.1. Vertical Distribution of $C(\xi,\eta,0)$ at Various ξ. Since the concentration of tracer along the plume axis was generally equal to the maximum value of the time-averaged concentration C, it will be assumed that

$$C(\xi,\eta,0) = C_{max}(\xi,\eta,\zeta) \tag{5.21}$$

where C_{max} = maximum value of C at ξ and η, and $\zeta = z/d$. A dimensionless variable $\beta(\xi,\eta)$ is defined such that

$$\beta(\xi,\eta) = \frac{C(\xi,\eta,0)}{Q_s/W\overline{u}d}\,. \tag{5.22}$$

To visualize the depth variation of tracer concentration on the vertical axial plane, values of β calculated from measurements were plotted as functions of η at several ξ. In contrast to the close agreement between the experimental and theoretical distributions of $\overline{M}_0(\xi,\eta)$ shown in Figure 5.14, curves fitted to measured $\beta(\xi,\eta)$ at low ξ, were generally different from those of $\overline{M}_0(\xi,\eta)$ predicted by theory. This is, of course, a reflection of the difference in the rates of transverse mixing at various levels of the flow. Since measurements have demonstrated that the transverse distribution of C is

Gaussian at all ξ and η (see for example Figure 5.1), combination of Eqs. 5.19 and 5.22 and the Gaussian distribution of C results, for given ξ and η, in the relationship

$$\overline{M}_0(\xi,\eta) = \sqrt{2\pi}\,\frac{\sigma(\xi,\eta)}{W}\,\beta(\xi,\eta)\,, \qquad (5.23)$$

where $\sigma(\xi,\eta)$ = standard deviation of the transverse distribution of C at the given ξ and η. Vertical profiles of $\beta(\xi,\eta)$ are, therefore, the same as those of $\overline{M}_0(\xi,\eta)$ modified by the variation of $\sigma(\xi,\eta)$.

It was found that regardless of the modification of $\overline{M}_0(\xi,\eta)$ due to $\sigma(\xi,\eta)$, the level of maximum $\beta(\xi,\eta)$ also rose or fell exactly as in the measured values of $M_0(\xi,\eta)$ shown in Figure 5.15. The "bouncing" phenomenon was also measured at identical stations.

5.F.2. Longitudinal Attenuation of the Tracer Concentration Along the Plume Axis. Figures 5.16 through 5.19 show the attenuation of tracer concentration, expressed as $\beta(\xi,\eta)$, along the plume axis and at different levels of the flow for the injection level η_h = 0.850, 0.632, 0.368, and 0.051 respectively. The curves are extrapolated beyond ξ = 8.2 for $\xi \rightarrow 0.0$. The plots show that very near the source, the decay rates were vastly different at various levels of the flow. At all levels except η_h, $\beta(\xi,\eta)$ initially increased with ξ and then diminished with further increase of ξ. At distances greater than a critical value denoted as ξ_a, the concentration decayed at a constant power of ξ at all values of η for any given experiment. Therefore the depth-averaged value $\overline{\beta}(\xi)$ was expressed as

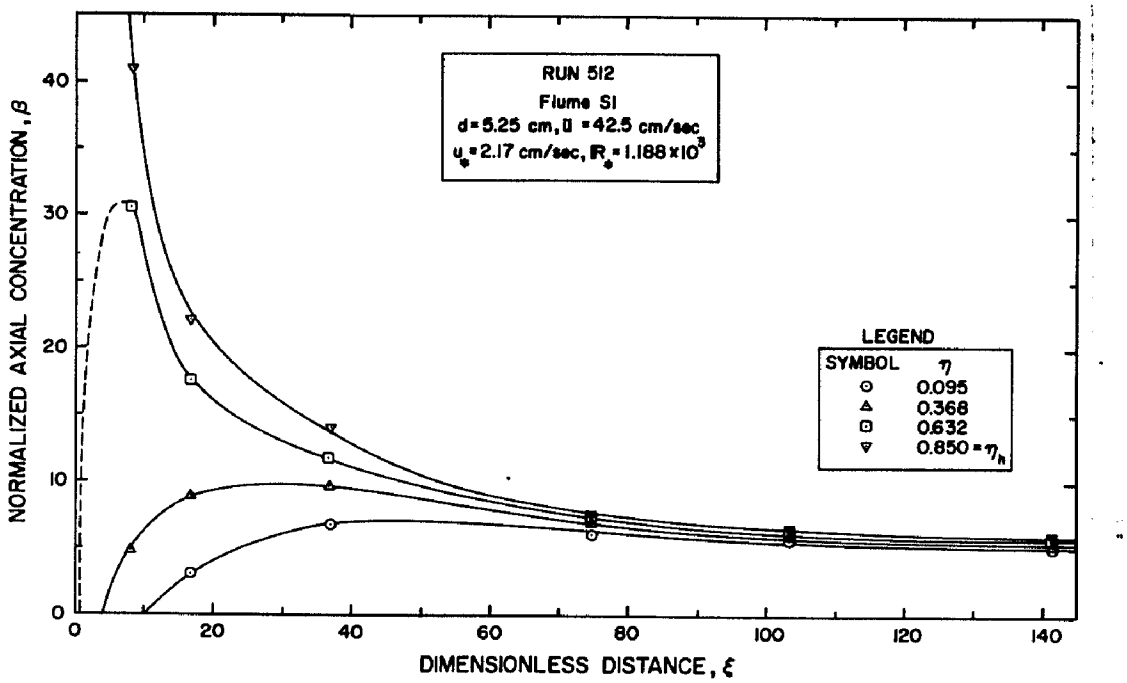

Fig. 5.16. Attenuation of the normalized tracer concentration β at four levels of the flow η on the vertical axial plane; RUN 512, $\eta_h = 0.850$

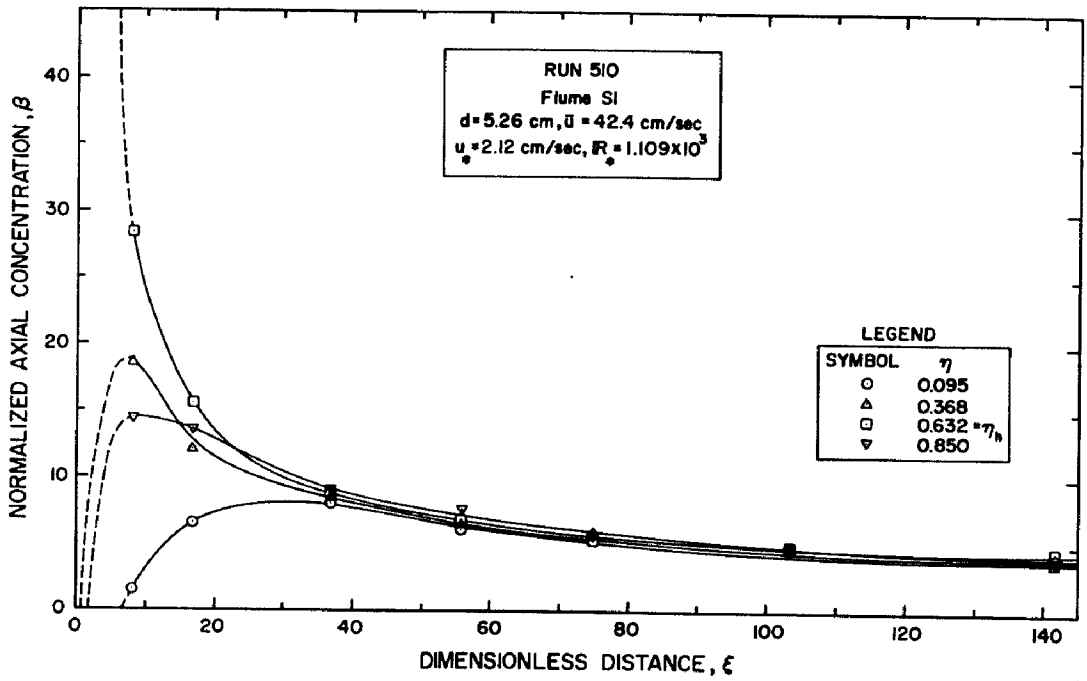

Fig. 5.17. Attenuation of the normalized tracer concentration β at four levels of the flow η on the vertical axial plane; RUN 510, $\eta_h = 0.632$

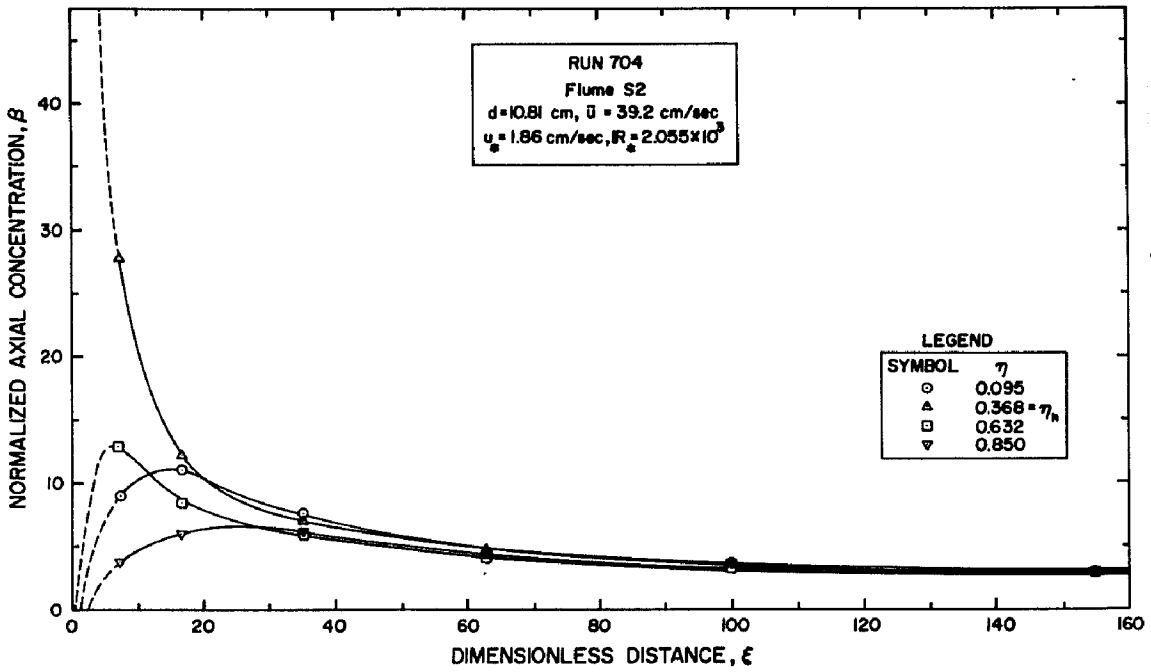

Fig. 5.18. Attenuation of the normalized tracer concentration β at four levels of the flow η on the vertical axial plane; RUN 704, $\eta_h = 0.368$

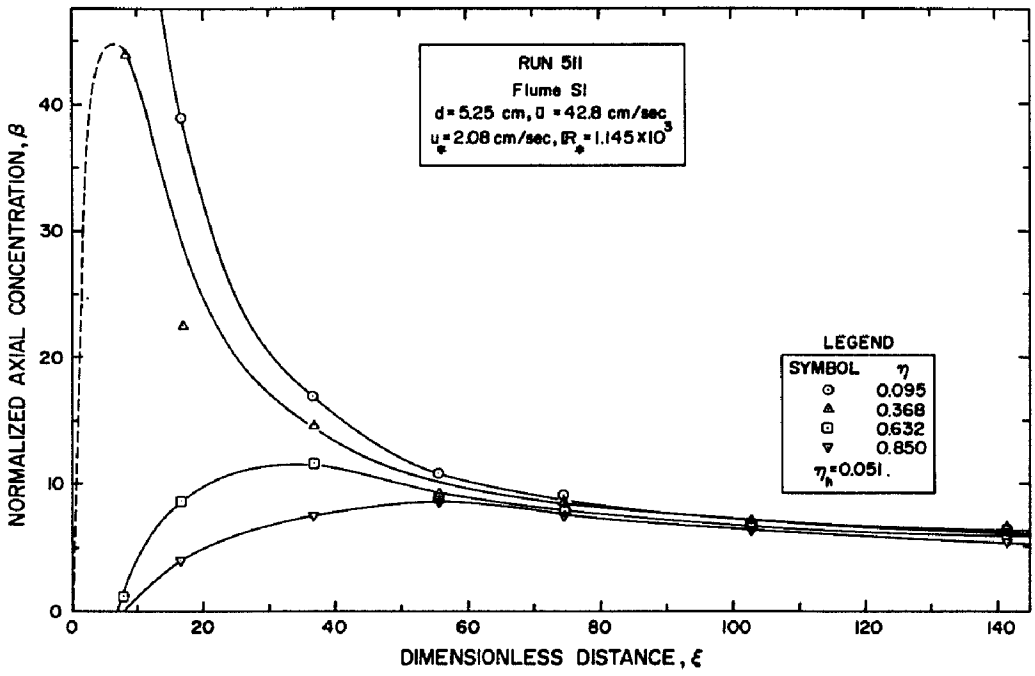

Fig. 5.19. Attenuation of the normalized tracer concentration β at four levels of the flow η on the vertical axial plane; RUN 511, $\eta_h = 0.051$

$$\bar{\beta}(\xi) \propto \xi^{-\alpha}, \tag{5.24}$$

where α = constant. Figures 5.16 through 5.19 show, as expected, that ξ_a was smallest when the source was located near the flow mid-depth.

To evaluate the asymptotic decay rate, the depth mean value of $\beta(\xi,\eta)$, designated as $\bar{\beta}(\xi)$, was calculated at various distances ξ. A log-log plot of $\bar{\beta}(\xi)$ versus ξ was developed and for each experiment, the slope of the straight line fitted to the points equalled α. To estimate ξ_a, an imaginary line was drawn at a tangent to the fitted straight line to the first point, in the neighborhood of $\xi = 0$, which deviated more than 20% from the fitted asymptote. The value of ξ at the point of tangency was used as ξ_a.

Figure 5.20 shows plots of $\bar{\beta}$ versus ξ for RUNS 512, 704, 511 and 510. In the accompanying legend the flow depths d, levels of tracer injection η_h, and exponents of the decay curve α are shown. Points of ξ_a are indicated on the plots. It is evident that the points plotted very close to the fitted straight lines and that ξ_a is relatively small regardless of the flow depth or the level of tracer injection.

Table 5.5 summarizes the values of ξ_a and α for the twenty experiments where measurements were made at two or more levels of the flow. The flow depths covered ranged from 1.69 to 21.97 cm. The table includes hydraulic data tabulated in Columns 1 through 3, the level of tracer injection in Column 6 and in Column 7,

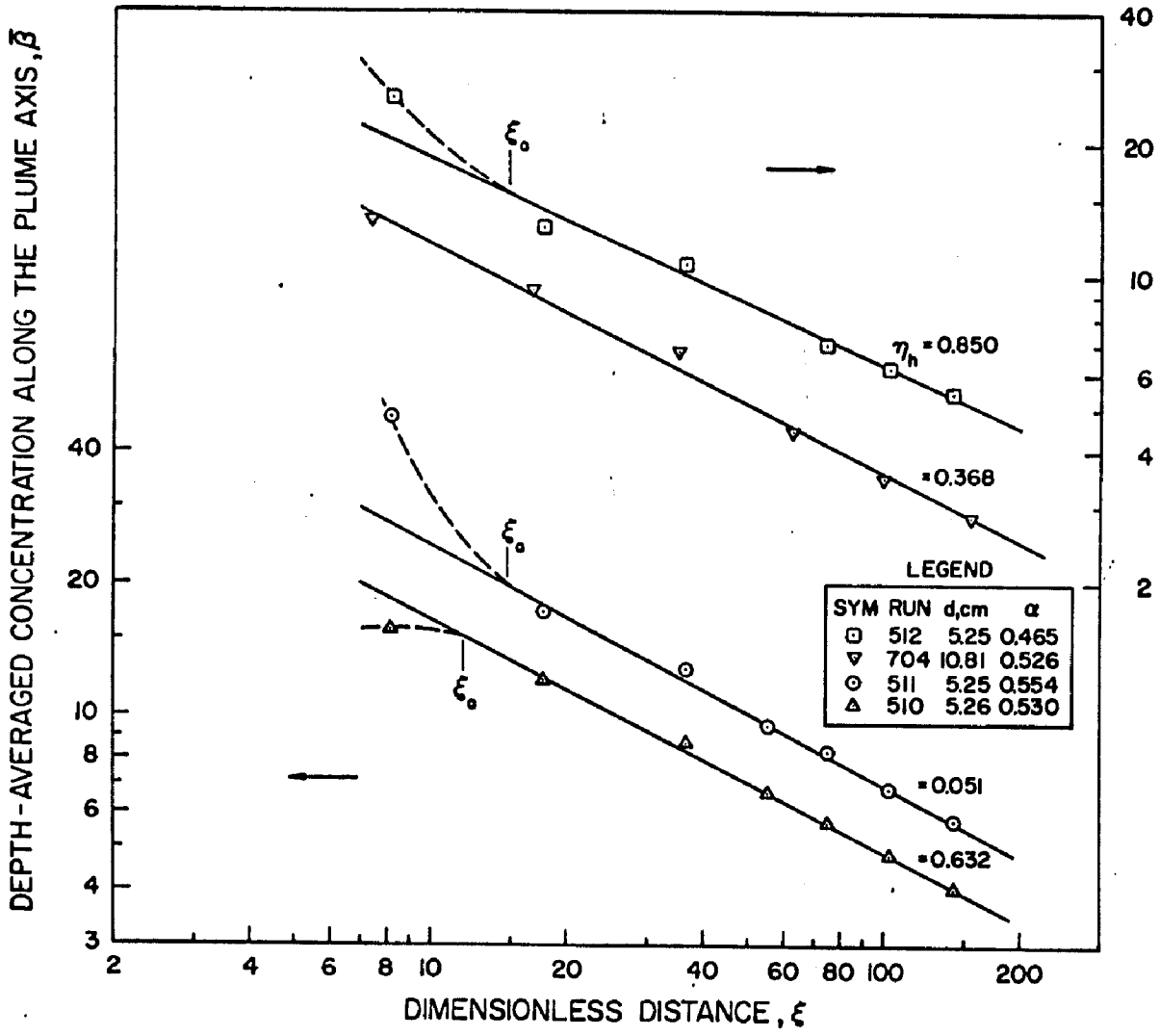

Fig. 5.20. Attenuation of the depth-averaged concentration $\bar{\beta}$ on the vertical axial plane for four levels of tracer injection; RUNS 512, 704, 511, 510

Table 5.5 Summary of measured parameters related to the decay of tracer concentration along z=0.

RUN	Flume Identif. Code *	Flow Depth d cm	Tracer Injection Level η_h	ξ_ℓ §	ξ_a †	Decay Exponent α †	RUN
1	2	3	4	5	6	7	1
705	S2	1.69	0.368	60.0	55.1	0.452	705
706	S2	2.75	0.368	14.5	25.4	0.519	706
707	S2	2.74	0.368	0.0	24.8	0.472	707
506	S1	2.95	0.368	0.0	40.7	0.414	506
703	S2	3.46	0.368	0.0	39.0	0.506	703
509	S1	5.25	0.368	0.0	18.0	0.545	509
511	S1	5.25	0.051	5.3	14.8	0.554	511
512	S1	5.25	0.850	6.3	14.5	0.465	512
508	S1	5.26	0.368	0.0	15.2	0.447	508
510	S1	5.26	0.632	3.4	11.9	0.530	510
702	S2	5.41	0.129	8.1	18.1	0.536	702
701	S2	5.53	0.391	9.0	9.8	0.563	701
607	S1	10.70	0.368	7.8	8.7	0.480	607
704	S2	10.81	0.368	0.0	12.9	0.526	704
708	S2	17.31	0.368	2.9	4.7	0.526	708
603	S1	17.34	0.368	2.2	3.7	0.602	603
709	S2	21.97	0.368	3.5	3.6	0.650	709
407	R2	8.66	0.368	8.1	11.5	0.601	407
404	R2	10.36	0.368	5.8	15.5	0.610	404
406	R2	17.07	0.368	0.0	8.8	0.676	406

NOTES:

* S=smooth; R=rough; 1=85-cm flume; 2=110-cm flume.

§ ξ_ℓ=value of ξ beyond which $\overline{\sigma^2}$ grows linearly with ξ.

† ξ_a=value of ξ beyond which $\overline{\beta}(\xi)$ decays at a constant rate. For $\xi \geq \xi_a$, $\overline{\beta}(\xi) \sim \xi^{-\alpha}$.

the normalized distance ξ_ℓ beyond which $\overline{\sigma^2}$ grew linearly with ξ. In all cases ξ_a was greater than ξ_ℓ, with $\xi_\ell = 0.0$ in several experiments. The average value of ξ_ℓ for $d \geq 2.75$ cm was 4.1. For $d = 1.69$ cm, $\xi_\ell = 60.0$. The average value of ξ_a was 18.3 decreasing from a high of 55.1 for the lowest depth to a low of 3.6 for the deepest flow where $d = 21.97$ cm. For a given flow, ξ_a was generally smaller when tracer was injected near the mid-depth than when η_h was near the water surface or the bottom boundary.

The rate of attenuation of $\overline{\beta}(\xi)$, in general, was highest when d was greatest. Where the flow depth was about 2 cm, $\alpha \approx 0.46$. However when $d \approx 20$ cm, $\alpha \approx 0.60$. The decay rate was also high when the flume bottom was roughened with rocks. Thus for RUNS 404 and 704 where the flow depths were 10.36 cm and 10.81 cm respectively, α was 0.610 for RUN 404 with the rough bottom and 0.526 for RUN 704 for the flume with hydraulically smooth boundaries. The average value of α for all experiments was 0.534 indicating a decay rate of $\overline{\beta}(\xi)$ slightly greater than the $(-\frac{1}{2})$-power predicted by Eq. 2.62 for one-dimensional transverse mixing.

This means that although $\overline{\sigma^2}$ grew linearly with x (since $\xi_a > \xi_\ell$), the depth mean concentration along $z = 0$ decayed at a rate controlled by both transverse and vertical mixing. For a two-dimensional model in which concentration distribution is Gaussian in both lateral and vertical directions with $y = z = 0$ coincident with the mode of the distribution, the continuity equation predicts that

$$\beta(\xi) \sim (D_y D_z)^{-\frac{1}{2}}/\xi,$$

where D_y, D_z are the mixing coefficients in the y and z directions respectively. Thus if both D_y and D_z are constant, $\beta(\xi) \propto \xi^{-1}$. This means that mixing in the two directions causes a decay rate exponent of ξ twice that for one-dimensional mixing. As the vertical distribution of tracer varies from uniform to Gaussian, α increases from 0.50 to 1.00. Realization of a value of α greater than 0.50 is believed therefore to be a result of the two-dimensionality of the mixing process. Thus the greater the flow depth the larger is α as indicated in Table 5.5. Roughening of the flume bottom intensified mixing and accelerated the decay in the concentration along the plume axis. Hence α is larger when the flume bottom was roughened with rocks than when it was smooth.

To estimate the error involved in the use of Eq. 2.62 for computation of the transverse mixing coefficient, RUN 702 for which $\alpha = 0.536$ was selected. This run was chosen because its measured value of α was very close to the mean value for all experiments which was 0.534. Using the value of $\overline{\beta}(\xi)$ measured at $\xi = 200$, and assuming that $\beta(\xi) \sim \xi^{-0.50}$, a depth-averaged cross-wise mixing coefficient was calculated by use of Eq. 2.62 and found to be 1.58 cm^2/sec. As expected this was less than the value of 1.62 cm^2/sec determined from the linear growth of the depth-averaged variance expressed in Eq. 5.5. The error incurred, however, was only -2.5%. Thus for an increase in α from 0.500 to 0.536 (a change of about 7%), the error involved in predicting $\overline{D}_z$ by the one-dimensional model was only -2.5%.

5.G. ISO-CONCENTRATION MAPS

5.G.1. Tracer Distribution on Cross-sectional Planes.

Figures 5.21, 5.22, and 5.23 show the distribution of tracer on cross-sectional planes for the injection levels $\eta_h = 0.051$, 0.368, and 0.850 respectively. The flow depth d was 5.25 cm for the three cases. The iso-concentration contours were obtained from curves of C versus z measured at four levels of the flow and six or seven stations from the source. The crosses shown on the plots are points where tracer concentration was measured. Concentration values shown on the contour lines are in arbitrary units. Multiplication of these values by α_c, also given for each figure, reduces them to dimensionless values of the form expressed in Eq. 5.22.

The iso-concentration maps clearly demonstrate the effect of η_h in the concentration distribution within the plume. In Figure 5.21 where $\eta_h = 0.051$, the core of maximum concentration quickly dropped to the flume bottom. As $x \geq 543$ cm, tracer distribution became approximately uniform with depth and the level of maximum concentration was no longer easily discernible. When $\eta_h = 0.850$, however, the peak concentration rose to the water surface generating basin-shaped contours which persisted for large x. As shown in Figure 5.23, concentration distribution was non-uniform even for $x = 743$ cm. As expected, injection of tracer near the mid-depth enhanced the attainment of uniform distribution with depth. Thus in Figure 5.22 where $\eta_h = 0.368$ the zone of maximum concentration initially sank to the flume bottom but then rebounded to near mid-

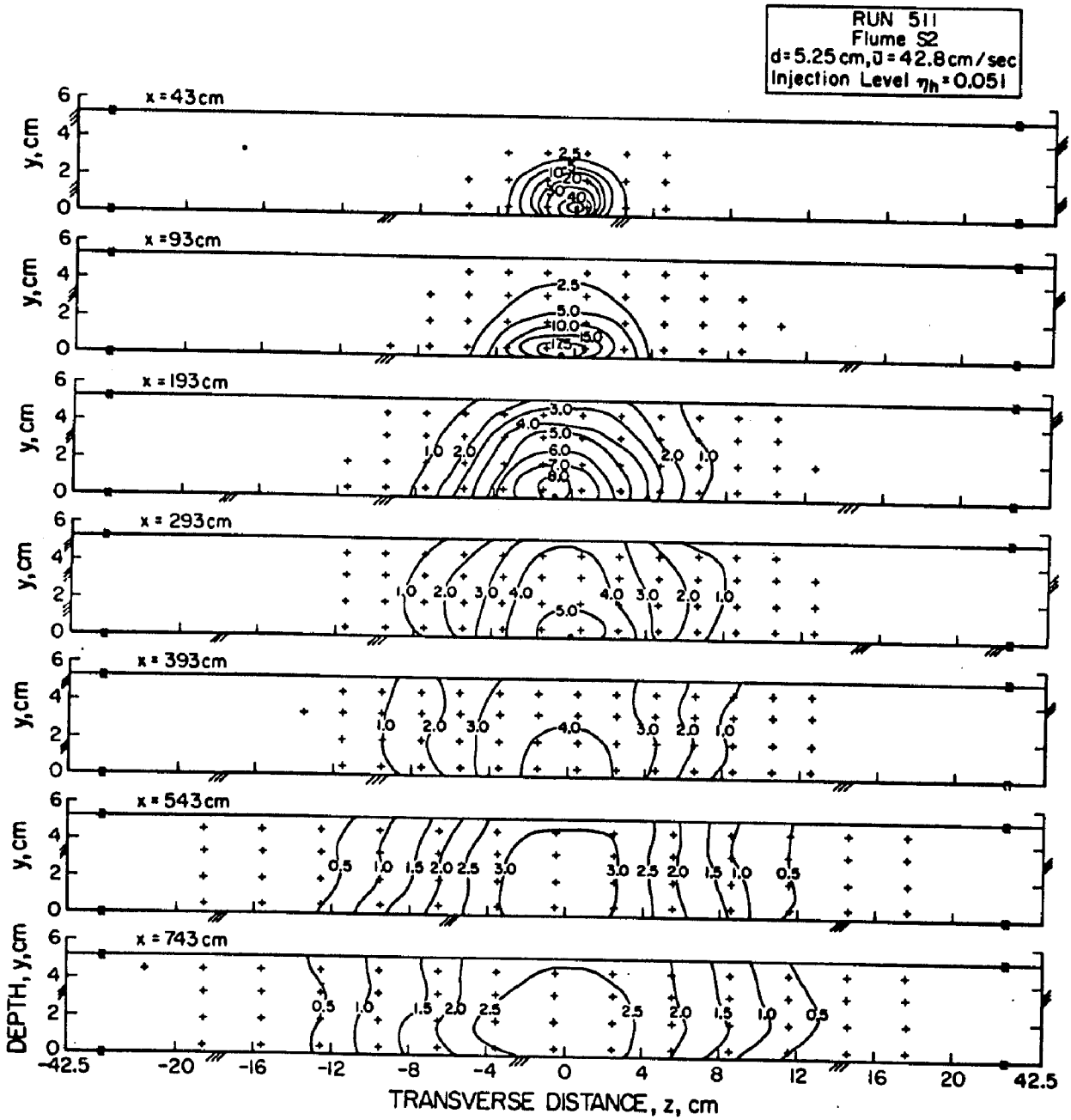

Fig. 5.21. Iso-concentration contours on cross-sectional planes. Crosses show points where tracer was detected. Concentration values on the contour lines are rendered dimensionless (as in Eq. 5.22) when multiplied by 2.08; RUN 511, $\eta_h = 0.051$

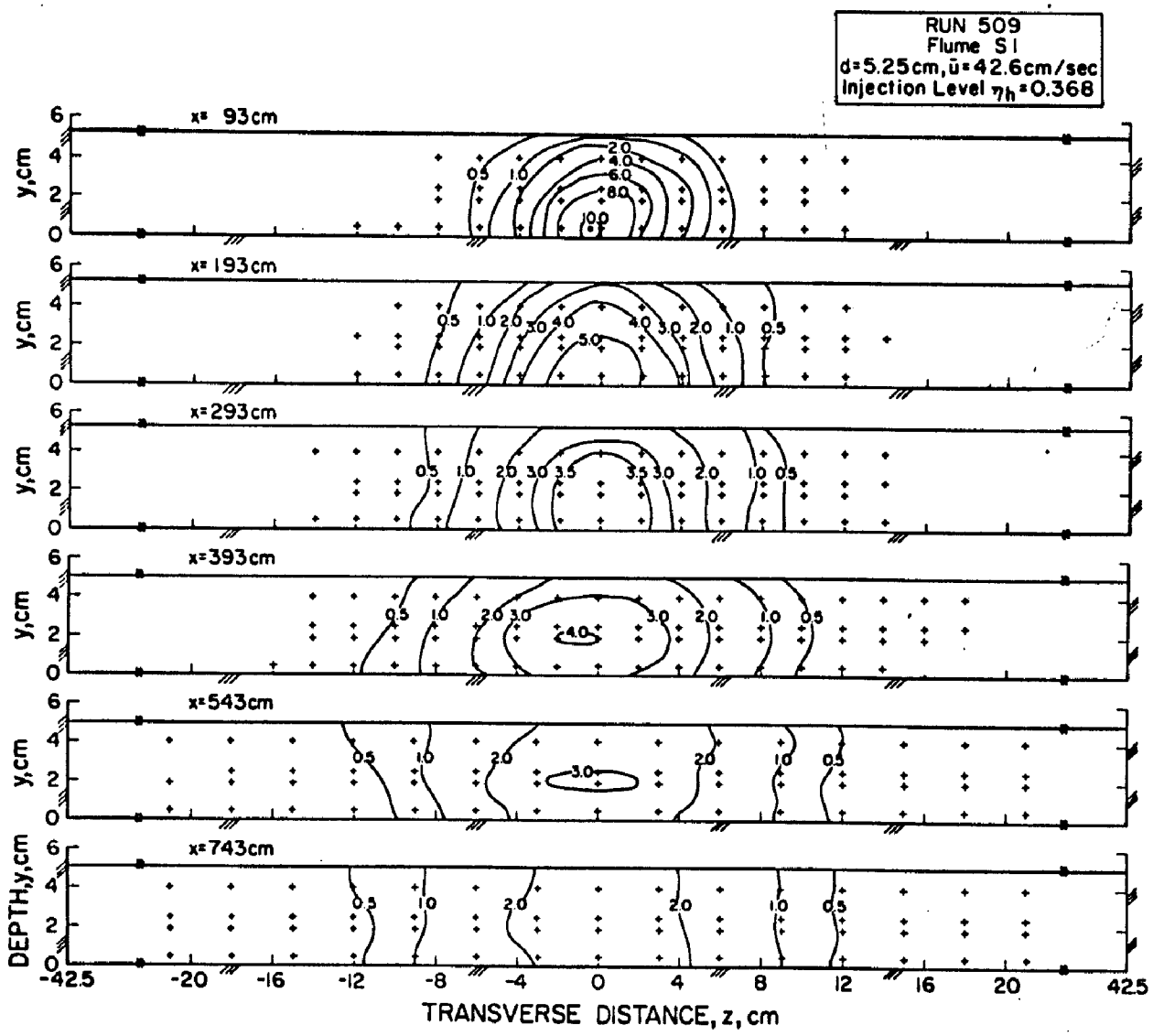

Fig. 5.22. Iso-concentration contours on cross-sectional planes. Crosses show points where tracer was detected. Concentration values on the contour lines are rendered dimensionless (as in Eq. 5.22) when multiplied by 1.56; RUN 509, $\eta_h = 0.368$

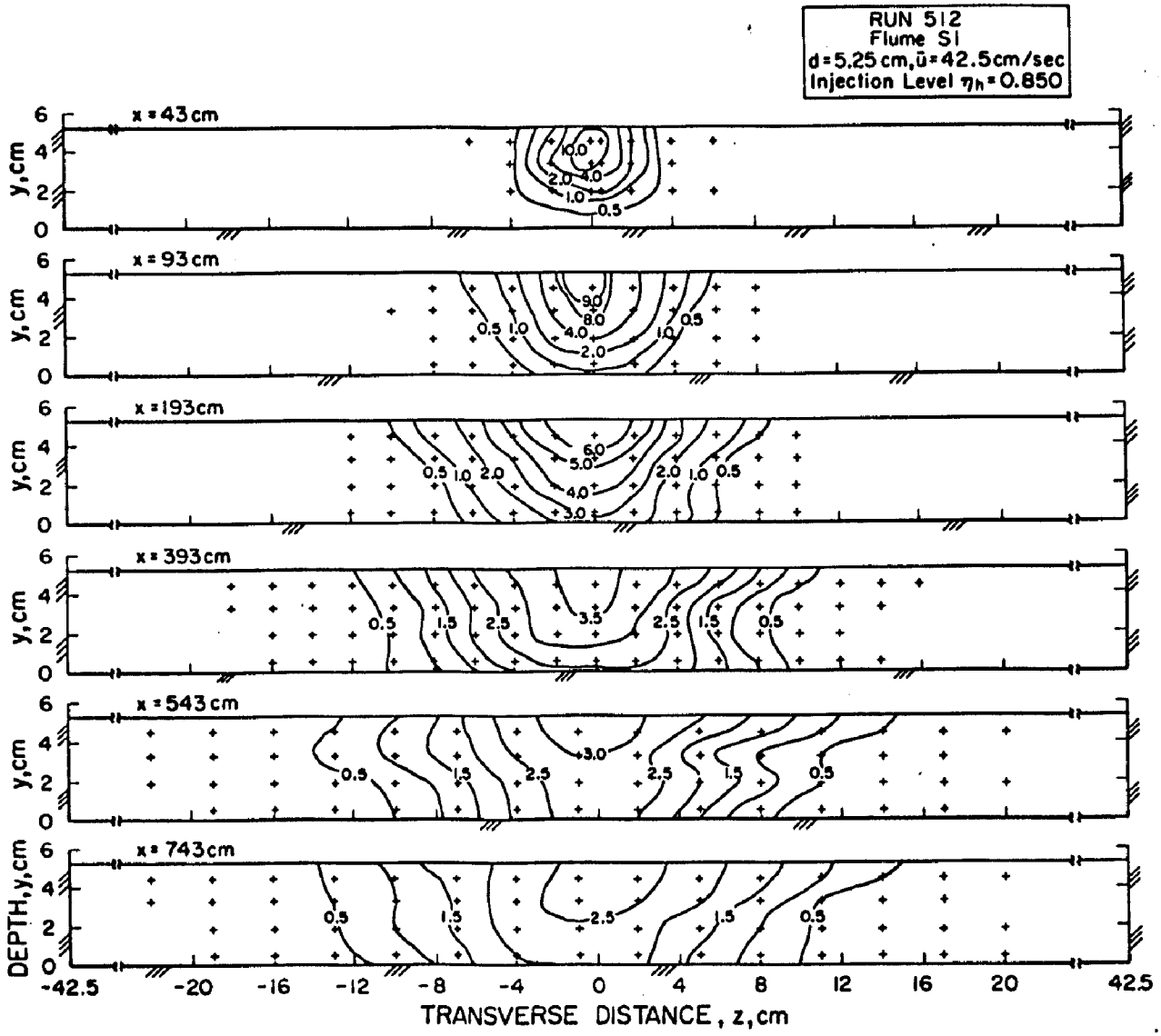

Fig. 5.23. Iso-concentration contours on cross-sectional planes. Crosses show points where tracer was detected. Concentration values on the contour lines are rendered dimensionless (as in Eq. 5.22) when multiplied by 2.11; RUN 512, $\eta_h = 0.850$

depth. Meanwhile the tracer mixed quickly over the flow depth giving rise to essentially vertical contour lines for $x \geq 543$ cm.

The iso-concentration contours of Figures 5.21 through 5.23, therefore, conform with the variation of $\overline{M}_0(\xi, \eta)$ discussed in Section 5.E. They also show that, on a given cross-sectional plane, the principal axes of the cloud are directed along the y and z axes. This indicates that at a fixed x, the z and y axes chosen in Chapter 2 for the description of the mixing process are indeed generally oriented in the principal directions. Consequently the mixing coefficient tensor can be diagonalized as stated in Chapter 2.

5.G.2. Tracer Distribution on Lateral Planes Parallel to the Flume Bottom. Iso-concentration contours were also constructed at planes parallel to the flume bottom, and located at the levels of the flume where tracer concentration was measured. Figure 5.24 shows a typical set of maps developed for RUN 512 at the four levels $\eta = 0.850$, 0.632, 0.368, and 0.095. The flow depth $d = 5.25$ cm, the flume width $W = 85$ cm, and the source was located at the flume center at the level $\eta_h = 0.850$. The conversion factor α_c for the concentration units shown on the contour lines is 2.11.

Figure 5.24 shows that, on each plane, iso-lines progressed from an elliptical distribution in the plume interior to near parabolic at the boundary as C decreased. At the level of tracer injection, the extreme contour line (in this case $C = 0.5$) was wedge-shaped for $x \leq 100$ cm, becoming parabolic for larger x. At other levels, however, the plume edge (i.e. $C = 0.50$) were essentially parabolic

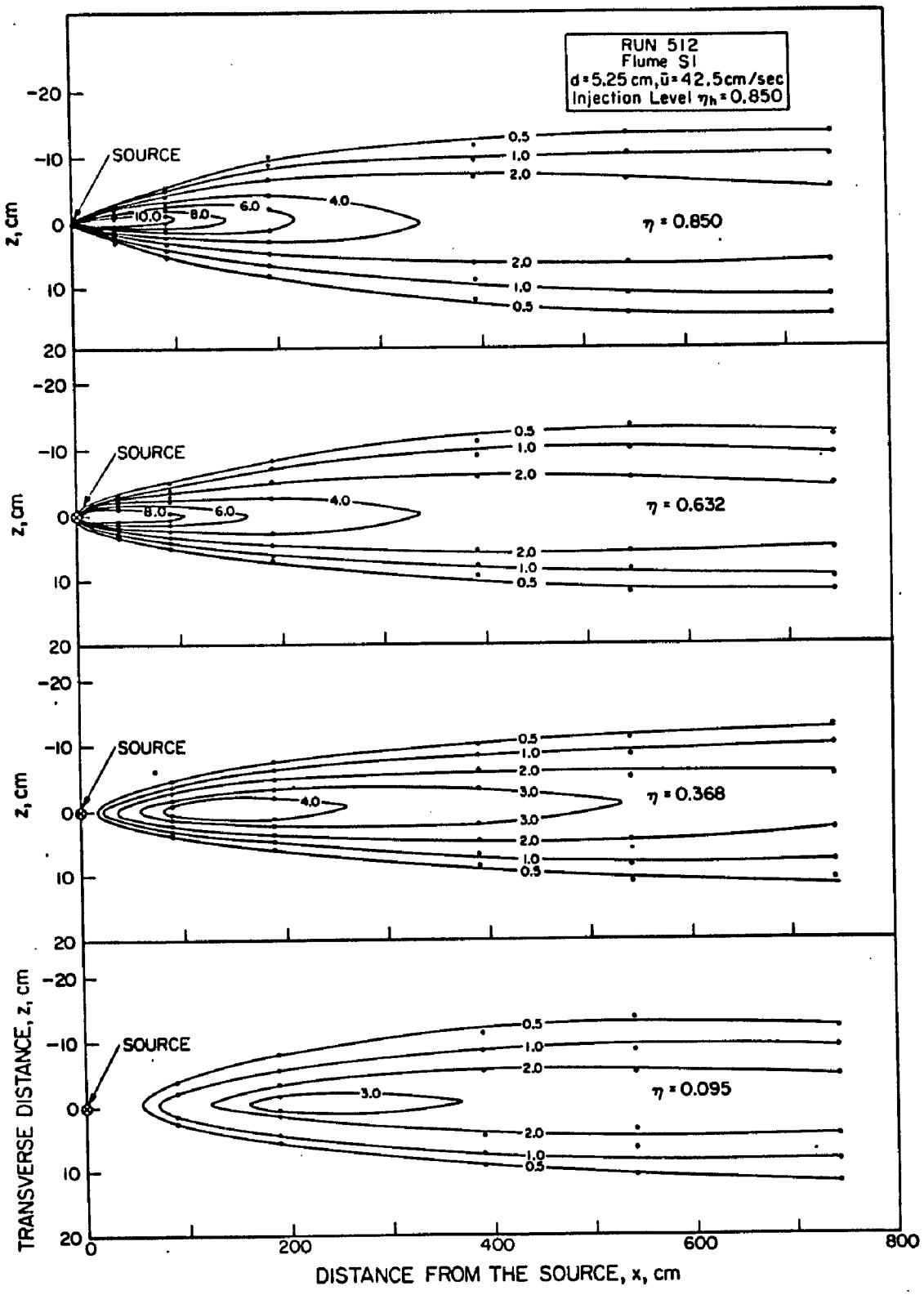

Fig. 5.24. Iso-concentration contours plotted on transverse planes (parallel to the flume bottom) at four levels of the flow. Concentration values on the contour lines are rendered dimensionless (as in Eq. 5.22) when multiplied by 2.11; RUN 512, $\eta_h = 0.850$

for $x \leq 743$ cm. It should be mentioned that all iso-lines of $C > 0$ will eventually revert to the plume axis at large x.

Further examination of Figure 5.24 reveals that the value of x at which tracer concentration was maximum on a given transverse plane increased from $x = 0$ for the plane $\eta = \eta_h = 0.850$ to approximately $x = 243$ cm for $\eta = 0.095$. If this distance is normalized by d and represented as ξ_m, then for a given η, ξ_m varies with the height of tracer injection η_h. Values of ξ_m were evaluated by interpolation from iso-concentration contours such as those shown in Figure 5.24. The results for three levels of tracer injection $\eta_h = 0.850$, 0.368, and 0.095, are plotted in Figure 5.25.

5.H. SUMMARY

This chapter has presented the results related to time-averaged concentration measurements. It has been shown that the transverse distribution of tracer for the continuous point source in a shear flow is Gaussian for ξ extending from 4 to 611. The variance of the distribution grows linearly with x both on fixed transverse planes and as a depth average. A coefficient of transverse mixing was calculated for various levels of the flow η and as a depth-integrated value $\overline{D}_z$. Measurements showed that $\overline{D}_z/u_* d$ is a decaying function of the aspect ratio of the flow, $\lambda = d/W$. Near source behavior of the plume agrees with theoretical prediction. Detailed distribution of tracer within the plume was illustrated with iso-concentration maps on cross-sectional and transverse planes.

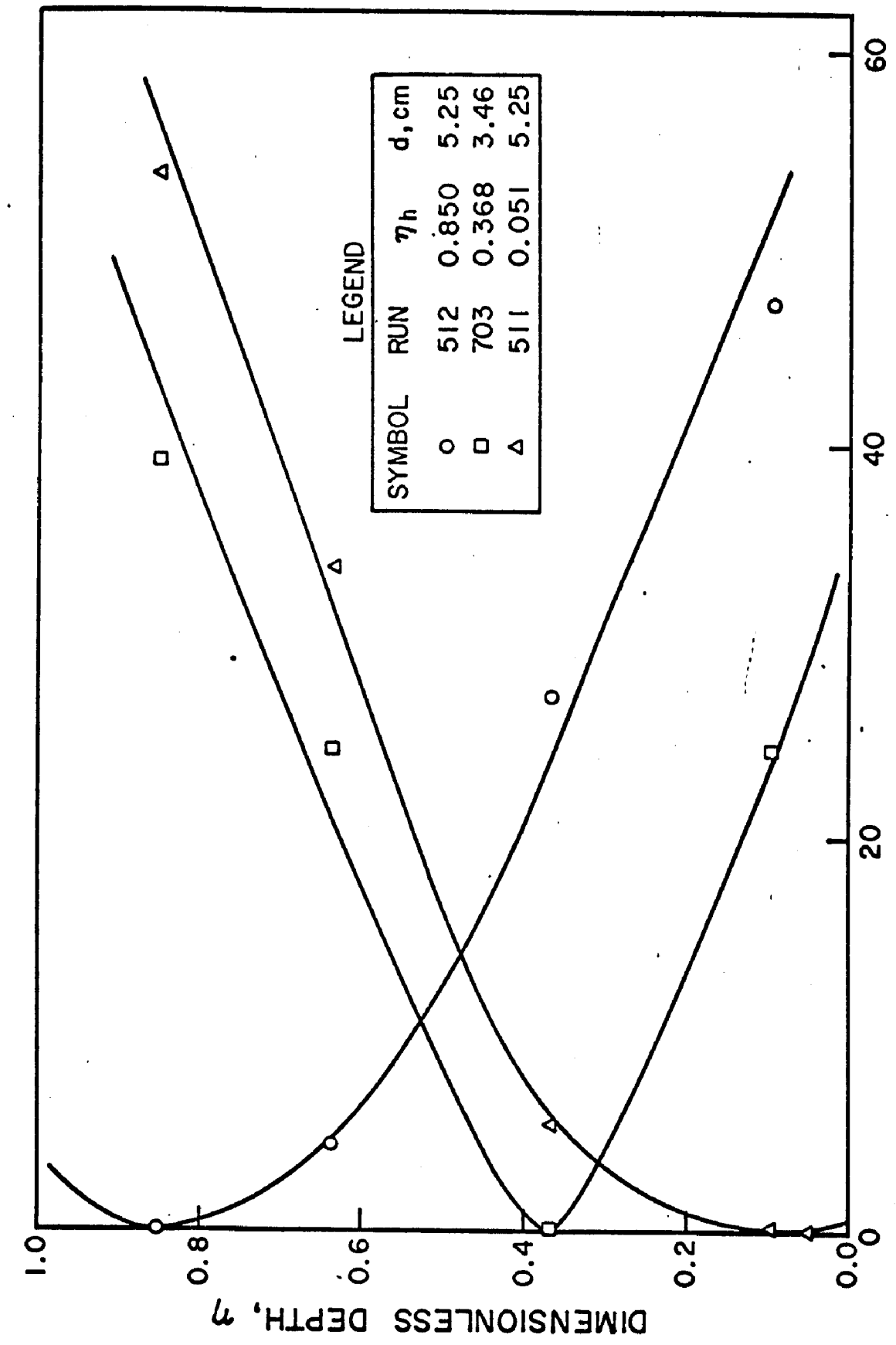

Fig. 5.25. Dimensionless distances ξ_m from the source where concentration is maximum at given levels of the flow η for injection levels η_h = 0.850, 0.368, and 0.095

The next step is to examine the contribution of the temporal variations of tracer concentration and of plume boundaries to the overall transverse mixing. Results of this phase are presented in the next chapter.

CHAPTER 6

PRESENTATION AND DISCUSSION OF EXPERIMENTAL RESULTS (Phase II)

This chapter summarizes the experimental investigation of the temporal fluctuations of concentration, as outlined in Chapter 3. First the fluctuating plume front model is assumed and the motion of the plume front was studied by use of the intermittency factor concept. Then the fluctuating plume model proposed by Gifford (16) was applied to the photo studies and the variances characterizing the motion of the plume centroid and the instantaneous concentration distributions were calculated. Finally the results of the statistical analyses of the variation of tracer concentration at fixed points within the plume are presented. A discussion of the results is included wherever appropriate.

6.A. PARAMETERS ASSOCIATED WITH THE PLUME FRONT OSCILLATION MODEL

6.A.1. The Transverse Distribution of the Intermittency Factor.

The intermittency factor, as defined by Eq. 3.32, indicates the fraction of the total sampling time that a fixed point is within a fluctuating plume. It is obtained by integrating the intermittency function $h(z,t)$ which is related to the concentration $c(z,t)$ as follows:

$$h(z,t) = \begin{cases} 1, & c(z,t) > C_t \\ 0, & c(z,t) \leq C_t \end{cases} \qquad (3.31)$$

where $c(z,t)$ is the instantaneous concentration at the point z, and

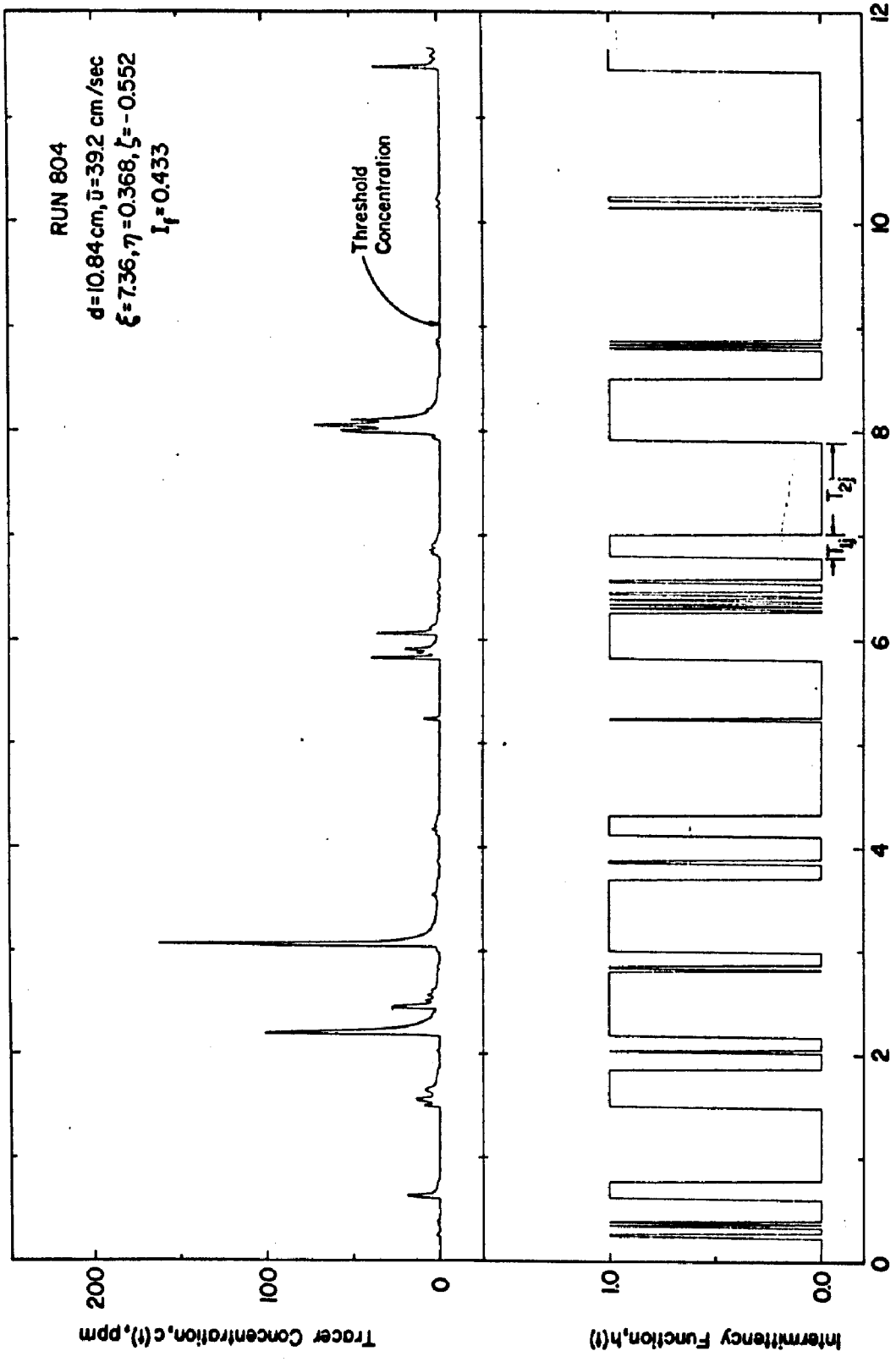

Fig. 6.1. Plots of digitized concentration data c(t) and the corresponding intermittency function, h(t). Sampling rate = 60 samples/sec. Typical periods of "occurrence" T_{1j} and "non-occurrence" T_{2j} are shown on H(t); RUN 804.

C_t is the threshold concentration. The threshold was chosen slightly (about 7×10^{-4} % of initial tracer concentration) above the mean background concentration to eliminate background noise and reduce the contribution due to the tails of the signals--a result of the finite response frequency of the detection system.

Figure 6.1 shows plots of a measured concentration signal c(t) recorded at a point within the plume. The corresponding intermittency function h(t) calculated for the same signal using Eq. 3.31 is shown directly below c(t). The intermittency factor I_f determined from 22 seconds of the data shown was 0.433. Also shown on the plot of h(t) are typical values of the period of occurrence T_{1j}, and the period of non-occurrence T_{2j} used for the calculation of probability densities $p_1(T_1)$ and $p_2(T_2)$ respectively.

Figure 6.2 illustrates the transverse distribution of I_f for three flow depths: d = 5.36, 10.84, and 17.07 cm corresponding to RUNS 802, 804, and 406 respectively. For each run the measurements were made on the lateral plane $\eta = \eta_h = 0.368$, and at distances x = 80, 180, 380, 780, 1180, and 1580 cm from the source. In general the plots were restricted to one side of the flow ($z < 0$) except for x = 80 cm where I_f was calculated for $-\infty < z < \infty$ in RUNS 802 and 804 to demonstrate the symmetry of $I_f(z)$ about z = 0. It is immediately evident that the $I_f(z)$-distribution was similar for all normal depths, and at all stations. The region of intermittency ($0 < I_f(z) < 1.0$) at a given distance from the source, however, increased with increasing depth, d.

That the fluctuation of the plume edge was accentuated by an

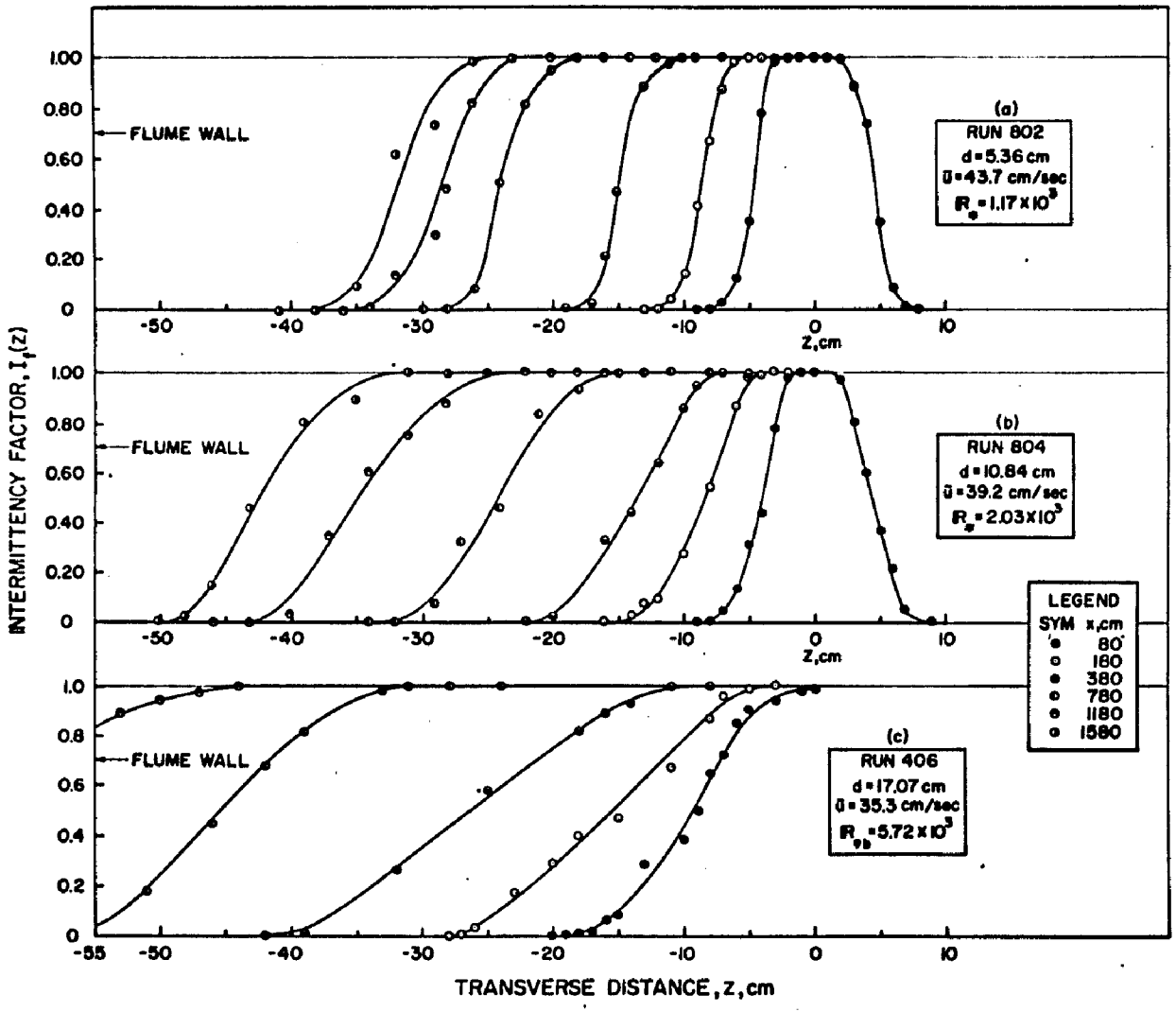

Fig. 6.2. Transverse distribution of the intermittency factor for three normal depths d. Measurements were made at the level of tracer injection $\eta_h = 0.368$ and at the same stations for all runs; RUNS 802, 804, 406.

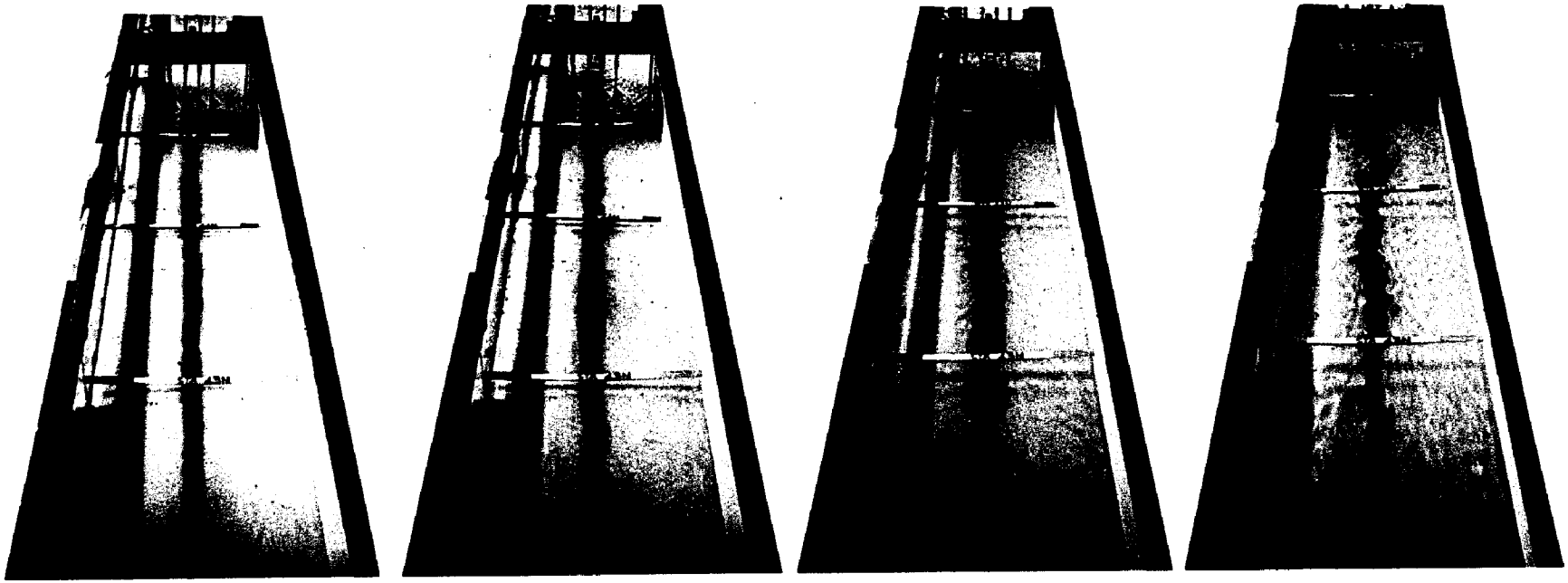

d = 2.01 cm	d = 5.26 cm	d = 10.7 cm	d = 17.34 cm
$\bar{u}$ = 46.9 cm/sec	$\bar{u}$ = 42.3 cm/sec	$\bar{u}$ = 42.6 cm/sec	$\bar{u}$ = 36.9 cm/sec
R_* = 350	R_* = 1,109	R_* = 2,210	R_* = 3,181

Fig. 6.3. Photographs of the tracer plume taken in flume S1 for four different depths d

increase in d is also illustrated by the photographs of Figure 6.3. The pictures were taken in flume S1 and the source was located at Station 42.0 m (flume entrance is Station 33.50 m). Conductivity probes are shown just downstream of Station 45.0 m. The photographs show that as d increased from d = 2.01 cm to d = 17.34 cm, the plume varied from an essentially straight ribbon to one with extensively fluctuating edges. It should be pointed out that the plume edge as measured by the probes extends substantially beyond the apparent limits in the photographs.

The intermittency factor distributions plotted in Figure 6.2 were determined only at the level of tracer injection. To investigate the variation of the I_f distribution with depth, measurements were made at four levels of the flow: $\eta = 0.095$, 0.368, 0.632, and 0.850 for RUN 808 where $\mathbb{R}_* = 2.938 \times 10^3$, and d = 17.32 cm. The resulting distributions are shown in Figure 6.4. Injection level $\eta_h = 0.368$, and the measuring station was located at x = 380 cm. The distribution of $I_f(z)$ at $\eta = 0.095$ and 0.368 were virtually identical. However, as η increased the core of continuous record Δ decreased owing to the decrease in the plume width as compared to the fluctuation of the plume edge. At $\eta = 0.850$, the plume half-width was smaller than the width of the region of intermittency--thus $I_f < 1.00$ even at z = 0. The distributions, however, were similar and the intermittency region, $W_f - \Delta$, was essentially constant for all levels η. Therefore the location of $I_f = 0.50$ approached $\zeta = 0$ as $\eta \rightarrow 1.0$. From Figure 6.4 it was concluded that the distribution at the flow level $\eta = \eta_h = 0.368$ best typified the fluctuation of the plume front. Therefore further

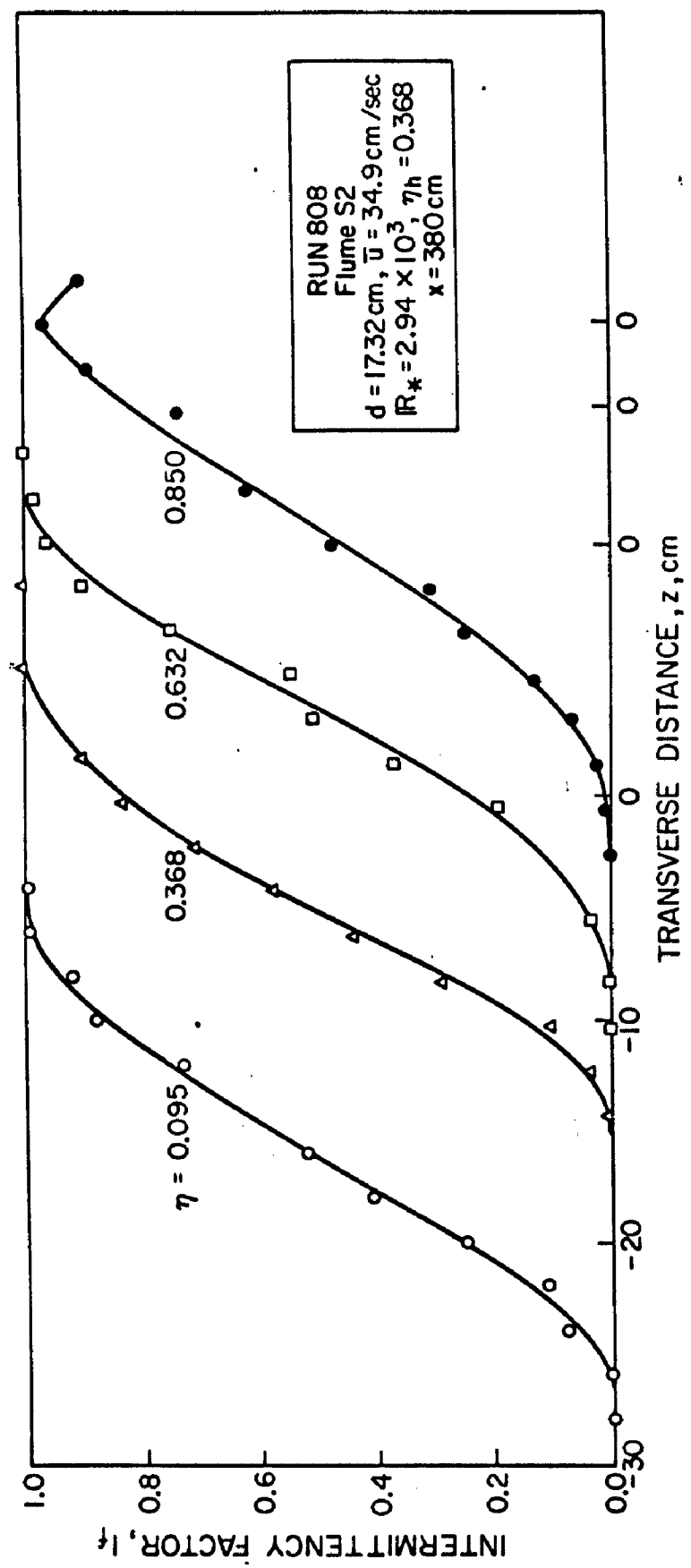

Fig. 6.4. Transverse distribution of the intermittency factor at various levels of the flow η. All measurements were made at $x = 380$ cm from the source; RUN 808.

measurements of I_f were confined to this level.

To establish self-similarity of the transverse distribution of the intermittency factor, I_f was calculated, for RUN 808, at four stations: x = 80, 180, 380, and 780 cm. The result shown in Figure 6.4 was replotted in Figure 6.5 as functions of the normalized transverse distance $(z - \tilde{Z})/\sigma_I$. The mean position of the plume front $\tilde{Z}$ and the variance of the intermittency distribution σ_I^2 were calculated numerically by Eqs. 3.43 and 3.44 respectively. Figure 6.5 shows that all points plotted closely on the universal curve:

$$I_f = \tfrac{1}{2}(1 + \text{erf}\, \xi_I) \tag{6.1}$$

where

$$\xi_I = \frac{z - \tilde{Z}}{\sqrt{2}\,\sigma_I}.$$

This indicates that the transverse position of the plume front was a normally distributed random variable because the intermittency factor distribution is equivalent to the cumulative probability distribution of the position of the plume front. This distribution is similar to those obtained by Klebanoff (13) for the laminar-turbulent interface of the boundary layer, by Townsend (45) for the plane wake, by Corrsin and Kistler (11) for the round jet, and by Demetriades (12) for the axisymmetric compressible wake. By comparing Eqs. 6.1 and 3.39, it is found that the characteristic half-width of the zone of intermittency L is given by

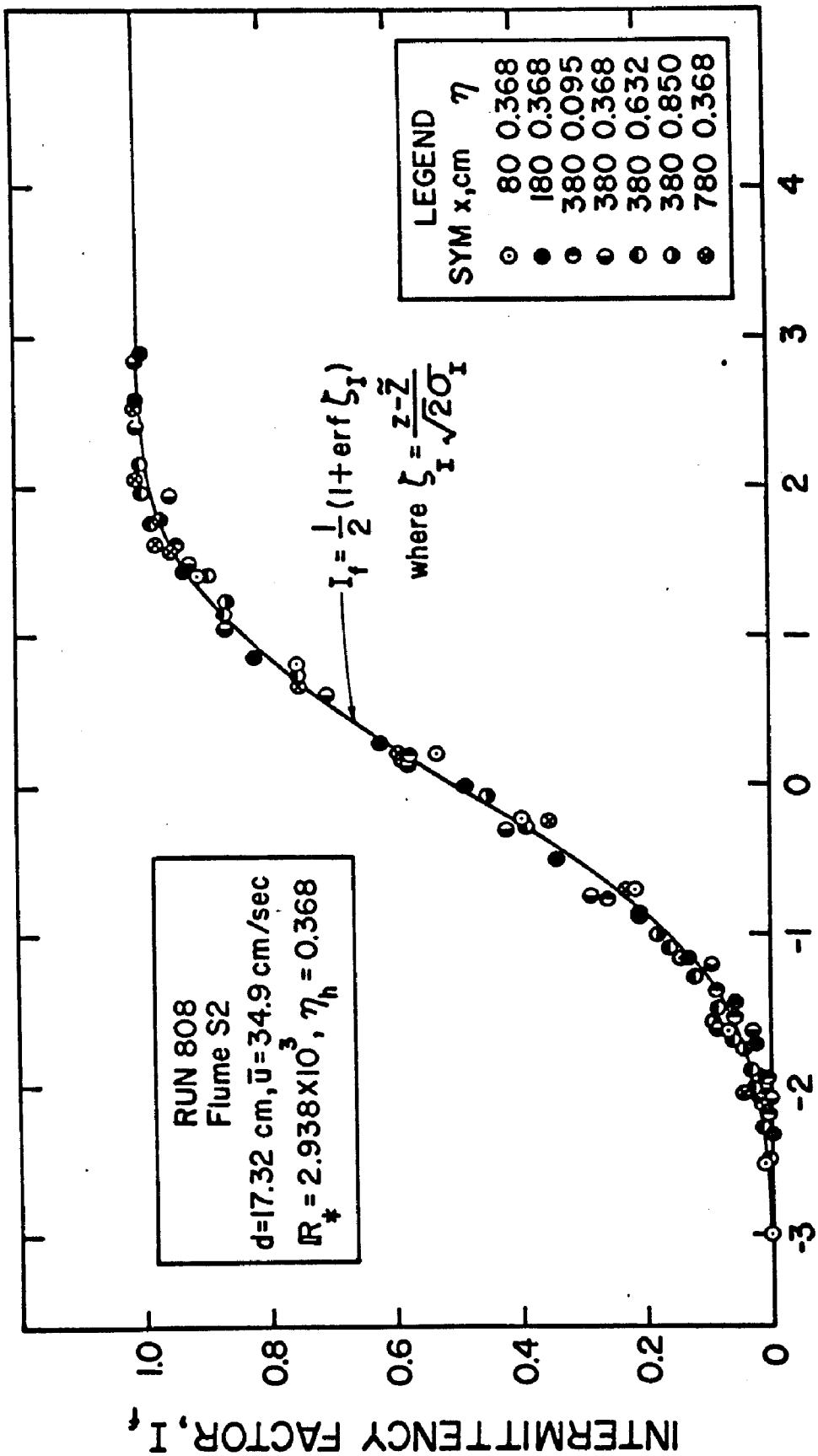

Fig. 6.5. Representation of the transverse distribution of the intermittency factor on a universal curve. Measurements were made at four stations and four levels at one station; RUN 808.

$$L = 2\sqrt{2}\,\sigma_I . \tag{6.2}$$

Thus the width of the intermittency region is $2L = 5.64\,\sigma_I$. From Eqs. 6.1 and 3.33, the probability density function, i_f, for the position of the plume front becomes

$$i_f = \frac{1}{\sqrt{2\pi}\,\sigma_I} \exp\left[-(z - \tilde{Z})^2/2\sigma_I^2\right], \tag{6.3}$$

a representation symmetrical about the mean position of the plume front $z = \tilde{Z}$. It should be noted that Eqs. 6.1, 6.2, and 6.3 are universal relationships but both $\tilde{Z}$ and σ_I are functions of x.

6.A.2. Growth of the Geometric Parameters W_f, $\tilde{Z}$, Δ, and σ_I^2 of the Intermittency Region with distance x.

a. Overall characteristics. Figure 6.6 shows for RUN 802 the growth with distance x of the maximum limit of the intermittency zone, $|z| = W_f$, the limit of the central core, $|z| = \Delta$, and the mean position of the plume front, $|z| = \tilde{Z}$. Both W_f and Δ were determined directly from curves of the I_f distribution (such as those in Figure 6.2) as the values of $|z|$ where I_f first attained the value of zero and unity respectively. The mean position $\tilde{Z}$ of the front was calculated numerically using Eq. 3.43. In all cases the origin of the z-axis was modified slightly to coincide with the point where $C = C_{max}$.

It was found that, within the reach of the measurements ($x \leq 15.8$ m), W_f and Δ grew at different rates. This characteristic will be discussed further in later sections. As evident from Figure 6.6, $\tilde{Z} \approx \frac{1}{2}(\Delta + W_f)$ indicating that the i_f distribution was symmetrical

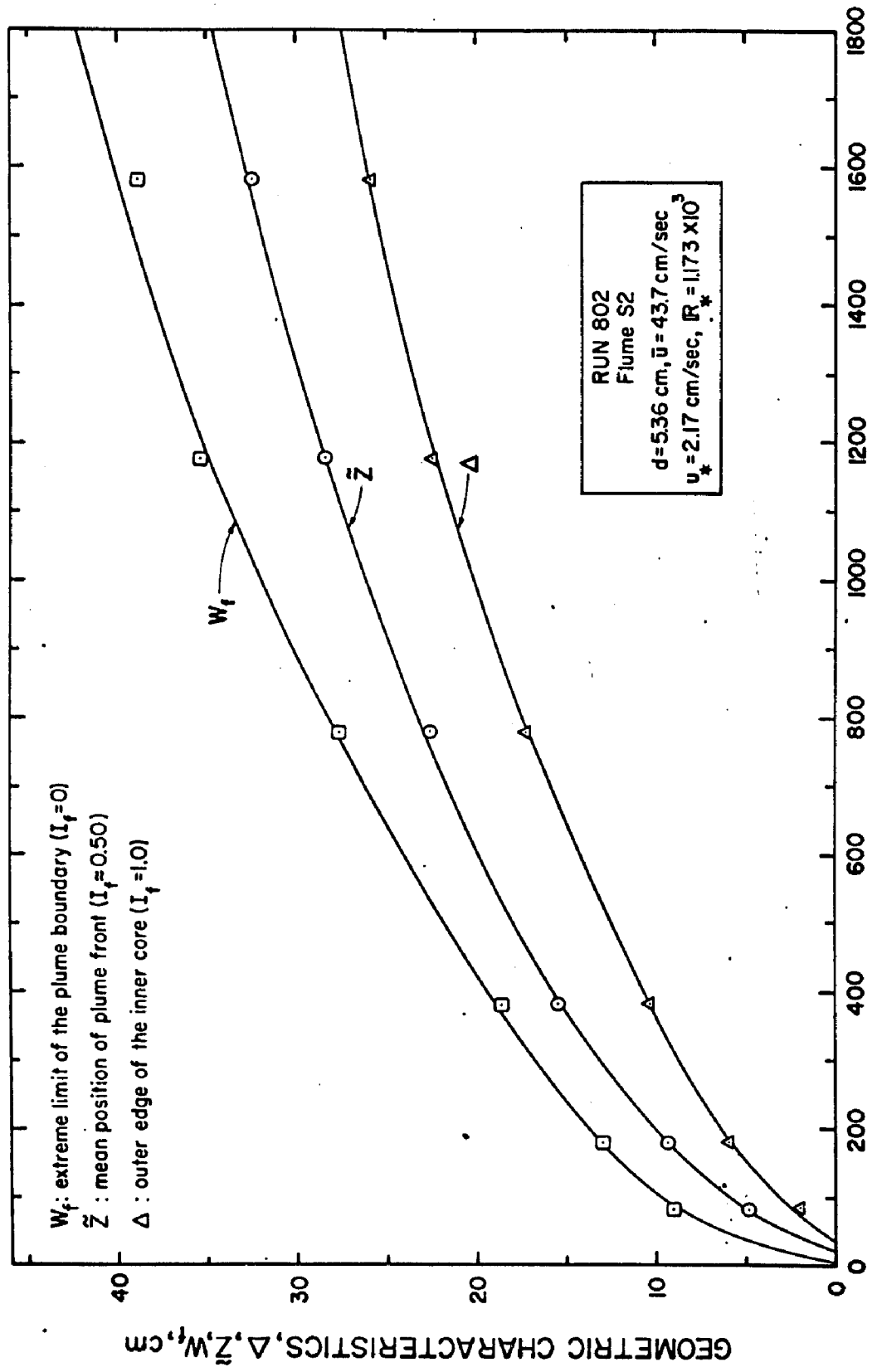

Fig. 6.6. Growth of the geometric characteristics of the region of intermittency; RUN 802.

about $\tilde{Z}$ as implied by Eqs. 6.1 and 6.3. To further verify this symmetry, $\tilde{Z}$ was compared to $z_{0.5}$ which denoted the value of $|z|$ where $I_f = 0.50$. The comparison is shown in Table 6.1 for RUNS 804 and 808. The deviation, ϵ, of $z_{0.5}$ from $\tilde{Z}$ was within 0.6 cm for all cases. The average value of $|\epsilon|$ was 0.4 cm which corresponded to a mean value of $|\epsilon|/\tilde{Z} = 2.7\%$. It was therefore concluded that $z_{0.5}$ essentially coincided with $\tilde{Z}$ and that W_f and Δ were equidistant from $\tilde{Z}$. Thus once W_f and $\tilde{Z}$ were known, Δ could be deduced by $\Delta = 2\tilde{Z} - W_f$.

Table 6.1

Comparison Between $\tilde{Z}^{\dagger}$ and $z_{0.5}{}^{\ddagger}$

x m	$\tilde{Z}$ cm	$z_{0.5}$ cm	$\epsilon^{\S}$ cm	$\tilde{Z}$ cm	$z_{0.5}$ cm	ϵ cm
	RUN 804 (d = 10.84 cm)			RUN 808 (d = 17.34 cm)		
0.80	6.2	5.9	-0.3	4.5	4.2	-0.3
1.80	10.6	10.1	-0.5	9.5	9.4	-0.1
3.80	14.3	14.1	-0.2	18.0	18.4	0.4
7.80	25.2	25.4	0.2	25.7	25.1	-0.6
11.80	35.8	36.4	0.6			
15.80	43.1	43.6	0.5			

† $\tilde{Z}$ = mean position of the plume front

‡ $z_{0.5}$ = value of $|z|$ where $I_f = 0.50$

§ $\epsilon = z_{0.5} - \tilde{Z}$

To analyze the rates of growth of W_f, $\tilde{Z}$, and Δ, it was necessary to define a virtual origin, x_v, of W_f as the value of x where $W_f = 0$. Since, as demonstrated by Figure 6.6, the region of intermittency extended to the plume axis near $x = 0$, Δ attained a zero value at a distance x_I downstream of the source. Values of x_I and x_v were determined for all experiments: the former by extrapolating curves fitted to measured limits of the central core to the point on the x-axis where $\Delta = 0$, the latter by fitting parabolas to plotted values of W_f versus x by the least square method. The result is listed in Table 6.2.

Table 6.2

Values of x_v and x_I Determined for Various Experiments

RUN	Flume	Flow Depth d cm	Shear Velocity u_* cm/sec	Friction Reynolds Number† $\mathbb{R}_*$ ($\times 10^{-3}$)	x_v ‡ cm	x_I § cm
802	S2	5.36	2.17	1.17	8	37
804	S2	10.84	1.86	2.03	27	25
808	S2	17.32	1.66	2.94	41	148
405	R2	6.81	5.01	3.39	-66	15
404	R2	10.36	5.05	4.97	-10	35
406	R2	17.07	3.64	5.72	-5	125

† The bed shear velocity u_{*b} was used in RUNS 405, 404, and 406

‡ x_v = position at which $W_f(x_v) = 0$ by extrapolation

§ x_I = value of x where the limit of the central core intersects the plume axis

It is observed from the table that for experiments performed in the flume with smooth boundaries $x_v > 0$. When the flume bottom was roughened with rocks $x_v < 0$. The significant point, however, was not the sign of x_v but the fact that in each set of experiments (rough versus smooth), x_v increased with the flow depth d. It was found that, for the smooth boundary experiments, x_v could be represented empirically by

$$\left(\frac{x_v}{d}\right)^{\frac{1}{2}} = 0.37\left(\sqrt{\frac{8}{f_*}} - 16.85\right), \qquad (6.4)$$

where f_* = friction factor. According to Table 6.2, x_I depended on the flow depth increasing from $x_I \approx 30$ cm for $d \approx 10$ cm to a maximum value of 148 cm for $d = 17.32$ cm, regardless of whether the flume bottom was smooth or rough.

b. Prediction of the extreme limit of the plume boundary, W_f. Dimensional analysis was used to develop a universal curve representing all experimental measurements of W_f. The variables selected were W_f, the extreme limit of the plume boundary; $\chi = x - x_v$, the value of x corrected for the virtual origin x_v; u_* (or u_{*b}), the (bed) shear velocity; and $\bar{u}$, d, and ν, the mean flow velocity, the flow depth, and the kinematic viscosity respectively. Thus

$$W_f = g(\chi, d, u_*, \bar{u}, \nu) \qquad (6.5)$$

where g represents an unknown function. Similarity argument then predicts that

$$\frac{W_f}{d} = g_1\left(\frac{\chi}{d}, \frac{\bar{u}d}{\nu}, \frac{u_* d}{\nu}\right), \tag{6.6}$$

where g_1 is still an unknown function. Since both $\bar{u}d/\nu$ and u_*d/ν were large in all experiments and the flow was thus fully turbulent, it was reasoned that W_f/d depended on the roughness of the flow boundaries but not on the value of the Reynolds numbers. The characteristic variable needed was therefore a frictional parameter which could be derived from Eq. 6.6 as the ratio of the Reynolds numbers. Hence

$$\frac{W_f}{d} = g_2\left(\frac{\chi}{d}, \frac{u_*}{\bar{u}}\right). \tag{6.7}$$

For a given experiment (i.e. $u_*/\bar{u}$ = constant), measured values of W_f/d were plotted against χ/d on log-log scales. It was found that

$$\frac{W_f}{d} \propto \left(\frac{\chi}{d}\right)^{\gamma_1} \tag{6.8}$$

where the constant exponent $\gamma_1 = \frac{1}{2}$. To incorporate the frictional parameter, $(W_f/d)^2$ was plotted against $(\chi/d)(u_{*b}/\bar{u})$ using u_* for the smooth and u_{*b} for the rough bottom experiments. As shown in Figure 6.7, the points fell on two well-defined parallel lines: A, for the smooth bottom experiments, and B for the experiments performed when the flume bottom was roughened with rocks. By multiplying $(\chi/d)(u_{*b}/\bar{u})$ by a factor R_w, however, lines A and B collapsed into one and, as shown in Figure 6.8, all points plotted on the universal curve

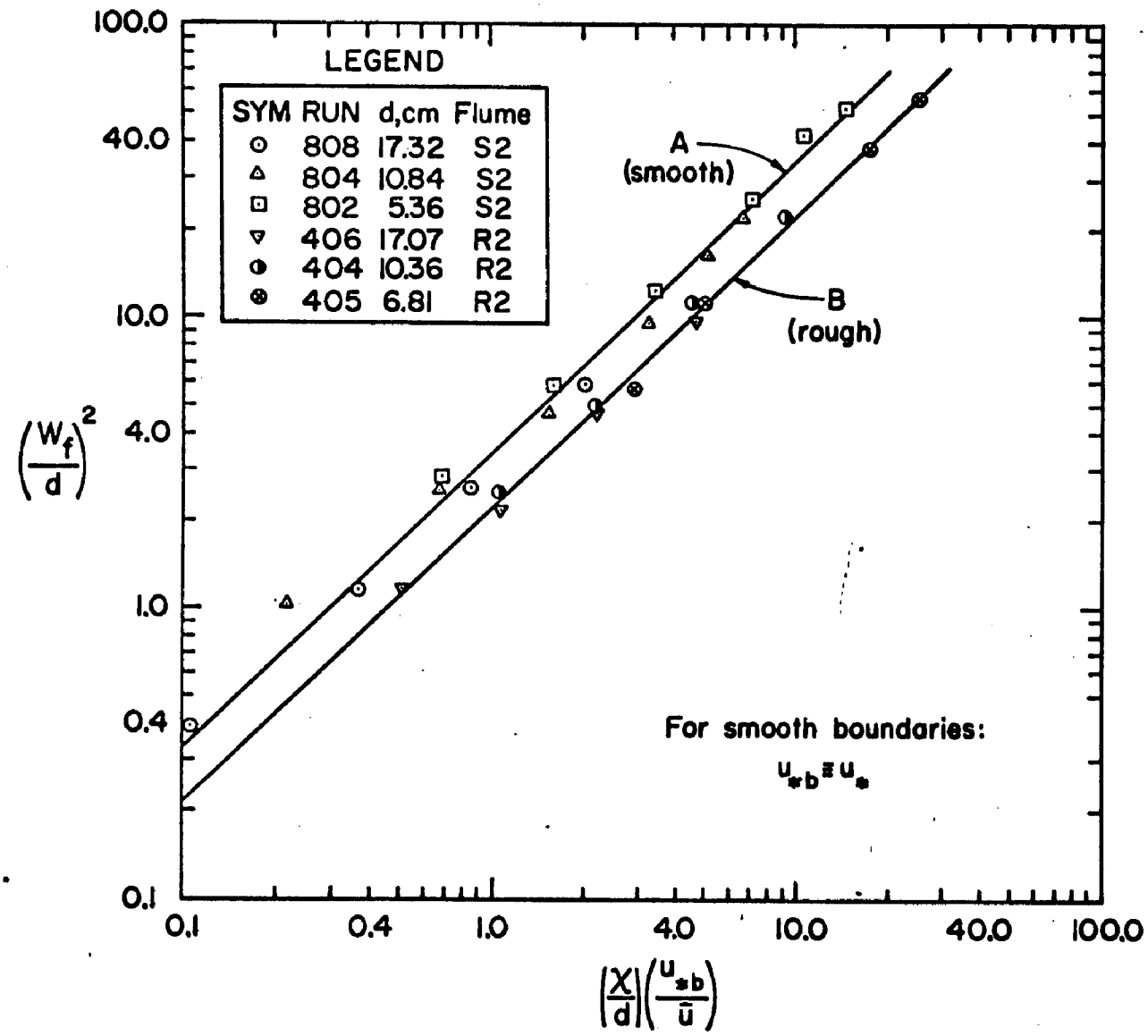

Fig. 6.7. Plots of $(W_f/d)^2$ versus $(\chi/d)(u_{*b}/\bar{u})$ for experiments performed in flume 2 with the bottom hydraulically smooth (A) or rough (B); RUNS 808, 804, 802, 406, 404, 405.

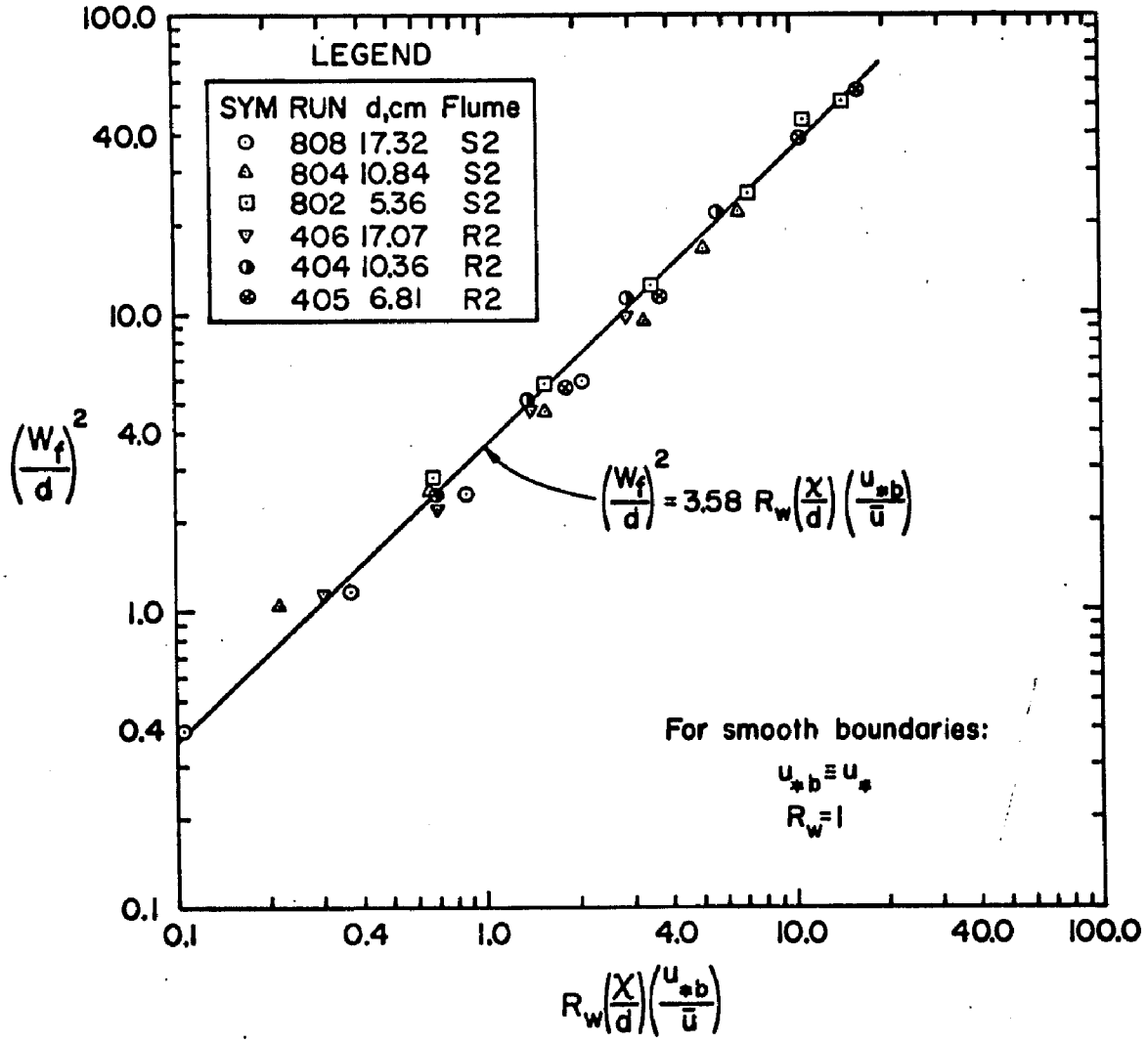

Fig. 6.8. Universal representation of the growth of the extreme limit W_f of the plume boundary (where $I_f = 0.0$) for all experiments; RUNS 808, 804, 802, 406, 404, 405.

$$\left(\frac{W_f}{d}\right)^2 = 3.58\, R_w \left(\frac{\chi}{d}\right)\left(\frac{u_{*b}}{\bar{u}}\right) \qquad (6.9)$$

where

$$R_w = (f_s/f_r)^{1/4}, \qquad (6.10)$$

f_s, f_r are, respectively, the mean values of the bed friction factors for the smooth boundary and rough bottom experiments. For the smooth boundary, the bed shear velocity u_{*b} becomes the shear velocity u_* and $R_w = 1.0$. Thus the R_w correction is necessary only for the hydraulically rough boundary flows. With Eq. 6.9, the extreme limit W_f of the fluctuating plume front can be predicted for given normal flow conditions.

c. Prediction of the mean position $\tilde{Z}$ of the plume edge. From dimensional and physical reasoning similar to the arguments in the last section, a universal curve was established for the growth of $\tilde{Z}$ with distance from the source. Log-log plots of $\tilde{Z}/d$ versus χ/d for various experiments yielded a representative relationship

$$\left(\frac{\tilde{Z}}{d}\right) \propto \left(\frac{\chi}{d}\right)^{\gamma_2} \qquad (6.11)$$

where the exponent $\gamma_2 = 2/3$. This value of γ_2 was compared with those previously reported in the literature for other flows. The results are shown in Table 6.3.

From the table it is evident that γ_2 varied from 1.0 for the round jet to 1/3 for the axisymmetric compressible wake. The value of γ_2 obtained in the present study was essentially equal to that

Table 6.3

Values of the Exponents γ_2 and γ_3 for Different Flows

Source	Kind of Flow†	γ_2‡	γ_3‡	Method of Determination of γ_2 and γ_3
1	2	3	4	5
Towsend (45)	Two-dimensional wake	1/2	≈ 1/2	Experimental
Corrsin and Kistler (11)	Growth of the turbulent boundary layer	0.65	0.70	Theoretical approximation
		0.63±0.1	0.67±0.1	Experimental
	Round jet	1.0	1.0	Theoretical
		0.88±0.05	1.06±0.05	Experimental
Demetriades (12)	Axisymmetric compressible wake	1/3	1/3	Experimental
Present Study	Transverse growth of a plume in a turbulent shear flow	2/3	1/3	Experimental

† All measurements listed, except in the present study, were made for air flow in a wind tunnel

‡ $\left(\frac{\tilde{Z}}{d}\right) \propto \left(\frac{X}{d}\right)^{\gamma_2}$; $\left(\frac{\sigma_I}{d}\right) \propto \left(\frac{X}{d}\right)^{\gamma_3}$

postulated and measured by Corrsin and Kistler (11) for the growth of a turbulent boundary layer next to the wall of a wind tunnel. A strong similarity between the two processes was again indicated. The first indication of this similarity was the fact that the transverse distributions of the intermittency factor measured by Klebanoff (13), and Corrsin and Kistler (11) for the boundary layer were virtually identical to those calculated for the plume front fluctuation in the present study.

To develop a universal curve, $\tilde{Z}/d$ was plotted against $(\chi/d)^{2/3}(u_{*b}/\bar{u})$ on log-log scales. Two parallel lines were again found to fit the measurements; one for the smooth boundary experiments, the other for the rough bottom. Further calculations showed that the two lines merged into one represented by

$$\frac{\tilde{Z}}{d} = 3.31\, R_z \left(\frac{\chi}{d}\right)^{2/3} \left(\frac{u_{*b}}{\bar{u}}\right), \tag{6.12}$$

where

$$R_z = (f_s/f_r)^{1/3}. \tag{6.13}$$

When the flume was smooth, $u_{*b} \equiv u_*$, and $R_z = 1$.

Measured values of $\tilde{Z}$ for both smooth boundary and rough bottom experiments are plotted in Figure 6.9. It is evident that all points closely fitted the universal curve of Eq. 6.12. For large χ, however, experimental points increasingly deviated from Eq. 6.12 showing a growth rate slower than the equation would predict. There was a strong indication that very far from the source, $\tilde{Z}/d$ grew as a parabolic function of (χ/d) just as W_f/d did. The present measure-

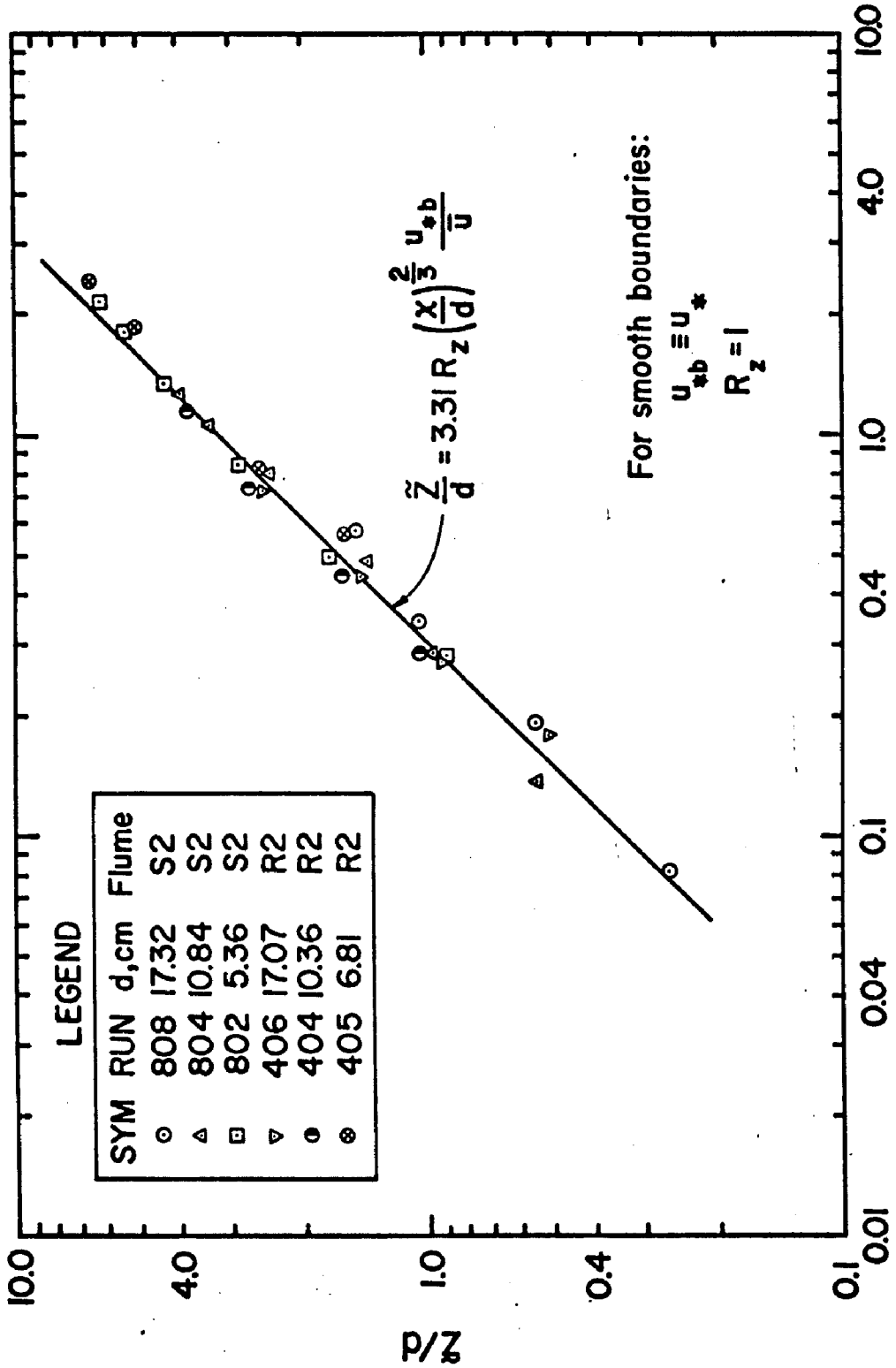

Fig. 6.9. Universal representation of the growth of the mean position of the plume front $\tilde{Z}$ (where $I_f \approx 0.50$) for all experiments; RUNS 808, 804, 802, 406, 404, 405.

ments in the flume, however, did not extend to distances far enough from the source to conclusively verify this tendency.

Eq. 6.12 can therefore be used to calculate $\tilde{Z}$ given a uniform flow condition. From Eq. 6.9, W_f can also be predicted. Thus the outer limit of the central core Δ may be derived from the relation $\Delta = 2\tilde{Z} - W_f$.

d. Growth of the variance σ_I^2 of the region of intermittency. The variance σ_I^2 of the transverse distribution of the position of the plume front was calculated numerically by Eq. 3.44. By appropriate plots, it was established that for each experiment (smooth boundary or rough bottom), σ_I initially grew according to the relation:

$$\left(\frac{\sigma_I}{d}\right) \propto \left(\frac{x}{d}\right)^{\gamma_3} \tag{6.14}$$

where the exponent $\gamma_3 = 1/3$. This value of γ_3 was again compared to those obtained for other flows. The comparison is presented in Table 6.3. It shows that $\gamma_2 = \gamma_3$ for other flows previously reported in the literature but, in the present study, $\gamma_2 = 2\gamma_3$.

For all experiments in the flume, it was found that expression 6.14 could be more explicitly written as

$$\left(\frac{\sigma_I}{d}\right)^2 = K_1\left(\frac{x}{d}\right)^{2/3} \frac{u_{*b}}{\bar{u}} \tag{6.15}$$

where, for the smooth boundary runs, $K_1 = 0.23$, 0.16, and 0.11 for $\mathbb{R}_* = 2938$, 2026, and 1173 respectively. For the rough bottom boundary, $K_1 = 0.23$, 0.10, and 0.04 for $\mathbb{R}_{*b} = 5716$, 4973, and 3388

respectively. The power law relationship of Eq. 6.15 was valid only as long as $(\sigma_I/d) < 0.4$. As (χ/d) increased beyond this point, σ_I/d began to taper off and in some cases σ_I/d actually decreased with increasing χ/d. Thus if the amplitude of the plume front oscillation (along z for fixed x and y) is characterized by $2\sigma_I$, the maximum relative amplitude attained in all experiments:

$$\left(\frac{2\sigma_I}{d}\right)_{max} \approx 0.8. \qquad (6.16)$$

The variance σ_I^2 was also compared to the total variance σ^2 of the transverse distribution of the mean tracer concentration calculated by Eq. 5.3. The ratio $(\sigma_I/\sigma)^2$ was plotted against χ/d for each experiment. As expected the ratio decreased with increasing χ/d according to the power law

$$\left(\frac{\sigma_I}{\sigma}\right)^2 = K\left(\frac{\chi}{d}\right)^{-1/3} \qquad (6.17)$$

The constant of proportionality K in Eq. 6.17 again decreased with decreasing friction Reynolds number.

6.A.3. Temporal Characteristics of the Plume Front Oscillation.

a. Frequency of "zero occurrence" $\omega_0(z)$. The rate at which the intermittency function $h(z,t)$ changed from zero to unity at a fixed point was denoted as $\omega_0(z)$, the frequency of zero occurrence at the point z. From the definitions of $I_f(z)$ and $\omega_0(z)$, it was reasoned that

$$\omega_0(z) = 0 \quad \text{for} \begin{cases} I_f = 0.0 \\ I_f = 1.0 \end{cases} \tag{6.18}$$

and that as $I_f \rightarrow 0.50$, $\omega_0(z)$ approached a maximum value. Since the oscillation of the plume front has been shown by the distribution of $I_f(z)$ illustrated in Figure 6.5 to be a normally distributed random function, it is expected that the distribution of $\omega_0(z)$ should also be normal. From a theory postulated by Rice (65), it was deduced that $\omega_0(z)$ could be represented by

$$\omega_0(z) = \bar{\omega}_0 \exp\left[-(z-\tilde{Z})^2/2\sigma_I^2\right] \tag{6.19}$$

a distribution similar to the density function i_f. The mean value $\bar{\omega}_0$ corresponds to the zero-frequency at the mean position of the plume front $\tilde{Z}$ where $I_f = 0.50$.

The zero-frequency $\omega_0(z)$ at a fixed point z was computed from the digitized record by first counting the total number of times that $h(z,t)$ on consecutive time digits, changed from zero to unity. Then this value was divided by the total sampling time to give $\omega_0(z)$ in Hz. It is thus evident that $\omega_0(z)$ is extremely sensitive to the signal to noise ratio. At stations near the source where this ratio was high, $\omega_0(z)$ was readily evaluated with reasonable reliability. For large x, however, tracer concentration was low and so were the signal to noise ratio and the attenuation of the recorder. Thus, the calculated $\omega_0(z)$ was distorted by the background noise giving rise to unreasonably high values especially in the neighborhood of $I_f \approx 0.0$. In general, only those values of $\omega_0(z)$ measured near the source or in

the neighborhood of $I_f = 0.50$ were considered reliable and usable for further calculations.

The transverse distribution of the zero-frequency was studied by plotting the cumulative values of $\omega_0(z)$ on arithmetic probability scales. Examples are shown in Figure 6.10 for RUN 404. The plotted points closely fitted the Gaussian lines drawn for each value of x. The standard deviations of the fitted Gaussian lines were 2.20, 2.75, and 3.75 cm for $x = 80$, 180, and 380 cm respectively. The corresponding σ_I calculated from I_f distributions were 2.34, 3.17, and 3.88 cm. This indicated that $\omega_0(z)$ was closely represented by Eq. 6.19. Typical values of $\bar{\omega}_0$ evaluated at $I_f \approx 0.50$ and shown in Figure 6.10 were approximately 4.4 Hz and essentially constant for all x.

To verify if $\bar{\omega}_0(x)$ was due to the Kármán vortex street generated by the tracer injector, the vortex shedding frequency, n_i, was computed for the hydraulic conditions of RUN 404 as an example. Using the mean flow velocity $\bar{u} = 42.8$ cm/sec, the outside diameter of the tracer injector $d_i = 3.175$ mm, and the kinematic viscosity $\nu = 1.052 \times 10^{-2}$ cm^2/sec, the Strouhal number was found to be

$$\frac{n_i d_i}{\bar{u}} = 0.21$$

Thus the frequency of vortex shedding by the injector $n_i = 28.4$ Hz. However, the values of $\bar{\omega}_0(x)$ for plume fluctuations determined for RUN 404 were, respectively 4.33, 4.77, 4.19 and 4.47 Hz for $x = 80$, 180, 380, and 780 cm. Similarly for other experiments, the vortex shedding frequency greatly exceeded the plume oscillation frequency. As further verification, the tracer was injected on the water surface

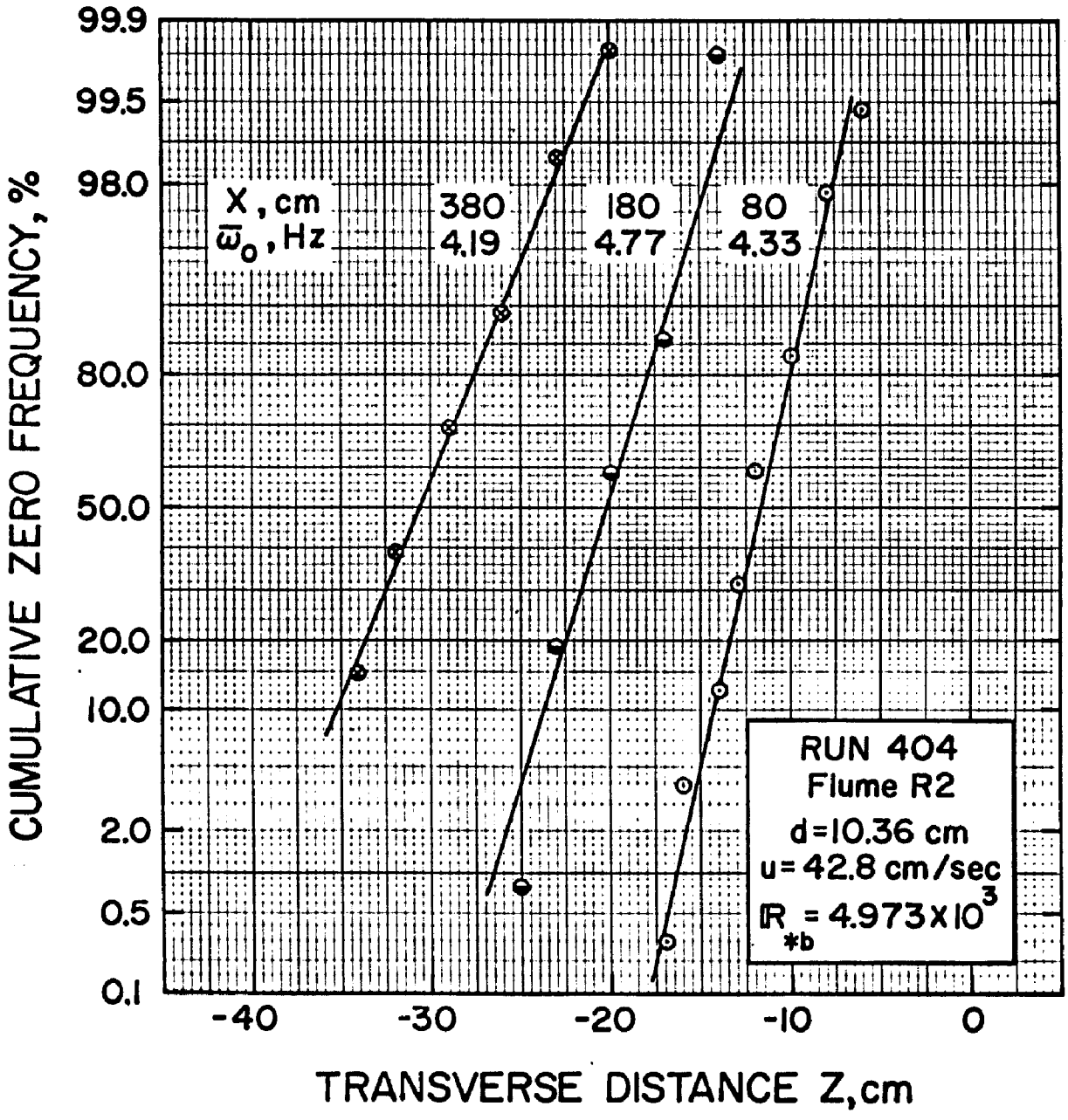

Fig. 6.10. Transverse distribution of the frequency of zero occurrence ω_0. Cumulative values of ω_0 are plotted on arithmetic probability scales. Fitted lines are Gaussian; RUN 404.

without the injector touching or penetrating the flow. Even then plu
edge fluctuation was observed.

It was thought, therefore, that the weak periodicity exhibited
by the plume front oscillation was not a response to the vortices she
by the tracer injector. This and the fact that $i_f(z)$ was Gaussian
strongly suggested that the fluctuation of the plume front was a resu
of a diffusion process generally characteristic of turbulent mixing.

b. Characteristic period, wave length and amplitude of the frontal oscillation. The fluctuation of the plume front exhibited a weak per
odicity. Thus a characteristic period $\overline{T}_0(x)$ was defined such that

$$\overline{T}_0(x) = 1/\overline{\omega}_0(x). \qquad (6.$$

From Eq. 3.46, a characteristic longitudinal length scale or wave length $L_f(x)$ was defined by

$$L_f(x) = u_c \overline{T}_0(x), \qquad (3.$$

where u_c is a convective velocity in the longitudinal direction. Si
tracer was injected at $\eta_h = 0.368$ and the level of concentration me
urements, $\eta = 0.368$, u_c was essentially equal to the mean flow velocity $\overline{u}$. Therefore the normalized (or relative) wave length $L_f(x)/d$ was evaluated by the relation

$$\frac{L_f(x)}{d} = \frac{\overline{u}\,\overline{T}_0(x)}{d}. \qquad (6.$$

Table 6.4 lists the calculated values of $L_f(x)/d$ (at several distances x) for several runs. As indicated, $L_f(x)/d$ was essenti

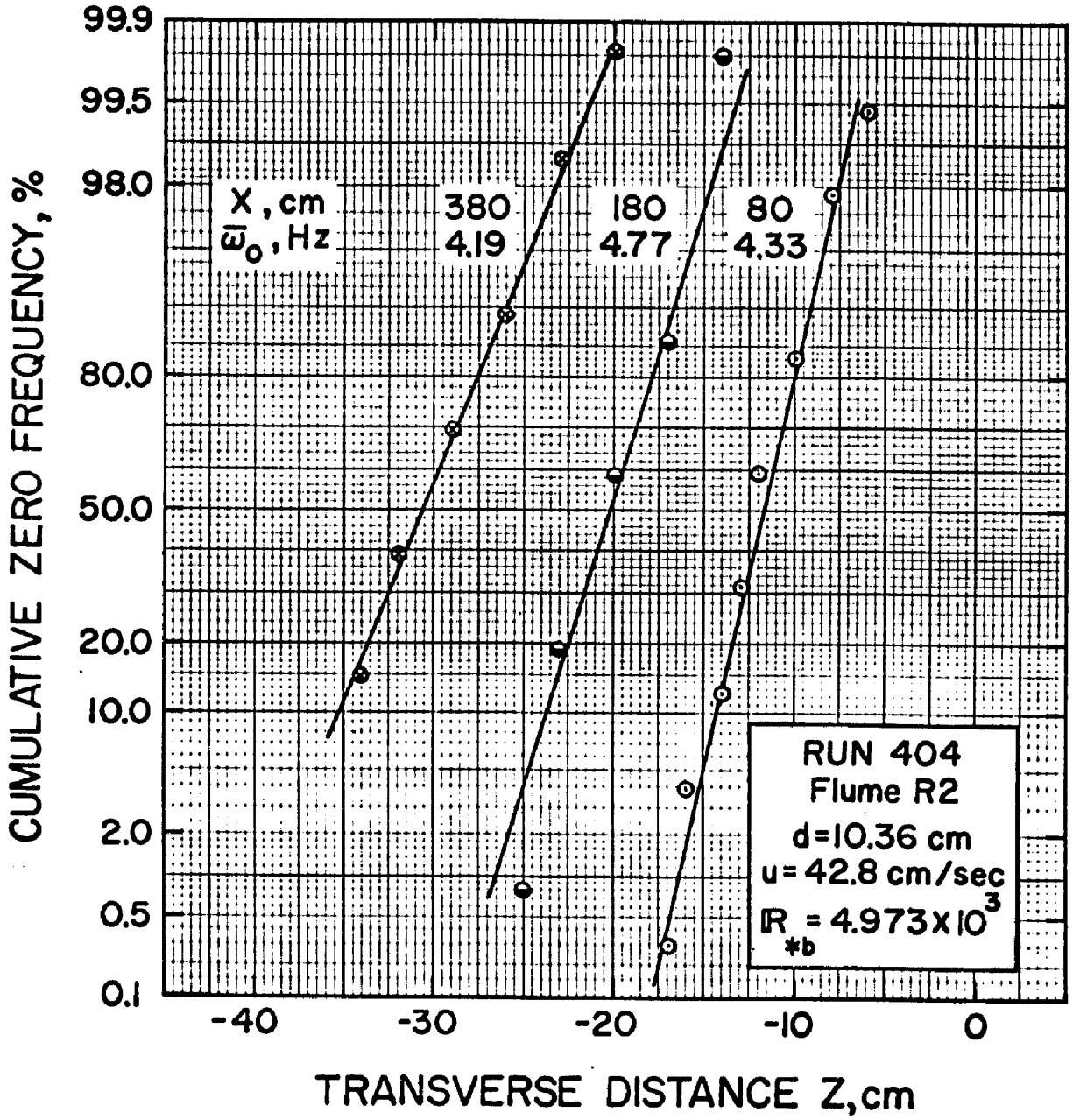

Fig. 6.10. Transverse distribution of the frequency of zero occurrence ω_0. Cumulative values of ω_0 are plotted on arithmetic probability scales. Fitted lines are Gaussian; RUN 404.

without the injector touching or penetrating the flow. Even then plume edge fluctuation was observed.

It was thought, therefore, that the weak periodicity exhibited by the plume front oscillation was not a response to the vortices shed by the tracer injector. This and the fact that $i_f(z)$ was Gaussian strongly suggested that the fluctuation of the plume front was a result of a diffusion process generally characteristic of turbulent mixing.

b. Characteristic period, wave length and amplitude of the frontal oscillation. The fluctuation of the plume front exhibited a weak periodicity. Thus a characteristic period $\overline{T}_0(x)$ was defined such that

$$\overline{T}_0(x) = 1/\overline{\omega}_0(x). \tag{6.20}$$

From Eq. 3.46, a characteristic longitudinal length scale or wave length $L_f(x)$ was defined by

$$L_f(x) = u_c \overline{T}_0(x), \tag{3.46}$$

where u_c is a convective velocity in the longitudinal direction. Since tracer was injected at $\eta_h = 0.368$ and the level of concentration measurements, $\eta = 0.368$, u_c was essentially equal to the mean flow velocity $\overline{u}$. Therefore the normalized (or relative) wave length $L_f(x)/d$ was evaluated by the relation

$$\frac{L_f(x)}{d} = \frac{\overline{u}\,\overline{T}_0(x)}{d}. \tag{6.21}$$

Table 6.4 lists the calculated values of $L_f(x)/d$ (at several distances x) for several runs. As indicated, $L_f(x)/d$ was essentially

Table 6.4

Relative Wave Length of $L_f(x)/d$ of the Plume Front Oscillation

RUN	Flume	Flow Depth d, cm	x, cm				Average $\overline{L}_f/d$
			80	180	380	780	
1	2	3	4				5
802	S2	5.36	1.49	1.55	1.04		1.39
804	S2	10.84	1.46	0.79	1.14	1.06	1.11
808	S2	17.32	0.58	0.91	0.61		0.70
405	R2	6.81	1.13	0.86			1.00
404	R2	10.36	0.96	0.86	0.98	0.92	0.93
406	R2	17.07	0.32	0.50	0.36		0.39

invariant with x for any given experiment. It is evident from Column 5, that for comparable flow depths, the average value of the relative wave length, $\overline{L}_f/d$, is smaller for the rough than for the smooth boundary experiments. This indicates that the characteristic transverse scale decreases with intensification of turbulence. One can speculate that accentuation of turbulence intensity effectively breaks up the larger eddies.

The amplitude of the plume front oscillation was represented by $2\sigma_I$. As stated in subsection 6.A.2.d, $2\sigma_I$ grew with increasing x reaching a maximum value of 0.8 d for the same experiments shown in Table 6.4. Thus the maximum steepness of the oscillating plume

front expressed as $(2\sigma_I)_{max}/\overline{L}_f$ was approximately unity for all experiments. For a given experiment, therefore, the characteristic width of the region of intermittency increased with x until the fluctuation amplitude $2\sigma_I$ was nearly equal to the characteristic wave length of the plume front. As x increased further, the width of the intermittency region decreased with x.

c. Probability densities $p_1(T_1)$, $p_2(T_2)$, and $p(T)$ of the intermittency function $h(z,t)$ at a fixed point. The probability densities $p_1(T_1)$ for the duration of occurrence T_1 (when $c(t) > C_t$), and $p_2(T_2)$ for the duration of non-occurrence T_2 (when $c(t) \leq C_t$) of the intermittency function $h(z,t)$ were determined according to the method outlined in Chapter 3. Typical values of T_1 and T_2 are shown in Figure 6.1. The densities $p_1(T_1)$, $p_2(T_2)$ calculated for RUN 904 at ξ = 7.4, 16.6 71.9, and 108.9 are plotted in Figure 6.11. For ξ = 7.4 and 16.6, 56 seconds (3360 samples) were analyzed, and for ξ = 71.9 and 108.9, 24.3 seconds (1456 samples). Histograms representing $p_1(T_1)$ are shown as solid lines. For $p_2(T_2)$ the lines are dotted. Experimental curves--solid for $p_1(T_1)$ and dotted for $p_2(T_2)$--were fitted to the histograms. The ordinates were normalized according to Eq. 3.47. The time scale of the abscissa is in the units of 1/60 sec. Maximum values of T_1 were 1.18, 2.55, 1.30, and 0.84 sec for ξ = 7.4, 16.6, 71.9, and 108.9 respectively.

The probability density $p(T)$ for the combined occurrence and non-occurrence periods is plotted in Figure 6.12 for the same points shown in Figure 6.11. The time scale is in units of 1/60-sec and

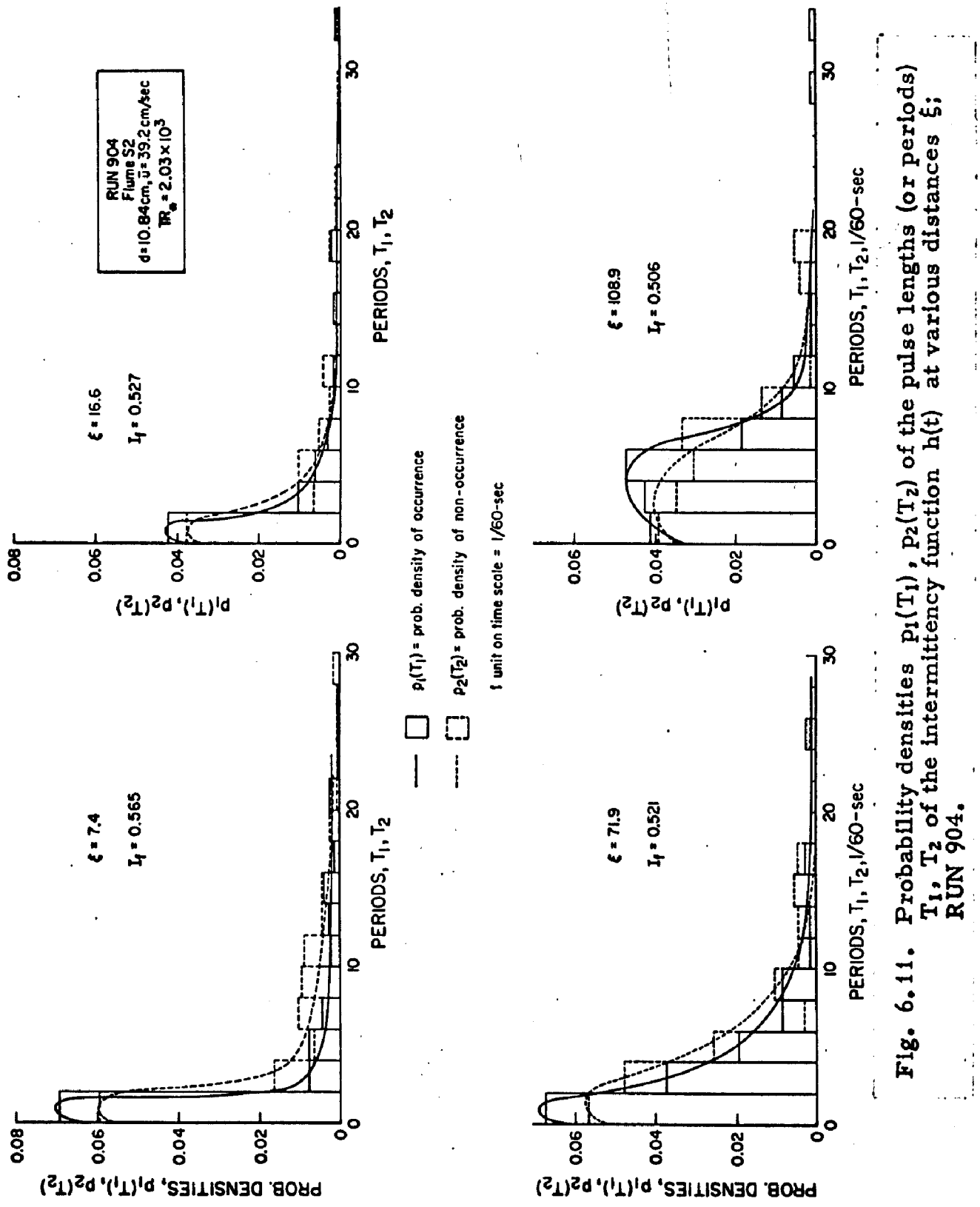

Fig. 6.11. Probability densities $p_1(T_1)$, $p_2(T_2)$ of the pulse lengths (or periods) T_1, T_2 of the intermittency function h(t) at various distances ξ; RUN 904.

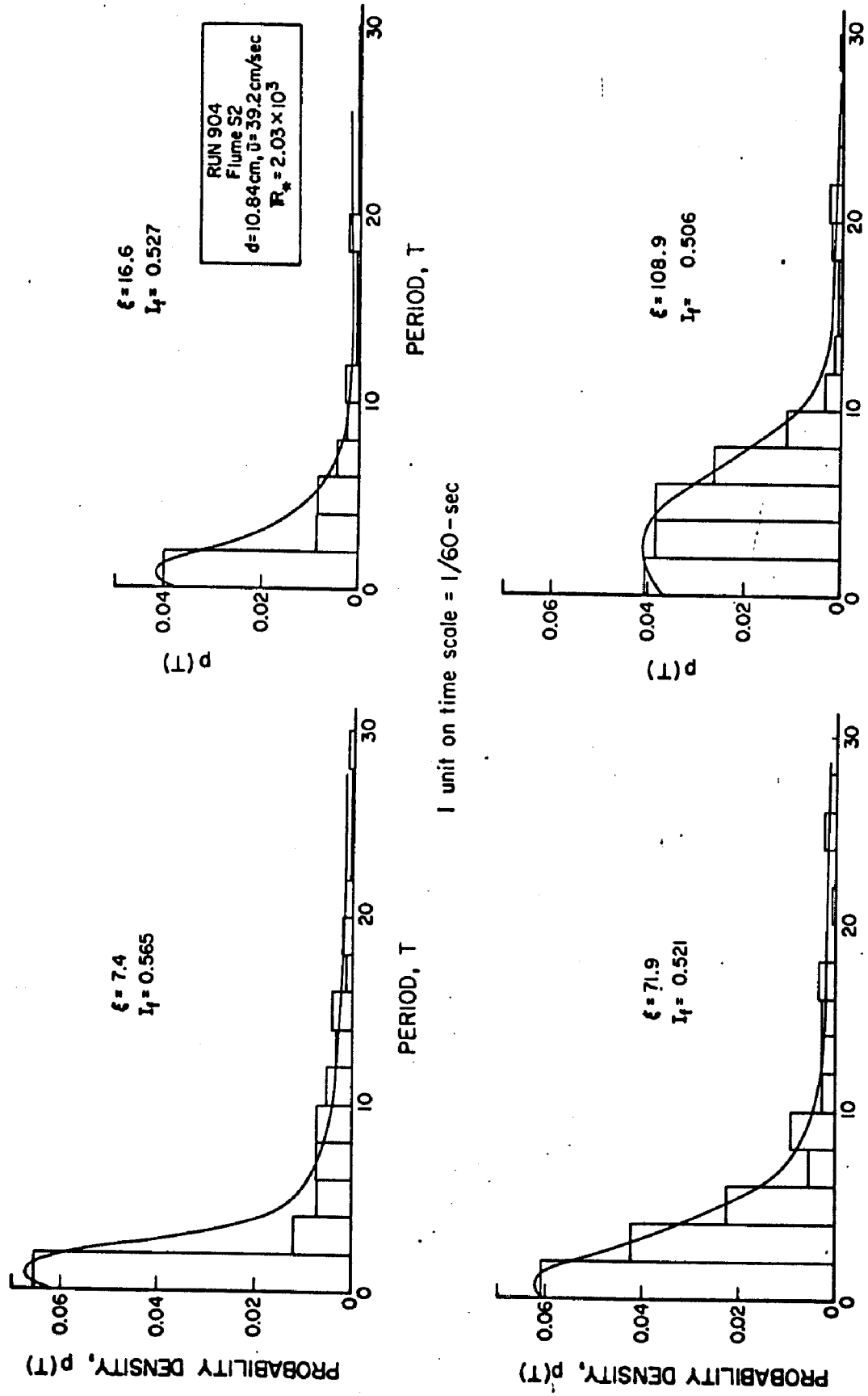

Fig. 6.12. Probability density p(T) for the combined periods (or pulse lengths) of occurrence and non-occurrence of the intermittency function h(t) at various distances ξ; RUN 904.

$p(T)$ was normalized for each ξ in accordance with Eq. 3.48. Representative curves were fitted to each histogram as in Figure 6.11.

Figures 6.11 and 6.12 show that the shape of each of the distributions of $p_1(T_1)$, $p_2(T_2)$, and $p(T)$ was essentially invariant with ξ. In general the short periods dominated long pulse lengths. The result was a positively skewed distribution with more than 50% occurrence within a period of 0.067 sec for $\xi \leq 16.6$. As ξ increased, the distributions broadened as larger pulses became increasingly more important. Since $p(T)$ was normalized according to Eq. 3.48, the broadening of the density distributions caused an attenuation of the peak of $p(T)$ with increasing ξ.

The overall shapes of the $p_1(T_1)$ and $p_2(T_2)$ distributions were similar to those calculated by Corrsin and Kistler (11) for the fluctuation of the edge of the turbulent boundary layer. This again indicates a similarity between the growth of the wall boundary layer and the transverse spread of a plume in a turbulent shear flow.

d. Cross-correlation analysis of $h(z,t)$ for two points located at $z = \tilde{Z}$ and $z = -\tilde{Z}$. A cross-correlation analysis of the intermittency function was made at five stations. At each station, the two points compared were located at $z \approx \tilde{Z}$ and $z \approx -\tilde{Z}$ where $I_f \approx 0.5$ and at the same flow level.

The procedure consisted in first determining the two points at a given station where, for $\eta = \eta_h$, $I_f \approx 0.50$. A probe was then placed at each of the points and the tracer concentration at both locations were monitored simultaneously, digitized at 60 samples/sec, and stored on

two separate channels of the magnetic tape.

The intermittency functions $h_1(-\tilde{Z},t)$ and $h_2(\tilde{Z},t)$ were computed respectively for the probes located at $z = -\tilde{Z}$ and $z = \tilde{Z}$ for the particular station. The two functions h_1 and h_2 were then compared at identical times t at intervals of 1/60-sec and the result recorded according to the following designations:

(i) ON-ON, if $h_1 = h_2 = 1.0$

(ii) OFF-OFF, if $h_1 = h_2 = 0.0$

(iii) ON-OFF, if $h_1 = 1.0$, and $h_2 = 0.0$

(iv) OFF-ON, if $h_1 = 0.0$, and $h_2 = .0$

The ratio of the total number of ON-ON and OFF-OFF cases to the total number of samples within the sampling period was termed INSTABILITY; the rest of the sampling period was called MEANDER.

Measurements for the cross-correlation analysis were made in RUN 904. The flow depth was 10.84 cm, the mean flow velocity $\bar{u} = 39.2$ cm/sec, and the level of tracer injection $\eta_h = 0.368$. For the analysis, 3360 samples were used for $\xi = 7.4$, 16.6, and 35.0. For $\xi = 71.9$ and 108.9, 1456 samples were analyzed. The results of the calculations are summarized in Table 6.5.

Column 1 identifies the positions of the probes: $\tilde{Z}$ and $-\tilde{Z}$. Column 2 lists the values of I_f at each point. Although these values were slightly greater or less than 0.50, they were considered sufficiently close to 0.50 for the purposes of the analysis. The slope of the transverse distribution of I_f was very steep near $I_f = 0.50$ (especially for small ξ). Thus a slight deviation of I_f from 0.50 caused negligible errors in the estimation of the mean front position. If, for a particular

Table 6.5. Cross-Correlation Analysis of $h(z,t)$ at the Two Points $z \approx -\tilde{Z}$ and $z \approx \tilde{Z}$ (RUN 904)

Position of the Probe	Interm. Factor I_f	Zero Freq. ω_0, Hz	ON-ON	OFF-OFF	ON-OFF	OFF-ON	Per Cent INSTA-BILITY	Per Cent MEANDER
1	2	3	4	5	6	7	8	9
$\xi = 7.4$								
$-\tilde{Z}$	0.531	3.86	872	841	913	734	50.98	49.02
$\tilde{Z}$	0.478	3.00						
$\xi = 16.6$								
$-\tilde{Z}$	0.494	2.54	642	825	1018	875	43.66	56.34
$\tilde{Z}$	0.452	3.41						
$\xi = 35.0$								
$-\tilde{Z}$	0.557	4.82	1120	524	750	966	48.93	51.07
$\tilde{Z}$	0.621	4.07						
$\xi = 71.9$								
$-\tilde{Z}$	0.521	4.77	438	247	320	451	47.05	52.95
$\tilde{Z}$	0.611	4.98						
$\xi = 108.9$								
$-\tilde{Z}$	0.506	4.98	370	376	367	343	51.24	48.76
$\tilde{Z}$	0.490	6.29						

probe, $I_f > 0.50$, the number of ON events would be increased and the OFF events decreased for that probe. When $I_f < 0.50$, the reverse would be true.

The frequency of zero occurrence ω_0 calculated from the intermittency function is tabulated in Column 3. The total number of ON-ON, OFF-OFF, ON-OFF, and OFF-ON events is listed respectively in Columns 4, 5, 6, and 7. The fraction of INSTABILITY and that of MEANDER both expressed in per cent are entered in Columns 8 and 9 respectively.

Cross-correlation analysis was undertaken to verify which of two hypotheses governed the fluctuation of the plume front. The first is the instability (or equilibrium) hypothesis, described by Townsend (66). It postulates that the indentations of the plume edge result from a growth-decay cycle of the large eddies which effect plume spreading and macroscale mixing. Thus the region of intermittency would be a consequence of a pulsating motion of the plume boundaries transverse to the flow direction. If mixing is due, entirely, to this hypothesis, then the parameter INSTABILITY of Table 6.5 would be nearly 100%, and MEANDER would have a value near zero.

The second hypothesis, advanced by Gifford (16), assumes that, at any given ξ (expecially for large ξ), the plume width is essentially constant. Fluctuation of the plume edges is therefore due to the meandering of the entire plume with the plume centroid wandering randomly along a transverse line normal to the flow. This model has been discussed in Chapter 3 and illustrated in Figure 3.1. If the plume front variation is completely due to this reasoning, MEANDER of

Table 6.5 would be 100% and INSTABILITY zero.

A careful scrutiny of Table 6.5, however, reveals that at all ξ,

$$\text{INSTABILITY} \approx \text{MEANDER} \approx 0.50, \tag{6.22}$$

indicating that pulsating and meandering motions contributed to the wrinkle of the plume edge. Thus for $\xi \geq 7.4$ neither hypothesis seemed to dominate the other. Further examination of the table shows that, for each ξ, there was a fairly uniform distribution of events in the ON-ON, OFF-OFF, ON-OFF, and OFF-ON slots. The closer the values of I_f for h_1 and h_2 were near 0.50 (for example at $\xi = 108.9$), the better was the uniformity. This meant, therefore, that the opposite edges of the plume also fluctuated independently of each other and that this test could not distinguish plume edge fluctuation from a purely random process.

From the results of Table 6.5 and the transverse distribution of the intermittency factor shown in Figure 6.5, it is concluded that the fluctuation of plume edge for $\xi \geq 7.4$ seems to be a random motion with a Gaussian distribution about the mean front position. The fluctuation is due to both the meandering of the plume centroid and the growth-decay cycle of the overall plume width. However, if the channel alignment is not straight or the flow cross section is not uniform, strong lateral gradients of velocity would intensify plume meandering. This would thus dominate the growth-decay cycle as the principal mixing mechanism and indeed increase the overall width of the plume and eventually the transverse mixing coefficient.

6.B. ANALYSIS OF PLUME VARIATION USING THE FLUCTUATING PLUME MODEL

Figure 6.13 shows the temporal variation of the instantaneous plume boundaries at fixed stations. The data were obtained during RUN 300 from the motion picture study described in Chapter 3. In Figure 6.13, the points are plotted at intervals of 1/6-sec and at each station, five seconds of data is shown as illustration. Calculations were made at ξ = 3.2, 4.1, 5.0, 5.7, 6.5, 7.5, 8.6, and 9.5 with the flow depth d = 17.00 cm. As explained earlier, plume boundaries became indistinct at greater distances from the source.

A casual observation of Figure 6.13 seemed to indicate that plume meandering completely dominated the variation of the plume width. This was certainly true for $\xi \leq 6.5$, where the mean size of the plume width was still small compared to the flow depth. However, as ξ increased further, plume width variation became increasingly important. This is illustrated in Figure 6.14 which shows the temporal variation of the instantaneous plume width at fixed stations for the same plume boundaries shown in Figure 6.13. Figure 6.14 clearly demonstrates that the variation of the plume width was certainly not small compared to the oscillation of the plume centroid for $7.5 \leq \xi \leq 9.5$, and that, for all ξ, the variation was weakly periodic suggesting a cyclic phenomenon characteristic of the instability hypothesis.

From data similar to those plotted in Figure 6.13, various parameters associated with the fluctuating plume and described in Chapter 3 were calculated. Table 6.6 lists the results. The mean width W_a of the instantaneous plume tabulated in Column 1, was

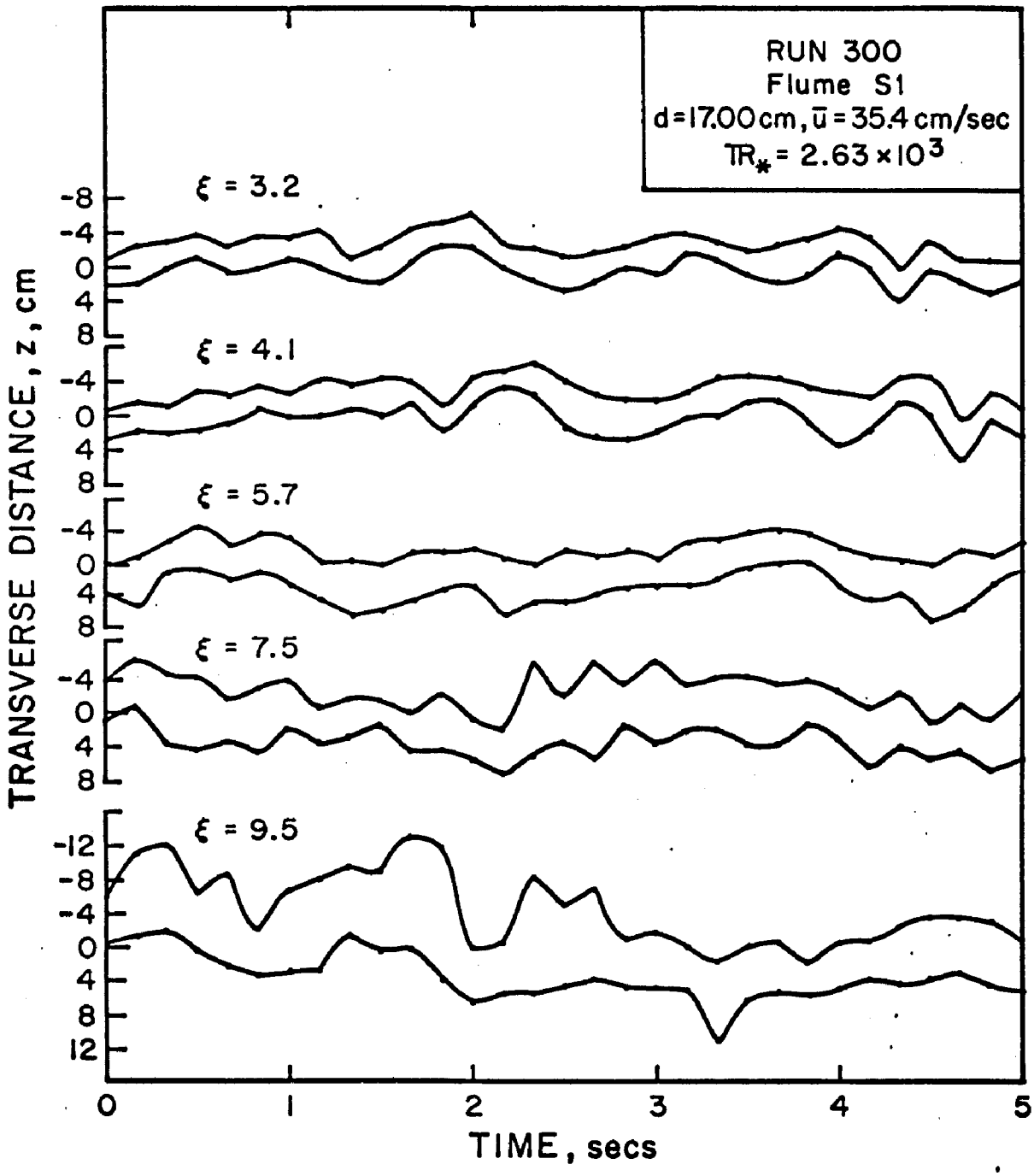

Fig. 6.13. Temporal variation of the plume boundaries at fixed stations downstream of the source. Five seconds of data plotted at intervals of 1/6-sec is shown at each station; RUN 300.

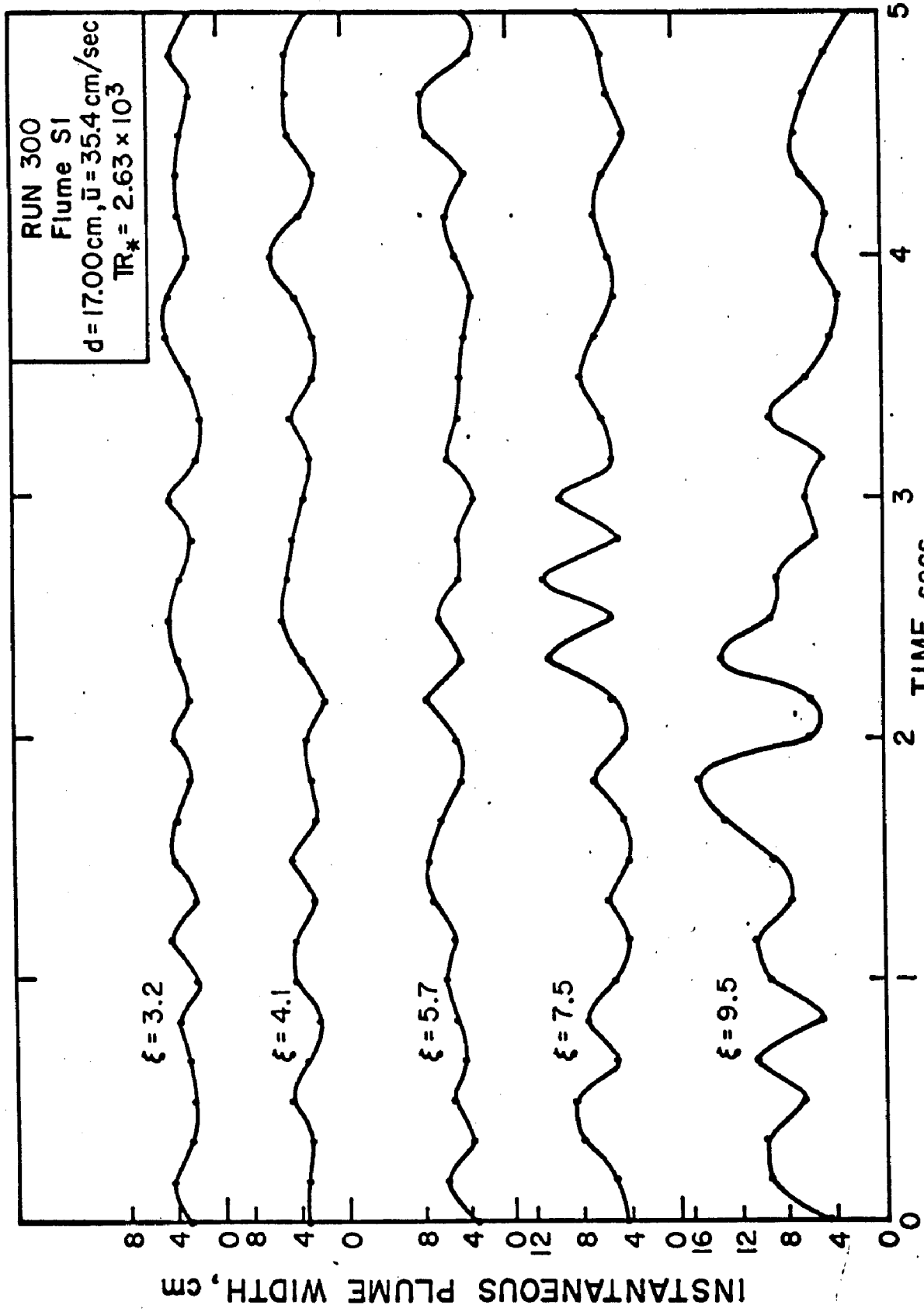

Fig. 6.14. Temporal variation of the instantaneous plume width at fixed stations for the plume boundaries shown in Figure 6.13; RUN 300.

Table 6.6

Parameters Associated With the Fluctuation Plume (RUN 300)

ξ	W_a † cm	$\frac{W_a}{d}$ ‡	σ_w^2 § cm^2	$\overline{\sigma_f^2}$ †† cm^2	σ_g^2 ‡‡ cm^2	σ_M^2 §§ cm^2	$\frac{\sigma_g^2}{\sigma_M^2}$	$\frac{\sigma_w^2}{\sigma_g^2}$
	1	2	3	4	5	6	7	8
3.2	3.28	0.19	0.48	0.70	1.65	2.35	0.70	0.29
4.1	3.62	0.21	0.96	0.88	2.14	3.02	0.71	0.45
5.0	4.96	0.29	1.51	1.63	2.71	4.34	0.62	0.56
5.7	5.44	0.32	1.83	1.97	3.51	5.48	0.64	0.52
6.5	5.60	0.33	2.48	2.12	3.71	5.83	0.63	0.67
7.5	5.70	0.34	3.18	2.23	3.20	5.43	0.59	0.99
8.6	7.98	0.47	8.12	4.49	8.32	12.81	0.65	0.98
9.5	7.92	0.47	6.68	4.33	10.17	14.50	0.70	0.66

† W_a = mean plume width (Eq. 6.23)

‡ Flow depth d = 17.00 cm

§ σ_w^2 = variance of the plume width (Eq. 6.24)

†† $\overline{\sigma_f^2}$ = mean variance of the instantaneous concentration distribution (Eq. 3.49)

‡‡ σ_g^2 = variance of the fluctuation of the plume centroid (Eq. 3.50)

§§ σ_M^2 = variance of the mean concentration distribution (Eq. 3.25)

calculated by

$$W_a = \frac{1}{N} \sum_{i=1}^{N} W(i) \tag{6.23}$$

where $W(i)$ = instantaneous plume width at the i^{th} time interval, and N = total number of picture frames analyzed. In general, N was near 100, and the time interval was 1/6-sec. Column 2 shows the plume width W_a/d relative to the flow depth. The variance σ_w^2 of the plume width was evaluated by

$$\sigma_w^2 = \frac{1}{N} \sum_{i=1}^{N} W^2(i) - W_a^2 \, . \tag{6.24}$$

Values of σ_w^2 are listed in Column 3.

The variances $\overline{\sigma_f^2}$ of the instantaneous concentration distribution, σ_g^2 of the plume centroid, and σ_M^2 of the mean concentration distribution calculated, respectively, by Eqs. 3.49, 3.50, and 3.14 are tabulated in Columns 4, 5, and 6. The ratios of the variances σ_g^2/σ_M^2 and σ_w^2/σ_g^2 are entered in Columns 7 and 8. It should be mentioned that $\sigma_M^2 = \overline{\sigma^2}$, the depth-averaged variance of the transverse distribution of the mean tracer concentration calculated in Phase I.

Table 6.6 shows that the mean width of the instantaneous plume and all variances tabulated generally increased with ξ. The variance σ_g^2 due to the fluctuation of the plume centroid was consistently greater than the mean variance $\overline{\sigma_f^2}$ of the instantaneous cross-wise distribution of the tracer concentration at all ξ. Hence the ratio of σ_g^2 to the total variance σ_M^2 was always greater than 0.50 (an average value of 0.66).

Therefore for $\xi \leq 9.5$ (i.e. $x \leq 161.5$ cm), approximately 66% of the cross-wise mixing coefficient was due solely to the transverse oscillation of the plume centroid.

That the plume width variation became increasingly significant with increasing ξ is illustrated by the values of the ratio of the variances σ_w^2 and σ_g^2 listed in Column 8. As ξ increased from 3.2 to 8.6, σ_w^2/σ_g^2 steadily grew from 0.29 to 0.98. This indicated that, except very near the source, temporal variation of the plume width at a fixed station was significantly effective in determining the overall size of the plume.

The fluctuating plume analysis therefore shows that near the source, transverse oscillation of the plume centroid is the dominating motion of the plume. As x increases however, plume width variation becomes increasingly important such that near $x/d = 8$, the variances of the plume width and the centroidal motion are approximately equal.

6.C. CONCENTRATION VARIATIONS AT FIXED POINTS WITHIN THE PLUME

6.C.1. Transverse Distribution of the Intensity of Concentration Variation.

Figure 6.15 shows the transverse distribution of the rms σ_s of the concentration variation at various distances from the source. RUN 804 is used as an example, and all measurements were made at the level of tracer injection $\eta_h = 0.368$. All distributions were assumed symmetric about the plume axis $\zeta = 0$.

It is evident that at a fixed distance ξ from the source, each distribution was flat-topped with σ_s remaining at a fairly constant value

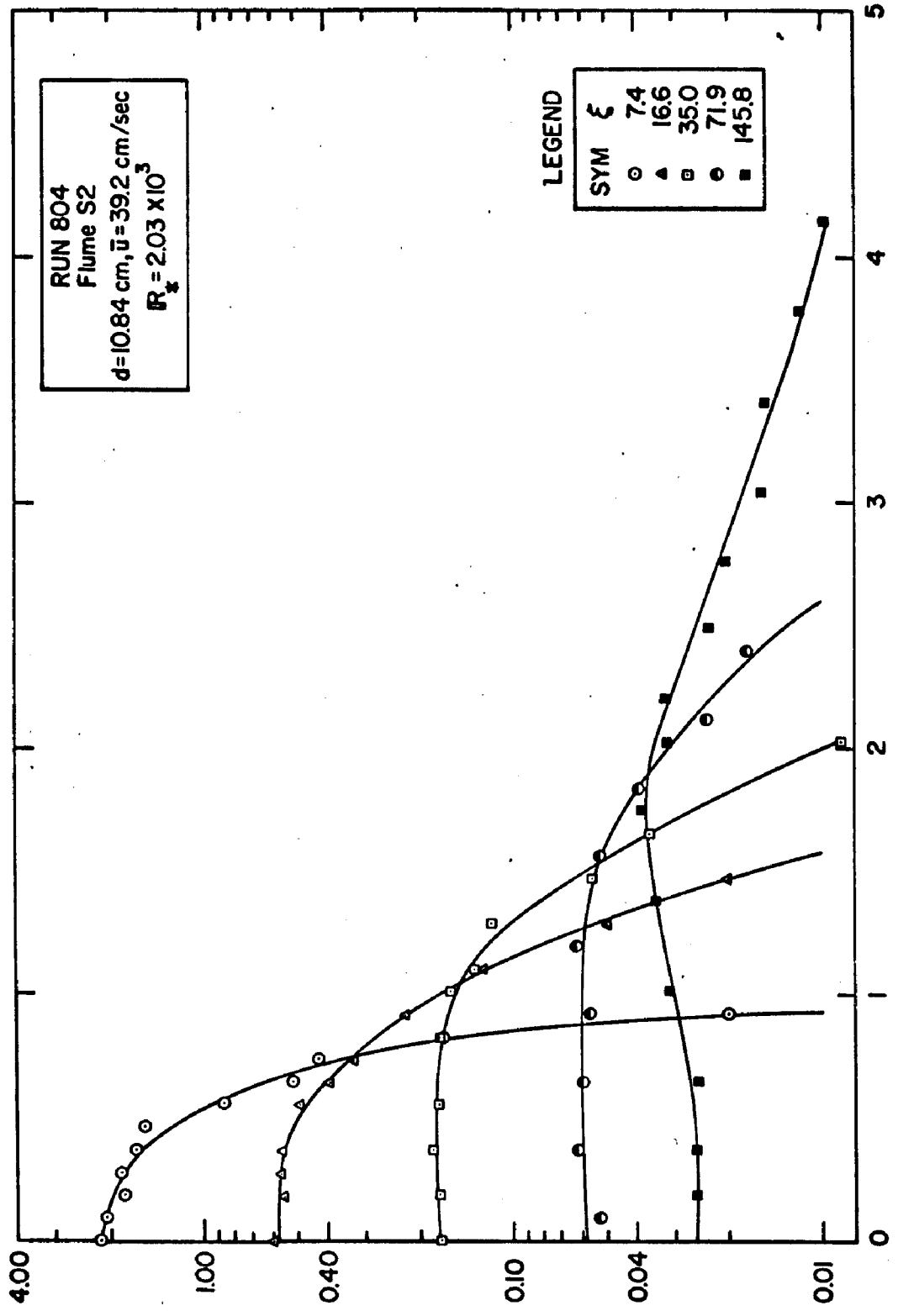

Fig. 6.15. Transverse distribution of the rms σ_s of the concentration fluctuation at various distances ξ from the source. Measurements made at the level of tracer injection $\eta_h = 0.368$; RUN 804.

near the plume axis and then dropping off at larger distances from the axis. The value of $|\zeta| = |z/d|$ where σ_s began to decrease increased with distance from the source. At $\xi = 145.8$, σ_s increased slightly with increasing $|\zeta|$ before decreasing at large distances from the plume axis. The σ_s distributions of Figure 6.15 are similar to those measured by Lee and Brodkey (51) for a continuous point source in a pipe flow.

Along the plume axis $z = 0$, σ_s decayed as a power of ξ such that $\sigma_s(0) \propto \xi^{-1.5}$. Thus the mean square fluctuation (msf) would decay as

$$s(0) \propto \xi^{-3.0}. \qquad (6.25)$$

This compares with $s(0) \propto \xi^{-3.0}$ measured by Becker et al. and reported by Csanady (15) for a continuous point source in an air stream of a pipe flow. Measurements by Lee and Brodkey (51) for a continuous point source in a turbulent water flow in a pipe indicated an attenuation rate $s(0) \propto \xi^{-1.9}$. For grid-generated turbulence, $s \propto \xi^{-3/2}$.

Transverse distributions of the coefficient of variation $C_v = \sigma_s/C$ were also developed. Typical plots are shown in Figure 6.16. Again the measurements were made in RUN 804 at the level of tracer injection $\eta_h = 0.368$. The plots show that at a given ξ, C_v was minimum but non-zero (about 1.0 or less) at or very near the plume axis, and increased with the transverse distance from the plume axis. The minimum value of C_v near or along the plume axis was denoted as V_1. A maximum value V_2 of C_v was attained near the edge of the plume at a point W_c from the point of minimum non-zero C_v. As $|\xi|$ increased further, C_v decreased--very sharply near the source and less distinctly far away.

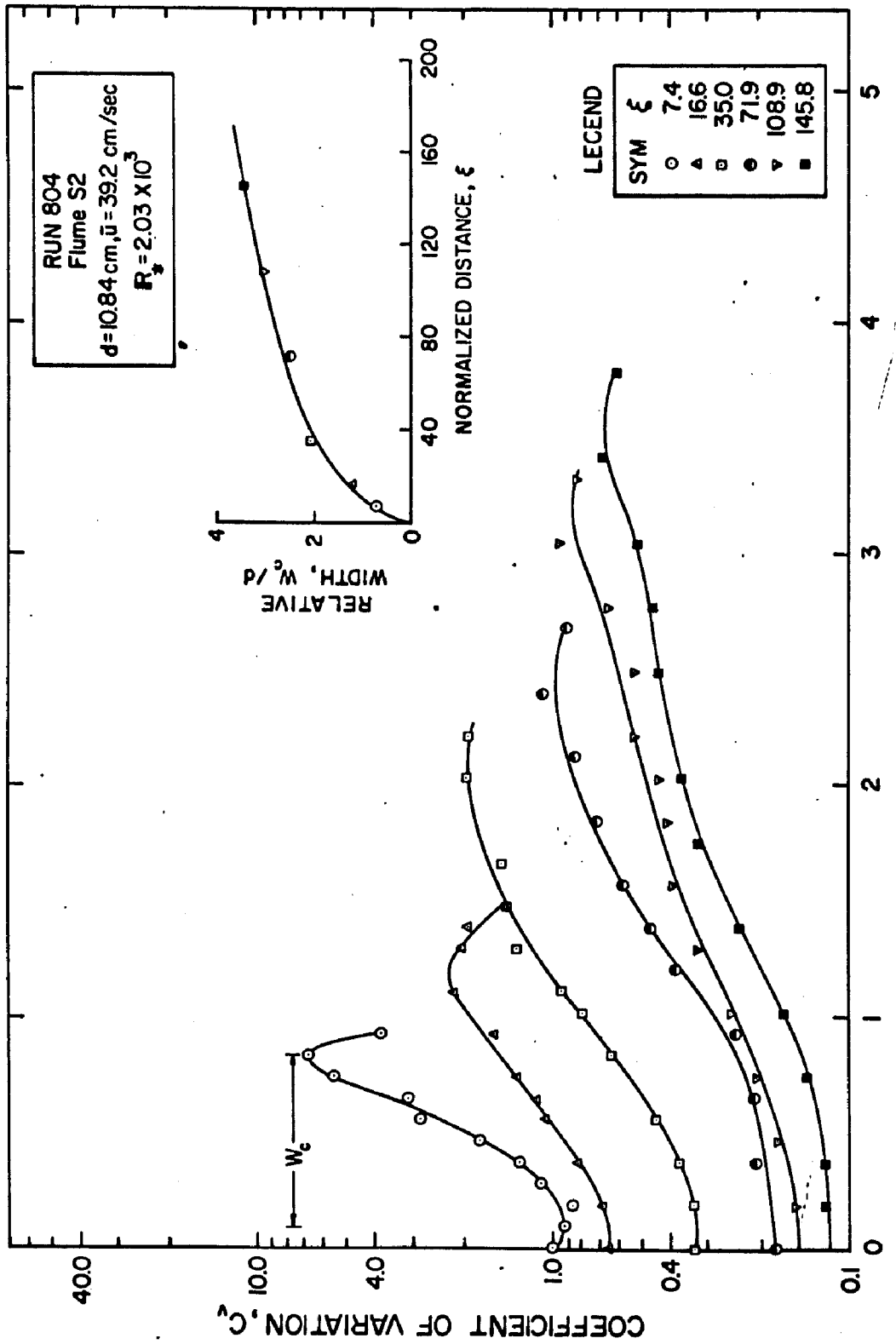

Fig. 6.16. Transverse distributions of the coefficient of variation $C_v = \sigma_s/C$ at several ξ. Measurements made at the level $\eta = \eta_h = 0.368$; RUN 804.

The relative effective width W_c/d of the C_v distribution grew with ξ. As shown in the inset of Figure 6.16, this growth was parabolic--an indication that V_2 probably occurred at a fixed position relative to the transverse distribution of the intermittency factor, I_f. Further investigation revealed that for all ξ, $C_v = V_2$ where $I_f = 0.05$. From Figure 6.5, this corresponds to the point where

$$\frac{z - \tilde{z}}{\sigma_I} = -1.5, \qquad (6.26)$$

which is a position near the extreme outer edge of the plume.

6.C.2. Distribution of the Peak-to-Average Ratio, P_a.

Figure 6.17 shows the transverse distribution of the peak-to-average ratio P_a for $\zeta \leq 0$ at $\xi = 7.4$, 16.6, 35.0, 71.9, 108.9, and 145.8 as calculated in RUN 804. The flow depth was 10.84 cm and all measurements were made at the level of tracer injection $\eta_h = 0.368$.

The distributions were very closely similar to those of C_v shown in Figure 6.16. At a given ξ, P_a increased from a low value P_1 (about 5.0 at $\xi = 7.4$ for RUN 804) at or very near the plume axis to a maximum P_2 (about 126 for $\xi = 7.4$ for RUN 804) near the plume edge.

The effective width W_p of the P_a distribution measured as the transverse distance between the points of P_1 and P_2 increased with distance from the source. As shown in the inset of Figure 6.17, the growth rate was parabolic--such that at a given ξ, $W_p \approx W_c$. As a result of the close similarity between the two sets of distributions,

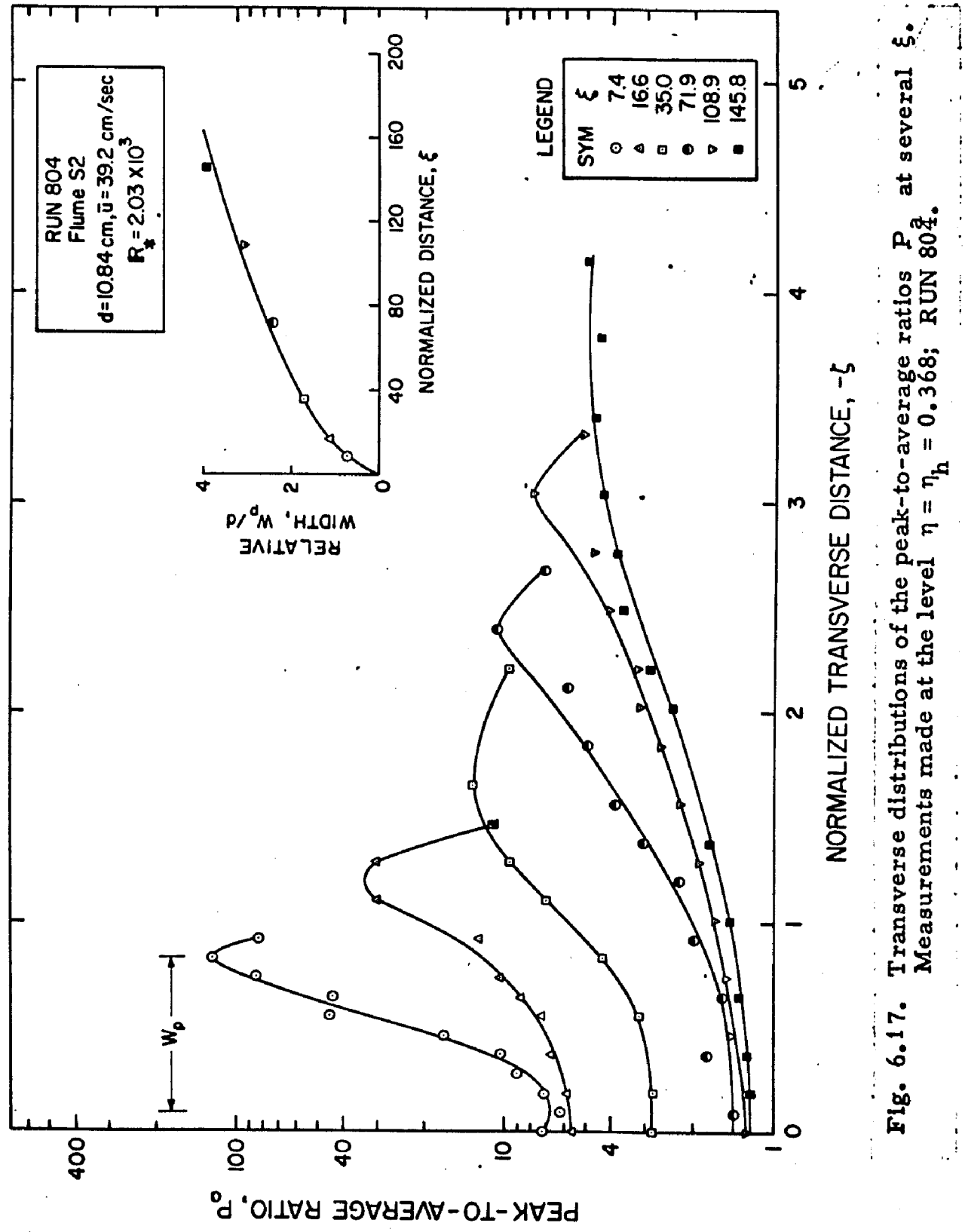

Fig. 6.17. Transverse distributions of the peak-to-average ratios P_o at several ξ. Measurements made at the level $\eta = \eta_h = 0.368$; RUN 804.

points of maximum and minimum P_a coincided with those of C_v. This means therefore that within the plume, the region of high (or low) peak values relative to the mean concentration C is coincident with the region of high (or low) msf relative to C.

It was found that the peak-to-average ratios P_1 (along $\zeta = 0$) and P_2 (along $\zeta = W_p/d$), attenuated with distance from the source. As shown in Figure 6.18, both V_1 and V_2 decayed approximately as the (-0.80)-power of ξ. The peak-to-average ratios P_1 and P_2 also decayed as $\xi^{-0.80}$ but P_1 approached an asymptotic value fairly rapidly. In the present study $P_1 \rightarrow 1.10$ usually for $\xi \geq 100$. Theoretically the ultimate asymptote of P_a is 1.0 as $\xi \rightarrow \infty$.

Comparison of the preceding results with the summary shown in Table 3.1 reveals that P_a decayed more rapidly in atmospheric turbulence than in the present flume measurements. In the atmosphere, $P_a \propto \xi^{-1.0}$. Along $\zeta = 0$, $C(= C_{max}) \propto \xi^{-1.0}$. Hence the instantaneous peak concentration along the plume axis varies as $\xi^{-2.0}$. From the present study, $P_1 \propto \xi^{-0.80}$ and $C_{max} \propto \xi^{-0.53}$. Therefore the instantaneous peak concentration along $\zeta = 0$ varies approximately as $\xi^{-1.33}$. The accelerated decay rate in the atmosphere is due to both three-dimensionality and the enormous range of eddy sizes found in the atmosphere.

For mixing in the atmosphere, the plume size is such that the eddies effecting the mixing are within the inertial subrange. Thus using Eq. 3.15 proposed by Gifford (16, 53), $P_a \propto \xi^{-1}$ since $\overline{\overline{\sigma_f^2}} + \sigma_g^2 \propto \xi^2$ and $\overline{\overline{\sigma_f^2}} \propto \xi^3$ (see for example Okubo (67)). At large ξ, the plume size is so large that both $\overline{\overline{\sigma_f^2}} + \sigma_g^2$ and $\overline{\overline{\sigma_f^2}}$ are propor-

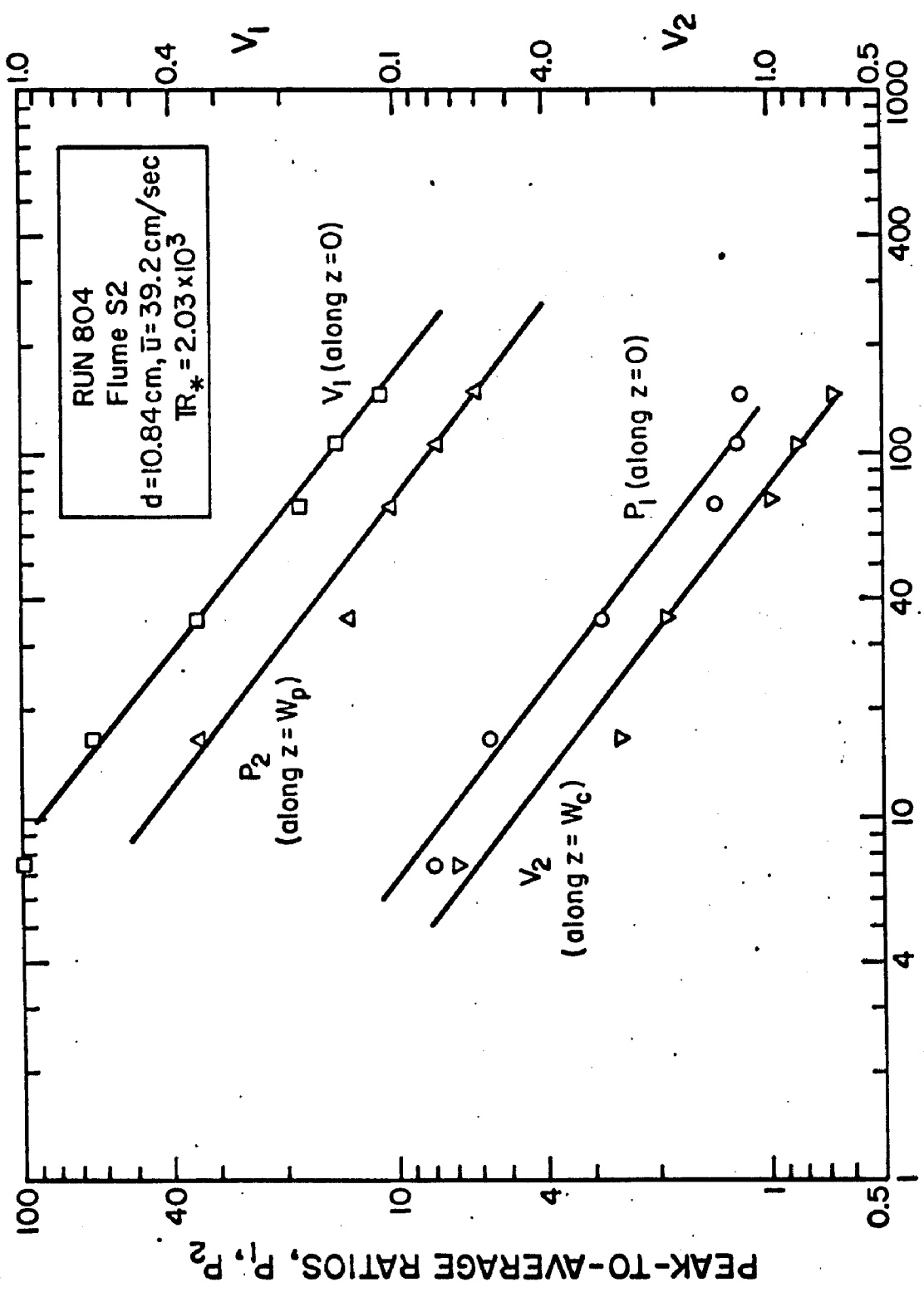

Fig. 6.18. Attenuation of the peak-to-average ratios P_1 (along $z = 0$), P_2 (along $z = W_p$), and of the coefficients of variation V_1 (along $z = 0$), V_2 (along $z \equiv W_c$) with ξ; RUN 804.

tional to ξ. Hence as $\xi \rightarrow \infty$, $P_a \rightarrow 1.0$. In the flume, the plume width is of the same order as the flow dimensions and hence of the scale of trubulence. Again as $\xi \rightarrow \infty$, $P_a \rightarrow 1.0$. But the range of ξ where eddies are within the inertial subrange is very small (very close to the source). Hence the range of ξ over which measurements were made in the flume is intermediate between $P_2 \propto \xi^{-1.0}$ and $P_2 \propto \xi^{0}$, as the present results indicate.

6.C.3. Probability Density Functions of Concentration Variations. The probability density function $g(c')$ for concentration fluctuations at fixed points was determined as outlined in Chapter 3. It was found that a more adequate analysis required a higher sampling rate and greater probe sensitivity than were used during the experiments.

Nevertheless, some broad conclusions could be drawn from the present study. It was discovered, for example, that various forms of $g(c')$ prevailed at different parts of the plume. Very near the source, $g(c')$ was strongly skewed and Rayleigh type indicating a dominance of low concentration levels at points where σ_s was high. Farther away from the source and within the plume interior, $g(c')$ was generally symmetrical about $c' = 0$, and was either bimodal or weakly Gaussian. Along the plume edges both near the source and far away, $g(c')$ was again strongly skewed.

In view of the complicated nature of the fluctuations, it was felt that a more sensitive detection system be used for further detailed study of the probability density of the fluctuation of concentration.

6.D. SUMMARY DISCUSSION (Phase II)

The temporal variation of tracer concentration was analyzed using three models. The first was a fluctuating plume front model which utilized the concept of intermittency to distinguish three regions of the plume cross section:

a. a central core of continuous record above the threshold concentration,

b. an intermediate region where tracer concentration was only intermittently above the threshold,

c. an outer region where the threshold was never exceeded.

The second model considered the entire plume as fluctuating back and forth transverse to the direction of flow. The variances of the instantaneous, transverse concentration distribution $\overline{\sigma_f^2}$, of the fluctuation of the plume centroid σ_g^2, and of the instantaneous plume width variation σ_w^2 were determined and related to each other.

The third model determined the intensity and probability density of concentration variation at fixed points within the plume. The rms-value and the temporal coefficient of variation were determined. Peak-to-average values were calculated.

At any given level of the flow, a plume cross section could, therefore, be characterized by four parameters: (i) the mean tracer concentration C above the threshold, C_t, (ii) the intermittency factor I_f which denotes the fraction of the total time that tracer concentration exceeds C_t, (iii) the rms-value σ_s which indicates the intensity of concentration fluctuations about the mean C, and (iv) the frequency of zero occurrence ω_0 which is the frequency at which the front $C = C_t$

sweeps by a fixed point in one direction only. Typical transverse distributions of these variables normalized by their maximum values at the fixed station and level of flow are plotted in Figure 6.19. All values were measured in RUN 804 at the level of tracer injection and at a distance $x/d = 16.6$ from the source.

Figure 6.19 shows the relative positions of the various distributions from each other. The curve of the rms distribution $\sigma_s(\zeta)$ lay between those of the mean concentration $C(\zeta)$ and the intermittency factor $I_f(\zeta)$. The 50% intermittency factor occurred at a point where the rms-value was 32% and the mean tracer concentration only 12% of their respective maximum values along the plume axis. The point of maximum ω_0 was usually close to its theoretical point of occurrence: $I_f = 0.50$.

The intermittency factor concept was found to be a very useful tool for analyzing concentration fluctuation. It not only furnished values of the duration and frequency of occurrence of concentration above the threshold but also provided a link between the fluctuation studies of Phase II and the analysis of the mean concentration of Phase I. Since the extreme limit, W_f, of the plume boundary where $I_f = 0$ and the standard deviation σ of the transverse distribution of the mean tracer concentration grew parabolically, the two parameters were related as simple ratios. It was found that for the smooth-boundary experiments,

$$\frac{W_f}{2\sigma} = 1.75, \tag{6.27}$$

and for the rough-bottom flume,

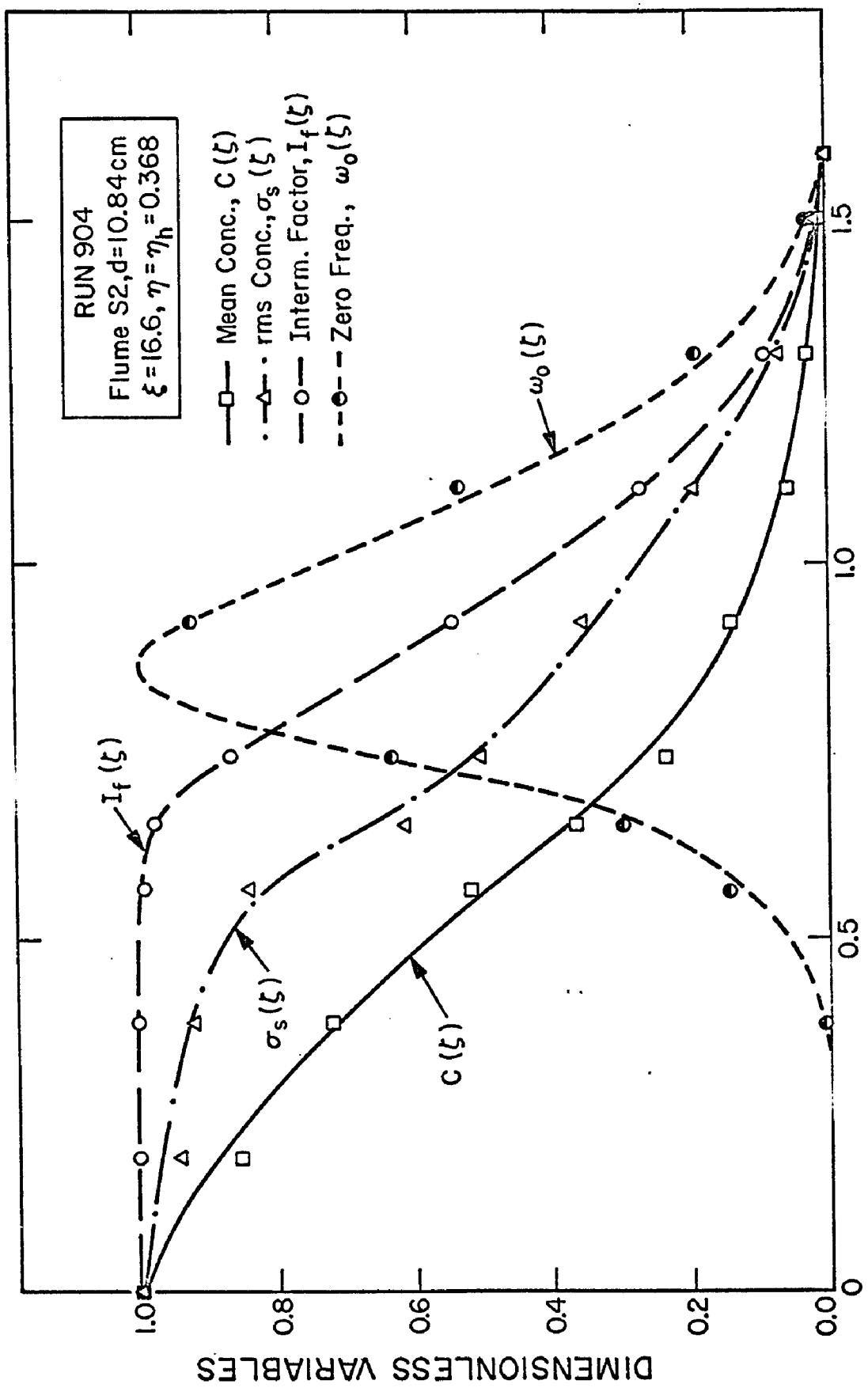

Fig. 6.19. Typical transverse distributions of the mean concentration C, the rms of concentration fluctuation σ_s, the intermittency factor I_f, and the frequency of zero occurrence ω_0 at a fixed distance x/d = 16.6 from the source; RUN 804.

$$\frac{W_f}{2\sigma} = 1.61. \qquad (6.28)$$

The intermittency factor analysis, however, could not distinguish the transverse fluctuation of the plume front from a purely random phenomenon. It showed nevertheless that for $x/d \geq 7.4$, the motion of the opposite edges of the plume was not predominantly due to either of two hypotheses: the meandering of the entire plume or the pulsation of the plume width.

The fluctuating plume model showed that near the source ($x/d \leq 9.5$), the fluctuation of the plume centroid contributed substantially to the overall width of the plume at any fixed station with $\sigma_g^2/\overline{\sigma^2} \approx 0.66$. The temporal variation of the plume width became increasingly important with distance from the source such that as x/d increased from 3.2 to 8.6, $\sigma_w^2/\overline{\sigma^2}$ increased from 0.29 to 0.98.

Statistical analysis revealed that at a given station, the fluctuation intensity of tracer concentration was greater near the plume axis and decreased at large transverse distances z from the axis (i.e. near the plume edges). The result was a flat top distribution illustrated in Figures 6.15 and 6.19. Thus the coefficient of variation C_v was low near the plume axis, increased to a maximum V_2 near the plume edges and then dropped off for further increase in z. Similarly the peak-to-average ratio P_a at a given station was small ($= P_1$) near or at $z = 0$, increased to a maximum P_2 near the plume edges and decreased as z increased further. It was found that both V_2 and P_2 occurred where $I_f = 0.05$.

It should also be noted that near the source ($x = 80$ cm for

example) $P_1 \approx 7.0$ and P_2 could be as high as 200. Both P_1 and P_2 attenuated as the (-0.8)-power of x, and at large x P_1 approached an asymptotic value of approximately 1.10.

CHAPTER 7

SUMMARY AND CONCLUSIONS

A set of experiments was performed in an open-channel to establish the characteristics of transverse mixing in a turbulent shear flow. A neutrally-buoyant tracer was continuously injected at ambient velocity at a point within the flow. Injection was parallel to the flow. Tracer concentrations were measured at various locations downstream of the source and analyzed in two phases. In Phase I, distributions of the time-averaged concentration were studied. In Phase II, concentration variations were analyzed. A summary of the principal results is given below.

7.A. RESULTS RELATED TO PHASE I

1. The transverse distribution of the time-averaged tracer concentration C was Gaussian at all levels of the flow. This self-similarity was preserved at all distances x downstream of the source (extending from 4 to 611 times the depth) regardless of whether the flow boundaries were hydraulically smooth or rough. (Figures 5.1, 5.2, and 5.3).

2. The variance σ^2 of the transverse distribution of C (evaluated numerically by Eq. 5.3) grew linearly with x at all levels of the flow. The depth-mean value $\overline{\sigma^2}$ of the variance also grew as a linear function of x. (Figures 5.4 through 5.8).

3. A depth-averaged coefficient of transverse mixing $\overline{D}_z$ was

defined and calculated by the relation

$$\overline{D}_z = \frac{1}{2}\,\overline{u}\,\frac{d\overline{\sigma^2}}{dx}\,, \qquad (5.5)$$

where $\overline{u}$ = mean flow velocity at a flume cross section. A generalized form of the transverse mixing coefficient was derived from the convective-diffusion equation and evaluated by

$$D_z(x,y) = \frac{1}{2}\left[u\,\frac{\partial\sigma^2}{\partial x} - \frac{\partial}{\partial y}\left(D_y\,\frac{\partial\sigma^2}{\partial y}\right)\right], \qquad (7.1)$$

where u is the flow velocity at the flow level y, and D_y is the vertical diffusivity. Since the transverse distribution of C was Gaussian at a given flow level y, a mixing coefficient could be defined for that level (of homogeneous turbulence) by

$$D_z(y) = \frac{1}{2}\,u\,\frac{\partial\sigma^2}{\partial x}\,. \qquad (5.9)$$

4. The normalized depth-averaged transverse mixing coefficient $\overline{\theta} = \overline{D}_z/u_*d$ was found to depend on the aspect ratio, $\lambda = d/W$, where d = flow depth, W = flume width, and u_* = (bed) shear velocity. The dimensionless coefficient $\overline{\theta}$ decreased with increasing λ ranging from 0.24 at $\lambda = 0.015$ to 0.093 at $\lambda = 0.200$. Comparison of the present results with measurements by past investigators showed that at a given λ, $\overline{\theta}$ for field experiments was about twice the value measured in laboratory flumes. (Figures 5.9 and 5.10).

5. The transverse mixing coefficient D_z evaluated by either Eq. 7.1 or Eq. 5.9 varied over the depth tending to be greatest near

the water surface where the flow velocity was highest. (Figures 5.11 through 5.13).

6. Near source behavior of the plume was studied by calculation of the depth variation of material within the plume. Numerical solution of the convective-diffusion equation assuming that the vertical distribution of D_y was parabolic agreed very closely with experimental measurements for various levels of tracer injection η_h. This indirectly confirms that the vertical profile of D_y is indeed parabolic. (Figures 5.14 and 5.15).

7. The vertical distribution of the normalized concentration β along the plume axis was skewed because of the vertical variations of u, D_y, and D_z. The point of maximum β initially rose to the water surface when tracer was injected at levels $\eta_h \geq 0.632$, and dropped to the flume bottom for $\eta_h \leq 0.50$. On attaining the limiting level ($\eta = 1.0$ or 0.0), the point of maximum β "rebounded" into the flow interior.

8. The maximum mean concentration $C(x,y,0)$ along the plume axis, attenuated, for a given experiment, as a power of x at all levels of the flow. The attenuation for $x/d > 18.3$, could be represented by $C(x,y,0) \propto x^{-\alpha}$. The exponent α approached 0.50 for low aspect ratios λ and increased with increasing λ. The attenuation rate was accentuated by flume boundary roughness with $\alpha \approx 0.61$ when the flume bottom was roughened with rocks. (Figures 5.16 through 5.20; Table 5.5).

9. Iso-concentration maps developed on cross-sectional and lateral planes (parallel to the flume bottom) were used to establish

detailed distribution of material within the plume, and to locate zones of high tracer concentration. (Figures 5.21 through 5.25).

7.B. RESULTS RELATED TO PHASE II

The temporal variation of concentration was analyzed by three methods. The first is the intermittency factor model which defined an intermittency factor I_f as the fraction of the total time that tracer concentration exceeded the threshold C_t (or background) concentration at a given point. The second characterized the entire plume as a cloud fluctuating across the flow direction. Motion pictures of the plume were taken from above the water surface and the plume boundaries used to compute different variances. In the third method, fluctuations of the tracer concentration at fixed points were analyzed by the usual statistical method. The principal results of all analyses are summarized below.

1. By utilizing the intermittency factor technique, the plume cross section was characterized by three regions: a central core where tracer concentration was always greater than the threshold C_t ($I_f = 1.0$), an intermediate region of intermittency where concentration was only intermittently above C_t ($0 < I_f < 1.0$), and an outer zone where the threshold was never exceeded. (Figure 3.4).

2. At given distance x downstream of the source and level of flow y, the transverse distribution of the intermittency factor was self-similar and could be represented universally by the error function relationship:

$$I_f(\zeta) = \frac{1}{2}(1 + \text{erf}\, \zeta_I) \qquad (6.1)$$

where

$$\zeta_I = \frac{z - \tilde{Z}}{\sqrt{2}\,\sigma_I} ,$$

$\tilde{Z}$ = mean position of the plume front (or plume edge where the concentration equalled C_t) calculated by Eq. 3.43, and σ_I = standard deviation of the I_f-distribution calculated by Eq. 3.44. Eq. 6.1 indicates therefore that the position of the plume front is normally distributed. (Figure 6.5).

3. The geometric characteristics of the plume front fluctuation were studied. The extreme limit of the intermittency region where $I_f = 0.0$ was denoted by W_f; the outer edge of the inner core of continuous record by Δ; the mean position of the plume front where $I_f \approx 0.50$ by $\tilde{Z}$; and the variance of the I_f-distribution by σ_I^2. Since the fluctuations of the plume fronts were assumed symmetric about the plume axis $z = 0$, measurements were made only on one side and W_f, Δ, and $\tilde{Z}$ were measured from $z = 0$. From dimensional analysis it was found that measured values of W_f closely fitted the curve:

$$\left(\frac{W_f}{d}\right)^2 = 3.58\, R_w \left(\frac{\chi}{d}\right)\left(\frac{u_{*b}}{\bar{u}}\right) \qquad (6.9)$$

where $R_w = (f_s/f_r)^{1/4}$, and f_s, f_r are, respectively, the mean values of the bed friction factors for the smooth boundary and rough bottom experiments, χ = value of x corrected slightly for the virtual origin of W_f, and u_{*b} = bed shear velocity. For the smooth boundary, u_{*b}

becomes u_* and $R_w = 1.0$.

Dimensional analysis also showed that the mean position of the plume front could be represented by

$$\left(\frac{\tilde{Z}}{d}\right) = 3.31\ R_z\left(\frac{\chi}{d}\right)^{2/3}\left(\frac{u_{*b}}{\bar{u}}\right) \qquad (6.12)$$

where $R_z = (f_s/f_r)^{1/3}$. Since $\tilde{Z}$ was half-way between the outer edge of the central core Δ and W_f, Δ could be calculated by $\Delta = 2\tilde{Z} - W_f$.

The variance σ_I^2 of the I_f-distribution initially grew as the 2/3-power of χ/d and attained a maximum value $2\sigma_I/d \approx 0.8$. (Figures 6.6, 6.7, 6.8, and 6.9).

4. The frequency at which the plume front sweeps by a point was denoted as the frequency of "zero occurrence" ω_0. It was found that $\omega_0(z)$ was normally distributed about $z = \tilde{Z}$ attaining a maximum value $\overline{\omega_0}$ at $z = \tilde{Z}$ and becoming zero at $I_f = 0$ and $I_f = 1.0$. Calculations showed that this frequency was unrelated to the vortex shedding of the tracer injector but that plume front oscillation was a result of a diffusive type process characteristic of turbulent mixing. The characteristic wave length of the front oscillation was approximately equal to the flow depth. (Figure 6.10; Table 6.4).

5. The intermittency factor measurements were linked to Phase I of this study by the fact that W_f could be related to the standard deviation σ of the transverse distribution of the mean concentration. For the smooth-boundary experiments,

$$\frac{W_f}{2\sigma} = 1.75 \qquad (6.27)$$

and for the rough-bottom flume

$$\frac{W_f}{2\sigma} = 1.61 \ . \qquad (6.28)$$

6. A cross-correlation analysis was made of the opposite edges of the plume by comparing the ON (when $c > C_t$) and OFF (when $c \leq C_t$) events of the two points where $z = \tilde{Z}$ and $z = -\tilde{Z}$. This was done to test if plume front oscillation was a result of a pulsating motion of the plume width or a meandering of the entire plume. The test could not distinguish the plume front fluctuation from a purely random behavior, and indicated that neither motion dominated the other for $x/d \geq 7.4$. (Table 6.5).

7. From analysis of the motion pictures of the plume, the second method of analysis showed however that very near the source ($x/d < 6.5$), oscillation of the plume centroid was a dominating contributor to the total variance of the cross-wise mean concentration distribution. But as x increased, plume width variation became increasingly important so that at about $x/d = 10.0$, the variance σ_w^2 due to plume width variation was approximately equal to the variance σ_g^2 of the oscillation of the plume centroid. For $x/d \leq 10$, σ_g^2/σ^2 was approximately 0.66. (Figures 6.13, 6.14; Tables 6.5, 6.6).

8. Statistical analysis revealed that the transverse distribution of the rms-value σ_s of the concentration fluctuation was roughly self-similar at all x. The rms-value was highest near the plume axis and decayed near the edges--giving rise to a "flat top" distribution. The msf along the plume axis decayed as the (-3)-power of x as compared to the

(-3/2)-power measured for grid-generated turbulence. (Figure 6.15).

The transverse distribution of the coefficient of variation $C_v = \sigma_s/C$ was very similar to that of the peak-to-average ratio P_a with each variable increasing from a low value near the plume axis to a maximum near the plume edges. Maximum P_a (denoted as P_2) and maximum C_v (denoted as V_2) occurred where $I_f = 0.05$. The low values of P_a and C_v near or along the plume axis were designated P_1 and V_2 respectively. It was found that P_1, P_2, V_1, and V_2 attenuated approximately as the (-0.8)-power of x with P_1 approaching an asymptotic value of 1.10. Near the source P_1 could be as large as 10 and P_2 as 200. (Figures 6.16, 6.17, and 6.18).

9. Statistical analysis also showed that various forms of the probability density function $g(c')$ could be measured at different parts of the plume. In most sections of the plume, $g(c')$ was strongly skewed and it was only very near the plume axis that $g(c')$ became moderately symmetric about $c' = 0$. Better instrumentation and further study are, however, recommended.

10. Typical transverse distributions and the relative positions of the mean concentration C, the rms-value σ_s, the intermittency factor I_f, and the zero frequency ω_0 are summarized by the plots shown in Figure 6.19.

LIST OF SYMBOLS

a_t	attenuation values on analog recorder
A_0	cross-sectional area of tracer injector
c	instantaneous tracer concentration
C	time mean value of the tracer concentration
c'	c-C: concentration fluctuation
C_b	background concentration
C_{max}	peak value of C at given x and y
C_0	initial tracer concentration at injection
C_t	threshold concentration
C_v	σ_s/C: coefficient of variation
d	normal depth
$d_{ij}(t)$	generalized dispersion; Eq. 2.28
D	characteristic lateral mixing coefficient
D_p	transverse mixing coefficient for floating particles
D_s	diffusion coefficient for msf
D_{ij}	mass transfer coefficient tensor
D_x, D_y, D_z	turbulent mixing coefficient in the x, y, and z directions respectively
$\overline{D}_y, \overline{D}_z$	depth-averaged values of D_y, and D_z respectively
e	2.718...
E	mean rate of energy dissipation per unit mass of fluid
E_{ij}	eddy viscosity tensor
$f(x_1;y,z,t)$	instantaneous concentration distribution at fixed station x_1
f_*	mean friction factor for smooth flume boundaries

f_{*b}	bed friction factor
f_s	mean value of the friction factor for smooth-boundary experiments in Phase II
f_r	mean value of the friction factor for rough-bottom experiments in Phase II
$\mathbb{F}$	Froude number
$F(y,t)$	$\int_{-\infty}^{\infty} f(x_1;y,z,t)\, dz$
g	acceleration due to gravity
$g(c')$	frequency density of the concentration fluctuation
$h(z,t)$	intermittency function at a fixed point z defined by Eq. 3.31
$i_f(z)$	$\frac{\partial I_f(z)}{\partial z}$: probability density function
$I_f(z)$	intermittency factor defined as the function of the total time that a threshold concentration is exceeded at a point z
$I(n), J(n)$	Fourier coefficients
K	a constant
K_z	displacement of the plume centroid in the z-direction
ℓ, L_z, L_1	characteristic length scales
L	characteristic half-width of the intermittency region
L_f	longitudinal length scale of the oscillation of the plume front
$\overline{L}_f$	mean value of L_f
M_q	q^{th} moment of the transverse distribution of C ($p = 0,1,2,\ldots$); Eq. 2.21
M_{2n}	M_2/d^2
$\overline{M}_0(\xi,\eta)$	$M_0(\xi,\eta)/(Q_s/\overline{u}d)$; Eq. 5.19
n_i	frequency of vortex shedding
$p(T)$	probability density of both "occurrence" and "non-occurrence" of the intermittency function

$P(\underline{x},t)$	probability that a point defined by position vector $\underline{x}$ lies within a marked fluid at time t
P_a	peak-to-average ratio
P_c	cumulative value of the mean concentration; Eq. 5.1
P_1	peak-to-average ratio along the plume axis
P_2	maximum value of P_a at given x and y
$p_1(T_1)$	probability density of the "occurrence" pulse lengths
$p_2(T_2)$	probability density of the "non-occurrence" pulse lengths
Q	flow discharge
Q_s	source strength for tracer; Eq. 2.61
r	hydraulic radius
r_t	rise time of the probes
R	source strengh/unit volume
$\mathbb{R}$	Reynolds number
$R(t')$	Lagrangian correlation coefficient; Eq. 2.24
$R(\omega)$	amplitude ratio of excitation frequency ω
$\mathbb{R}_*$	friction Reynolds number defined by Eq. 4.7
R_w	$(f_s/f_r)^{1/4}$
R_z	$(f_s/f_r)^{1/3}$
s	$\overline{c'^2}$, mean square fluctuation
s_k	skewness factor
S	sink strength/unit volume
S_f	energy slope
S_0	flume slope
t	time
t_0	arbitrary time base

T_m	sampling period or period of averaging; Eq. 2.7
T_1	pulse length (of "occurrence") when the threshold is exceeded
T_2	pulse length (of "non-occurrence") when the threshold is not exceeded
$T_0(z)$	period of the plume front oscillation at point z
$\overline{T}_0(z)$	mean value of $T_0(z)$
u,v,w	time-averaged velocity components in the x, y, and z directions respectively
$\overline{u}$	mean velocity through flume cross section
u_*	$\sqrt{\tau_0/\rho}$: shear velocity
u_a	depth-integrated flow velocity at a lateral position z
u_{*b}	bed shear velocity
u_i	instantaneous fluid velocity in the x_i direction, i = 1,2,3
u_i'	fluctuating component of u_i, i = 1,2,3
$\overline{u}_n$	u_a/u_*
u_0	injection velocity of tracer
u_{max}	maximum velocity at the water surface
U_i	time-mean velocity in the x_i direction; i = 1,2,3
v_*	a characteristic velocity
V_1	coefficient of variation along the plume axis
V_2	maximum value of C_v at given x and y
W	flume width
W_a	time-averaged value of the instantaneous plume width
W_f	extreme limit of the plume boundary where $I_f = 0.0$; Fig. 3.5
W(i)	effective width of the transverse distribution of concentration at the instant i

x	Cartesian coordinate in the direction of flow
x_i	coordinate in the i^{th} direction for $i = 1,2,3$
x_I	point where the inner core of continuous record ($I_f = 1.0$) intersects the plume axis
x_v	value of x at the virtual origin of W_f
$X_i(t)$	i^{th} component of the fluid particle displacement in time t
y	Cartesian coordinate in the vertical direction
z	Cartesian coordinate transverse to flow
$z_0(x_1;y)$	centroid of the time-mean concentration distribution at station x_1
$z_{0.5}$	value of z where $I_f = 0.50$
$z_c(x_1,y,t)$	centroid of the instantaneous concentration distribution at station x_1
$\tilde{Z}$	z-value of the mean position of the plume front at a given station and flow level; Fig. 3.5
$Z_f(t)$	z-position of the plume edge (front) at the instant t
α	exponent of ξ for attenuation of the mean concentration along plume axis; Eq. 5.24
$\beta(\xi,\eta)$	$c(\xi,\eta,0)/(Q_s/\bar{u}d)$, normalized concentration along the plume axis; Eq. 5.22
$\bar{\beta}(\xi)$	depth-averaged value of $\beta(\xi,\eta)$
γ	intermittency factor as it relates to turbulent or non-turbulent motion
γ_2	exponent: $\tilde{Z} \propto x^{\gamma_2}$
γ_3	exponent: $\sigma_I \propto x^{\gamma_3}$
$\delta(\ )$	Diract delta function
Δ	outer edge of the inner core of continuous record (where $I_f = 1.0$); Fig. 3.5
ϵ	error

ϵ_{ij} turbulent transport coefficient for a scalar

ϵ_m molecular diffusivity

ζ z/d: dimensionless transverse distance from plume axis

η y/d: dimensionless vertical distance from flume bottom

η_H dimensionless height of tracer injection from flume bottom

η_m value of η where, for a given station, M_0 is maximum

θ D_z/u_*d: dimensionless transverse mixing coefficient

$\overline{\theta}$ depth-averaged value of θ for entire reach of measurement

θ_p D_p/u_*d

$\theta_a(x)$ depth-averaged value of θ at a given station x

$\theta_1(\eta)$ dimensionless transverse mixing coefficient due to shear only; Eq. 5.10

κ von Kármán constant

λ d/W: the aspect ratio

λ_ϕ concentration microscale

ν kinematic viscosity

ξ x/d: dimensionless or normalized distance from the source

ξ_a value of ξ beyond which $\overline{\beta}(\xi)$ decays at a constant power of ξ

ξ_ℓ value of ξ beyond which $\overline{\sigma^2}$ grows linearly with ξ

π 3.14159...

ρ fluid density

σ^2 variance of the transverse distribution of the mean tracer concentration; Eq. 2.56

$\overline{\sigma^2}$ depth-averaged value of σ^2

σ_f^2 variance of the instantaneous transverse concentration distribution

σ_g^2 variance of the transverse fluctuation of the plume centroid

σ_I^2 variance of the distribution of the intermittency factor; Eq. 3.44

σ_M^2 $\sigma_f^2 + \sigma_g^2$

$\overline{\sigma_n^2}$ $\overline{\sigma^2}/d^2$: normalized variance

σ_p^2 variance of the transverse distribution determined by use of the probability method; Eq. 5.2

σ_s root-mean-square value of the concentration fluctuation

σ_w^2 variance of the plume width variation

τ local shear stress

τ_0 mean bottom shear stress

ϕ scalar concentration

Φ time mean value of ϕ

$\Phi_f(\lambda)$ curve fitted to plot of $\overline{\theta}$ versus λ for field experiments

$\phi(\omega)$ phase shift of excitation frequency ω

$\Phi(\lambda)$ curve fitted to plot of $\overline{\theta}$ versus λ for laboratory experiments

χ $x-x_v$: value of x corrected for the virtual origin of the ${}^vW_f(x)$ distribution

Ψ rate of dissipation of mean square concentration fluctuation

ω excitation frequency

$\omega_0(z)$ frequency of zero occurrence at point z

$\overline{\omega_0}$ value of ω_0 where the intermittency factor = 0.50

LIST OF REFERENCES

1. Elder, J. W., "The Dispersion of Marked Fluid in Turbulent Shear Flow", Journal Fluid Mechanics, Vol. 5, pp. 544-560, 1959.

2. Fischer, H. B., "Longitudinal Dispersion in Laboratory and Natural Streams", Report No. KH-R-12, W. M. Keck Laboratory of Hydraulics and Water Resources, California Institute of Technology, Pasadena, California, 1966.

3. Smith, F. B., "The Diffusion of Smoke from a Continuous Elevated Point-Source Into a Turbulent Atmosphere", Journal Fluid Mechanics, Vol. 2, pp. 49-76, 1957.

4. Vanoni, V. A., "Transportation of Suspended Sediment by Water", Transactions ASCE, Vol. 111, pp. 67-133, 1946.

5. Al-Saffar, A. M., "Eddy Diffusion and Mass Transfer in Open Channel Flow", Ph. D. Thesis, University of California, Berkeley, California, 1964.

6. Sullivan, P. J., "Dispersion in a Turbulent Shear Flow", Ph. D. Thesis, University of Cambridge, 1968.

7. Fischer, H. B., "Transverse Mixing in a Sand-Bed Channel", U. S. Geol. Survey Prof. Paper 575-D, pp. D267-D272, 1967.

8. Yotsukura, N., Fischer, H. B. and Sayre, W. W., "Measurement of Mixing Characteristics of the Missouri River Between Sioux City, Iowa, and Plattmouth, Nebraska", U. S. Geol. Survey Water-Supply Paper 1899-G, 1970.

9. Davar, K. S., "Diffusion From a Point Source Within a Turbulent Boundary Layer", Ph. D. Thesis, Colorado State University, Fort Collins, Colorado, 1968.

10. Townsend, A. A., "Local Isotropy in the Turbulent Wake of a Cylinder", Australian Journal of Scientific Research, Ser. A, Vol. 1, pp. 161-174, 1948.

11. Corrsin, S., and Kistler, A. L., "Free-Stream Boundaries of Turbulent Flows", NACA Report 1244, 1955.

12. Demetriades, A., "Turbulent Front Structure of an Axisymmetric Compressible Wake", Journal Fluid Mechanics, Vol. 34, pp. 465-480, 1968.

LIST OF REFERENCES (Continued)

13. Klebanoff, P. S., "Characteristics of Turbulence in a Boundary Layer with Zero Pressure Gradient", NACA Tech. Note 3178, 1954.

14. Fielder, H. and Head, M. R., "Intermittency Measurements in the Turbulent Boundary Layer", Journal Fluid Mechanics, Vol. 25, pp. 719-735, 1966.

15. Csanady, G. T., "Concentration Fluctuations in Turbulent Diffusion", Journal of Atm. Sciences, Vol. 24, pp. 21-28, 1967.

16. Gifford, F., "Statistical Properties of a Fluctuating Plume Dispersion Model", Advances in Geophysics, Vol. 6, pp. 117-137, 1959.

17. List, E. John, "The Stability and Mixing of a Density-Stratified Horizontal Flow in a Saturated Porous Medium", Report No. KH-R-11, W. M. Keck Laboratory of Hydraulics and Water Resources, California Institute of Technology, Pasadena, California, 1965.

18. Boussinesq, M. J., "Essai sur la Theorie des Eaux Courants", Memoirs, Presente par divers Savents, L'Academie de l'Institut de France, Vol. 23, pp. 1-680, 1877.

19. Reynolds, O., "On the Extent and Action of the Heating Surface of Steam Boilers", Reprint, Papers on Mechanical and Physical Subjects, Cambridge University Press, Vol. 1, pp. 81-85, 1900.

20. Batchelor, G. K. and Townsend, A. A., "Turbulent Diffusion", Surveys in Mechanics, Cambridge University Press, pp. 352-399. 1956.

21. Mickelsen, W. R., "Measurements of the Effect of Molecular Diffusivity in Turbulent Diffusion", Journal Fluid Mechanics, Vol. 7, pp. 397-400, 1960.

22. Dagan, Gedeon, "Dispersivity Tensor for Turbulent Uniform Channel Flow", Journal Hydraulics Division, ASCE, Vol. 95, No. HY5, pp. 1699-1712, 1969.

23. Sutton, O. G., "The Problem of Diffusion in the Lower Atmosphere", Quart. Jour. Royal Meteorol. Society, Vol. 73, pp. 257-281, 1947.

LIST OF REFERENCES (Continued)

24. Davies, D. R., "Three-Dimensional Turbulence and Evaporation in the Lower Atmosphere, I and II", Quart. Jour. of Mech. and Applied Math., Vol. 3, pp. 51-73, 1950.

25. Yih, C. S., "Similarity Solution of a Specialized Diffusion Equation", Trans. American Geophysical Union, Vol. 33, pp. 356-360, 1952.

26. Aris, R., "On the Dispersion of a Solute in a Fluid Flowing Through a Tube", Proc. Royal Society, Ser. A, Vol. 235, pp. 67-77, 1956.

27. Saffman, P. G., "The Effect of Wind Shear on Horizontal Spread From an Instantaneous Ground Source", Quart. Jour. Royal Meteorol. Society, Vol. 88, pp. 382-393, 1962.

28. Taylor, G. I., "Diffusion by Continuous Movements", Proc. London Math. Society, Ser. 2, Vol. 20, pp. 196-212, 1921.

29. Van Driest, E. R., "An Experimental Investigation of Turbulence Mixing as a Factor in the Transportation of Sediment in Open Channel Flow", Ph. D. Thesis, California Institute of Technology, Pasadena, California, 1940.

30. Kalinske, A. A. and Pien, C. L., "Eddy Diffusion", Industrial and Engineering Chemistry, Vol. 36, pp. 220-223, 1944.

31. Orlob, G. T., "Eddy Diffusion in Open Channel Flow", University of California, Berkeley, Sanitary Engineering Research Lab., Contribution 19, 1958.

32. Orlob, G. T., "Eddy Diffusion in Homogeneous Turbulence", Jour. Hydraulics Div., ASCE, Vol. 85, No. HY9, pp. 75-101, 1959.

33. Batchelor, G. K., "Diffusion in a Field of Homogeneous Turbulence", Australian Jour. of Scientific Research, Ser. A, Vol. 2, pp. 437-450, 1949.

34. Monin, A. S., "Survey of Atmosphereic Diffusion", Advances in Geophysics, Vol. 6, pp. 29-40, 1959.

35. Sayre, W. W., and Chang, F. M., "A Laboratory Investigation of Open-Channel Dispersion Processes for Dissolved, Suspended, and Floating Dispersants", U. S. Geol. Survey Prof. Paper 433-E, 1968.

LIST OF REFERENCES (Continued)

36. Kolmogoroff, A. N., "The Local Structure of Turbulence in Incompressible Viscous Fluid For Very Large Reynolds Numbers", Acad. Sci. URSS (Doklady), Vol. 30, No. 4, pp. 301-305, 1941.

37. Batchelor, G. K., "The Application of the Similarity Theory of Turbulence to Atmosphereic Diffusion", Quart. Jour. Royal Meteorol. Society, Vol. 76, pp. 133-146, 1950.

38. Sayre, W. W., and Chamberlain, A. R., "Exploratory Laboratory Study of Lateral Turbulent Diffusion at the Surface of an Alluvial Channel", U. S. Geol. Survey Circular 484, 1964.

39. Prych, E. A., "Effects of Density Differences on Lateral Mixing in Open-Channel Flows", Report No. KH-R-21, W. M. Keck Laboratory of Hydraulics and Water Resources, California Institute of Technology, Pasadena, California, 1970.

40. Engelund, F., "Dispersion of Floating Particles in Uniform Channel Flow", Jour. Hydraulics Div., ASCE, Vol. 95, No. 4, pp. 1149-1162, 1969.

41. Pien, C. L., "Investigation of Turbulence and Suspended Material Transportation in Open Channels", Ph. D. Dissertation, Graduate College of the State University of Iowa, Iowa City, Iowa, 1941.

42. Glover, R. E., "Dispersion of Dissolved or Suspended Materials in Flowing Streams", U. S. Geol. Survey Prof. Paper 433-B, 1964.

43. Patterson, C. C. and Gloyna, E. F., "Dispersion Measurement in Open Channels", Jour. Sanitary Engineering Div., ASCE, Vol. 91, No. SA3, pp. 17-29, 1965.

44. Batchelor, G. K., "Note on Free Turbulent Flows With Special Reference to the Two-Dimensional Wake", Jour. Aero. Sciences, Vol. 17, pp. 441-445, 1950.

45. Townsend, A. A., "The Fully Turbulent Wake of a Circular Cylinder", Australian Jour. of Scientific Research, Ser. A, Vol. 2, pp. 451-468, 1949.

46. Starr, V. P., "The Physics of Negative Viscosity Phenomena", McGraw-Hill, New York, N. Y., 1968.

LIST OF REFERENCES (Continued)

47. Batchelor, G. K., Townsend, A. A., and Howells, I. D., "Small Scale Variation of Convected Quantities Like Temperature in Turbulent Fluid", Journal Fluid Mechanics, Vol. 5, pp. 113-134, 1959.

48. Hinze, J. O., "Turbulence", Mc Graw-Hill, New York, N. Y., 1959.

49. Becker, H. A., Rosensweig, R. E., and Gwozdz, J. R., "Turbulent Dispersion in a Pipe Flow", Report AFCRL-63-727, Fuel Research Laboratories, M.I.T., Cambridge, Mass., 1963.

50. Gibson, C. H., and Schwarz, W. H., "Detection of Conductivity Fluctuations in a Turbulent Field", Journal Fluid Mechanics, Vol. 16, pp. 357-364, 1963.

51. Lee, J. and Brodkey, R. S., "Turbulent Motion and Mixing in a Pipe", American Institute of Chem. Engineering Journal, Vol. 10, No. 2, pp. 187-193, 1964.

52. Lowry, P., Mazzarella, D. A., and Smith, M. E., "Ground Level Measurements of Oil-Fog Emitted From a Hundred-Meter Chimney", Meteorlogical Monographs, Vol. 1, No. 4, pp. 30-35, 1951.

53. Gifford, F., "Peak to Average Concentration Ratios According to a Fluctuating Plume Dispersion Model", International Jour. of Air Pollution, Vol. 3, No. 4, pp. 253-260. 1960.

54. Smith, M. E., "The Variation of Effluent Concentrations From an Elevated Point Source", Archives of Industrial Health, Vol. 14, pp. 56-58, 1956.

55. Bradbury, L. J. S., "The Structure of a Self-Preserving Turbulent Plane Jet", Journal Fluid Mechanics, Vol. 23, pp. 31-64, 1965.

56. Gartshore, I. S., "An Experimental Examination of the Large-Eddy Equilibrium Hypothesis", Journal Fluid Mechanics, Vol. 24, pp. 89-98, 1966.

57. Sandborn, V. A., "Measurement of Intermittency of Turbulent Motion in a Boundary Layer", Journal Fluid Mechanics, Vol. 6, pp. 221-240, 1959.

LIST OF REFERENCES (Continued)

58. Vanoni, V. A., Brooks, N. H., and Raichlen, F., "A 40-Meter Precision Tilting Flume", Tech. Memo. No. 67-3, W. M. Keck Laboratory of Hydraulics and Water Resources, California Institute of Technology, Pasadena, California, 1967.

59. Vanoni, V. A., and Brooks, N. H., "Laboratory Studies of the Roughness and Suspended Load of Alluvial Streams", Report M. R. D. Sediment Series No. 11, Sedimentation Laboratory, California Institute of Technology, Pasadena, California, pp. 100-106, 1957.

60. Lamb, D. E., Manning, F. S., and Wilhelm, R. H., "Measurement of Concentration Fluctuations With an Electrical Conductivity Probe", American Institute of Chem. Engineering Journal, Vol. 6, No. 4, pp. 682-685, 1960.

61. Walters, E. R., and Rea, J. B., "Determination of Frequency Characteristics From Response to Arbitrary Input", Jour. Aero. Sciences, Vol. 17, pp. 446-452, 1950.

62. Ogura, Y., "The Influence of Finite Observation Intervals on the Measurement of Turbulent Diffusion Parameters", Jour. of Meteorology, Vol. 14, pp. 176-181, 1957.

63. Laufer, John, "Investigation of Turbulent Flow in a Two-Dimensional Channel", National Advisory Committee for Aeronautic (NACA) Report No. 1053, 1951.

64. Fischer, H. B., "The Effect of Bends on Dispersion in Streams", Water Resources Research, Vol. 5, No. 2, pp. 496-506, 1969.

65. Rice, S. O., "Mathematical Analysis of Random Noise", The Bell System Technical Journal, Vol. 24, No. 1, pp. 46-108, 1945.

66. Townsend, A. A., "The Mechanism of Entrainment in Free Turbulent Flows", Journal Fluid Mechanics, Vol. 26, pp. 689-715, 1966.

67. Okubo, Akira, "A Review of Theoretical Models for Turbulent Diffusion in the Sea", Journ. of the Oceanographical Society of Japan, 20th Anniversary Vol., pp. 286-320, 1962.

APPENDIX

Table A.1 Variances σ^2 (cm^2) of the transverse concentration distributions at various distances ξ and flow levels η; all experiments included.

RUN (d, cm)	η* ξ	61.1	94.1	159.9	225.8	324.1	455.1
507 (1.52)	0.368	4.98	6.45	14.70	14.03	17.23	38.92
	ξ	47.4	106.5	224.9	402.4	639.1	994.1
	η						
705 (1.69)	0.368	2.0	6.6	14.3	32.2	51.4	67.8
	0.750	3.2	7.8	15.1	31.3	50.0	70.2
	AVG†	2.6	7.2	14.7	31.8	50.7	69.0
	ξ	29.1	65.5	138.2	247.3	392.7	610.9
	η						
706 (2.75)	0.368	2.95	6.11	16.84	36.06	59.19	90.76
	0.236	3.52	8.02	18.72	35.66	49.86	85.85
	0.800	3.68	9.77	20.05	34.47	54.09	87.42
	AVG	3.38	7.97	18.54	35.40	54.38	88.01
707 (2.75)	0.368	3.82	8.52	15.92	30.59	52.41	79.94
	0.250	3.10	7.45	16.33	30.58	47.71	74.82
	0.750	3.28	7.93	16.36	36.29	51.85	82.37
	AVG	3.40	7.97	16.20	32.49	50.66	79.04
	ξ	31.9	65.4	99.3	184.0	252.0	
	η						
506 (2.95)	0.30	5.59	10.43	15.50	40.18	41.49	
	0.89	6.55	12.59	16.19	25.42	44.40	
	AVG	6.06	11.51	15.85	32.80	42.95	
	ξ	23.1	52.0	109.8	196.5	312.1	485.5
	η						
703 (3.46)	0.368	3.40	9.34	20.52	35.16	53.38	90.77
	0.095	3.66	8.73	20.81	36.71	58.37	90.06
	0.632	3.84	8.69	19.90	35.90	54.79	87.89
	0.860	3.65	10.44	20.85	33.88	56.19	95.10
	AVG	3.64	9.30	20.52	35.41	55.68	90.96

Table A. 1 (Continued)

RUN (d, cm)	ξ / η	8.2	17.7	36.8	55.8	74.9	103.4	141.5
509 (5.25)	0.368		5.43	12.51	18.07	23.46	36.47	38.42
	0.095		7.78	13.67	17.97	27.60	35.25	38.56
	0.290		8.33	12.49	18.49	25.24	30.67	39.73
	0.480		8.50	16.31	17.60	26.44	34.07	47.50
	0.760		7.40	11.40	19.32	26.27	39.10	47.58
	AVG		7.49	13.28	18.29	25.80	35.11	42.36
511 (5.25)	0.095	1.49	5.23	12.69	16.68	20.27	36.89	37.68
	0.368	1.59	6.40	13.28	19.74	23.27	34.62	44.39
	0.632	2.40	5.21	12.34	19.06	22.71	31.33	42.12
	0.850	0	3.68	12.08	14.49	24.90	33.99	48.73
	AVG	1.37	5.13	12.60	17.49	22.79	34.20	43.23
512 (5.25)	0.850	1.30	4.72	14.37		29.70	47.86	58.34
	0.095	0	6.38	13.20		25.25	29.03	48.88
	0.368	2.29	4.72	10.37		22.45	35.13	37.40
	0.632	1.56	4.28	11.82		24.09	41.82	39.27
	AVG	1.29	5.03	12.44		25.37	38.46	45.97
508 (5.26)	0.368		5.21	13.43	18.43		31.62	31.79
	0.190		5.70	11.99	18.47		30.62	44.90
	0.855		4.91	15.11	17.40		29.48	41.70
	AVG		5.27	13.51	18.10		30.57	39.46
510 (5.26)	0.632	1.82	5.02	13.91	20.86	22.62	31.10	43.16
	0.095	1.63	5.53	13.74	16.04	20.69	31.45	49.55
	0.368	1.61	6.52	11.29	28.90	23.41	36.75	61.00
	0.850	1.42	5.22	13.14	22.19	22.15	42.96	54.76
	AVG	1.62	5.57	13.02	22.00	22.22	35.57	52.12

702 (5.41)	ξ / η	14.8	33.3	70.2	125.7	199.6	310.5
	0.129	4.10	13.09	27.85	57.14	82.72	128.95
	0.391	4.82	14.45	28.29	47.62	76.10	126.74
	0.663	5.26	13.48	27.92	51.94	84.67	123.49
	0.855	4.94	11.67	26.52	48.43	78.04	131.91
	AVG	4.78	13.17	27.65	51.28	80.38	127.27

Table A. 1 (Continued)

RUN (d, cm)	ξ / η	14.5	32.5	68.7	122.9	213.3	303.7
701 (5.53)	0.391	5.10	13.52	25.84	48.67	84.81	121.20
	0.128	4.79	0	28.37	0	92.01	137.24
	0.855	4.59	12.83	29.88	52.16	94.85	140.38
	AVG	4.83	13.21	28.03	50.42	90.56	132.91
	ξ / η	9.2	20.8	43.8	90.0	136.1	
407 (8.66)	0.368	21.2	57.8	100.0	207.4	354.0	
	0.632	21.2	49.0	84.6	210.3	376.1	
	AVG	21.2	53.4	92.3	208.9	365.0	
	ξ / η	7.7	17.4	36.7	75.2	113.9	
404 (10.36)	0.368	23.2	70.5	105.2	262.1	421.0	
	0.632	20.3	60.8	121.0	228.0	396.0	
	AVG	21.8	65.7	113.1	245.1	409.0	
	ξ / η	4.0	8.7	18.0	36.7	50.7	69.4
607 (10.70)	0.368	2.78	6.25	19.10	44.36	61.53	83.86
	0.095	2.47	9.06	15.24	43.25	54.76	80.65
	0.632	2.29	6.03	18.11	48.05	59.13	78.31
	0.850	0	2.51	13.44	33.83	55.13	82.38
	AVG	2.51	5.96	16.47	42.37	57.64	81.30
	ξ / η	7.4	16.7	35.1	62.9	100.0	155.2
704 (10.81)	0.368	8.65	23.47	46.20	79.39	133.89	241.07
	0.095	7.70	24.11	57.84	100.73	147.11	224.09
	0.632	7.32	24.53	48.84	98.30	157.30	252.45
	0.850	5.54	25.56	54.20	99.90	155.24	239.83
	AVG	7.30	24.42	51.77	94.58	148.39	239.36

Table A.1 (Continued)

RUN (d, cm)	ξ / η						
406 (17.07)		4.7	10.6	22.3	45.7	63.3	
	0.368	26.0	64.0	149.0	303.0	420.0	
	0.632	33.6	64.0	154.0	289.0	396.0	
	AVG	29.8	64.0	151.5	296.0	408.0	
708 (17.31)	ξ / η	4.6	10.4	21.9	39.2	62.4	99.4
	0.368	8.08	33.21	79.64	102.28	231.94	336.46
	0.095	6.30	26.15	68.50	120.30	222.51	306.63
	0.632	5.47	26.03	64.68	126.39	194.95	313.21
	0.850	0	0	62.62	100.63	161.81	257.80
	AVG	6.61	28.46	68.86	112.40	202.80	303.53
603 (17.34)	ξ / η	2.5	5.4	11.1	22.7	31.3	42.8
	0.368	3.15	9.34	25.65	43.78	64.58	95.75
	0.095	0	7.57	27.03	54.90	89.74	124.40
	0.632	0	8.63	29.80	58.66	87.52	124.86
	0.850	0	0	25.65	49.19	74.58	105.49
	AVG	3.15	6.39	27.03	51.63	79.11	112.63
709 (21.97)	ξ / η	3.6	8.2	17.3	31.0	49.2	
	0.368	7.91	27.16	75.60	149.09	189.29	
	0.095	0	26.71	69.60	131.89	216.42	
	0.850	0	0	57.18	141.00	198.70	
	AVG	7.91	26.94	67.46	140.66	201.47	

NOTES:

* The first value of η listed is the level of injection η_h. For RUN 511, $\eta_h = 0.051$.

† AVG = averages of the non-zero values of σ^2.

Table A.2. Reference guide to Experiments and Figures

RUN	Flume Ident. Code†	Normal Depth d cm	Figures Where Experiment is Cited	Corresponding Pages
507	S1	1.52	5.9	152
705	S2	1.69	5.9	152
707	S2	2.74	5.8,5.9	148, 152
706	S2	2.75	5.1,5.4,5.9	133, 142, 152
706V	S2	2.75	4.15	111
806	S2	2.77	4.18	118
506	S1	2.95	5.9	152
703	S2	3.46	5.9,5.25	152, 185
509	S1	5.25	5.8,5.9,5.14, 5.15,5.22	148, 152, 166, 168, 180
511	S1	5.25	5.8,5.9,5.11, 5.12,5.15,5.19, 5.20,5.21,5.25	148, 152, 157, 160, 168, 172, 174, 149, 185
512	S1	5.25	5.9,5.11,5.15, 5.16,5.20,5.23, 5.24,5.25	152, 157, 168, 171, 174, 181, 183, 185
508	S1	5.26	4.13,5.9	101, 152
510	S1	5.26	5.9,5.14,5.15, 5.17,5.20	152, 166, 168, 171, 174
802	S2	5.36	6.2,6.6,6.7, 6.8,6.9	190, 197, 202 203, 207
702	S2	5.41	5.8,5.9	148, 152
701	S2	5.53	5.5,5.8,5.9	143, 148, 152
405	R2	6.81	5.3,6.7,6.8, 6.9	135, 202, 203, 207
407	R2	8.66	5.9	152
404	S2	10.36	5.9,6.7,6.8, 6.9,6.10	152, 202, 203, 207, 212
404V	R2	10.36	4.16	112
607	S1	10.70	5.6,5.9	144, 152
704	S2	10.81	5.8,5.11, 5.13,5.18,5.20	148, 157, 161, 172, 174
804	S2	10.84	4.24,6.1,6.2, 6.7,6.8,6.9, 6.15,6.16,6.17, 6.18,6.19	127, 188, 190, 202, 203, 207, 229, 231, 233, 235, 239

Table A.2. (Continued)

RUN	Flume Ident. Code†	Normal Depth d cm	Figures Where Experiment is Cited	Corresponding Pages
904	S2	10.84	4.19,4.20,4.21, 4.22,4.23,6.11, 6.12	120, 121, 123, 124, 126, 216, 217
300	S1	17.00	6.13,6.14	224, 225
406	R2	17.07	5.9,6.2,6.7, 6.8,6.9	152, 190, 202 203, 207
708	S2	17.31	5.2,5.7,5.9	134, 145, 152
708V	S2	17.31	4.16	112
808	S2	17.32	6.4,6.5,6.7, 6.8,6.9	193, 195, 202 203, 207
603	S1	17.34	5.8,5.9	148, 152
709	S2	21.97	4.14,5.9	106, 152

†For flume identification, S denotes smooth boundaries and R rough bottom. Flume 1 is 85-cm side, Flume 2 110-cm.